Sensitivities of Beta Decay Neutrino Experiments to New Physics

James Alexander Lane Canning

A dissertation submitted in partial fulfillment

of the requirements for the degree of

Doctor of Philosophy

of

University College London.

Department of Physics and Astronomy

University College London

August 28, 2024

I, James Alexander Lane Canning, confirm that the work presented in this thesis is my own. Where information has been derived from other sources, I confirm that this has been indicated in the work.

Abstract

Neutrino experiments form a key pillar of the search for physics beyond the Standard Model. Single beta decay experiments are the only direct means of measuring the absolute values of the neutrino masses. In addition, the discovery of neutrinoless double beta decay would imply the existence of the first known Majorana fermion. However, single beta decay experiments also have the opportunity to search for many other types of new physics. This includes new physics operating at higher energy scales as well as the production of new sterile neutrinos, measured through their effect on the energy and angular distributions for the emitted electron. Lorentz violating effects could also have a significant impact through modifications to the Fermi interaction or to the fermion propagators. The sensitivity to this new physics is considered for the next generation of single beta decay experiments, based upon the new technology of Cyclotron Radiation Emission Spectroscopy. Overall, I find significant potential for the improvement of existing limits and novel sensitivities in certain cases. In double beta decay the precise measurement of the spectral shape and decay rate are important for determining the effective double beta decay mass. Whilst neutrinoless double beta decay is still undetected, and dominated by large nuclear matrix element uncertainties, such precision measurements may be essential in the future. To that purpose, I study the impact of two correction factors on the conventional double beta spectrum: radiative corrections to the decay and the electromagnetic interaction between the two emitted electrons. I show the impact they have on the spectrum and the sensitivity of current experiments to their effects.

Impact Statement

Whilst the current best understanding of the fundamental physics that underlies all of existence, the Standard Model, has been shown to have great predictive power, there are still many questions that remain unsolved in the world of particle physics. In order to progress further in our understanding, precise experimental measurements will be taken to search for discrepancies and hints of new physics. In this thesis I aim to highlight some of the ways in which the next generation of experiments can be used to probe for these new effects.

Single beta decay experiments are soon to enter a new technological era in their attempt to measure the mass of the neutrino. The results included here consider a range of different effects which could be measured using these data as well as how improving the experiments to measure additional variables could offer improved or even novel sensitivity to some effects. The search for neutrinoless double beta decay is essential for understanding the fundamental nature of neutrinos. If the process were discovered it would have profound implications not only in particle physics but also in cosmology and astrophysics. I discuss here some of the effects which need to be considered in order to measure this process accurately.

The results included herein should be of interest to both theorists and experimentalists working in neutrino physics and beyond. This work helps to motivate and interpret experimental results in fundamental science. This will maximise the efficiency of these experiments and increase investment in scientific progress. Whilst these results do not have direct technical applications, the development of our understanding of the world has led to many technological advancements which underlie much of modern life.

UCL Research Paper Declaration

1. **For a research manuscript that has already been published:**

   (a) **What is the title of the manuscript?** Sensitivity of Future Tritium Decay Experiments to New Physics

   (b) **Please include a link to or doi for the work:**
   `https://link.springer.com/article/10.1007/JHEP03(2023)144`

   (c) **Where was the work published?** JHEP

   (d) **Who published the work?** Springer

   (e) **When was the work published?** March 2023

   (f) **List the manuscript's authors in the order they appear on the publication:** James A. L. Canning, Frank F. Deppisch & Wenna Pei

   (g) **Was the work peer reviewed?** Yes

   (h) **Have you retained the copyright?** Yes

   (i) **Was an earlier form of the manuscript uploaded to a preprint server?** `https://arxiv.org/abs/2212.06106v2`

   ⊠ *I acknowledge permission of the publisher named under 1d to include in this thesis portions of the publication named as included in 1c.*

2. **For multi-authored work, please give a statement of contribution covering all authors:** The work completed in this paper is largely my own with

some support from my supervisor Frank Deppisch and my fellow student Wenna Pei. In this thesis Figs. 3.1, 3.2, 3.4 and 5.1 were created by F. Deppisch and Fig. 5.3 by W. Pei.

3. **In which chapter(s) of your thesis can this material be found?**

   Chapters 3, 4 & 5

e-Signatures confirming that the information above is accurate :

Candidate: James Canning

Date: 26/03/2024

Supervisor signature: Frank Deppisch

Date: 27/03/2024

Acknowledgements

I would like to thank my supervisor Frank for the many hours of discussion and guidance he has given me over the last few years. I am also grateful for the many interesting conversations I have had with my fellow PhD students Graham, Zhong and Noor and particularly Wenna without whom I couldn't have made it this far. Thank you to everyone who worked hard to organise the different conferences, lectures and events I have attended throughout my PhD, these were not only fascinating experiences to discuss and learn about the broad range of physics research but also invaluable opportunities to connect with other students in the field. Finally, I have to give immense thanks to all my friends and family who have supported me throughout this journey, especially my parents for always having such faith in me.

Contents

List of Figures

List of Tables

Chapter 1

Introduction

The Standard Model of particle physics represents our current best understanding of the subatomic world around us. It is the culmination of over a century of theoretical and experimental work from the discovery of the first fundamental particle, the electron, in 1897 [1] to the detection of the Higgs Boson in 2012 [2, 3]. Neutrinos form a key part of the Standard Model and the outstanding questions that they pose and the experimental discrepancies they highlight mean that they will play a significant role in our next steps as we begin to search beyond the Standard Model.

The neutrino was first posited as the solution to a significant problem challenging the study of radioactive beta decay. In this decay there was seemingly a violation of both energy conservation and spin statistics in its observed decay products (unlike those of alpha and gamma decays which had fixed energies and conserved angular momentum). This led to the postulation by Wolfgang Pauli of an additional, thus-far unseen spin-1/2 particle, the particle that we now know as the 'neutrino' [4]. Such a particle would have to be light enough to not cause a significant nuclear recoil and sufficiently weakly interacting to have remained undetected up to that point. A theory incorporating this particle was quickly developed in a 1933 paper by Enrico Fermi [5] in which he highlighted the potential for measuring the mass of this neutrino by observing the high energy 'endpoint' of the observed electron energy spectrum.

Despite the great challenge of detecting such an elusive particle, the electron neutrino was first detected in 1953 by the work of Reines and Cowan [6]. In their

experiment anti-neutrinos produced in the sun and captured by inverse beta decay led to the dual signatures of an emitted positron and recoiling nucleus which were interpreted as the first direct detection of a neutrino. Given the evidence for three generations of matter in both the quark and leptonic sectors, including the discoveries of the muon [7] and tau [8] in 1937 and 1975, respectively, there was an expectation that further generations of neutrino should also exist. This was confirmed with the detection of their neutrino counterparts, the muon neutrino in 1962 by a collaboration at the Brookhaven National Laboratory [9] and the tau neutrino in 2001 by the DONUT collaboration [10]. Further light generations of neutrinos are not expected. Measurements of the decay rate of the Z boson (which interacts with all known fermions) are consistent with only three generations of matter (provided $m_\nu < M_Z/2 \approx 45.6\,\mathrm{GeV}$) [11]. Furthermore, measurements of the relativistic, effective neutrino degrees of freedom from their impact upon matter clustering and galaxy formation also finds that only 3 generations are to be expected [12].

Throughout this time of discovery, the underlying theory behind how neutrinos interact with the other fundamental particles was being developed. The first of these developments came in the discovery of parity violation in the weak force. Although the strong force had been shown to largely obey parity (i.e., spatial inversion) symmetry, in 1957 Lee and Yang proposed that such a theory might be violated in the weak interaction [13] with the massless (anti-)neutrinos emitted being with a fixed (right) left helicity (using the modern choice for assigning particle/anti-particle status rather than their choice). This was then rapidly confirmed in the groundbreaking experiment by Wu et.al. which found maximal violation of parity as well as charge conjugation symmetry violation [14]. This ultimately led to the conclusion by Feynman and Gell-Mann that the weak force must take the form of a vector-axial interaction, with all of the interacting particles being left-handed and anti-particles being right-handed [15].

However, despite these developments of the weak theory problems still remained. The force was still described as a contact interaction between all four particles involved, this implied non-unitarity for the interaction at high

energies. By building upon the 1954 paper of Yang and Mills that first suggested the idea of gauged symmetries under local transformations of fields [16], Schwinger (1957) [17] first constructed a non-Abelian gauged theory of the weak interaction. This was then extended by Glashow (1961) [18] and Salam & Ward (1964) [19] into a new weak theory involving the addition of a new neutral boson, the *Z*, and requiring manual symmetry breaking to give the heavy bosons the required masses. The issue of artificially inducing symmetry breaking was finally resolved with the theories developed by Englert & Brout [20], Higgs [21] and Guralnik, Hagen & Kibble [22] in 1964. By introducing a massive, charged scalar with a vacuum expectation value they were able to define a mechanism in which the electroweak symmetry was spontaneously broken, with the three massless Nambu-Goldstone bosons generated being absorbed into the three heavy weak bosons, thus giving them mass. This was formalised with the creation of the electroweak theory in 1967 by Weinberg [23] and in 1968 by Salam [24] with the previous weak theory being described as a combination of the weak and hypercharge forces, spontaneously broken by the Higgs mechanism to give the electromagnetic force mediated by the massless photon and the weak force mediated by two charged and one neutral heavy bosons.

At the same time as the development of the weak theory, the strong theory was also being explored to explain the myriad of rapidly and more slowly decaying heavy particles detected in cosmic ray showers [25, 26]. Gell-Mann's 1961 paper on the 'eightfold way' first recognised the underlying pattern in the properties of these heavy states [27]. This led him to subsequently develop in 1964 (simultaneously with Zweig) the underlying theory that all such states, called 'baryons' and 'mesons', were composed of an underlying set of fundamental particles called 'quarks' [28, 29]. This theory, however, had numerous problems, most importantly that such quarks had never been observed as free particles, nor did there seem to exist other massless, long-range bosons that could mediate such a force in the way the photon does for quantum electrodynamics (QED) [30]. Whilst the development of Higgs' spontaneous symmetry breaking allowed for the giving of mass to inter-

mediate bosons, it was the work of Gross & Wilczek [31] and Politzer [32] who recognised that the asymptotic freedom (i.e. weakening at short distances) of non-abelian gauge theories better matched the experimental data coming from collider experiments for the internal properties of baryons and mesons. This formulation of the strong force introduced three new integer 'colour' charges (called 'red', 'blue' and 'green') with the force being mediated by eight massless bosons called 'gluons'.

With this development, the theoretical foundations for the Standard Model were complete. Three generations of matter interact through three fundamental forces, the strong, the weak and the hypercharge. At lower energies the vacuum expectation value of the Higgs spontaneously breaks the electroweak segment, giving masses to the weak bosons and leaving a residual electromagnetic interaction. This mechanism also gives masses to all of the fermions, apart from the neutrinos which remain massless due to lacking a right-handed counterpart and a coupling to the Higgs.

Despite the immense predictive power of the Standard Model, for phenomena such as the electron magnetic moment [33] and the existence of the weak bosons [34, 35], there are still many outstanding problems which mean that the theory is incomplete. Some of these are theoretical problems: the question of why the Higgs mass is so small when it is expected to receive very large quantum corrections from its interactions with high energy physics [36]; the unexplained absence of a strong CP violating phase when it is expected to be of O(1) [37], and the fact that the SM has 19 free parameters whose values are unpredicted by theory (or can take any value within a particular range) [38]. Others are experimental discrepancies including the anomalous muon magnetic moment as measured at Fermilab [39] and the lack of direct detection of dark matter or energy [40, 41].

One further problem for the Standard Model is the discovery of neutrino oscillations and its implication for neutrino masses. The possibility of neutrinos oscillating between different flavour states was first suggested by Pontecorvo in 1968 [42] building upon his previous work on neutrino oscillations and the suggestion of Maki, Nakagawa and Sakata that the flavour states of neutrinos may be mixings

of mass states [43]. Pontecorvo accurately predicted that terrestrial experiments to measure the flux of electron neutrinos produced by the sun would find a deficit compared to that calculated using solar models, a result verified by the Homestake experiment in 1968 [44]. The final proof that this reduction was being caused by oscillations came jointly from the Super Kamiokande, SNO and KamLAND experiments between 1999 and 2003 [45, 46, 47]. These results had profound consequences as they implied that at least two of the three neutrino generations have mass, a result inconsistent with the Standard Model [48] [1].

Given the discovery of neutrino masses, neutrinos initially appeared to be a potential candidate for dark matter with, if they were the sole contributor, their masses being required to satisfy $\sum m_\nu = 15$ eV [50]. However, this is now known to be incompatible with many different measures of the neutrino mass. Experiments measuring the matter distribution of the universe, such as Planck, are sensitive to neutrinos because their free streaming erased anistropies in the early universe. However, such bounds are highly model dependent and vary significantly with the choice of data sets and free parameters. Some analyses have placed limits in the range $\sum m_\nu < 0.12 - 0.54$ eV at 95% CL [51]. A confirmed measurement of this quantity could potentially provide information not only about the absolute neutrino masses but also their mass ordering, given that the oscillation mass splittings imply limits on the sum of masses of $\sum m_\nu \gtrsim 0.06$ eV or 0.10 eV depending upon which neutrino is the lightest.

Whilst oscillation experiments are able to determine the difference between neutrino masses, they are insensitive to their absolute value and give no indication as to how their masses are generated. In addition to cosmological measures the other two currently competitive ways of measuring their absolute values are through single beta decay and neutrinoless double beta decay. Single and double beta decay, the subjects of this thesis and explained in greater detail in future chapters, involve the nuclear decay in which $d \rightarrow u + e^- + \overline{\nu}_e$, where u/d are up/down

---

[1]Alternative explanations for neutrino oscillations, not requiring neutrino masses, include Lorentz/CPT violation which add terms which mix the different neutrino flavours. However, so far it has not been possible to reproduce all of the neutrino oscillation experimental results using such a model [49].

quarks, e^- is an electron and $\overline{\nu}_e$ is an electron anti-neutrino. Single beta decay is sensitive to the neutrino mass through its impact on the energy spectrum of the emitted electron [52]. In neutrinoless double beta decay, if the neutrino has equal particle and anti-particle states (called 'Majorana') then the double decay can occur $2d \rightarrow 2u + 2e^-$. The rate of this process would be directly dependent upon the neutrino masses because of the requirement of a neutrino helicity flip and would identify the neutrino as the first known Majorana fermion [53].

Single beta decay experiments are the only guaranteed method to directly measure the neutrino mass (with double beta decay experiments requiring that the neutrino is found to be Majorana). The current best limit comes from the KATRIN experiment which measures the integrated spectrum close to the maximum electron energy and has placed a limit on the effective single beta decay mass (defined in Section 3.3.1) of $m_\beta < 0.8$ eV [54]. Whilst the experiment is currently still in operation, there are limitations on how small a mass it can measure given its underlying technology. This has led to work being done on a new generation of experiments based upon the technique of Cyclotron Radiation Emission Spectroscopy (CRES) which will attempt to use the detection of cyclotron radiation to precisely measure the individual electron energies. This, along with a change to use atomic rather than molecular tritium, will allow for unprecedentedly high energy resolution and statistics along with sensitivity to a much greater range of the energy spectrum. Development is currently running both for the Project 8 experiment [55] and the CRES Demonstration Apparatus (CRESDA) [56]. For this future generation of experiments there is the potential of sensitivity to many additional effects beyond those for which they are primarily designed, a selection of these being the subject of this thesis. There is also continued work being performed on increasing the magnitude and precision of double beta decay experiments including for LEGEND-1000 [57] and KamLAND2-Zen [58]. Crucially, if neutrinoless double beta decay is discovered, precision measurements of the rate will be essential as an additional means of identifying the neutrino masses. This thesis will discuss two corrections that affect the theoretical prediction for this rates.

In this thesis I will be studying the effects of multiple different examples of exotic physics within single beta decay as well as an additional correction to the exotic process of neutrinoless double beta decay. In Chapter 2, I will describe in greater detail the foundations of the Standard Model and how neutrinos sit within it. In Chapter 3, I will: derive the expected energy and angular spectra for single and double beta decay; explain the correction factors to this derivation; describe the current and future single and double-beta decay experiments and give my statistical approach to measuring exotic physics. In Chapter 4, I will analyse the effect of exotic currents on the single beta decay spectrum and in Chapter 5, I will expand this to the production of heavy, sterile states. In Chapter 6, I will look at the sensitivity to two Lorentz violating effects on the single-beta decay spectrum. Finally, in Chapter 7, I will explain how to apply two key corrections to the double-beta decay spectrum and the significance of their impact. A summary of results will be given in the final conclusion in Chapter 8.

Chapter 2

The Standard Model and Beyond

In this chapter I will give a description of the Standard Model as it currently stands. Working up from the underlying Lorentz structure I discuss the particles that make up the Standard Model, how they interact and how their masses are generated. Finally, I will discuss the ways in neutrino oscillations imply physics beyond the Standard Model and how neutrino masses could be added.

2.1   Lorentz Structure

The Standard Model of particle physics is formulated in the mathematical language of a quantum field theory (QFT) - a theory of particles evolving under local interactions which obey special relativity. The fundamental objects (i.e. particles) of this theory are states of well defined Lorentz structure. They are characterised by their representation under the two copies of the Lie algebra $sl(2, \mathbb{C})$ which make up the connected component of Lorentz transformations (i.e. boosts and rotations) which neither invert the time nor spatial directions. This representation is denoted by the label (i, j) where i and j take integer or half-integer values (e.g. $0, 1/2, 1...$). This is often simplified for the three types of particle observed in nature, with these referred to as spin-0 for $(0, 0)$, spin-1/2 for $(1/2, 0)$ or $(0, 1/2)$ and spin-1 for $(1/2, 1/2)$. These particles are then further grouped into two categories, bosons and fermions. Bosons are those states with integer spin, they also obey the spin-statistics law that under the exchange of identical bosons any interaction will remain unchanged. Fermions are states with half-integer spin which obey the anti-commutation relation

Name	Scalar	Weyl Spinor		Dirac Spinor	Vector
Notation	ϕ	ψ_L	ψ_R	Ψ	A^μ
Representation	$(0,0)$	$\left(\frac{1}{2},0\right)$	$\left(0,\frac{1}{2}\right)$	$\left(\frac{1}{2},0\right) \oplus \left(0,\frac{1}{2}\right)$	$\left(\frac{1}{2},\frac{1}{2}\right)$

Table 2.1: Particle categories as defined by their Lorentz properties.

that two interactions related by the exchange of two identical states are opposite in sign. This has the significant property of forbidding two fermions from occupying the same quantum state, a law now known for its 1925 discoverer as the Pauli exclusion principle [59].

All particles are expected to follow the special relativity dispersion relation $E^2 - |\vec{p}|^2 = m^2$ where E is its energy, $|\vec{p}|$ the magnitude of its momentum and m its mass. In the language of a QFT, for a scalar field $\phi(x)$ this becomes the Klein-Gordon equation:

$$\partial_\mu \partial^\mu \phi = m^2 \phi, \tag{2.1}$$

where $\mu = 0,...,3$ labels the temporal and spatial derivatives. The definition of the state 'scalar' and others is given in Table 2.1.

The equivalent expression for the vector state A^μ is the Proca equation:

$$\partial_\mu \partial^\mu A^\nu - \partial^\nu \partial_\mu A^\mu + m^2 A^\nu = 0. \tag{2.2}$$

For spinors, there are two different states corresponding to the two different spin-1/2 representations. These are labelled as ψ_L and ψ_R for reasons that will be explored later. It is impossible to construct equations for each of these spinors individually that also include a mass. The equation that can be derived is for massless spinors which will satisfy

$$i\sigma^\mu \partial_\mu \psi_L = 0, \quad i\overline{\sigma}^\mu \partial_\mu \psi_R = 0 \tag{2.3}$$

where $\sigma^\mu = (1, \sigma^i)$, $\overline{\sigma}^\mu = (1, -\sigma^i)$ form the basis for hermitian 2×2 matrices. In

order to create a term involving mass a new combined object needs to be created, Ψ, which transforms in the representation $(1/2, 0) \oplus (0, 1/2)$. This has:

$$\Psi = \begin{pmatrix} \psi_L \\ \psi_R \end{pmatrix}, \qquad (i\gamma^\mu \partial_\mu - m)\Psi = 0, \qquad (2.4)$$

where Ψ is here written explicitly in the chiral basis, the γ^μ are 4×4 matrices and satisfy the defining relation $\frac{1}{2}\{\gamma^\mu, \gamma^\nu\} = \eta^{\mu\nu}$, the metric tensor. In this equation, the mass term couples together the two types of Weyl spinors. Showing this again in the chiral basis, in terms of the two Weyl fields this equation is

$$\begin{pmatrix} i\sigma^\mu \partial_\mu \psi_L - m\psi_R \\ i\overline{\sigma}^\mu \partial_\mu \psi_R - m\psi_L \end{pmatrix} = 0, \qquad (2.5)$$

which shows explicitly how introducing a mass term necessarily requires mixing of right and left-handed Weyl fermions which is why massive equations cannot be defined for them each individually.

Ultimately, the above Eqs. (2.1), (2.2) and (2.4) give the free evolution of these spin-0, 1/2 and 1 states.

2.2 Gauge Theories

Given the equations that dictate the free propagation of these fields, the next key stage is to consider how to include interactions. In order to describe this, it is more helpful to change to using the Lagrangian formalism. For example, the appropriate Lagrangian for a spin-1/2 fermion which will obey the Dirac equation as above is

$$\mathscr{L}_{\text{Dirac}} = \overline{\Psi}(i\gamma^\mu \partial_\mu - m)\Psi, \qquad (2.6)$$

where $\overline{\Psi} = \Psi^\dagger \gamma^0$ and $\dagger$ hermitian conjugation.

Interestingly, such a Lagrangian has a symmetry (or redundancy) in the choice of Ψ with the redefinition $\Psi \to e^{i\alpha}\Psi$, for α a real number, leaving the resulting Lagrangian and thus state evolution unchanged. This implies that there is an under-

lying redundancy in the choice to use a 4-component spinor to describe the state. This arbitrariness means that any two states related by this transformation must in fact be the same state, without any physical difference. Taking this even further, if the principle is maintained that all physical interactions must be local, and thus the choice of notation at one place in space-time is independent of the choice at another, it should be possible to redefine the spinor at each point in space-time independently of each other. In other words it should be possible to take $\alpha \to \alpha(x)$, a function of space-time co-ordinates. However, such a change clearly causes a problem given the derivative with the transformation giving

$$\partial_\mu \Psi \to \partial_\mu (e^{i\alpha}\Psi) = e^{i\alpha}\partial_\mu \Psi + ie^{i\alpha}\Psi\partial_\mu \alpha. \tag{2.7}$$

The solution to this comes in recognising that there are two objects in this term, it can be required that as well as the transformation of Ψ there should also be a change in ∂_μ to maintain the form of the expression. The modified form of this, called D_μ the 'covariant' derivative, will transform and can be found by requiring

$$D_\mu \Psi \to D'_\mu (e^{i\alpha}\Psi) \overset{!}{=} e^{i\alpha}D_\mu \Psi,$$
$$\Rightarrow D'_\mu = D_\mu - i(\partial_\mu \alpha). \tag{2.8}$$

Inspiration for where such an object can be found comes from looking at the Proca equation once more. In the massless case the Lagrangian for this is given by

$$\mathscr{L}_{\text{Proca}} = -\frac{1}{4}F_{\mu\nu}F^{\mu\nu}, \quad F^{\mu\nu} = \partial^\mu A^\nu - \partial^\nu A^\mu. \tag{2.9}$$

This equation again has a gauge redundancy with the transformation $A^\mu \to A^\mu + \partial^\mu \alpha$ describing the same object. By comparing this to what is required from the modified derivative, it's clear that the required transformation properties can be satisfied by using the form $D_\mu = \partial_\mu - iA_\mu$ with the A_μ and the Ψ transforming simultaneously as given.

The question then arises what happens if there are multiple fermionic fields in

our theory. Are they each allowed to transform with their own individual α each of which simultaneously transforming a different A_μ? In principle, yes. However, it is also possible that they could all interact with the same vector field but with different strengths. Thus the final form of the covariant derivative is chosen to be

$$D_\mu = \partial_\mu - iqA_\mu \to \partial_\mu - iqA_\mu - iq\partial_\mu\alpha, \quad \Psi \to e^{iq\alpha}\Psi \qquad (2.10)$$

where q is a number which can take different values for different fermions.

Looking back at the Dirac Lagrangian, it can now be seen that there has been induced an interaction term $\mathscr{L}_{A\Psi\Psi} = -iqA_\mu\overline{\Psi}\gamma^\mu\Psi$ allowing for the exchange of four-momentum between the different states represented by the spinors and vector. The value of q is then the strength of this interaction and is given the name of 'charge'. Overall, what has been described is called a U(1) gauge symmetry, so called because the transformation of the fermion is given by an element of the group U(1). This is the basis for quantum electrodynamics.

Whilst U(1) is the simplest example of a gauge theory, it is possible to consider the use of other groups to describe interactions involving fermions. This is called a non-abelian gauge theory when the chosen group is non-commutative. These types of groups have multiple degrees of freedom with the transformations most often being expanded in a basis of 'generator' matrices. Thus in going from U(1) to a non-abelian theory, $\alpha \to \alpha^a T^a$ where the T^a form a basis of matrices for the transformation and $\alpha^a = \alpha^a(x)$ are functions which parameterise the space-time dependent transformations. Different objects transform under the action of this group according to their representation under the group. There are an infinite number of different representations for the SU(N) groups but of interest here are the trivial, fundamental and adjoint representations. Whilst the spinors could transform under any representation, for all cases considered within the standard model the spinors will transform either trivially or under the fundamental representation of the group. This means that a number of spinors equal to the dimension of this representation (which for SU(N) is N) will be coupled to each other and are often depicted as a single vector transforming under the fundamental. Similarly to before, this takes

the form

$$\begin{pmatrix} \Psi_1 \\ \vdots \\ \Psi_N \end{pmatrix} \rightarrow \begin{pmatrix} \Psi'_1 \\ \vdots \\ \Psi'_N \end{pmatrix} = \exp(iq\alpha^a T^a) \begin{pmatrix} \Psi_1 \\ \vdots \\ \Psi_N \end{pmatrix}, \tag{2.11}$$

for T^a being $N \times N$ matrices in the fundamental representation. This gives the transformed fields Ψ' as a linear combination of original fields Ψ.

From the way in which the vector fields have been included in the covariant derivative, they will be promoted to $N \times N$ matrices. This is often decomposed using the generators of the group into a set of $N^2 - 1$ fields written as $A_\mu^a(X)$. This field will transform in the adjoint representation of the group as

$$A_\mu^a T^a \rightarrow A'^a_\mu T^a = A_\mu^a \, UT^aU^{-1} + (\partial_\mu U) \, U^{-1}, \tag{2.12}$$

where $U = \exp(iq\alpha^a T^a)$ (this expression clearly reduces to the original case when U is abelian). This, again, gives the transformed fields A'^a as a linear combination of original fields A^a.

Analogously to before, the covariant derivative is defined as $D_\mu = \partial_\mu - iqA_\mu$ where now all parts are $N \times N$ matrices with an implicit identity matrix multiplying the derivative. In index notation, this gives a Dirac Lagrangian

$$\mathscr{L}_{\text{Dirac}} = \overline{\Psi}_i \gamma^\mu (\partial_\mu \delta_{ij} - iqA_\mu^a (T^a)_{ij}) \Psi_j, \tag{2.13}$$

with $i, \, j$ running from 1 to N and a taking values from 1 to the number of generators, $N^2 - 1$.

To account for the non-abelian nature of these vector fields a redefinition of the electromagnetic field tensor is required to the form

$$F^{\mu\nu} = \frac{i}{q}[D^\mu, D^\nu] = \partial^\mu A^\nu - \partial^\nu A^\mu - iq[A^\mu, A^\nu], \tag{2.14}$$

$$\Rightarrow F_a^{\mu\nu} = \frac{i}{q}[D^\mu, D^\nu]_a = \partial^\mu A_a^\nu - \partial^\nu A_a^\mu + qA_b^\mu \, A_c^\nu f_{abc}, \tag{2.15}$$

where the square brackets denote commutation and f_{abc} is the structure constant of the group in question defined as $[T^a, T^b] = f_{abc}T^c$ for the generators of the group.

The new form of the Lagrangian, in order to preserve its gauge invariance, is

$$\mathscr{L}_{\mathrm{F}^2} = -\frac{1}{2}Tr[F_{\mu\nu}F^{\mu\nu}] = -\frac{1}{4}F_{\mu\nu}^a F^{a,\mu\nu}, \tag{2.16}$$

where the normalisation of the generators of the adjoint has been chosen to have $Tr[T^a T^b] = \frac{1}{2}\delta^{ab}$.

This final result is significant as it introduces triplet and quartic terms in the Lagrangian for the vector fields, meaning they can interact directly between themselves. These terms are proportional to the structure constant f_{abc} and thus vanish for abelian theories. This will cause substantial differences in the behaviour of the fields, as described below.

This entire procedure can also be applied to scalar fields. The scalar will transform in the same way as the spinor in Eq. (2.11), in the fundamental representation of the group. The Klein-Gordon equation is modified in the same way as the Dirac equation with the derivative taking its covariant form to give (in the case of a complex scalar)

$$\mathscr{L}_{\mathrm{KG}} = (D_\mu\phi)^*(D^\mu\phi) - m^2\phi^*\phi. \tag{2.17}$$

Due to the presence of two copies of the covariant derivative, there will be terms which appear quadratically in the vector field. This will have significant consequences later.

2.3 The Standard Model

Given these fundamental mathematical building blocks, it is now possible to describe the Standard Model. The Standard Model is composed of bosons, of spin 0 and 1, and fermions, of spin-1/2. Its matter (fermionic) content is composed of three generations, with five types of Weyl fermion in each generation. Notably, all of these fields in the Standard Model are massless, apart from the Higgs which has

	SU(3)$_C$	SU(2)$_W$	U(1)$_Y$
H	**1**	**2**	$\frac{1}{2}$
Q_L	**3**	**2**	$\frac{1}{6}$
u_R	**3**	**1**	$\frac{2}{3}$
d_R	**3**	**1**	$-\frac{1}{3}$
l_L	**1**	**2**	$-\frac{1}{2}$
e_R	**1**	**1**	-1
G	**8**	**1**	0
W	**1**	**3**	0
B	**1**	**1**	0

Table 2.2: Representations (SU(3)$_C$ and SU(2)$_W$) and hypercharges (U(1)$_Y$) of all Standard Model fields.

a mass-like term. Including masses for gauge fields is forbidden because it violates gauge symmetry for all abelian and non-abelian fields. Similarly, combining left and right Weyl spinors into a Dirac spinor is forbidden as the left and right spinors are charged differently under the different gauges.

The following is a description of the spin-1 vector fields, the five fermionic fields and the spin-0 Higgs Boson. A summary of the UV Standard Model components is given in Table 2.2.

2.3.1 Spin-1 Vectors

There are three spin-1 vector fields within the Standard Model, each one mediating one of the three fundamental forces. The Lagrangian for their kinetic terms is

$$\mathcal{L}_{\text{Vector}} = -\frac{1}{2}Tr[G_{\mu\nu}G^{\mu\nu}] - \frac{1}{2}Tr[W_{\mu\nu}W^{\mu\nu}] - \frac{1}{4}B_{\mu\nu}B^{\mu\nu}. \qquad (2.18)$$

The SU(3)$_C$ kinetic term, $G_{\mu\nu}$ and the SU(2)$_W$ kinetic term, $W_{\mu\nu}$, are matrices and functions of their respective fields, G_μ and W_μ, as in Eq. (2.14) and the U(1)$_Y$ kinetic term, $B_{\mu\nu}$, is a function of B_μ as in Eq. (2.9).

The force obeying the U(1)$_Y$ abelian symmetry is called the hypercharge and has only one mediating field. Fermions charged under this force have different charges which are expressed as multiples of the fundamental charge g'. The force

with the non-abelian symmetry $SU(2)_W$ is called the weak force. The number of interacting states, given by the dimension of the adjoint of the symmetry, is three. All states charged under this symmetry have a charge given as $q = g$. Finally, the other non-abelian symmetry, $SU(3)_C$, is called the strong force. This has eight mediating fields and a fundamental charge $q = g_s$. For both of the non-abelian forces, the form of the Lagrangian means that there will be self-interactions between the vector fields of the same type, with both three and four point vertices.

2.3.2 Quarks

The fermion states which are charged under the SU(3) gauge group are called quarks. They come in three varieties and follow the Lagrangian

$$
\begin{aligned}
\mathscr{L}_{\text{Quark}} = & \overline{Q_L} i\gamma_\mu (\partial^\mu - ig_s G^\mu - igW^\mu - i(g'/6)B^\mu)Q_L \\
& + \overline{u_R} i\gamma_\mu (\partial^\mu - ig_s G^\mu - i(2g'/3)B^\mu)u_R \\
& + \overline{d_R} i\gamma_\mu (\partial^\mu - ig_s G^\mu + i(g'/3)B^\mu)d_R,
\end{aligned}
\tag{2.19}
$$

where the inclusion of a further two generations with identical charges has been omitted.

The left-handed Weyl fermions of this type are charged under both $SU(3)_C$ and $SU(2)_W$. They are in the fundamental representation of $SU(3)_C$, with an interaction between 3 different 'colour' varieties, and are also charged under $SU(2)_W$, meaning they have 2 'weak' varieties. Overall, this means there are a total of six states which carry this level of charge. They also all carry a hypercharge of 1/6.

Additionally, there are two right-handed, quark Weyl fermions. Both types are charged under $SU(3)_C$ but not under $SU(2)_W$, meaning that there are 3 varieties of each. They are differentiated by their hypercharge, with one, called up-type, having hypercharge 2/3 and the other, called down-type, having hypercharge $-1/3$.

2.3.3 Leptons

Those fermion states not charged under $SU(3)_C$ are called leptons. They come in two types with a Lagrangian

$$\mathscr{L}_{\text{lepton}} = \overline{l_L} i \gamma_\mu (\partial^\mu - i g W^\mu + i(g'/2) B^\mu) l_L$$
$$+ \overline{e_R} i \gamma_\mu (\partial^\mu + i g' B^\mu) e_R, \tag{2.20}$$

where again a further two identically charged generations have been omitted.

The left-handed fermions of this type are charged under $SU(2)_W$ and thus come in two varieties. They also carry hypercharge -1/2. The right-handed fermions are uncharged in $SU(2)_W$ and thus come only in a single variety called electron-like. They do, however, carry a hypercharge of -1.

2.3.4 Higgs Boson

The Higgs boson is a spin-0 boson which interacts with nearly all of the other Standard Model fields. The kinetic part of the Lagrangian for the Higgs, including interactions with the other bosons, is

$$\mathscr{L}_{\text{Higgs}} = (D_\mu H)^\dagger D^\mu H + \mu^2 H^\dagger H - \lambda (H^\dagger H)^2, \tag{2.21}$$
$$D_\mu = \partial_\mu - i g W_\mu - i(g'/2) B_\mu, \tag{2.22}$$

where μ^2 and λ are self-coupling constants. It is worth noting that whilst $\mu^2 H^\dagger H$ looks similar to the conventional mass term for a scalar field, the sign is opposite to that in Eq. (2.17). This is very significant for the form the Standard Model takes at low energies.

The Higgs boson is a scalar charged under $SU(2)_W$ and thus comprised of two scalar fields. It also carries a hypercharge of 1/2. As well as interacting with the other bosons and itself, it also couples to nearly all of the fermions through its Yukawa interactions. Crucially these interactions include both left and right handed

Weyl fermions. They take the form

$$\mathscr{L}_{\text{Yukawa}} = -Y_{ij}\overline{d_{Ri}}H^{\dagger}Q_{Lj} - \tilde{Y}_{ij}\overline{u_{Ri}}\tilde{H}^{\dagger}Q_{Lj} - \lambda_{ij}\overline{e_{Ri}}H^{\dagger}l_{Lj} + h.c., \qquad (2.23)$$

where $\tilde{H} = i\sigma^2 H^*$, for σ^2 the Pauli matrix, Y_{ij}, $\tilde{Y}_{ij}$ & λ_{ij} are coupling constants coupling the ith and jth generations of each type of fermion and $h.c.$ denotes taking the hermitian conjugate to maintain hermiticity. $\tilde{H}$ is merely a field redefinition of H with a hypercharge -1/2.

In determining the types of Yukawa couplings possible, it is important to ensure that the combination of fields within the Lagrangian are gauge invariant. Firstly, this means that the two fermions must be both quarks or both leptons to maintain SU(3)$_C$ invariance. SU(2)$_W$ invariance is maintained by coupling the Higgs to exactly one left-handed state. Finally, U(1)$_Y$ is ensured through cancellation of the hypercharges, this dictates whether H or $\tilde{H}$ is used (noting that the hermitian conjugation of the right-handed fermion and H inverts the charge). Overall, there are three combinations of fermions that meet these conditions: the left-handed quark fields Q_L with either of the right-handed up-like u_R or down-like d_R and the left-handed lepton field l_L with the right-handed electron-like e_R. For each of these pairings there are three generations that can be used for either of the left and right-handed fermions with the value of the Yukawa coupling constants (Y, $\tilde{Y}$ or λ) being different for each choice of generational pair.

2.4 Higgs Field Perturbations and the Low Energy Standard Model

The properties of the Higgs field depend heavily on the form of the potential it feels due to its self interaction: $V(H^{\dagger}H) = -\mu^2 H^{\dagger}H + \lambda(H^{\dagger}H)^2$. In the early universe, the Higgs field existed within a heat bath with all of the other Standard Model fields at finite temperature and interacting with the Higgs field. These interactions provided a positive quantum correction to the Higgs potential, modifying the quadratic part such that $-\mu^2 \rightarrow aT^2 - \mu^2$ with T the temperature and a a constant function of

the coupling parameters. When T is sufficiently large this quadratic prefactor will thus be positive. In this case, the minimum of the Higgs potential will be at $H = 0$ and fluctuations in the field can be calculated about this as normally expected in Quantum Field Theories. However, as the universe cooled this prefactor changed to being negative, leading to a phase transition. Once $T = 0$, the Higgs potential has a different minimum at $\langle H \rangle^\dagger \langle H \rangle = \mu^2/(2\lambda) = v^2/2$. Instead of being perturbed around 0, at low temperatures the Higgs field should instead be evaluated around this minimum value (also known as the expectation value as it is the average value for small fluctuations). The field H is reparameterised as $H = \langle H \rangle + h$ with $\langle H \rangle$ being the constant expectation value and h the dynamical field. The solution to $\langle H \rangle^\dagger \langle H \rangle = \mu^2/(2\lambda) = v^2/2$ constrains only one of the Higgs' four degrees of freedom, but using the SU(2)$_W$ and U(1)$_Y$ redundancies the conventional choice can be made to take $\langle H \rangle^\dagger = 1/\sqrt{2}(0, v)$ (writing H explicitly as an SU(2)$_W$ doublet). This however creates a problem, as the new dynamical field, h, no longer follows the gauge transformation properties of H and appears to break the gauge invariances of the terms in which the Higgs appears in the Lagrangian. This can be seen explicitly by looking at what happens to the Higgs potential

$$
\begin{aligned}
V(h) =& \lambda \left(H^\dagger H - \frac{\mu^2}{2\lambda} \right)^2 - \frac{\mu^4}{4\lambda} \\
=& \lambda \left(\frac{v^2}{2} + \langle H \rangle^\dagger h + h^\dagger \langle H \rangle + h^\dagger h \right)^2 - \frac{\mu^4}{4\lambda}.
\end{aligned}
\tag{2.24}
$$

If the field h is transformed using the usual SU(2)$_W$ or U(1)$_Y$ gauge groups then the constant parts of this expression and $h^\dagger h$ are still invariant. However, the two terms of the form $h^\dagger \langle H \rangle$ do not follow the gauge symmetry under either of these as the expectation value is constant and doesn't cancel out the gauge transformation in h.

Crucially, the underlying gauge invariances have not been broken. This is merely a redefinition of the Higgs field with gauge transformations of the original field H still obeying the appropriate invariance. However, at low energies the perturbations around the minimum, the behaviour that will manifest as physical particles in the theory, do not follow this symmetry and thus the gauge redundancy appears

to have been lost. This result has great significance not only in the Higgs sector but for all the particles that have interactions with the Higgs. New combinations of these particles will be chosen which will all no longer directly follow the gauge symmetries. The boundary between the full and low energy forms of the Standard Model is the expectation value of the Higgs, at which the difference between the choice of H or h as the dynamical field is significant.

For the fermions, the impact of this is felt due to the Yukawa interactions which now introduce Dirac mass terms. For example, in the leptonic sector writing the left-handed pair as an explicit SU(2)$_W$ doublet, $l_L = (v_L, e_L)^\mathsf{T}$, gives

$$\mathscr{L}_m = Y\, \bar{e}_R\, \frac{1}{\sqrt{2}} \begin{pmatrix} 0 \\ v \end{pmatrix}^\dagger \begin{pmatrix} v_L \\ e_L \end{pmatrix} + h.c. = \frac{Yv}{\sqrt{2}}\, \bar{e}_R\, e_L + h.c., \qquad (2.25)$$

where we have chosen the same letter e to refer to the left and right-handed fermion fields to denote that they are now coupled in a Dirac spinor field through their mass $m = Yv/\sqrt{2}$. This procedure can be repeated for all the Yukawa coupling terms, giving mass to the new Dirac states of the electron, the up quark and the down quark. Each generation of fermionic states will have different Yukawa coupling values and thus will pick up different masses. This has led to the use of separate names for each of the fermions of each generation. The full way in which this is realised is explored later in Section 2.5. Notably, the only fermion to not obtain a mass in this process is the neutrino which lacks a right-handed Weyl spinor v_R and a Yukawa coupling to the Higgs. The addition of such a particle would be simple but is not included in the Standard Model as there is no direct evidence for the existence of such a state. Methods for generating neutrino masses will be discussed later.

A similar process of mass generation happens to the bosons that couple to the Higgs field through the covariant derivative kinetic term

$$\mathscr{L}_{\text{Higgs}} \supset (D_\mu H)^\dagger (D^\mu H)$$

$$= \left(\left(\partial_\mu - \frac{ig'}{2} B_\mu - ig W_\mu \right) H \right)^\dagger \left(\left(\partial^\mu - \frac{ig'}{2} B^\mu - ig W^\mu \right) H \right). \qquad (2.26)$$

Expanding the W boson in the basis of the generators of SU(2) symmetries, and expanding H around its expectation value and rearranging gives

$$\mathscr{L}_{\text{Higgs}} \supset \frac{g^2 v^2}{4} \frac{1}{\sqrt{2}} \left(W_\mu^1 - iW_\mu^2 \right) \frac{1}{\sqrt{2}} \left(W^{\mu 1} + iW^{\mu 2} \right)$$
$$+ \frac{(g^2 + g'^2) v^2}{8} \frac{1}{\sqrt{g^2 + g'^2}} (g W_\mu^3 - g' B_\mu) \frac{1}{\sqrt{g^2 + g'^2}} (g W^{\mu 3} - g' B^\mu). \qquad (2.27)$$

In other words, the bosonic fields are recombined into new states $W_\mu^\pm = 1/\sqrt{2}(W_\mu^1 \pm iW_\mu^2)$ and $Z_\mu = 1/\sqrt{g^2 + g'^2} \ (g W_\mu^3 - g' B_\mu)$ with masses $M_W = gv/2$ and $M_Z = \sqrt{g^2 + g'^2} \ v/2$, respectively. Significantly, the orthogonal field combination $A_\mu = 1/\sqrt{g^2 + g'^2} \ (g' W_\mu^3 + g B_\mu)$ does not pick up a mass term. This is the field that shall henceforth be called the 'photon'.

As stated before, gauge transformations are broken by mass terms which take the form $W_\mu W^\mu$. Again, in this case the symmetries are not broken because terms of this form have arisen from gauge invariant terms involving the Higgs, they are merely being obscured by the choice of new field definitions which do not individually have these symmetries. For these fields, the interaction they mediated has been broken, they will continue to impact upon the fermions at low energies only through effective operators (as discussed later). However, for the field that remains massless there is a new gauge symmetry that can be defined. Rearranging of the kinetic terms for the weak and hypercharge shows that A^μ can propagate as a massless boson following Lorentz symmetry. Furthermore, the re-expression of the covariant derivative in terms of this field takes the form,

$$D^\mu \supset -ie \, A^\mu (T^3 + Y), \qquad (2.28)$$

where T^3 and Y are elements of the representations of the corresponding fermion being acted upon ($T^3 = \sigma^3$ or 0 depending upon whether the field is charged under SU(2)$_W$ and Y is the hypercharge multiplied by the identity), $e = gg'/\sqrt{g^2 + g'^2}$ and $\sin \theta_W = g'/\sqrt{g^2 + g'^2}$ is the Weinberg angle.

The residual gauge symmetry mediated by A^μ is U(1)$_Q$ with the subscript to

	SU(3)$_C$	U(1)$_Q$	Massive?
h	**1**	0	✓
u, c, t	**3**	$\frac{2}{3}$	✓
d, s, b	**3**	$-\frac{1}{3}$	✓
e, μ, τ	**1**	-1	✓
ν_e, ν_μ, ν_τ	**1**	0	✗
G	**8**	0	✗
$W^\pm$	**1**	± 1	✓
Z	**1**	0	✓
A	**1**	0	✗

Table 2.3: Representations (SU(3)$_C$) and charge (U(1)$_Q$) of all Standard Model fields as well as the number of fields of each type (per generation for fermions).

distinguish it from the hypercharge. It acts diagonally due to the diagonal form of T^3 and Y, in other words it doesn't mix between any of the different types of fermion. The redefined Z^μ boson is similarly also diagonal. The $W^\pm$ bosons however are non-diagonal and will link together particles that were in the same SU(2)$_W$ doublet. Despite the redefined massive fields not being explicit gauge bosons, they will still appear as mediators within interactions but now suppressed by their masses $1/M_W^2$, $1/M_Z^2$. Due to the self-interaction in the non-abelian theory of SU(2)$_W$, the $W_\mu^\pm$ bosons are charged under the residual U(1)$_Q$ symmetry. The A^μ and Z^μ are, however, completely neutral. As the gluons G^μ have no interaction with the Higgs, they remain massless and require no redefinition. A summary of the new charges and field combinations is given in Table 2.3.

In summary, at low energies the Standard Model has one massive scalar particle, 3 massive and one massless fermion per fermion generation, and 3 massive and 9 massless bosons. The SU(3)$_C$ gluon is unchanged and mediates the strong force between the two types of quark fermions, the up and down. The SU(2)$_W$ and U(1)$_Y$ bosons have mixed leaving a residual U(1)$_Q$ charge. This charge is mediated by the massless photon which interacts with all fermions, apart from the neutrino, and with the heavy charged W bosons. The massive bosons mediate a short-range weak force, suppressed by their heavy masses, which still only interacts with the

left-handed component of the Dirac fermions.

2.5   Yukawa Couplings and the CKM Matrix

For the quarks at low energies the Yukawa terms will take the form

$$\mathscr{L}_{\text{Quark Mass}} = -\frac{v}{\sqrt{2}} Y_{ij}\, \overline{d_{Ri}}\, d_{Lj} - \frac{v}{\sqrt{2}} \tilde{Y}_{ij}\, \overline{u_{Ri}}\, u_{Lj} + h.c., \tag{2.29}$$

where u_L (d_L) denotes the upper (lower) component of Q_L, $i = 1,\ 2,\ 3$ denotes the generation of particle and Y_{ij} & $\tilde{Y}_{ij}$ are the Yukawa couplings for the up-like and down-like states.

When considering the free evolution of states, it is less convenient mathematically to consider them as continuously mixing between different generations. Instead, the states should be redefined with a choice that diagonalises the mass matrix to give three particles which each evolve independently obeying $E^2 - |\vec{p}|^2 = m^2$. Each of the left and right-handed fermion components can be redefined separately using unitary (to preserve probability normalisation and the correct form of the kinetic Lagrangian) 3×3 matrices $V_{L,R}^{u,d}$. The redefined states are related using

$$u_L' = V_L^u\, u_L, \quad u_R' = V_R^u\, u_R, \tag{2.30}$$

$$d_L' = V_L^d\, d_L, \quad d_R' = V_R^d\, d_R, \tag{2.31}$$

where the redefinition matrices are chosen to give new, diagonalised mass matrices

$$M_u = V_R^u \left(\frac{v}{\sqrt{2}}\tilde{Y}\right) V_L^{u\dagger}, \quad M_d = V_R^d \left(\frac{v}{\sqrt{2}}Y\right) V_L^{d\dagger}. \tag{2.32}$$

Whilst this now makes the evolution of free states more convenient, it is important to go back to the interaction terms and rewrite them in this new choice of basis. In particular, the weak terms, involving the weak bosons $W^{\pm}$ and both up-like and down-like states, will now take a different form due to the way that the up-like and down-like states have transformed independently. Looking at the weak Lagrangian

for the quarks (including an implicit sum over generations i):

$$\mathcal{L}_{\text{Quark Weak}} \propto -i\,\overline{d}_{Li}\,\gamma^{\mu}\,W_{\mu}^{-}\,u_{Li} + h.c.$$

$$= -i\,\overline{d}'_{Lj}\,\gamma^{\mu}\,W_{\mu}^{-}\,(V_L^d\,V_L^{u\dagger})_{jk}\,u'_{Lk} + h.c. \qquad (2.33)$$

Crucially, the matrix $V_L^d V_L^{u\dagger} \neq I$, the identity. For the interaction between the first generation of the redefined states, u'_1 and d'_1, there is a reduction by a factor of $\left(V_L^d V_L^{u\dagger}\right)_{11}$ compared to the interaction between the first generation of the original states, u_1 and d_1. In addition, whilst there was no interaction between different generations of the u and d states, there are now terms that allow transitions between different generations of the u' and d' states. This will occur whenever there is a non-zero mixing term $\left(V_L^d V_L^{u\dagger}\right)_{ij} \neq 0$ for $i \neq j$. This combination of the left and right mixing matrices is called the CKM matrix after Cabibbo [60], Kobayashi and Maskawa [61] who first hypothesised its existence, $V_{\text{CKM}} = V_L^d V_L^{u\dagger}$. The CKM matrix is, by construction, unitary meaning that it should have at most 9 degrees of freedom. The freedom in field definitions (6 fields but reduced to 5 degrees of freedom because an equal shift in all fields would cancel out) can be used to simplify this to parameterisation by three real mixing angles and one real CP violating phase (discussed in more detail later). In this paramaterisation

$$V_{\text{CKM}} = \begin{pmatrix} 1 & 0 & 0 \\ 0 & c_{23} & s_{23} \\ 0 & -s_{23} & c_{23} \end{pmatrix} \begin{pmatrix} c_{13} & 0 & s_{13}e^{-i\delta_{CP}} \\ 0 & 1 & 0 \\ -s_{13}e^{i\delta_{CP}} & 0 & c_{13} \end{pmatrix} \begin{pmatrix} c_{12} & s_{12} & 0 \\ -s_{12} & c_{12} & 0 \\ 0 & 0 & 1 \end{pmatrix}, \qquad (2.34)$$

where $c_{ij} \equiv \cos\theta_{ij}$, $s_{ij} \equiv \sin\theta_{ij}$ for the three mixing angles θ_{12}, θ_{13} & θ_{23}, and δ_{CP} is the CP violating phase. Experimentally the CKM has thus far been found to be unitary and only slightly deviates from the identity with the diagonal elements being ≥ 0.973 [62].

Interaction terms involving the photon, Z boson and gluons are all unaffected by this field redefinition as they include terms like $\overline{u}u$ and $\overline{d}d$ for which the unitary

transformation matrices cancel leaving the interaction diagonal and unchanged in magnitude.

For the leptons the Yukawa interaction is

$$\mathscr{L}_{\text{Lepton Mass}} = -\frac{v}{\sqrt{2}}\lambda_{ij}\,\overline{e_{Ri}}\,e_{Lj} + h.c. \tag{2.35}$$

where e_L is the lower component of l_L in the chiral basis. Identically to before, the states are redefined using unitary matrices to diagonalise the mass matrix

$$e'_L = U^e_L\,e_L, \quad e'_R = U^e_R\,e_R, \quad M_e = U^e_R\left(\frac{v}{\sqrt{2}}\lambda\right)U^{e\dagger}_L. \tag{2.36}$$

Crucially, unlike in the quark sector there is no Yukawa coupling involving the other component of l_L because there is no ν_R to pair with it. This means that when looking at the weak force interaction

$$\mathscr{L}_{\text{Lepton Weak}} \propto -i\,\overline{e}_{Li}\,\gamma^\mu\,W^-_\mu\,\nu_{Li} + h.c.$$
$$= -i\,\overline{e}'_{Li}\,\gamma^\mu\,W^-_\mu\,\nu'_{Li} + h.c. \tag{2.37}$$

where the redefined $\nu'_L = U^{e\dagger}_L\,\nu_L$ has been chosen to cancel out the rotation matrix coming from the electron part. This is possible because the neutrinos are massless and thus mixing between the generations is arbitrary. So overall, this means that within the leptonic sector of the Standard Model the weak force does not induce transitions between different generations and there is no equivalent of the CKM matrix.

2.6 Helicity and Chirality

When first considering the Lorentz properties of Weyl fermions the states were given the notations left or right-handed depending upon their transformation properties under the $SU(2)_W$ representation of the Lorentz group. However, it was not clearly defined in what sense these fields are 'left' or 'right' handed. This relates to two properties of spinors, their chirality and their helicity.

The chirality of a fermion is dictated by its transformation under the Lorentz group. Defining $\gamma^5 = i\gamma^0\gamma^1\gamma^2\gamma^3$ the left/right handed chiral states can alternatively be defined as eigenspinors with

$$\gamma^5\Psi = \pm\Psi, \tag{2.38}$$

where the left (right) chiral state corresponds to the minus (plus) sign. This can be seen clearly in the chiral basis in which $\gamma^5 = diag(-1, -1, 1, 1)$. This clearly operates oppositely on the left and right-handed Weyl spinor components of the Dirac spinor as originally defined in Eq. (2.4). Recalling that the original definition came from the form of Lorentz transformation, this property is inherently Lorentz invariant. It is however physically unmeasurable for free states as it has no impact on the free evolution of a state with left and right-handed Weyl fermions obeying the same equation, Eq. (2.3), up to a parity inversion (defined later). Chirality is thus only observable when an interaction is introduced that violates parity, such as the weak force which only interacts with left-handed states.

Helicity is instead defined by considering differences in the kinematics of the spinor state. The helicity is defined as

$$h = \frac{\hat{s} \cdot \vec{p}}{|\vec{p}|}. \tag{2.39}$$

The helicity is a convenient quantity as it can be directly measured for any particle, most famously using the Stern-Gerlach experiment in which a magnetic field is used to infer the spin and from which it was demonstrated that the spin of particles is quantised.

If Eq. (2.3) is used with the assumption that ψ follows an exponential form $\exp(ip \cdot x)$ and has a well-defined spin then the condition is reached $E = \pm\hat{s} \cdot \vec{p}$. Comparing this to the helicity equation above, along with the massless dispersion relation $E = |\vec{p}|$, shows that for massless states $h = \pm 1$ with positive for the right-handed states and negative for the left-handed states. Given this, for massless fermions the helicity eigenvalue and chirality eigenvalue are exactly identical,

$h\Psi = \gamma^5\Psi = \pm\Psi$. Even for massive states, if their energy is much larger than their mass then this result will be approximately recovered.

In the low-energy Standard Model the fields are best defined in terms of Dirac spinors with mass. For these states the helicity and chirality operators are still applicable but they are no longer identical and the state is not necessarily an eigenstate of either. In the chirality case this can be seen from Eq. (2.5) in which the mass term mixes together states of left and right-handed chirality. For the helicity this can be understood by the fact that the angle between the spin and momentum of a particle can be changed by Lorentz boosting with a speed faster than the particle.

States of well-defined chirality and helicity can be projected out of the Dirac spinor through a projection operator. Recognising that $(\gamma^5)^2 = 1$ and $h^2 = 1$ means that projection operators can be defined for both in the form

$$P_c = \frac{1}{2}(1 \pm \gamma^5), \quad P_h = \frac{1}{2}\left(1 \pm \frac{\hat{s} \cdot \vec{p}}{|\vec{p}|}\right) \tag{2.40}$$

with, again, the positive sign giving a right-handed state and the negative a left-handed state.

2.7 Discrete Symmetries and CPT Invariance

As well as the continuous symmetry of Lorentz transformations (parametrised by a continuous variable), there are a set of discrete transformations which are in some cases symmetries of the interacting theory. These are inversion of charge, parity and time. All free states are invariant under each of these individually, both the original and transformed states obey the same evolution equations. However, as discussed before, the weak theory breaks the individual charge and parity symmetries due to it only interacting with left-handed Weyl fermions (or right-handed anti-fermions).

2.7.1 Charge Inversion

The charge of a particle, under a certain gauge transformation, gives the relative magnitude and sign of the interaction compared to other particles interacting in the same theory. It appears as the parameter q within the covariant derivative, as in

Eq. (2.10). Charge inversion supposes taking $q \rightarrow -q$ for all the charges under which the particle interacts. Whilst the state $\overline{\Psi}$ has inverted charge compared to Ψ it also has the opposite chirality. Instead, a charge conjugated state Ψ^c can be defined which has opposite charge but the same chirality. This field is related to the original by

$$\Psi^c = \eta_c \, \gamma^0 \, \mathbb{C} \, \Psi^*, \tag{2.41}$$

where $\eta_c = \pm 1$ is a particle dependent number called the 'intrinsic charge' and $\mathbb{C}$ is a matrix satisfying the property $\mathbb{C}^{-1} \gamma_\mu \mathbb{C} = -\gamma_\mu^{\mathsf{T}}$.

2.7.2 Parity Inversion

Parity inversion is the process of inverting all of the spatial dimensions, $\vec{x} \rightarrow -\vec{x}$. This not only affects the spatial coordinates upon which the fields vary but also the internal degrees of freedom within the field. A parity inverted Weyl fermion will have opposite chirality to its original state. Defining $\bar{x}^\mu = (t \, , \, -\vec{x})$, the parity inverted fermion field is given by

$$\Psi^p(\bar{x}) = \eta_p \, \gamma^0 \, \Psi(\bar{x}), \tag{2.42}$$

where similarly $\eta_p = \pm 1$ is the 'intrinsic parity'. For spin-0 fields, the value of $\eta_p = 1$ is called a scalar and $\eta_p = -1$ a pseudoscalar. Similarly for spin-1 fields, they are called vector and axial fields, respectively.

2.7.3 Time Inversion

Time inversion occurs similarly but with inversion of the temporal dimension $t \rightarrow -t$. A time inverted fermion will have

$$\Psi^t(\bar{x}) = \eta_t \, \mathbb{C}^{-1} \, \gamma^5 \, \Psi(-\bar{x}), \tag{2.43}$$

where η_t is a numerical factor satisfying $|\eta_t| = 1$ and $\mathbb{C}$ is as before.

2.7.4   CP Violation and the CPT Theorem

The violation of C and P symmetry in the weak force is evident when considering the properties of the Weyl fermions listed in Table 2.2. The left and right-handed states have different charges, meaning that a parity transformed left-handed state has no right-handed equivalent with the same being true for charge transformations. For the Standard Model at low energies, this is most evident when considering neutrinos. There exists no right-handed neutrino or left-handed anti-neutrino meaning that decays to left-handed neutrinos must violate C and P symmetry. The combined CP symmetry is also violated due to the CP violating phase in the CKM matrix, Eq. (2.34). CP transformations of processes will conjugate the CKM matrix, $V_{\mathrm{CKM}} \to V_{\mathrm{CKM}}^{*}$ meaning the complex components from the CP phase will lead to different interaction rates. An example of this is in the decay of Kaons, in which the difference between the CP related states $u\bar{s}$ and $s\bar{u}$ leads to CP violation in the partial decay rates.

On the other hand, it is still believed that transformations under C, P and T simultaneously are symmetries of the Lagrangian. This theorem is based upon the calculation that, in general, a unitary (and thus probability conserving), local, Lorentz-invariant QFT in flat space-time (i.e. following the principles of Special Relativity) will be CPT invariant. This means that all CP violation must be matched by an equivalent T violation and has significant consequences. This includes that matter and anti-matter states of the same field must have equal masses and that the decay rates of said states must be equal. Whilst the CPT theorem came from assuming Lorentz invariance, it is not necessarily the case that all Lorentz violation would break CPT symmetry.

2.8   Beyond the Standard Model: Neutrino Oscillations and Mixing

Unlike in the quark sector, in which the two constituents of the left-handed Q_L are matched by the two right-handed u_R and d_R, there is only one right-handed component in the leptonic sector of the Standard Model, e_R. This means that, as explained

previously, the neutrino, ν, remains massless and there is no field redefinition between the flavour and mass eigenstates. However, this is known not to be true from experimental measurements of neutrino propagation[1].

As discussed in the introduction, neutrino oscillations were first discovered in the measurement of solar neutrinos in the Homestake experiment of 1968 [44]. This experiment sought to measure neutrinos created in the various fusion processes in the sun which easily propagate to the earth due to their weak interaction strength [63]. It did so by measuring the weak process of neutrino capture, with chlorine being turned into argon which could be easily measured through subsequent decays. The experiment found that the flux of neutrinos observed coming from the sun was approximately one third of that expected from solar calculations. Whilst initially it was assumed that there was some flaw in the theoretical calculations or experimental method, the conclusion was later reached that instead the electron neutrinos being produced in the sun were mixing into muon or tau neutrinos in their propagation. This conclusion was verified by the further experiments of Super Kamiokande, SNO and KamLAND in 1999-2003 [45, 46, 47]. The Homestake experiment was only sensitive to charged current interactions, in which a $W^{\pm}$ is exchanged leading to the production of an electron from an electron neutrino. The neutrinos had insufficient energy to generate a muon or tau so muon or tau neutrinos couldn't be detected. The later experiments, however, were also sensitive to neutral current processes, with the exchange of a Z^0 leaving the neutrino unchanged, a process in which all three flavours of neutrino can partake. The nuclear fusion within the sun is predicted to produce only electron neutrinos. By measuring the neutral and charged currents, these experiments could verify that the total flux across all three flavours was equal to that predicted with the electron neutrinos partially changing into other flavours.

In order to explain this new phenomenon inspiration was sought from the quark sector. The mixing between different flavour eigenstates can be described by an equivalent to the CKM matrix, the Pontecorvo Maki Nakagawa Sakata (PMNS) ma-

---

[1]As mentioned before, attempts to describe neutrino oscillations using Lorentz violation are unable to recreate all of the experimental oscillation measurements [49].

trix. It too can be parametrised by three mixing angles and one CP-violating phase, identically to Eq. (2.34) (unless the neutrinos are Majorana, as will be discussed in Section 2.9.3). The 3σ range for the absolute values of the PMNS measured by experiments are [64]

$$|U_{\text{PMNS}}| = \begin{pmatrix} 0.800 - 0.844 & 0.515 - 0.581 & 0.139 - 0.155 \\ 0.229 - 0.516 & 0.438 - 0.699 & 0.614 - 0.790 \\ 0.249 - 0.528 & 0.462 - 0.715 & 0.595 - 0.776 \end{pmatrix} \qquad (2.44)$$

with the value of δ_{CP} for normal ordering being 261^{+51}_{-59} degrees. Unlike the CKM matrix, the PMNS has much larger off-diagonal elements with all terms in the matrix being $\gtrsim 0.1$ [65]. The experimental uncertainties on these values are still significant, up to 40% for 3σ uncertainty, meaning that it isn't yet possible to assess whether this matrix is unitary.

The PMNS matrix is implemented by considering the flavour eigenstates (those that appear directly coupled to the electron in the weak interaction term Eq. (2.37)) as being composed of a mixture of mass eigenstates (those that propagate freely according to the conventional dispersion relation). Mathematically this means

$$\nu_\alpha = \sum_i U_{\alpha i} \nu_i \qquad (2.45)$$

where $\alpha = e, \mu, \tau$ labels the flavour eigenstate, $i = 1, 2, 3$ labels the mass eigenstate and $U_{\alpha i}$ is the PMNS matrix element.

The similarity between the PMNS and CKM matrices implies that they should arise from a similar scenario, that of a difference between the flavour and mass eigenstates of the particles. For the CKM, this mixing comes from both types of quark having mass matrices that are non-diagonal for the flavour states. Applying this same idea to the leptonic sector would thus requires that the neutrinos also have a mass, something not predicted by the Standard Model. The idea of neutrinos mixing due to a mass was first proposed by Pontecorvo [42] and Maki, Nakagawa

and Sakata [43] before the first measurements of neutrino disappearance. For the simplified model of only two generations, if the flavour eigenstate is interpreted as a mixture of mass eigenstates $v_e = \cos\theta\, v_1 + \sin\theta\, v_2$ for PMNS mixing angle θ and mass states v_i, then the probability of disappearance (assuming the masses are much less than their energy) is [64]

$$P(v_e \rightarrow v_e) = 1 - \sin^2(2\theta)\sin^2\left(\frac{\Delta m^2 L}{4E}\right), \tag{2.46}$$

where L is the distance propagated, E is the energy of the neutrino and $\Delta m^2 = m_2^2 - m_1^2$ is the squared mass difference. Thus by measuring the flux of neutrinos for a range of energies, the mixing angle can be ascertained by looking at the peak reduction in flux and the difference in masses by the difference in energy values between peaks. In practice, oscillations have to be calculated in terms of three mass eigenstates and both disappearance (remaining flux of original state) and appearance (flux of different states) is used to measure the range of mixing angles. The CP-violating phase can be calculated by measuring equivalent probabilities for neutrinos and anti-neutrinos. The CP phase appears suppressed by many products of mixing angles and thus is subject to their uncertainties. This along with its small impact on the probabilities means that it has the greatest uncertainty [66].

Due to the squaring in the disappearance probability, the free propagation of neutrinos is insensitive to the sign of the mass difference between states. However, the interaction between electron neutrinos and electrons affects neutrino propagation through matter. In the case of solar neutrinos, the matter effect allows for the determination that the first mass state (the one which has the greatest electron neutrino component) is lighter than the second state (with second greatest component of the electron neutrino). However, the sign of the mass splitting between these states and the third state is unknown. Given the magnitude of this splitting ($|\Delta m_{31}^2| \gg |\Delta m_{21}^2|$) this leads to two possibilities: either the third state is heavier than the other two $m_1 < m_2 < m_3$ which is called 'normal ordering' (NO) or the third state is lighter $m_3 < m_1 < m_2$ which is called 'inverted ordering' (IO).

In addition to the measurements of solar, atmospheric and long-baseline neu-

trino propagation there are also short-baseline experiments, in which the neutrinos typically propagate over distances of around $10^2 - 10^3$ m with energies around $10^2 - 10^3$ MeV. Some experiments such as LSND [67] and MiniBooNE [68] have found an excess of electron anti-neutrinos in the final flux of these experiments, interpreted as $\overline{\nu}_\mu \to \overline{\nu}_e$ transitions. For these experiments this could be interpreted as evidence for an additional neutrino state, N, with a mass splitting of $\Delta m^2 \sim \text{eV}^2$ relative to the light neutrinos causing the process $\overline{\nu}_\mu \to \overline{N} \to \overline{\nu}_e$. Such states must not carry any charges, and are thus called 'sterile', because the measurement of the decay rate of the Z boson (which couples to all matter) to invisible states (neutrinos) is consistent only with three generations of neutrino. Whilst this does allow for super-heavy neutrinos, $m_\nu > M_Z/2$, any light states with splittings as above must be completely uncharged. In addition, any creation of N through mixing must be suppressed, implying a small mixing angle with the active states. Despite this, further searches for light sterile states from experiments, such as the successor MicroBooNE, have found inconsistent results, with MicroBooNE instead observing a deficit rather than excess of $\overline{\nu}_e$ [69]. Overall, there are significant tensions between the different appearance and disappearance data leaving the situation uncertain but with an overall preference for a splitting of $\Delta m^2 = 13 \text{ eV}^2$ [70].

2.9 Beyond the Standard Model: Neutrino Mass Generation

Given the overwhelming evidence for neutrino oscillations and the general consistency with the theory that this comes from neutrinos masses, the question then arises as to how neutrino masses are generated. In the Standard Model, neutrinos are massless and exist only as part of the left-handed lepton l_L without a right-handed counterpart. A range of different ways of generating this mass are considered in this section.

2.9.1 Dirac Mass

The simplest way in which to introduce neutrino masses is to follow the pattern of the Standard Model by introducing a right-handed state and coupling it via a Yukawa interaction with the Higgs. The new right-handed state would necessarily be neutral under $SU(3)_C$ as a lepton and neutral under $SU(2)_W$ as a right-handed state. It must also have no hypercharge so that at low energies it becomes electrically neutral under $U(1)_Q$. Thus the right-handed state is completely neutral, a singlet state under all symmetries, and called 'sterile'. The mass term would then be

$$\mathcal{L}_\nu \supset -\tilde{\lambda}_{ij}\overline{\nu}_{R,i}\tilde{H}^\dagger l_{L,j} + h.c. = -\overline{\nu}_{R,i}M_{ij}\nu_{L,j} + h.c. \quad . \tag{2.47}$$

This mass matrix M_{ij} would need to be diagonalised in the same way as before with

$$\nu_L' = U_L^\nu\,\nu_L, \quad \nu_R' = U_R^\nu\,\nu_R, \quad M_\nu = U_R^\nu\left(\frac{\nu}{\sqrt{2}}\tilde{\lambda}\right)U_L^{\nu\dagger}, \tag{2.48}$$

with the PMNS then being given by $U_{\text{PMNS}} = U_L^e U_L^{\nu\dagger}$.

Whilst this solution is perfectly valid, it requires a remarkably small Yukawa coupling. The Yukawa couplings inferred from mass measurements for the other fermions vary between around $10^{-6} - 1$ with 9 different states filling the full range of these values. For the neutrinos, however, the current experimental limits place the neutrinos at sub-eV masses (this will be discussed further in Chapter 3) meaning that the Yukawa couplings must be at most $\sim 10^{-12}$, six orders of magnitude smaller than that of the electron. Whilst theoretically possible, it is unappealing and would make more challenging the search for an origin for the Yukawa coupling values. This solution also requires the prediction of a brand new particle that is completely neutral apart from its interaction with the Higgs. Whilst there are many theories that predict the existence of light, neutral particles (such as to solve the Higgs hierarchy problem or explain cosmological evolution) [71] such predictions are experimentally uncomfortable as any such particle would be extremely challenging to directly detect. Both of these facts have led many to consider alternative explanations for the neutrino mass origins.

2.9.2   Effective Field Theories and the Weinberg Operator

Thus far, all of the operators considered in the Lagrangian have been of dimension-4 or less, meaning that they can be written as a product of fields with combined mass dimension less than or equal to 4, multiplied by a coupling constant of positive or zero mass dimension. Terms of this form are useful because they can be renormalised, with the infinities arising from loops in the quantum field theory being counteracted by counter terms to give finite predictions. However, terms of a higher dimension can be considered if it is assumed that they are only valid up to a certain energy scale. These are called Effective Field Theories (EFTs). The most famous example of this is the weak force with the high energy form being equivalent at low energies to the EFT

$$
\begin{aligned}
\mathscr{L}_{\text{Fermi}} = &- i g\, \overline{u}\, \gamma^\mu\, W_\mu^-\, (1 - \gamma^5)\, d - i g\, \overline{e}\, \gamma^\mu\, W_\mu^-\, (1 - \gamma^5)\, \nu_e + h.c. \\
&\rightarrow -\frac{\sqrt{2}\, g^2}{8\, M_W^2}\, \left[\overline{u}\, \gamma^\mu\, (1 - \gamma^5)\, d \right]\, \left[\overline{e}\, \gamma_\mu\, (1 - \gamma^5)\, \nu_e \right] + h.c.
\end{aligned}
\tag{2.49}
$$

where, as before, g is the weak force coupling and M_W the mass of the W boson. In this case, the W mass gives the high energy cutoff, calculations with the low energy form are valid below this energy scale but break down at higher energies (as can be seen from the loss of unitarity with the interaction rate scaling with the square of the energy up to infinity). The more accurate first term is valid at all energies scales (measured thus far) but the low energy format can be easier to calculate with and is a highly accurate approximation for energies $E \ll M_W$.

In general, EFT terms will have coefficients of negative mass dimension which can be written as c/Λ^n for some cutoff scale Λ. EFT terms will arise from renormalisable terms at higher energies, although it is possible to consider multiple scales of EFT. Many different forms of EFT are used to look for extensions beyond the Standard Model, all considering different cutoff scales and thus different propagating fields. Examples include the SMEFT which considers terms involving all the high energy Standard Model fields [72], LEFT which uses the low energy form of the Standard Model as described above [73] and HEFT which is similar to the SMEFT

but more general by not assuming the existence of the Higgs [74]. It isn't possible to uniquely find the high energy operators that generate an EFT given its terms, but measurement of EFT operators would provide evidence for additional physics beyond the Standard Model.

One way of introducing neutrino masses using an EFT term is the Weinberg operator. It supposes that there is some UV theory at a high energy scale Λ whose influence can be expressed at low energies in the form of an EFT operator. The advantage of this is that it doesn't require the creation of any new fields, such as ν_R, and it naturally explains the smallness of the neutrino mass due to the heavy cutoff scale. The operator is the only dimension-5 operator that can be created which satisfies the Standard Model gauge invariances and takes the form

$$\mathscr{L}_{\text{Weinberg}} = \frac{c_{ij}}{\Lambda}(\overline{l^c_{Li}}\,\tilde{H}^*)\,(\tilde{H}^\dagger\,l_{Lj}) + h.c., \tag{2.50}$$

$$\supset \overline{\nu^c_{Li}}\,m_{\nu ij}\,\nu_{Lj} + h.c., \tag{2.51}$$

for the mass matrix m_ν. In general, the mass matrix will be of order v^2/Λ for v the Higgs vacuum expectation value. In order for this to work, the UV theory would have to exist at an energy scale $\Lambda \sim 10^{12}v \approx 10^{14}$ GeV to give neutrino masses (assuming $c_{ij} \sim O(1)$) of $m_\nu \sim 0.1$ eV as expected (or at a higher scale for lower masses). This is an incredibly high energy scale compared to that reached by modern collider experiments, meaning that neutrino masses are a potential probe of much higher scales than other experiments.

If such an operator exists, it would also be significant as the first instance of Lepton Number Violation (LNV). In the Standard Model an accidental symmetry exists (meaning that it isn't enforced like the gauge redundancies) which ensures that the total number of leptons minus anti-leptons remains constant in any interaction. This operator, however, would allow for the process $HH \to \nu\nu$ to occur corresponding to an LNV of $\Delta L = 2$. This would be significant in cosmology where baryon number violation is sought to explain the observed matter-antimatter asymmetry in the universe and could be generated via leptogenesis [75].

2.9.3 Majorana Particles and the Neutrino Seesaw

In formulating the low energy form of the Standard Model, all of the fermionic particles were described as Dirac states following the Dirac equation. However, before the creation of the Standard Model Majorana suggested an alternative equation for free fermionic fields [76]

$$i\gamma^{\mu}\partial_{\mu}\Psi - m\Psi^{c} = 0, \tag{2.52}$$

which is identical to the Dirac equation, Eq. (2.4), but with the second field replaced with its charge conjugated field. Solutions to this equation are solutions of the Dirac equation but with the extra condition $\Psi = \Psi^{c}$. In terms of the left and right handed fields, $\psi_{L} = \psi_{R}^{c}$, in other words left and right-handed Weyl fields are related via charge conjugation. In practice, this means that particles and anti-particles are equivalent, up to a flip in their chirality. The 4-component field can then be written as $\Psi = \Psi_{L} + \Psi_{R} = \Psi_{L} + \Psi_{L}^{c}$ which clearly satisfies the previous requirement.

For all the particles in the Standard Model this cannot be the case, the left and right-handed fields transform in different representations of $SU(2)_{W}$ and with different hypercharges. However, for the right-handed neutrino there is nothing to forbid including a Majorana like term using the fact that it is completely uncharged under all forces. This is significant as it would add LNV and break this accidental symmetry in the Standard Model. Combining the Majorana term with other Dirac terms also involving the charge conjugated fields (and considering only one generation) gives a new mass term

$$
\begin{aligned}
-2\mathscr{L}_{\text{Majorana}} &= m_{D}\overline{\nu_{R}}\nu_{L} + m_{D}\overline{\nu_{L}^{c}}\nu_{R}^{c} + M\overline{\nu_{R}}\nu_{R}^{c} + h.c. \\
&= \begin{pmatrix} \overline{\nu_{L}^{c}} & \overline{\nu_{R}} \end{pmatrix} \begin{pmatrix} 0 & m_{D} \\ m_{D} & M \end{pmatrix} \begin{pmatrix} \nu_{L} \\ \nu_{R}^{c} \end{pmatrix} + h.c. \tag{2.53}
\end{aligned}
$$

Once again, it is most useful to find the states for which the mass matrix is diagonal. The interesting situation occurs if the assumption is made that $M \gg m_{D}$.

Then the eigenvalues of this mass matrix will be approximately M and $-m_D^2/M$ (the negative can be removed by a field rephasing) with the heavy state being approximately proportionate to $\nu_R + \nu_R^c$ and the light state $\nu_L + \nu_L^c$. Thus the addition of the Majorana mass term has led to two Majorana states, one light and one heavy. Assuming that the Dirac mass is generated via the Higgs as before, the smallness of the light neutrino can be explained as being due to the m_D/M suppression without the requirement for a Yukawa coupling much smaller than the other fermions'. This mechanism is called the 'Seesaw' because the larger the value of M, the smaller the light neutrino mass [77].

There are many different types of Seesaw depending upon the additional terms added. Also, in the full picture there should be three generations each of the left and right-handed neutrinos with the diagonalisation leading to mixing between generations as before. The PMNS matrix in this case will have two additional Majorana phases. This is because the constraint of being Majorana reduces the number of independent fields that can be redefined so these two phases cannot be removed. Alike the CP phase, these angles would be challenging to measure in oscillation experiments but could be significant in double-beta decay (discussed in the next chapter). Crucially, a method such as this allows for the possibility that neutrinos could be Majorana without violating the Standard Model forces. This would again allow for LNV and would represent the first Majorana particle ever identified.

The primary way of looking for such a state is through the search for Neutrino-less Double Beta Decay. Double beta decay occurs in states which are energetically forbidden from performing single beta decay (due to their nuclear configuration) but can decay with two simultaneous beta decay processes. Normally such a decay would emit two electron and two neutrinos. However, if neutrinos are Majorana then it is possible for the neutrino emitted in one of the decays to be reabsorbed in the other decay leading to a neutrinoless decay. The signature of such a decay would be a monoenergetic peak in the spectrum for the combined energy of the two electrons emitted. The change of the neutrino from right-handed at emission to left-handed at absorption requires a chirality flip, this means that the decay rate for this

process will be proportional to the effective double beta decay mass $m_{\beta\beta}$ as defined and discussed in more detail later in Section 3.5.

2.10   Beyond the Standard Model: Sterile Neutrinos

As mentioned before, there have been hints of further generations of neutrinos in neutrino oscillation data. These neutrinos would have to be sterile to have remained undetected thus far but could still potentially have many interesting consequences. Sterile neutrinos can easily be added to the standard neutrino picture at low energies; they would appear as extra generations which mix via an expanded PMNS matrix. Whilst it is possible that these sterile states could be stable, if they mix with the active states and are heavy enough then they will decay to the lighter neutrinos through the process $N \rightarrow \nu + \gamma$ [78]. Alternative models also include the possibility of a decay of the form $N \rightarrow \nu + \phi$ with the emission of ϕ, a new undetected boson [79].

Sterile neutrinos make valid dark matter candidates, the hypothesised particle(s) that would explain many astronomical properties such as galactic rotation curves and cosmological evolution. Dark matter is required to be electrically neutral, long-lived and massive, properties that are all matched by neutrinos. Active neutrinos are excluded due to their combined mass being too small and their coupling to the other particles too large. However, sterile neutrinos could fulfill these properties. The masses of such neutrinos are taken to be in the KeV range, with masses too small being disallowed by Pauli exclusion. For a given mass, there is a limit on the mixing between the active and sterile states from searches for X-rays given off in their decay [78].

The constraints on the highest mass neutrinos come from collider experiments where they could be produced in weak decays. These constraints are generally strongest in the GeV range [80]. Below this comes the oscillation experiments which probe the MeV range, constraints on high MeV masses can reach down to squared mixings of 10^{-9} [81]. Below this level, most of the constraints come from beta decay experiments (to be discussed later) with a range of elements. Whilst

all the beta decay constraints are highly mass dependent, in general their squared mixings are constrained at the $10^{-2} - 10^{-4}$ level.

Chapter 3

Single and Double Beta Decay: Spectrum and Experiments

In this chapter I will describe the process of beta decay with a particular emphasis on the decay of tritium. I will discuss the approximations that go into its derivation, the correction factors that need to be applied and the validity of the conventional spectral formula. I will also briefly discuss an approximate description for double beta decay. Finally, I will give an overview of the past, current and future single and double beta decay experiments as well as the statistical framework I will be using to assess the sensitivity of these experiments to new physics. The results and information included here regarding single beta decay and the statistical methodology largely follows that of my previously published work [82].

3.1 General Decay Spectrum

The process of tritium single beta decay is given by $T \rightarrow {}^3He + e^- + \overline{\nu}$. The property of primary interest throughout all single beta decay studies in this thesis is the decay spectrum. This will be expressed both in terms of the electron energy and the angle of its momentum direction. The total differential decay is an integral over the phase space of final states weighted by the squared matrix element. In the case of tritium

decay this is found by calculating

$$d\Gamma = \frac{1}{2m_{\mathrm{H}}} \frac{d^3\vec{p}_e}{(2\pi)^3 2E_e} \frac{d^3\vec{p}_v}{(2\pi)^3 2E_v} \frac{d^3\vec{p}_{\mathrm{He}}}{(2\pi)^3 2E_{\mathrm{He}}} |M|^2 (2\pi)^4 \delta^4(P_{\mathrm{H}} - P_{\mathrm{He}} - P_e - P_v).$$

(3.1)

where m_{H} is the tritium mass and P_i, E_i and $\vec{p}_i$ denote the 4-momentum, energy and 3-momentum, respectively, of particle i. $|M|^2$ is the squared matrix element derived from the Lagrangian and the factor of $\delta^4(...)$ is a 4-momentum conserving delta function.

The integral over the 3-momentum p_{He} can be performed trivially using the spatial part of the delta-function. Evaluating this integral in the tritium rest frame, $P_{\mathrm{H}} = (m_{\mathrm{H}}, \vec{0})$, allows for the expression of the remaining delta function in an angular form giving

$$\frac{d\Gamma}{dE_e d\Omega_e} = \frac{C(E_e)}{2^9 \pi^5 m_{\mathrm{H}}} \int_\Omega d\Omega_v \int_{E_v^-}^{E_v^+} dE_v |M|^2 \delta\left(\cos\theta_{ev} - \frac{\vec{p}_{\mathrm{He}}^2 - \vec{p}_e^2 - \vec{p}_v^2}{2|\vec{p}_e||\vec{p}_v|}\right), \quad (3.2)$$

where Ω_i is the solid angle of particle i, $E_v^\pm(E_e)$ is the maximum and minimum energies that the neutrino can take for a given electron energy and θ_{ev} is the angle between the electron and neutrino momentum directions. The factor $C(E_e)$ is a combination of all the additional correction factors, such as the Fermi function, that are required when considering atomic tritium; these will be discussed in greater detail in Section 3.4. The upper and lower bound energies $E_v^\pm(E_e)$ can be calculated by considering the neutrino energy when the electron and neutrino are emitted parallel or anti-parallel to each other. Using momentum conservation it can be shown that

$$\begin{aligned} \vec{p}_e \cdot \vec{p}_v =& \frac{1}{2}\left[m_{\mathrm{H}}^2 - m_{\mathrm{He}}^2 + m_e^2 + m_v^2 - 2m_{\mathrm{H}}E_e + 2E_v(E_e - m_{\mathrm{H}})\right] \\ =& \alpha - m_{\mathrm{H}}E_e - E_v(m_{\mathrm{H}} - E_e), \end{aligned}$$

(3.3)

where $\alpha = 1/2(m_{\mathrm{H}}^2 - m_{\mathrm{He}}^2 + m_e^2 + m_v^2)$ is defined by this expression. Squaring this, taking $(\vec{p}_e \cdot \vec{p}_v)^2 = p_e^2\, p_v^2$ (giving $\cos\theta_{ev} = \pm 1$ as required for parallel or anti-

parallel emission, corresponding to minimum and maximum neutrino energies) and solving for $E_\nu^\pm$ gives [83]

$$E_\nu^\pm(E_e) = \frac{(m_H - E_e)(\alpha - m_H E_e) \pm |\vec{p}_e| \sqrt{(\alpha - m_H E_e - m_\nu^2)^2 - m_{He}^2 m_\nu^2}}{m_{12}^2}, \quad (3.4)$$

where

$$m_{12}^2 = (P_H - P_e)^2 = m_H^2 - 2m_H E_e + m_e^2. \quad (3.5)$$

The maximum possible energy that the electron can take is found by considering the situation where both the neutrino and helium-3 are emitted as a composite object anti-parallel to the electron. Using 4-momentum conservation gives [84]

$$E_e^{\max} = \frac{m_H^2 + m_e^2 - (m_{He} + m_\nu)^2}{2m_H}. \quad (3.6)$$

Crucially, this quantity is dependent upon the neutrino mass. Evaluating this for $m_\nu = 0$ gives a maximum kinetic energy $E_e^{\max} - m_e \approx 18.59$ keV, in agreement with experiment [85]. It is useful at this point to define the quantity y as the amount by which the electron energy is below the maximum, or 'endpoint', value

$$y = E_e^{\max} - E_e. \quad (3.7)$$

This quantity is useful to define as the spectrum tends to zero as y goes to zero with the impact of the neutrino mass being greatest in this region, hence why it is often the focus of neutrino mass experiments. Re-expressing $E_\nu^\pm$ in terms of y gives

$$E_\nu^\pm(E_e) = \frac{(m_H - E_e)(m_H y + m_\nu^2 + m_{He} m_\nu) \pm |\vec{p}_e| \sqrt{(m_H y(m_H y + 2m_{He} m_\nu)}}{m_{12}^2}. \quad (3.8)$$

When considering the angular distribution of the electron emission, special care needs to be taken in treating the spin states of the particles. As spin-1/2 fermions, all of the particles can be in spin-up or spin-down states. Typically these are averaged (summed) over for initial (final) states. However, if the tritium is cho-

sen to be prepared in a particular spin state this is no longer the case (measuring the final state spins would be highly experimentally challenging so will not be considered here). Including the tritium spin is most easily done by inserting a spin projection operator for the tritium into the matrix element calculation before proceeding with the usual spin-sum procedure [86],

$$P_s = \frac{1}{2}(1 + \gamma^5 \slashed{S}), \quad S^\mu = \left(\frac{\vec{p} \cdot \hat{s}}{m}, \hat{s} + \frac{\vec{p} \cdot \hat{s}}{m(E+m)} \vec{p} \right), \tag{3.9}$$

where m and E are for the particle for which the spin is being fixed.

The projector P_s is chosen to satisfy $P_s u_{\vec{p},s'} = \delta_{s,s'} u_{\vec{p},s'}$ and $P_s v_{\vec{p},s'} = \delta_{s,s'} v_{\vec{p},s'}$ where $s, s' = \pm 1/2$ are spin states and u, v are the basis spinors of the associated particle. In the case of tritium at rest the spin 4-vector simplifies to $S_H^\mu = (0, \hat{s})$. Crucially, this will introduce terms into the matrix element of the form $P_i \cdot S_H = -|\vec{p}_i| \cos \theta_i$ where $i = e, v$ (recalling that $\vec{p}_{He} = -\vec{p}_e - \vec{p}_v$ from momentum conservation) and θ_e, θ_v are the angles between $\hat{s}$ and the momenta $\hat{p}_e$ and $\hat{p}_v$, respectively. As there is only a single factor of S_H there will only be a linear dependence upon these angles. There are no other physical angles upon which the matrix element could depend as the only independent 3-vectors are $\vec{p}_e$ and $\vec{p}_v$; their absolute directions are physically irrelevant due to the isotropy of the decay and their relative angle of θ_{ev} is fixed by the delta function in conserving energy. This means that the matrix element must take the form

$$|M|^2 = A(E_e, E_v) + B_e(E_e, E_v) \cos \theta_e + B_v(E_e, E_v) \cos \theta_v. \tag{3.10}$$

In order to evaluate the integral of $\cos \theta_v$ over Ω_v in Eq. (3.2) a particular choice of coordinates is required. The z-axis of this solid angle is chosen to be along $\hat{p}_e$ such that the polar angle is θ_{ev} and then the azimuthal angle is labelled as φ (choosing $\varphi = 0$ to be when $\hat{s}$, $\vec{p}_e$ and $\vec{p}_v$ are all co-planar). This means that θ_v can

be expressed using $\cos\theta_\nu = \sin\theta_e \sin\theta_{e\nu}\cos\varphi + \cos\theta_e\cos\theta_{e\nu}$ which gives

$$
\int_\Omega d\Omega_\nu \; \cos\theta_\nu \; \delta\left(\cos\theta_{e\nu} - \frac{\vec{p}_{\text{He}}^2 - \vec{p}_e^2 - \vec{p}_\nu^2}{2|\vec{p}_e||\vec{p}_\nu|}\right)
$$
$$
= \int_{-1}^{1} d\cos\theta_{e\nu}\int_0^{2\pi} d\varphi(\sin\theta_e\sin\theta_{e\nu}\cos\varphi + \cos\theta_e\cos\theta_{e\nu})
$$
$$
\delta\left(\cos\theta_{e\nu} - \frac{\vec{p}_{\text{He}}^2 - \vec{p}_e^2 - \vec{p}_\nu^2}{2|\vec{p}_e||\vec{p}_\nu|}\right)
$$

$$
= 2\pi\cos\theta_e\int_{-1}^{1} d\cos\theta_{e\nu}\;\cos\theta_{e\nu}\delta\left(\cos\theta_{e\nu} - \frac{\vec{p}_{\text{He}}^2 - \vec{p}_e^2 - \vec{p}_\nu^2}{2|\vec{p}_e||\vec{p}_\nu|}\right)
$$
$$
= 2\pi\cos\theta_e\frac{\vec{p}_{\text{He}}^2 - \vec{p}_e^2 - \vec{p}_\nu^2}{2|\vec{p}_e||\vec{p}_\nu|} = 2\pi\cos\theta_e\frac{\alpha - m_{\text{H}}E_e - E_\nu(m_{\text{H}} - E_e)}{|\vec{p}_e||\vec{p}_\nu|}. \tag{3.11}
$$

Given this, the differential decay rate as a function of electron properties is

$$
\frac{d\Gamma}{dE_e d\Omega_e} = a(E_e) + b(E_e)\cos\theta_e, \tag{3.12}
$$

which can be expressed as energy or angular dependent derivatives

$$
\frac{d\Gamma}{dE_e} = 4\pi a(E_e), \tag{3.13}
$$
$$
\frac{d\Gamma}{d\cos\theta_e} = \frac{\Gamma}{2}(1 + k\cos\theta_e), \tag{3.14}
$$

where the angular correlation factor is

$$
k = \int_{m_e}^{E_e^{max}} b(E_e)dE_e \left/ \int_{m_e}^{E_e^{max}} a(E_e)dE_e. \right. \tag{3.15}
$$

with a total decay rate

$$
\Gamma = 4\pi\int_{m_e}^{E_e^{\text{max}}} a(E_e)dE_e. \tag{3.16}
$$

If the ensemble of tritium nuclei are not fully polarised, a polarisation factor

must be included

$$f = \frac{N^\uparrow - N^\downarrow}{N^\uparrow + N^\downarrow}, \tag{3.17}$$

where $N^{\uparrow(\downarrow)}$ is the number or fraction of spin-up (-down) nuclei. Spin-up and down states are related by taking $\hat{s} \to -\hat{s}$ and thus $S^\mu \to -S^\mu$ which is why the terms cancel in the numerator. The spin projector would thus be modified to have $S^\mu \to fS^\mu$ in turn leading to $\cos\theta_e \to f\cos\theta_e$ in the final decay rate. As expected, equal populations of up and down states leads to $f = 0$ with the angular effects disappearing and total polarisation gives $f = 1$ where the previous result is recovered.

3.2 Standard Model Lagrangian

The beginning of any calculation of the matrix element for beta decay is Fermi's approximation of the process as a four-point contact interaction. In terms of the fundamental fermions it takes the form [5]

$$\mathscr{L}_{\text{Fermi}} = -\frac{G_F}{\sqrt{2}} V_{ud} \eta_{\mu\nu} \left[\bar{e}\gamma^\mu (1-\gamma^5)\nu_e \right] \left[\bar{u}\gamma^\nu (1-\gamma^5)d \right] + \text{h.c.}, \tag{3.18}$$

where h.c. denotes the hermitian conjugate, u and d are the up and down quarks, e the electron and ν_e the electron neutrino flavour eigenstate. The factor V_{ud} is the Cabbibo mixing angle which is the top-left element of the CKM matrix. This approximate form is an excellent approximation because the exchanged momentum q is much smaller than the W boson mass, $q \sim 20 \text{ keV} \ll M_W \sim 100 \text{ GeV}$.

In order to describe the beta decay of tritium, the up and down quarks need to be considered as constituents of tritium and helium-3 nuclei. As they are spin-1/2 states this is relatively simple mathematically. Through experimental measurements of the tritium half-life, it has been found that the use of the more complicated nuclear state of tritium leads to a modification of the axial vector part of the decay rate with an increase by a factor labelled as g_A [87]. Conversely, the vector part is predicted by the Conserved Vector Current (CVC) hypothesis to remain the same [88], nonetheless a factor of g_V is often included to maintain the possibility of deviation

being observed by experiments. Given this the Standard Model Lagrangian for the calculation of tritium beta decay is

$$\mathcal{L}_{\text{SM}} = -\frac{G_F}{\sqrt{2}} V_{ud} \left[\bar{e} \gamma^\mu (1 - \gamma^5) v_e \right] \left[\overline{^3\text{He}} \gamma_\mu \left(g_V - g_A \gamma^5 \right) {}^3\text{H} \right], \tag{3.19}$$

from which all results henceforth labelled as SM, or Standard Model, are derived. For my calculations the value $g_V = 1$ is used in agreement with CVC and the value of $g_A = 1.247$ is extrapolated from the half-life of tritium [89]. There are additional terms that also contribute to the hadronic part of the Lagrangian, such as the weak magnetic term, but these are suppressed by powers of $q/m_\text{H} \sim 10^{-5}$ ($m_\text{H} \sim 3$ GeV [83]) and thus can be safely neglected.

3.3 The Standard Model Case

Given the general framework above, now the Standard Model case can be evaluated by calculating the matrix element from Eq. (3.19). The matrix element to be evaluated is

$$\begin{aligned} |M_{\text{SM}}|^2 = {} & 16 G_F^2 |V_{ud}|^2 \\ & Tr[(\slashed{P}_{\text{He}} + m_{\text{He}}) \gamma^\lambda (g_V - g_A \gamma^5)(1 + \gamma^5 \slashed{s})(\slashed{P}_\text{H} + m_\text{H}) \gamma^\rho (g_V - g_A \gamma^5)] \\ & Tr[(\slashed{P}_e + m_e) \gamma_\lambda (1 - \gamma^5) \slashed{P}_\nu \gamma_\rho (1 - \gamma^5)], \end{aligned} \tag{3.20}$$

including the spin projection given by Eq. (3.9). When evaluated this gives

$$\begin{aligned} |M_{\text{SM}}|^2 = {} & 16 G_F^2 |V_{ud}|^2 \\ & \times \big\{ (g_A + g_V)^2 (P_e \cdot P_{\text{He}})(P_\nu \cdot P_\text{H}) + (g_A - g_V)^2 (P_e \cdot P_\text{H})(P_\nu \cdot P_{\text{He}}) \\ & + (g_A^2 - g_V^2) m_\text{H} m_{\text{He}} (P_e \cdot P_\nu) \\ & + (g_A^2 - g_V^2) m_{\text{He}} \left[(P_\text{H} \cdot P_\nu)(P_e \cdot S) - (P_\text{H} \cdot P_e)(P_\nu \cdot S) \right] \\ & + (g_A - g_V)^2 m_\text{H} (P_\nu \cdot P_{\text{He}})(P_e \cdot S) - (g_A + g_V)^2 m_\text{H} (P_e \cdot P_{\text{He}})(P_\nu \cdot S) \big\}. \end{aligned} \tag{3.21}$$

3.3.1 Energy Distribution

The evaluation of the spin-independent part of this gives

$$4\pi a_{\mathrm{SM}}(E_e) = \frac{G_F^2 |V_{ud}|^2}{2\pi^3} C(E_e) \sum_{i=1}^{3} |U_{ei}|^2 \frac{m_{\mathrm{H}}^2 |\vec{p}_e|}{m_{12}^2} \widetilde{y}_i \Theta(y_i)$$

$$\times \left\{ (g_V + g_A)^2 \left[\frac{m_{\mathrm{H}}(m_{\mathrm{H}} - E_e)}{m_{12}^2} \frac{m_{\mathrm{H}} E_e - m_e^2}{m_{12}^2} (y_i + \mu_i m_{\nu,i})(y_i + \mu_i m_{\mathrm{He}}) \right.\right.$$

$$\left. - \frac{m_{\mathrm{H}}^2 |\vec{p}_e|^2}{3m_{12}^4} \widetilde{y}_i^2 \right] + (g_V - g_A)^2 E_e \left(y_i + m_{\nu,i} \frac{m_{\mathrm{He}}}{m_{\mathrm{H}}} \right)$$

$$\left. + (g_A^2 - g_V^2) m_{\mathrm{He}} \frac{m_{\mathrm{H}} E_e - m_e^2}{m_{12}^2} (y_i + \mu_i m_{\nu,i}) \right\}, \tag{3.22}$$

where the sum is over all three neutrino eigenstates. The subscript i has been added to all quantities for which there is a neutrino mass dependence e.g. $y_i = E_e^{max}(m_i) - E_e$. Energy conservation is maintained by the Heaviside function $\Theta(y_i)$, $\mu_i = (m_{\nu,i} + m_{\mathrm{He}})/m_{\mathrm{H}}$ and $\widetilde{y}_i = \sqrt{y_i \left(y_i + m_{\nu,i} \frac{2m_{\mathrm{He}}}{m_{\mathrm{H}}} \right)}$. This expression matches that given in [89] with minor typos corrected.

Most often this expression is simplified by using that $m_{\mathrm{H}} \approx m_{\mathrm{He}} \gg E_e$, m_e, m_ν to give

$$4\pi a_{\mathrm{SM}}(E_e) \approx \frac{G_F^2 |V_{ud}|^2}{2\pi^3} C(E_e)(g_V^2 + 3g_A^2) m_{\mathrm{H}} m_{\mathrm{He}} \frac{m_{\mathrm{He}} |\vec{p}_e|}{m_{12}^2} \frac{m_{\mathrm{H}} E_e - m_e^2}{m_{12}^2}$$

$$\times \sum_{i=1}^{3} |U_{ei}|^2 \Theta(y_i) \sqrt{y_i \left(y_i + m_{\nu,i} \frac{2m_{\mathrm{He}}}{m_{\mathrm{H}}} \right)} \left(y_i + m_{\nu,i} \frac{m_{\nu,i} + m_{\mathrm{He}}}{m_{\mathrm{H}}} \right). \tag{3.23}$$

This is then often further simplified by the assumption that $y_i \gg m_\nu$ to give the effective single beta decay neutrino mass [90, 91]

$$4\pi a_{\mathrm{SM}}(E_e) \approx \frac{G_F^2 |V_{ud}|^2}{2\pi^3} C(E_e)(g_V^2 + 3g_A^2) m_{\mathrm{H}} m_{\mathrm{He}} \frac{m_{\mathrm{H}} |\vec{p}_e|}{m_{12}^2} \frac{m_{\mathrm{H}} E_e - m_e^2}{m_{12}^2} y_0 \sqrt{y_0^2 - m_\beta^2}, \tag{3.24}$$

where the effective single beta decay mass $m_\beta^2 = \sum_{i=1}^{3} |U_{ei}|^2 m_i^2$. Re-expressing in
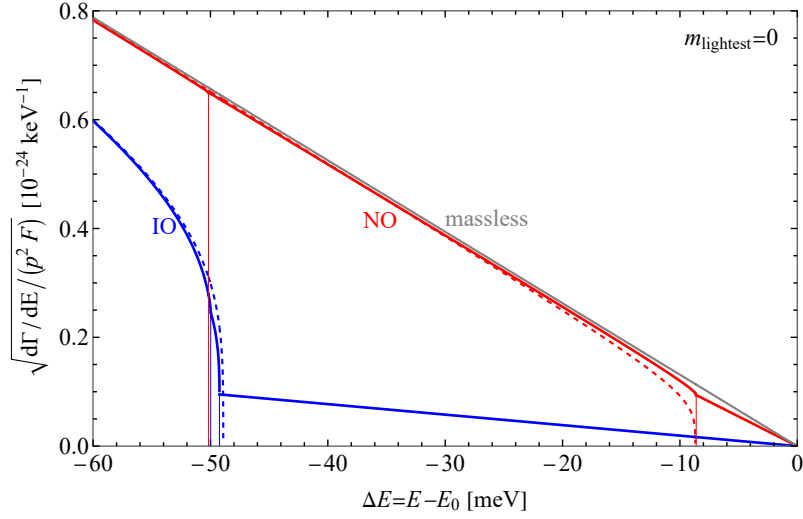
Figure 3.1: Kurie plot of the tritium energy distribution as measured from the zero-mass endpoint for a massless lightest neutrino with Normal Ordering (red) and Inverted Ordering (blue) of the three active neutrinos. The red (blue) dashed lines correspond to the effective m_β approximation for NO (IO) as given by Eq. (3.24). The gray line corresponds to the case of a single massless active neutrino. The vertical lines are the endpoints for the different neutrino masses

terms of $y_0 = y(m_\nu = 0)$ ensures that all of the neutrino mass dependence has been combined into m_β. Whilst this approximation is valid for the current generation of beta decay experiments (discussed further in Section 3.6), the study of [90] concludes that the more precise expression of Eq. (3.23) is required for the next generation of experiments given their higher energy resolution and exposure.

The full expression of Eq. (3.22) is plotted as a Kurie function (defined as $(d\Gamma/dE_e)/(|\vec{p}_e|^2 F(Z, E_e))$ in Fig. 3.1 for both the normal and inverted orderings with a lightest neutrino mass of zero. The three different endpoints due to the different neutrino masses are highlighted by the vertical lines and are clearly visible in the spectrum as kinks. They are located at values equal to their respective neutrino mass below the highest endpoint. Also plotted is the approximate expression Eq. (3.24), showing how it fails at these energies by giving only a single endpoint and a different rate.

3.3.2 Angular Distribution

Looking instead at the angular part of the spectrum, as will appear when the nuclei are polarised, gives

$$
\begin{aligned}
b_{\mathrm{SM}}(E_e) = {} & -\frac{G_F^2 |V_{ud}|^2}{8\pi^4} C(E_e) \frac{m_{\mathrm{H}}}{m_{12}^2} |\vec{p}_e|^2 \widetilde{y}_i \\
& \times \left\{ \left[(g_A - g_V)^2 m_{\mathrm{H}} + (g_A^2 - g_V^2) m_{\mathrm{He}} \frac{m_{\mathrm{H}}(m_{\mathrm{H}} - E_e)}{m_{12}^2} \right.\right. \\
& \left. + (g_A^2 - g_V^2) \frac{m_{\mathrm{H}} m_{\mathrm{He}}}{m_{12}^2} E_e + (g_A + g_V)^2 \frac{m_{\mathrm{H}}}{m_{12}^2}(\alpha - m_e^2) \right. \\
& \left. - (g_A + g_V)^2 \frac{m_{\mathrm{H}}^2}{m_{12}^2} (y_i + \mu_i m_{\nu,i}) \frac{m_{\mathrm{H}}(m_{\mathrm{H}} - E_e)}{m_{12}^2} \right] (y_i + \mu_i m_{\nu,i}) \\
& \left. - (g_A - g_V)^2 m_{\nu,i}^2 - \frac{1}{3}(g_A + g_V)^2 \frac{m_{\mathrm{H}}^3 (m_{\mathrm{H}} - E_e)}{m_{12}^4} \widetilde{y}_i^2 \right\}.
\end{aligned} \tag{3.25}
$$

This expression can be greatly simplified under the same approximation, as before, $m_{\mathrm{H}} \approx m_{\mathrm{He}} \gg E_e, m_e, m_{\nu_i}$,

$$
b_{\mathrm{SM}}(E_e) \approx -\frac{2g_A^2 - 2g_A g_V}{g_V^2 + 3g_A^2} \frac{|\vec{p}_e|}{E_e} a_{\mathrm{SM}}(E_e) \approx -0.12 \frac{|\vec{p}_e|}{E_e} a_{\mathrm{SM}}(E_e). \tag{3.26}
$$

This gives a value in Eq. (3.14) of $k = -0.0154$ meaning that the angular effect is at the 1% level on the spectrum depending upon the angle.

The angular effect is due to the impact of helicity and chirality effects on the decay. Decays mediated by a vector current (Fermi) lead to the emission of the neutrino and electron in an anti-aligned spin state (total spin $S = 0$) whereas axial current decays (Gamow-Teller) have an aligned spin ($S = 1$) [86]. The tritium and helium-3 are both spin-1/2 nuclei. This means that whilst Fermi decays are isotropic, the requirement of conservation of angular momentum means that the Gamow-Teller decay cannot have the fermion pair emitted with opposite angular momentum to the polarisation direction ($S_z \neq -1$). The anti-neutrino is a right-handed chiral state and, being nearly massless, will be approximately right-handed helical - it's momentum and spin will be aligned. Thus the greater possibility of spin in the 'upwards' direction leads to a greater possibility of momentum being upwards. Due to overall momentum conservation, this leads to a greater probability

for the electron to be emitted in the 'downwards' direction opposite to the nuclear spin.

3.4 Correction Factors

There are seven correction factors that need to be included in the function $C(E_e)$ to account for additional effects when considering atomic tritium rather than individual quarks [92, 93]. These are: the Fermi function, $F(E_e)$, which accounts for the Coulomb interaction between the helium-3 and the electron; a recoil correction to this function due to the motion of the helium, $Q(E_e)$ and a screening correction due to the orbital electron, $S(E_e)$; radiative corrections to the spectrum including an infinite sum over soft photons, $G(E_e)$; finite size nuclear effects, $L(E_e)$ & $B(E_e)$, and quantum statistics exchange between the emitted and orbital electron, expressed as a modified sum. These are described in the following subsections.

3.4.1 The Fermi Factor

The best known beta-decay correction factor is the Fermi function, which accounts for the Coulomb attraction between the helium nucleus and the emitted electron. It does this by considering the wave-function of an electron in a point source potential and evaluating the relative probability of such an electron being measured as being at the nuclear surface, R, with and without the nuclear charge [5]. The derivation here follows that as presented in [94].

The derivation begins from the Dirac Hamiltonian (expressed with energy relative to m_e such that $W = E_e/m_e$),

$$H\psi = W\psi = (i\gamma^0\vec{\gamma}\cdot\vec{\nabla} + V(r) + \gamma^0)\psi. \tag{3.27}$$

The spherical harmonics are categorised by defining the operator $K = \gamma^0(2S\cdot L + 1)$ where S is the spin operator and L the angular momentum operator. From this the spatial derivative can be re-expressed as

$$\vec{\gamma}\cdot\vec{\nabla} = \hat{r}\cdot\vec{\gamma}\frac{\partial}{\partial r} - \frac{\hat{r}\cdot\vec{\gamma}}{r}(\gamma^0 K - 1). \tag{3.28}$$

For a point source central potential, $V(r) = -\alpha Z/r$ with α the fine structure constant and Z the atomic number of the nucleus. Defining $J = L + S$, for this potential $[J^2, H] = [J_z, H] = [K, H] = 0$. Given this, it is worth choosing an eigenbasis of these operators using 2-spinor eigenstates χ_κ^μ where

$$J^2 \chi_\kappa^\mu = j(j+1)\chi_\kappa^\mu, \tag{3.29}$$

$$J_z \chi_\kappa^\mu = \mu \chi_\kappa^\mu, \tag{3.30}$$

$$(2S \cdot L + 1)\chi_\kappa^\mu = -\kappa \chi_\kappa^\mu, \tag{3.31}$$

which defines the eigenvalue κ which can be used to label the spherical harmonics. This then means that ψ can be separated (in the chiral basis) into radial and spherical functions as

$$\psi = \begin{pmatrix} g(r)\chi_\kappa^\mu \\ if(r)\chi_{-\kappa}^\mu, \end{pmatrix} \tag{3.32}$$

where f and g are real, energy dependent functions. The lower component has opposite sign κ to the upper component due to the form of $\gamma^0 = diag(1,1,-1,-1)$ in this basis choice. The functions f and g will then satisfy the simultaneous equations

$$\frac{df}{dr} = \frac{\kappa-1}{r}f - (W-1-V)g, \tag{3.33}$$

$$\frac{dg}{dr} = (W-V+1)f - \frac{\kappa+1}{r}g. \tag{3.34}$$

The condition is imposed that as $r \to \infty$ the field should tend towards that of a free particle i.e. the limiting behaviour of f and g should be

$$rf = -A(W-1)^{1/2}\sin(|\vec{p}|r+\delta), \tag{3.35}$$

$$rg = A(W+1)^{1/2}\cos(|\vec{p}|r+\delta), \tag{3.36}$$

for some phase, δ, and normalisation, A. δ has a logarithmic r dependence which has no impact upon physical results such as scattering amplitudes [94].

Solving the differential equations with this condition gives

$$\Phi = \frac{Ap(2pr)^{\gamma-1}e^{\pi\eta/2}|\Gamma(\gamma+i\eta)|}{\Gamma(2\gamma+1)}\left[e^{-i(pr+\xi)}(\gamma+i\eta)H(\gamma+1+i\eta,2\gamma+1,2ipr)\right],$$

$$f = i(W-1)^{1/2}(\Phi-\Phi^*),$$

$$g = (W+1)^{1/2}(\Phi+\Phi^*), \tag{3.37}$$

where $\eta = \alpha ZW/p$ and $\gamma^2 = \kappa^2 - \alpha^2 Z^2$. Γ is the usual gamma function and the hypergeometric function $H(\gamma+1+iy,2\gamma+1,2ipr)$ has the properties $H(a,b,0)=1$ and $H(a,b,x) \to \Gamma(b)/\Gamma(a)x^{a-b}e^x$ for $|x| \to \infty$.

The Fermi function is proportional to $\overline{\psi}\psi \propto f^2 + g^2$. Evaluating this at the nuclear radius $R_n \approx 2.88 \times 10^{-3}/m_e$ [93] such that $pR_n \ll 1$ (ie. $H, e^{-ipr} \approx 1$) and using the $1S_{1/2}$ state (ie. g_{-1} and f_1) gives

$$f^2 + g^2 = 2(1+\gamma)(2pR)^{2(\gamma-1)}e^{\pi\eta}\frac{|\Gamma(\gamma+i\eta)|^2}{(\Gamma(2\gamma+1))^2}\frac{2pW}{\pi}. \tag{3.38}$$

Normalising this by requiring that $F(0,W)=1$ gives

$$F(Z,W) = 2(1+\gamma)(2pR)^{2(\gamma-1)}e^{\pi\eta}\frac{|\Gamma(\gamma+i\eta)|^2}{(\Gamma(2\gamma+1))^2}, \tag{3.39}$$

the Fermi function. This derivation has made the assumption that Z is sufficiently small such that γ remains real, meaning that $Z < 138$ which is true for all observed nuclei. It also assumes a purely point-like central potential with the effect of the nuclear radius being merely accounted for by evaluating the wave-function at this point. Corrections to this are discussed in the next subsection.

The Fermi function is often presented in a more approximate form called the 'Simpson approximation' [95] which takes the form

$$F(Z,W) \approx \frac{2\pi\eta(1.002037 - 0.001427|\vec{p}|/E)}{1-e^{-2\pi\eta}} \tag{3.40}$$

where, as before, $\eta = \alpha ZW/|\vec{p}|$. The expression within the brackets is often also approximated as 1.

3.4.2 Finite Nucleus Corrections

In addition to the previous calculation, further modifications need to be made when considering the effect of the nuclear charge. The finite size of the nuclear charge can be accounted for by treating the nucleus as a uniform charge distribution with radius that gives the appropriate value for $\langle r^2 \rangle^{1/2}$ [96]. Using this gives [92]

$$L(Z,W) = 1 + \frac{13}{60}(\alpha Z)^2 - \frac{WR\alpha Z}{15}\frac{41 - 26\gamma}{2\gamma - 1} - \frac{\alpha ZR\gamma}{30W}\frac{17 - 2\gamma}{2\gamma - 1}, \tag{3.41}$$

which is often approximated for low Z as [97]

$$L_0(Z,W) = 1 + \frac{13}{60}(\alpha Z)^2 - WR\alpha Z - \frac{\alpha ZR}{2W}. \tag{3.42}$$

The other finite size nuclear effect is due to the variation of the neutrino and electron wavefunctions throughout the nucleus. It is important to account for this by convolving these with the nuclear wavefunction. This should be done differently for vector (Fermi) and axial-vector (Gamow-Teller) mediated currents with there being small differences in the correction factors for each. However, as the Gamow-Teller transition is larger in tritium and including both separately would be highly challenging (particularly given the interference between the two) I have chosen to follow the convention and use the Gamow-Teller version. This is given by

$$B(Z,W) = 1 + B_0 + B_1 W + B_2 W^2, \tag{3.43}$$

with

$$\begin{aligned}
B_0 &= -\frac{233}{630}(\alpha Z)^2 - \frac{1}{5}(W_0 R)^2 + \frac{2}{35}(W_0 R\alpha Z), \\
B_1 &= -\frac{21}{35}R\alpha Z + \frac{4}{9}W_0 R^2, \\
B_2 &= -\frac{4}{9}R^2,
\end{aligned} \tag{3.44}$$

where $W_0 = E_e^{\max}/m_e$.

3.4.3 Additional Coulomb Corrections

In addition to these effects, there are corrections to the Fermi function due to the nuclear recoil and the screening of the nucleus by the orbital electron.

Firstly, the recoil of the nucleus means that the nuclear potential isn't completely isotropic in the lab frame. Finding the average recoil velocity and accounting for the angular correlations gives an average corrected relative velocity between the electron and the nucleus. Factoring this out of the approximated Fermi function gives [98]

$$Q(Z,W,W_0) = 1 - \frac{\pi\alpha Z m_e^2}{m_{\text{He}}|\vec{p}_e|}\left(1 + \frac{1-(g_A/g_V)^2}{1+3(g_A/g_V)^2}\frac{W_0-W}{3W}\right). \qquad (3.45)$$

In addition to this, the single bound orbital electron around the tritium will act with a screening effect on the nuclear charge. This correction factor effectively replaces the energy factors in the Fermi function with equivalent energies reduced by the screening potential of a 1s orbital electron. This gives [97]

$$S(Z,W) = \frac{\overline{W}}{W}\left(\frac{\overline{k}}{k}\right)^{-1+2\gamma}\frac{\left|\Gamma(\gamma+i\overline{\eta})^2\right|}{\left|\Gamma(\gamma+i\eta)^2\right|}e^{\pi(\overline{\eta}-\eta)}, \qquad (3.46)$$

where $\overline{W} = W - V_0/m_e$, $\overline{k} = \sqrt{\overline{W}^2-1}$ and $\overline{\eta} = \alpha Z\overline{W}/\overline{k}$. Here, $V_0 = (76\pm10)$ eV is the nuclear screening potential of a 1s helium orbital electron [99].

3.4.4 Radiative Corrections

Radiative corrections to beta-decay come from the emission of soft photons (carrying negligible energy) from the initial tritium, final helium or electron. Considering soft photon emission to all orders removes an infrared divergence near the endpoint

and gives a correction factor [100]

$$
\begin{aligned}
G(E_e, E_e^{\max}) = {}& \left(\frac{E_e^{\max} - E_e}{m_e} \right)^{(2\alpha/\pi)t(\beta)} \left\{ 1 + \frac{2\alpha}{\pi} \left[t(\beta) \left(\ln 2 - \frac{3}{2} + \frac{E_e^{\max} - E_e}{E_e} \right) \right. \right. \\
& + \frac{1}{4}(t(\beta)+1) \left(2(1+\beta^2) - 2\ln\left(\frac{2}{1-\beta}\right) + \frac{(E_e^{\max} - E_e)^2}{6E_e^2} \right) \\
& \left. \left. + \frac{1}{2\beta} \left(L(\beta) - L(-\beta) + L\left(\frac{2\beta}{1+\beta}\right) + \frac{1}{2}L\left(\frac{1-\beta}{2}\right) - \frac{1}{2}L\left(\frac{1+\beta}{2}\right) \right) \right] \right\},
\end{aligned}
$$

$$(3.47)$$

where $\beta = |\vec{p}_e|/E_e$, $t(\beta) = \operatorname{arctanh}(\beta)/\beta - 1$ and $L(x) = \int_0^x \frac{\ln(1-y)}{y} dy$ is Spence's function.

3.4.5 Orbital Electron Level

In addition to the electron emitted in the process of beta decay, there is an orbital electron that will be initially bound within the tritium atom. It's important that the transition of this electron from the eigenstates of tritium to that of helium (including continuum emission) is considered as this affects the energy within the process. Furthermore, the indistinguishability of the two electrons means consideration is needed for the exchange of the two particles.

In order to calculate this the sudden approximation is used, in which a transition amplitude of the form $\langle b| U(t_2,t_1) |a\rangle$, for $U(t_2,t_1)$ some transition function from time t_1 to t_2, is approximated by the overlap $\langle b|a\rangle$ for $t_2 - t_1 \approx 0$ [101].

In practice, the energy of the orbital electron is accounted for by modifying the tritium and helium masses to give the combined mass of the atom. This will in turn affect the maximum emitted electron energy with

$$
E_e^{\max} \to
\begin{cases}
E_e^{\max}(n), \ m_{\mathrm{H}} \to m_{\mathrm{H}} + m_e - R_h, \ m_{\mathrm{He}} \to m_{\mathrm{He}} + m_e - 4R_h/n^2, \\
E_e^{\max}(\tau), \ m_{\mathrm{H}} \to m_{\mathrm{H}} + m_e - R_h, \ m_{\mathrm{He}} \to m_{\mathrm{He}} + m_e + 4R_h/\tau^2,
\end{cases}
\tag{3.48}
$$

where $n = 1, 2, \ldots$ is the integer-valued principle quantum number, $\tau = -2\alpha m_e/|\vec{p}_2|$ for $|\vec{p}_2|$ the momentum of the orbital electron which will be integrated over and $R_h = 13.61$ eV is the Rydberg energy [102]. The discrete values of n give the

He$^+$ State	Energy [eV]	Branching Ratio
$1s$	0	70.36%
$2s$	40.81	24.98%
$3s$	48.37	1.27%
$4s$	51.02	0.38%
$5s$	52.24	0.17%
continuum	≥ 54.42	2.63%

Table 3.1: Excitation energy above the ground state associated with final helium orbital electron states and the corresponding asymptotic branching ratios for detected electron energies much below the endpoint.

orbital energy levels in the case of a bound final state and τ parametrises the free energy in the case of displacement into the continuum. It is assumed that the orbital electron finishes in an s state but, given that it is the only bound electron (decays to two bound electrons would be undetectable), the energy and thus probability is unaffected by the final angular quantum numbers.

If the expression for decay to a single state is written as $d\Gamma/dE_e(E_e^{\mathrm{max}})$ then the full expression for the decay will be a weighted sum of decays to the states with different E_e^{max}, with the weightings accounting for the probability exchange of the two electrons. This is given by [103]

$$\frac{d\Gamma_{\mathrm{full}}}{dE_e} = \sum_{n=1}^{\infty} 2 \frac{d\Gamma}{dE_e}(E_e^{\mathrm{max}}(n)) \left[256 n^5 \frac{(n-2)^{2n-4}}{(n+2)^{2n+4}} + \frac{\alpha^2(\tau)}{n^3} - 16n \frac{(n-2)^{n-2}}{(n+2)^{n+2}} \alpha(\tau) \right]$$
$$+ \frac{1}{\pi} \int_{-\infty}^{\tau} \frac{d\tau'}{\tau'^4} \frac{d\Gamma}{dE_e}(E_e^{\mathrm{max}}(\tau')) \frac{2\pi\tau'}{e^{2\pi\tau'}-1} \left[\alpha^2(\tau) - \alpha(\tau)\alpha(\tau') + \alpha^2(\tau') \right],$$

(3.49)

where

$$a(\tau) = \exp\left[2\tau \arctan\left(-\frac{2}{\tau} \right) \right] \left(\frac{\tau^2}{1 + \frac{1}{4}\tau^2} \right)^2 .$$

(3.50)

The first line gives the discrete sum over decays to bound energy levels whilst the second integrates over the energy of a continuum electron up to it having the energy of the beta electron. For evaluation of this $(n-2)^{n-2} = 1$ for $n = 2$.
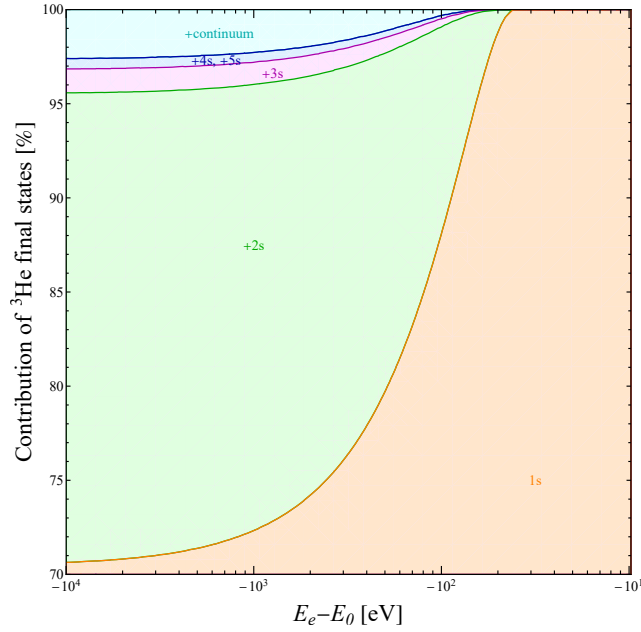
Figure 3.2: Fraction of decays to helium energy levels $1s$ (ground state), $2s$, $3s$, $4s + 5s$ of the orbital electron (higher levels neglected), as well emission of the orbital electron (continuum) as a function of the beta electron's energy below the endpoint.

The impact of this on the spectrum can be considered in two ways. In Table 3.1, based upon [101], the proportion of decays to each energy state when the detected electron is far from the endpoint is given. As can be seen, the proportion of decays to the $2s$ state is significant at nearly 25%. This is key because it introduces a second endpoint at a fixed energy below the primary one (corresponding to decays to $1s$). This could potentially be of interest as an additional signal for sterile neutrinos searches or other beta decay experiments that are based upon endpoint measurements.

Alternatively, the decays to different energy levels can be viewed as a function of the beta electron's energy below the endpoint. Decays very close to the endpoint are forbidden for any of the higher energy levels because of energy conservation. For decays in which the beta electron is less energetic, there is a chance of some of that energy being taken by the orbital electron. As the energy decreases the probability of such decays increases until tending towards the asymptotic values given before. This can all be seen in Fig. 3.2.

3.5 Double Beta Decay Spectrum

As described in Section 2.9.3, the primary means of searching for Majorana neutrinos is through the measurement of double beta decay with the hopes of detecting neutrinoless double beta decay. Calculating the decay rate for double beta decay is significantly more challenging than that of single beta decay due to the much greater dependence upon the internal dynamics of the decay nucleus. In the process, a sum over all potential intermediate nuclear states must be considered with the transition matrix elements between the initial, intermediate and final states being calculated. Direct calculation is currently analytically impossible, with instead an array of different models being used for the nuclear states to calculate transitions. Here I will discuss the fundamentals of the calculation and derive an approximate result sufficient for the later discussion.

The beginning of the calculation is similar to that of single beta decay, the effective Lagrangian appears as two copies of the single beta decay Lagrangian from before [104]

$$\mathscr{L}_{\beta\beta} = -\left(\frac{G_F}{\sqrt{2}}V_{ud}\right)^2 [\bar{e}\gamma_\mu(1-\gamma^5)\nu_e][\bar{\nu}_e^c\gamma_\rho(1-\gamma^5)e^c]$$
$$[\bar{p}\gamma^\mu(g_V - g_A\gamma^5)n][\bar{p}\gamma^\rho(g_V - g_A\gamma^5)n], \quad (3.51)$$

where, as described before, the superscript c denotes charge conjugation and the factors of g_V and g_A are nucleus dependent and not necessarily the same as that for tritium single beta decay.

There are two different ways of evaluating this Lagrangian into a matrix element. In the case of 2-neutrino double beta decay, $2\nu\beta\beta$, the two neutrinos will be emitted in the decay. Conversely, for neutrino-less double beta decay, $0\nu\beta\beta$, the neutrino will be an internal propagation line with the emitted neutrino from one decay being recaptured in the other.

To a good approximation, the calculation of the beta decay processes can be separated into three parts, a phase space calculation, the axial-vector coupling constant and a Nuclear Matrix Element (NME) [105]. This is often written as

$\Gamma = G \, g_A^4 \, |M|^2$ where G is the phase space factor, g_A is the axial-vector coupling as before and $|M|$ is the NME. The phase space calculation is relatively simple, as shall be shown below. As explained previously for Tritium, the value of g_A varies between different elements due to different amounts of 'quenching' and is often written as g_A^{eff}. However, the calculation of the nuclear matrix element, which must take account of all of the strong forces dynamics between the nucleons as well as the underlying symmetries, is highly complex. There are multiple different many-body methods which aim to estimate these quantities for each double beta decay element. However, their results often vary significantly with factors of up to 3 in the matrix element (meaning up to 9 in the decay rate which is proportional to its square) [106, 107].

Calculating this matrix element requires summing over all the different intermediate nuclear states. In order to simplify this process, the 'closure' approximation is used in which it is assumed that all of the intermediate states have an energy equal to the average of their energies. There are limitations in this approach with the approximation breaking down for certain nuclei [108]. In general, however, the results from closure have been found to agree with non-closure results to with an accuracy of around 10%, significantly smaller than the uncertainties between different nuclear matrix models [109].

From this point, following through the calculation gives the approximate matrix elements for $0\nu\beta\beta$ (M_0) and $2\nu\beta\beta$ (M_2) as [110]

$$|M_0|^2 \;\propto\; 4G_F^4 |V_{ud}|^4 H_\mu^\mu H_\rho^\rho m_{\beta\beta}^2 (2P_1 \cdot P_2), \tag{3.52}$$

$$|M_2|^2 \;\propto\; 4G_F^4 |V_{ud}|^4 H_\mu^\mu H_\rho^\rho (2P_1 \cdot P_2 K_1 \cdot K_2), \tag{3.53}$$

where H is the hadronic matrix element and some non-kinematic terms have been neglected. The 4-momenta $P_{1,2}$ refer to the two emitted electrons and $K_{1,2}$ to the two neutrinos (in the case of $2\nu\beta\beta$).

The effective double beta decay neutrino mass $m_{\beta\beta}$ is given by

$$m_{\beta\beta} = \left| \sum_{i=1}^{3} (U_{ei})^2 m_i \right|, \qquad (3.54)$$

where here the PMNS mixing elements will also have additional Majorana phases as the neutrino is Majorana. The proportionality of the decay to this quantity is because of the necessity for a chirality flip in the neutrino. This is because the produced neutrino in the first decay will be right-handed but must become left-handed in order to be reabsorbed into the second decay. The potential minimum value of $m_{\beta\beta}$ is very different in the cases of normal and inverted ordering. For normal ordering the Majorana phases mean that significant cancellation can occur with there effectively being no lower bound for its magnitude. This requires rather fine-tuning with the parameter space where this occurs being small [111] but some exotic flavour models may more favour this parameter region [112]. However, for inverted ordering the dominance of the necessarily heavy state ν_1 means there must be a lower bound of $m_{\beta\beta} = 18.6 \pm 1.2$ meV [113]. Many next-generation experiments hope to get close to this level (see Section 3.6.5).

For my calculations, I neglect the nuclear matrix elements which only have a small impact on the spectral shape. Thus the decay rates that I use are [104]

$$\frac{\Gamma_0}{dE_1 dE_2 d\cos\theta_{12}} \propto m_{\beta\beta}^2 E_1 E_2 |\vec{p}_1||\vec{p}_2| \left(1 \pm \frac{|\vec{p}_1||\vec{p}_2|\cos\theta_{12}}{E_1 E_2} \right) \delta(E_{0\nu\beta\beta}^{\max} - E_1 - E_2),$$

$$(3.55)$$

$$\frac{\Gamma_2}{dE_1 dE_2 d\cos\theta_{12}} \propto E_1 E_2 |\vec{p}_1||\vec{p}_2| (E_{2\nu\beta\beta}^{\max} - E_1 - E_2)^5 \left(1 \pm \frac{|\vec{p}_1||\vec{p}_2|\cos\theta_{12}}{E_1 E_2} \right),$$

$$(3.56)$$

where the subscripts 1 and 2 refer to the two electrons, θ_{12} is the angle between their momenta and the minus (plus) refers to a left (right) handed leptonic current. $E_{2\nu\beta\beta}^{\max}$ is the maximum available total energy for the electrons in the decay, the Q-value, for $2\nu\beta\beta$ and equivalently for $E_{0\nu\beta\beta}^{\max}$.

The maximum available total energies for the two emitted electrons is different
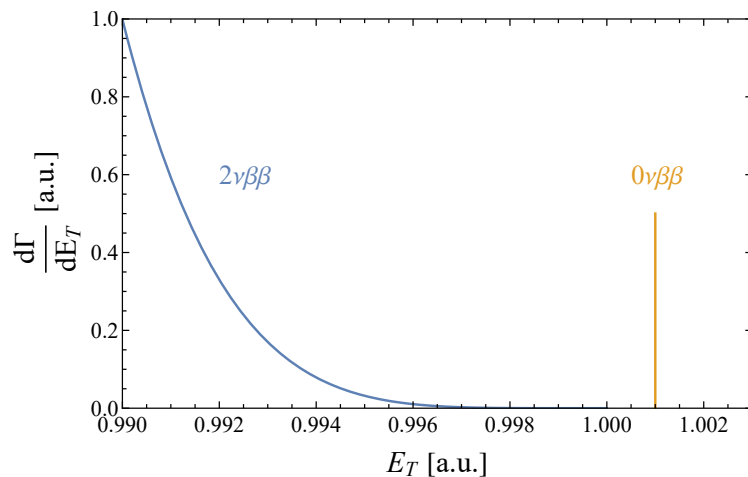
Figure 3.3: Spectrum for both $2\nu\beta\beta$ and $0\nu\beta\beta$ as a function of the total electron energy $E_T = E_1 + E_2$, focusing on the region near their endpoints. Both axes are in arbitrary units.

between $2\nu\beta\beta$ and $0\nu\beta\beta$ by a factor of $2m_\nu$. In both cases, the maximum energy corresponds to when the two electrons are emitted back to back with equal momenta with the former also including two neutrinos emitted at rest and the latter not. Thus $E_{2\nu\beta\beta}^{\text{max}} = m_i - m_f - 2m_\nu$ and $E_{0\nu\beta\beta}^{\text{max}} = m_i - m_f$ where m_i and m_f are the initial and final nuclear masses. As with single beta decay, there are thus three endpoints for $2\nu\beta\beta$, corresponding to the three different neutrino masses. However for $0\nu\beta\beta$ the kinematics require the total energy to take a single fixed value, as enforced by the δ-function in Eq. (3.56). This can be seen in Fig. 3.3 where, as a function of the total energy, the $2\nu\beta\beta$ spectrum follows a smooth decrease to the endpoint whereas the $0\nu\beta\beta$ is a mono-energetic peak at a point above the $2\nu\beta\beta$ endpoint.

The spectral shapes for both individual and total electron energies from these approximate forms are sufficiently close to more precise results calculated in [114] and other places for the purposes in the following chapters.

3.6   Current and Future Experiments

The current generation of single and double beta decay experiments are built upon years of development and improvement. However, as attempts to measure the neutrino mass or detect Majorana neutrinos continue, new techniques will be required to reach the levels of precision and exposure required.

3.6.1 Tritium Beta Decay: KATRIN and TRISTAN

The current strongest bound on the effective single beta decay mass comes from the KATRIN experiment. Its most recent results place a limit of $m_\beta < 0.8$ eV at 90% confidence limit (CL) [54]. This improved on the previous limits of 2.2 eV and 2.3 eV at 95% CL from the Troitsk and Mainz experiments, respectively [115, 116]. The KATRIN experiment works as a high-pass filter, the emitted electrons are collimated using a varying magnetic field with electrons below a certain energy being then rejected by an electric field. This creates a measurement of the integrated spectrum, the count being of all electrons above a certain energy up to the endpoint [54]. Once its full run is complete, the KATRIN experiment is expected to, in the absence of mass measurement, provide an upper bound of $m_\beta < 0.2$ eV [90]. The limitations on the size of this bound come from the systematic uncertainties in the collimation of the electron beam. A greater energy resolution would require a spatially larger magnetic field and thus a larger machine apparatus. Given that the main collimator is already 10 m in dimension, this would be financially and practically infeasible [117].

The KATRIN experiment is designed to focus on the endpoint of the beta decay spectrum as this is the region most sensitive to the impact of the neutrino mass. However, the impact of heavy sterile neutrinos could be found anywhere in the spectrum, with their endpoint being at a point below that of the light endpoint by an amount equal to their mass. Thus the KATRIN experiment in its current run is insensitive to sterile neutrinos much heavier than the 300 eV below the endpoint that it scans, their most recent search has placed limits only on sterile neutrinos with masses below around 2 keV [118]. In theory, to measure these heavier states the high-pass electric field could be reduced to measure a greater range of the spectrum. However, the current KATRIN detector is limited to measurements of up to 10^5 counts per second (cps) and measurements of the whole spectrum would need a detector capable of handling rates of up to 10^8 cps [119]. To fix this, an upgrade called TRISTAN is being currently developed. This new detection system aims to have an energy resolution of 300 eV which will enable measurement of

active-sterile mixing to a similar sensitivity as astrophysical results, equivalent to $\sin^2\theta \sim 10^{-6}$ [120]. TRISTAN is aiming to begin installation after the completion of KATRIN's main run in 2025 [121].

3.6.2 Future Tritium Experiments: Cyclotron Radiation and Project 8

Given the limitations on KATRIN-like experiments the future of the single beta decay measurements will have to be performed using novel techniques. The primary one of these currently in development is that of Cyclotron Radiation Emission Spectroscopy (CRES). When a charged particle enters a magnetic field its motion will bend and precess around the magnetic field lines and it will emit cyclotron radiation. The frequency of this radiation for an electron is

$$f = \frac{1}{2\pi}\frac{eB}{E_e},$$

(3.57)

where e is the electron charge, B the magnetic field and E_e the electron energy. This crucially depends upon the energy of the charged particle and, providing that the magnetic field can be sufficiently well controlled, the energy of the electron can thus be precisely calculated from measurements using the advanced technology that already exists for precision frequency measurements [55]. As this technology doesn't involve any filtering, such an experiment would potentially be sensitive to the entire energy spectrum. The Project 8 experiment aims to have a sensitivity of $m_\beta < 40$ meV [55] but with a target energy resolution across the entire spectrum of 100 eV [122]. The other significant change between Project 8 and KATRIN is the use of atomic rather than molecular tritium. Molecular tritium has an irreducible uncertainty of around 0.3 eV due to the internal energy dynamics between the two atoms [123]. This is too large to allow for measurements of m_β in the 'worst-case' scenario of the lightest neutrino being massless. In this case, oscillation mass splittings imply $m_\beta \sim 40$ meV in the inverted ordering case and $m_\beta \sim 9$ meV in the normal ordering case [124]. By using atomic tritium instead the Project 8 experiment is expected to reach this worst case scenario for inverted ordering, probing as

low as 40 meV.

Although Project 8 is expected to form the new frontier of single beta decay measurements, it is possible that even this will be insufficient to measure the neutrino mass in 'worst-case' scenarios. In an attempt to increase the energy resolution of measurements exploiting CRES technology, and hence to push the existing and proposed bounds even further, the Quantum Technologies for Neutrino Mass (QTNM) consortium, consisting of several UK institutes, has been formed with a proposal to make guaranteed direct neutrino mass measurements with the help of quantum technologies [56]. The development of this next-next-generation experiment is currently beginning with the CRES Demonstration Apparatus (CRESDA) which aims to address: the production and confinement of tritium atoms; mapping magnetic fields in the CRES detection region with high precision, and the realisation of high sensitivity microwave electronics devices for detection and characterisation of the cyclotron radiation.

3.6.3 Expected Statistics in Future Tritium Decay Experiments

Given their primary focus on measuring the neutrino mass, tritium decay experiments are quantified by their count rate within their area of interest near the endpoint. However, for the measurement of exotic currents and sterile neutrinos it is necessary to look at the entire spectrum, as I shall be modelling in later sections. With this in mind, it is worth considering what total count rates the next generation of experiments will be attempting to produce. The total count rate within a certain window, N_{win}, between energies E_1 and E_2 is easily calculated as

$$N_{\text{win}} = \frac{N_{\text{tot}}}{\Gamma} \int_{E_1}^{E_2} \frac{d\Gamma}{dE_e} dE_e, \tag{3.58}$$

for a total count rate across the entire spectrum of N_{tot} and a total decay rate Γ.

In the measurement of the neutrino mass, experiments are expected to focus in a window of around 1 eV below the endpoint. In Fig. 3.4 the proportional change in the count rate to that final 1 eV is shown as a function of the lightest neutrino mass for both the normal and inverted ordering. As mentioned before, the 'worst-case'
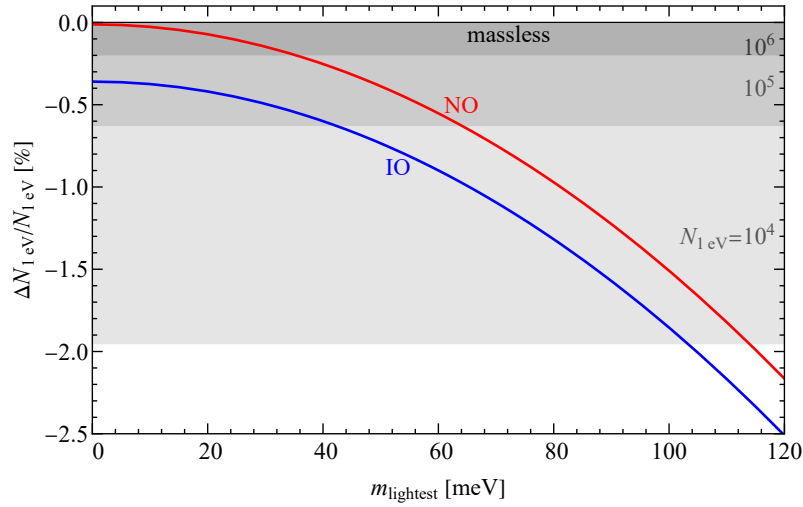
Figure 3.4: Percentage variation in the number of events in the final 1 eV of the tritium energy distribution as a function of the lightest active neutrino mass. The red line denotes the normal ordering case and the blue line the inverted ordering. The gray bands denote the 95% CL for a detectable change in the rate as a function of the total number of events in the final eV.

scenario is that of $m_{\text{lightest}} = 0$ in which the change in the count rate compared to all neutrinos being massless is minimal. It is clear from the figure that the difference in this worst-case between the normal and inverted ordering is significant. For normal ordering the proportional decrease is negligible but for inverted ordering even the worst case gives a decrease of around 0.37% in the count rate. Considering that the Poisonnian statistical fluctuation goes as $1/\sqrt{N_{1eV}}$ (which must be less than the effect of the neutrino mass in order for the masses to be detected) approximately $N_{1eV} \approx 2.8 \times 10^5$ events are required. This corresponds to, using Eq. (3.58), a total rate across the entire spectrum of $N_{\text{tot}} \approx 1.3 \times 10^{18}$. An experiment with this count rate would be able to distinguish between the normal and inverted orderings between the neutrino masses. The TRISTAN experiment is expected to have a total count rate of 10^{16} over its three year run period. In order for their detectors to not be overwhelmed they are reducing the tritium column density by a factor of 100 from KATRIN [121]. Thus, if they were able to maintain a KATRIN-like event rate they would measure 10^{18} events in this time period. This is the number I use throughout my calculations for sensitivities to new physics as it corresponds to this significant distinction point between normal and inverted ordering and is experimentally ac-

cessible within the near future.

3.6.4 Angular Measurements in Tritium Beta Decay

Polarised tritium nuclei have an angular isotropy, as shown by Eq. (3.25), which leads to a difference in the decay rate to the hemispheres aligned and anti-aligned to the nuclear spin. Angular measurements of polarised tritium decay have not been attempted in the past as they offer little additional sensitivity to the neutrino mass (as discussed in Section 5.1). However, their potential for the detection of exotic currents is significant, as shall be discussed later.

The primary challenge in generating the angular correlations is polarising the tritium nucleus. There has already been much interest in polarising tritium nuclei due to their use in nuclear fusion [125]. For example, the beam used at ANKE for COSY-Jülich is able to cool the tritium to 20 K, with a roughly 90% polarisation and roughly 95% disassociation (i.e. separation of the tritium molecule) [126]. This beam of tritium is storable once generated, with measurements finding no appreciable decrease in the polarisation over the order of hours [127].

However, given the immense precision required for the next generation of neutrino measurements, such levels of cooling and disassociation are insufficient. Due to the internal dynamics, molecular tritium has an endpoint 10 eV higher than that of atomic tritium [128]. Given the rapid increase in the spectrum below the endpoint over-contamination with molecular tritium could drown out the atomic spectrum. Project 8 thus aims to have a maximum fraction $T_2/T \leq 10^{-4}$ [128]. In order to prevent recombination this will be cooled to a temperature of around $130 - 170$ mK [129]. The experiment expects to use a magnetic trap in which ^{4}He is used to maintain contact with the walls. This will allow for cooling whilst preventing the tritium from recombining at the boundaries. The magnetic trap will hold any T due to its magnetic moment but will allow T_2, which has none, to freely escape [129, 130].

Designing an experiment that can polarise the tritium and measure the angular distribution may be challenging. However, the technology behind polarisation and storage already exists and the incorporation of magnetic trapping and guiding within

future experiments could also be used to enhance or maintain this polarisation. As shall be shown later, the full angular spectrum doesn't need to be measured, merely sensitivity to the hemisphere of emission is required. Tritium is not the beta decay element best suited to angular measurements due to its low Q-value; as can be seen in Eq. (3.26), the effect is greater for larger electron energies. However, tritium is the future of single beta decay experiments and the sensitivities it achieves are still significant and worthy of discussion.

3.6.5 Double-Beta Decay Experiments

Searches for neutrino-less double beta decay focus on a range of different double-beta decay elements. Current and future experiments use a range of techniques such as scintillation light, calorimeters and germanium detectors to measure the energies of the emitted electrons [131], the signature of $0\nu\beta\beta$ being a delta peak in the combined electron energies at the Q-value (i.e. total available kinetic energy) of the decay [132]. Current searches have yet to detect $0\nu\beta\beta$, with the strongest bound on the effective double-β decay mass, coming from Xenon-136 in the KamLAND-Zen experiment, of $m_{\beta\beta} < (36 - 156)$ meV [133]. In this thesis I will be performing analyses based upon experiments on four different atoms: Calcium-48, Germanium-76, Molybdenum-100 and Xenon-136. These have been chosen as they cover a range of Q-values and nuclear charges and are being used in current experiments [134]. For many experiments the aim is to reach the inverted ordering lower bound of $m_{\beta\beta} = 18.6 \pm 1.2$ meV [113]. A negative result within this range would rule out Majorana, inverted-ordered neutrinos.

The CANDLES experiment uses CaF_2 scintillation crystals to detect the emission of beta-electrons [135]. The crystals are surrounded by a liquid scintillation 4π shield which allows for the rejection of background photon events. The greatest background comes from contamination by thallium-208 and bismuth-212 within the calcium crystals, these are reduced through purification. The most recent CANDLES result found no detected events within the neutrino-less decay window with an expected background of one. This corresponds to a half-life lower bound of 5.6×10^{22} yr which gives an estimated upper bound on the neutrino mass of

$m_{\beta\beta} \leq 2.9 - 16$ eV.

Some of the strongest bounds on the neutrino mass come from germanium based experiments. In these, enriched germanium semiconductors serve as both the decaying medium and the detectors which maximises the detector efficiency [136, 137]. These detectors are surrounded by liquid argon which both shields and cools the detectors, along with a further water shield. The enrichment of the detectors and the strong background veto has led to some of the strongest bounds on the neutrino mass, with a lower bound half-life of 1.4×10^{26} yr at GERDA corresponding to an upper bound of $m_{\beta\beta} < 79 - 180$ meV [137]. With GERDA finishing taking results in 2019, the focus is now on LEGEND-200 - an upgrade within the GERDA apparatus with a 200kg source, reduced impurities and an improved scintillation detection [138]. It is currently taking data with performance verified to be matching expectations [138]. As well as this, the next generation experiment, LEGEND-1000, is currently in the design phase with a target 1000 kg mass aiming to detect neutrino masses down to $m_{\beta\beta} < 9 - 21$ meV [57].

Searches for $0\nu\beta\beta$ in molybdenum have taken the rather different approach of using precise bolometric measurements, called 'CROSS' technology. These detectors are cooled to below 10 mK and, as well as scintillation light, tiny oscillations due to decays are measured using crystals which convert motion into voltage or current pulses [139]. The benefit of such a technique is the extremely high energy resolution which helps to distinguish between the $2\nu\beta\beta$ and $0\nu\beta\beta$ spectra. The CUPID-Mo is a demonstration apparatus for the CUPID experiment. Results from the 1.5 year run of CUPID-Mo found no detection leading to a 1.8×10^{24} yr half life and thus $m_{\beta\beta} < 0.28 - 0.49$ eV. The main CUPID experiment is expected to run with a greater mass and for a longer amount of time, with a predicted sensitivity allowing for upper bounds on the neutrino mass of $m_{\beta\beta} < 10 - 17$ meV, covering the entire inverted ordering region [140].

The strongest bounds on the neutrino mass come from the KamLAND-Zen experiment which uses liquid xenon as a source and scintillator. The vast mass of the experiment has given the high enough statistics for such strong bounds, the

experiment began in 2011 with nearly 400 kg of xenon (KamLAND-Zen 400) but has now been upgraded to work with nearly 800 kg (KamLAND-Zen 800) [141]. This work has given a lower bound on the half life of 2.3×10^{26} yr [133]. The future upgrade of this experiment, KamLAND2-Zen, aims to increase the sensitivity of the experiment by reducing the largest background, spallation products of an electron and a photon, using machine learning [142]. This, along with an improved energy resolution from brighter scintillators, gives the potential of reaching $m_{\beta\beta} <$ 20 meV [143].

3.7 Statistical Approach to New Physics

Throughout most of this thesis the primary question will be whether a particular example of exotic or new physics is potentially observable in a given experiment. The way of approaching this will be in the form of a minimal-χ^2 test. Comparison of the value of the test statistic as a function of the parameters in question to the critical value will give the range of sensitivity for a particular parameter space. If there is no evidence for deviation beyond the expected result, the χ^2 provides an upper bound on the parameter in question, in my case at the 95% CL.

In order to perform the χ^2 the data needs to be broken into bins that can be summed over. Typically, this binning will be in either energy segments (for the energy of the beta-electron) or angular segments (for the angle between the beta-electron momentum and either the nuclear spin or a Lorentz-violating quantity). For the energy binning the number of bins is informed by the energy resolution of the experiment, the bin width is required to be larger than this value [90]. Unless otherwise stated, I always use 20 bins which is sufficient to satisfy this limit. Using a greater number of bins than this gives negligible additional sensitivity to new physics as the scale of variation of the effects (shown later) is typically larger than this bin width. For the angular distribution the number of bins is 2, corresponding to opposing hemispheres for the electron momentum direction. This is because, in most cases, there is a linear $\cos\theta$ dependence meaning that additional bins would give no additional information.

To reflect the experimental lack of sensitivity to the overall magnitude of the energy spectrum, a nuisance parameter, A, is used. This parameter is minimised and gives an additional contribution to the χ^2. Thus the test statistic is given by

$$t(X) = \min_A \left[\sum_{i=1}^{N_{\text{bins}}} \frac{(N_{\text{BSM}}^{(i)}(X) - (1+A)N_{\text{SM}}^{(i)})^2}{(1+A)N_{\text{SM}}^{(i)}} + \left(\frac{A}{\sigma_A} \right)^2 \right], \qquad (3.59)$$

where the subscript BSM denotes the spectrum with new physics (as a function of some parameter(s) X) and SM is the standard result. The parameter $\sigma_A = 2$ is set to give a (somewhat conservative) uncertainty on the value of the normalisation. In practice, this value has very little significance as for all of the calculations performed herein A will be found to be on the order of 10^{-4} or smaller.

One way in which the bins could be evaluated would be to run repeated random calculations, a series of Monte Carlo tests that capture the random fluctuations in the decay. However, this can be massively computationally expensive and provides little additional insight for Poissonian process like this. Instead, I use the methodology of the Asimov data set [144]. This sets the value in each bin to its expectation value and treats the test as a question of the presence of an additional signal on top of the background. Crucially, this means that rather than treating each bin as a random variable (meaning there are $N_{\text{bins}} - 1$ free parameters) the test is taken against the strength of this additional signal. This means in practice that there are as many free parameters as variables characterising the new physics. When testing for one signal variable the test is against the critical value 3.84 and for two it is against 5.99 at 95% CL.

Chapter 4

Exotic Currents within Tritium Beta Decay

Experimental measurements of single beta decay have shown that the weak interaction occurs dominantly via a $V - A$ or vector-axial interaction [15]. The interactions between the quarks and between the leptons contain the left handed projector $1 - \gamma^5$ which maximally breaks CP symmetry, as in Eq. (3.18). However, in considering the beta decay of nuclei this interaction is modified, in Eq. (3.19) this means the interaction between the helium and tritium has the form $g_V - g_A \gamma^5$. Whilst this has so far been found to match with experimental results, it is possible that other currents also contribute to single beta decay coming from higher energy physics beyond the Standard Model. In this chapter I study what the signature of such exotic currents would be in the single beta decay energy and angular spectra as well as tritium beta decay experiments' future sensitivities to them. The work in this chapter largely follows my previously published results in [82].

4.1   Contributions from an Exotic Lagrangian

In this chapter I analyse how the impact of physics beyond the Standard Model could be realised in single beta decay as an addition to the Standard Model Lagrangian term, Eq. (3.19). I consider this through the language of effective field theories (as described in Section 2.9.2). New physics can manifest itself in the Standard Model in the form of higher dimensional EFT terms. Of relevance for

Current	Hadronic	Leptonic
Scalar	$H_S = g_S\, \overline{^3\text{He}}\, {}^3\text{H}$	$j_S^{\pm} = \bar{e}(1 \pm \gamma^5)\nu_e$
Pseudoscalar	$H_P = g_P\, \overline{^3\text{He}}\, \gamma^5\, {}^3\text{H}$	$j_P^{\pm} = \bar{e}\,(1 \pm \gamma^5)\nu_e$
Vector/Axial	$H_{V \pm A}^{\mu} = \overline{^3\text{He}}\gamma^{\mu}(g_V \pm g_A\gamma^5)\, {}^3\text{H}$	$j_{V \pm A}^{\mu} = \bar{e}\gamma^{\mu}(1 \pm \gamma^5)\nu_e$
Tensor	$H_{T \pm}^{\mu\nu} = g_T\, \overline{^3\text{He}}\, \sigma^{\mu\nu}(1 \pm \gamma^5)\, {}^3\text{H}$	$j_{T \pm}^{\mu\nu} = \bar{e}\, \sigma^{\mu\nu}(1 \pm \gamma^5)\nu_e$

Table 4.1: Hadronic and leptonic currents expanded in the basis of gamma matrices.

single beta decay are the terms of dimension 6 which will come from some high energy scale Λ and will be weighted with a suppressing factor of c/Λ^2 where c is a dimensionless constant assumed to be of order 1. This new physics can be fully accounted for by considering all possible spinor bilinears which could appear in the Lagrangian, including scalar, pseudoscalar and tensor terms. A summary of all the different terms appears in Table 4.1, giving the form of the hadronic and leptonic parts of the Lagrangian. For example, a left-handed tensor term could contribute additionally to the Lagrangian in the form,

$$\mathcal{L}_{\text{H}} = -\frac{G_F}{\sqrt{2}}|V_{ud}|\varepsilon_T g_T \left[\overline{^3\text{He}}\sigma^{\mu\nu}(1-\gamma^5)^3\text{H}\right] \left[\bar{e}\sigma_{\mu\nu}(1-\gamma^5)\nu_e\right], \qquad (4.1)$$

where the tensor $\sigma^{\mu\nu} = \frac{i}{2}[\gamma^{\mu},\gamma^{\nu}]$, g_T is the tensor form factor and ε_T is a dimensionless multiplicative factor.

All of these terms include nuclear form factors $g_X = g_X(q^2)$ where q is the exchanged momentum between the nucleus and leptons. In the dipole approximation they take the form $g_X(q^2) = g_X(0)/(1 - q^2/M_X^2)^2$ where $q^2 \lesssim (18.6\text{ keV})^2$ and $M_X^2 \sim (1\text{ GeV})^2$ [89]. Thus it is safe to approximate them with the constant value $g_X(q^2) \approx g_X(0)$. The form factor values $g_S = 1.02$, $g_P = 349$, $g_T = 1.02$ are calculated from phenomenological studies and Lattice QCD [145, 146].

Any interaction involving one of these currents I call 'exotic'. The total con-

tribution of all the possible currents from Table 4.1 is

$$\mathscr{L}_{\text{exotic}} = -\frac{G_F}{\sqrt{2}} V_{ud} \left(\tilde{\varepsilon}_L H^{\mu}_{V-A} j_{\mu,V+A} + \varepsilon_R H^{\mu}_{V+A} j_{\mu,V-A} + \tilde{\varepsilon}_R H^{\mu}_{V+A} j_{\mu,V+A} \right.$$

$$+ \varepsilon_S H_S j_S^- + \tilde{\varepsilon}_S H_S j_S^+ - \varepsilon_P H_P j_P^- - \tilde{\varepsilon}_P H_P j_P^+$$

$$\left. + \varepsilon_T H^{\mu\nu}_{T-} j_{T-,\mu\nu} + \tilde{\varepsilon}_T H^{\mu\nu}_{T+} \tilde{j}_{T+,\mu\nu} \right). \tag{4.2}$$

The dimensionless constants ε_i, $\tilde{\varepsilon}_i$ give the interaction strength relative to the Standard Model $V - A$ Fermi coupling G_F. They can be potentially be complex valued. The subscript denotes the hadronic part and the presence (absence) of a tilde denotes a right (left)-handed leptonic part. They are related to the conventional effective field theory explanation above as $c/\Lambda^2 = \varepsilon G_F |V_{ud}|/\sqrt{2}$. Any effect beyond the Standard Model must be small compared to the conventional single beta decay strength to have escaped detection thus far. Thus I assume that $|\varepsilon| \ll 1$.

As mentioned, only the left-handed vector-axial term has been observed in experiments, meaning that constraints already exist on the ε_i parameters. A summary of these constraints is given in Table 4.2 where it has been adapted from [83, 147]. They largely come from beta-decay processes and LHC measurements with the strongest limit being given in the table. For the $\text{Re}(\varepsilon_S)$ the limits come from spin-0 nuclei decays [148] whilst for $\text{Im}(\varepsilon_S)$ the limits are from LHC measurements [149, 150]. For $\text{Re}(\varepsilon_T)$ the strongest bounds are from radiative pion decay [151] whilst the imaginary part comes from a search for time-reversal symmetry violation in lithium-8 [152]. For both $\tilde{\varepsilon}_S$ and $\tilde{\varepsilon}_T$ the best limits are from LHC measurements [150]. The strongest limits of ε_P and $\tilde{\varepsilon}_P$ come from pion decay measurements in the ratio of decays to electron and muon states [147, 153]. The limit on $\tilde{\varepsilon}_L$ comes from measurements of the beta decay parameters of many nuclei [154, 150]. Upper limits on $\text{Re}(\varepsilon_R)$ comes from measurements of CKM unitarity in beta decay experiments [155] whilst those for $\text{Im}(\varepsilon_R)$ come from triple angular correlations in neutron decay [156]. Finally, the strongest constraints on $\tilde{\varepsilon}_R$ come once again from LHC measurements [150]. Overall, the strength of constraints that exist vary considerably between the different currents being considered. This is due, as shall

Coupling	$|\mathrm{Re}\,\varepsilon|$	$|\mathrm{Im}\,\varepsilon|$
ε_S	8×10^{-3}	1×10^{-2}
$\tilde{\varepsilon}_S$	1.3×10^{-2}	1.3×10^{-2}
ε_P	4.6×10^{-7}	2×10^{-4}
$\tilde{\varepsilon}_P$	2×10^{-4}	2×10^{-4}
ε_T	1×10^{-3}	1×10^{-3}
$\tilde{\varepsilon}_T$	3×10^{-3}	3×10^{-3}
$\tilde{\varepsilon}_L$	6×10^{-2}	6×10^{-2}
ε_R	5×10^{-4}	5×10^{-4}
$\tilde{\varepsilon}_R$	5×10^{-3}	5×10^{-3}

Table 4.2: Experimental upper bounds on the real and imaginary parts of the exotic coupling strengths at 90% CL.

be seen in more detail later, to the particular spectral modifications caused by each current as well as the limitations of each individual method of measurement.

4.2 Exotic Decay Rate

In order to calculate the effect of exotic currents, I follow the same procedure as in Sections 3.1 and 3.3. As well as the Standard Model term, additional exotic currents can be included from Eq. (4.2) to the interaction Lagrangian. Within the matrix element they will add coherently to the previous terms as they produce the same output particles. The squared matrix element will be composed of standard, purely exotic and interference terms

$$|M|^2 = |M_{\mathrm{SM}}|^2 + \mathrm{Re}(\varepsilon_Y)|M_{LL,Y}|^2 + |\varepsilon_Y|^2 |M_Y|^2, \qquad (4.3)$$

where ε_Y parameterises the particular current with M_{SM} the Standard Model result of Eq. (3.21), interference term $M_{LL,Y}$ (the label *LL* referring to the left-handed vector-axial form of the hadronic and leptonic currents used for the Standard Model result) and purely exotic term M_Y.

This will in turn carry through to both the energy and angular spectra:

$$a(E_e) = a_{\text{SM}}(E_e) + \text{Re}(\varepsilon_Y)a_{LL,Y}(E_e) + |\varepsilon_Y|^2 a_Y(E_e), \tag{4.4}$$

$$b(E_e) = b_{\text{SM}}(E_e) + \text{Re}(\varepsilon_Y)b_{LL,Y}(E_e) + |\varepsilon_Y|^2 b_Y(E_e), \tag{4.5}$$

where a_{SM} and b_{SM} enter into the decay rate using Eqs. (3.22) and (3.25).

Given the upper bounds already existing on the parameters $|\varepsilon_Y| \ll 1$ (see Table 4.2) the terms with left-handed leptonic currents will have dominant exotic contributions from the interference term. However, for the case of right-handed leptonic currents the purely exotic term will dominate. This is because of the requirement for a chirality flip for these currents which will render the interference term proportional to m_ν. For example, for the contribution with left-handed hadronic current and right-handed leptonic current (with coefficient $\tilde{\varepsilon}_L$) the matrix elements are

$$
\begin{aligned}
|M_{LL,LR}|^2 = 16G_F^2|V_{ud}|^2 m_\nu m_e \{ & 2(g_A^2 - g_V^2)m_{\text{H}}m_{\text{He}} + (g_A^2 + g_V^2)P_{\text{H}} \cdot P_{\text{He}} \\
& - 2g_A g_V m_{\text{H}} P_{\text{He}} \cdot S \}
\end{aligned} \tag{4.6}
$$

$$
\begin{aligned}
|M_{LR}|^2 = 16G_F^2|V_{ud}|^2 \\
\times \{ & (g_A - g_V)^2 (P_e \cdot P_{\text{He}})(P_\nu \cdot P_{\text{H}}) + (g_A + g_V)^2 (P_e \cdot P_{\text{H}})(P_\nu \cdot P_{\text{He}}) \\
& + (g_A^2 - g_V^2)m_{\text{H}}m_{\text{He}}(P_e \cdot P_\nu) \\
& - (g_A^2 - g_V^2)m_{\text{He}} [(P_{\text{H}} \cdot P_\nu)(P_e \cdot S) + (P_{\text{H}} \cdot P_e)(P_\nu \cdot S)] \\
& - (g_A + g_V)^2 m_{\text{H}}(P_\nu \cdot P_{\text{He}})(P_e \cdot S) + (g_A - g_V)^2 m_{\text{H}}(P_e \cdot P_{\text{He}})(P_\nu \cdot S) \},
\end{aligned} \tag{4.7}
$$

where the purely exotic result is here identical to the Standard Model result except with $g_A \to -g_A$ and $S \to -S$. The difference between the two is equivalent to taking $\gamma^5 \to -\gamma^5$ (which has no impact on the final result because it appears in even numbers of products) alongside $g_A \to -g_A$ and $S \to -S$. Also, here the interference term is indeed proportional to the neutrino mass. The presence of the factor $m_\nu m_e$ rather than $P_\nu \cdot P_e$ leads to an approximate reduction of $m_\nu m_e / E_\nu E_e$.

This can then be used to calculate the exotic decay rates which are in this case

$$
a_{LL,LR}(E_e) = \frac{G_F^2 |V_{ud}|^2}{2\pi^3} C(E_e) \sum_{i=1}^{3} |U_{ei}|^2 m_e m_{v,i} \frac{m_{\mathrm{H}}|p_e|}{m_{12}^2} \widetilde{y}_i \Bigg[2(g_A^2 - g_V^2) m_{\mathrm{He}}
$$

$$
+ (g_A^2 + g_V^2)(m_{\mathrm{H}} - E_e) - (g_A^2 + g_V^2)\frac{m_{\mathrm{H}}(m_{\mathrm{H}} - E_e)}{m_{12}^2}(y_i + \mu m_v) \Bigg], \qquad (4.8)
$$

$$
b_{LL,LR}(E_e) = -\frac{G_F^2 |V_{ud}|^2}{2\pi^3} C(E_e) \sum_{i=1}^{3} |U_{ei}|^2 g_A g_V m_e m_{v,i} |p_e|^2 \frac{m_{\mathrm{H}}}{m_{12}^2}\widetilde{y} \Bigg[1 - \frac{m_{\mathrm{H}}}{m_{12}^2}(y_i + \mu m_v) \Bigg],
$$

$$(4.9)$$

$$
4\pi a_{LR}(E_e) = \frac{G_F^2 |V_{ud}|^2}{2\pi^3} C(E_e) \sum_{i=1}^{3} |U_{ei}|^2 \frac{m_{\mathrm{H}}^2 |\vec{p}_e|}{m_{12}^2}\widetilde{y}_i \Theta(y_i)
$$

$$
\times \Bigg\{ (g_V - g_A)^2 \Bigg[\frac{m_{\mathrm{H}}(m_{\mathrm{H}} - E_e)}{m_{12}^2} \frac{m_{\mathrm{H}}E_e - m_e^2}{m_{12}^2}(y_i + \mu_i m_{v,i})(y_i + \mu_i m_{\mathrm{He}})
$$

$$
- \frac{m_{\mathrm{H}}^2 |\vec{p}_e|^2}{3m_{12}^4}\widetilde{y}_i^2 \Bigg] + (g_V + g_A)^2 E_e \left(y_i + m_{v,i}\frac{m_{\mathrm{He}}}{m_{\mathrm{H}}} \right)
$$

$$
+ (g_A^2 - g_V^2) m_{\mathrm{He}} \frac{m_{\mathrm{H}}E_e - m_e^2}{m_{12}^2}(y_i + \mu_i m_{v,i}) \Bigg\}, \qquad (4.10)
$$

$$
b_{LR}(E_e) = \frac{G_F^2 |V_{ud}|^2}{8\pi^4} C(E_e) \frac{m_{\mathrm{H}}}{m_{12}^2}|\vec{p}_e|^2 \widetilde{y}_i
$$

$$
\times \Bigg\{ \Bigg[(g_A + g_V)^2 m_{\mathrm{H}} + (g_A^2 - g_V^2) m_{\mathrm{He}} \frac{m_{\mathrm{H}}(m_{\mathrm{H}} - E_e)}{m_{12}^2}
$$

$$
+ (g_A^2 - g_V^2)\frac{m_{\mathrm{H}}m_{\mathrm{He}}}{m_{12}^2}E_e + (g_A - g_V)^2 \frac{m_{\mathrm{H}}}{m_{12}^2}(\alpha - m_e^2)
$$

$$
- (g_A - g_V)^2 \frac{m_{\mathrm{H}}^2}{m_{12}^2}(y_i + \mu_i m_{v,i})\frac{m_{\mathrm{H}}(m_{\mathrm{H}} - E_e)}{m_{12}^2} \Bigg](y_i + \mu_i m_{v,i})
$$

$$
- (g_A + g_V)^2 m_{v,i}^2 - \frac{1}{3}(g_A - g_V)^2 \frac{m_{\mathrm{H}}^3 (m_{\mathrm{H}} - E_e)}{m_{12}^4}\widetilde{y}_i^2 \Bigg\}, \qquad (4.11)
$$

where the sum is over all three neutrino eigenstates (the sum over different orbitals is suppressed within the correction factors). Energy conservation is maintained by the Heaviside function $\Theta(y_i)$, $\mu_i = (m_{v,i} + m_{\mathrm{He}})/m_{\mathrm{H}}$ and $\widetilde{y}_i = \sqrt{y_i \left(y_i + m_{v,i}\frac{2m_{\mathrm{He}}}{m_{\mathrm{H}}} \right)}$ where $y_i = E_{e,i}^{\max} - E_e$. Again the purely exotic terms are related to the Standard
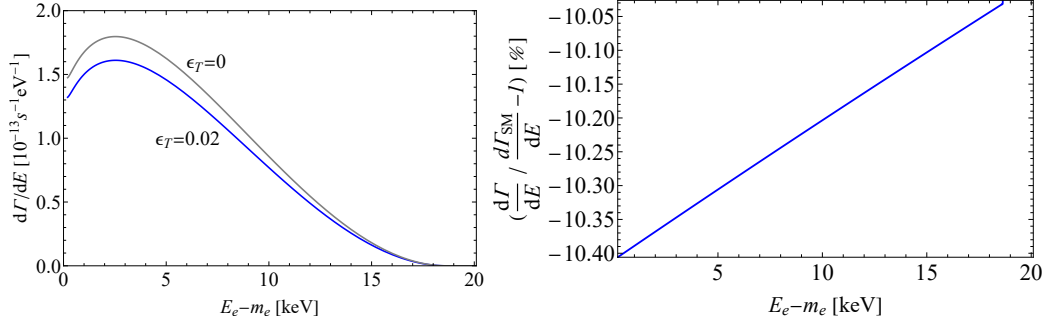
Figure 4.1: Left: Electron energy distribution, in terms of the electron kinetic energy, in the SM ($\varepsilon_T = 0$) and with a left-handed tensor current, $\varepsilon_T = 0.02$. Right: Relative deviation between the two spectra.

Model result by $g_A \to -g_A$ alongside an overall sign flip in b_{LR}. Looking at the result for $a_{LL,LR}$ it can be seen that the approximate ratio of this to the Standard Model result is $m_\nu m_e / E_e y \approx m_\nu / y \lesssim 10^{-5}$. This is the case for all of the terms with right-handed leptonic currents. A full list of decay rates for the purely exotic and the interference terms can be found in Appendix A.

The impact of a single exotic current upon the energy spectrum can be seen in Fig. 4.1 for an exaggeratedly large value of $\varepsilon_T = 0.02$. Whilst the inclusion of a tensor current does cause a significant reduction in the overall energy spectrum, the change is approximately constant, being slightly greater at lower energies. Similarly, the impact of exotic currents on the angular spectrum can be seen in Fig. 4.2. The impact on the angular spectrum is here seen through the change in the value of the angular correlation factor k from Eq. (3.14). Recalling that $k_{SM} = -0.0154$, this means that these currents are causing a reduction in the magnitude of the correlation. The difference in the impact between the two currents comes from the different spectral shapes, the ε_R proportional current has a dominant contribution from its interference term whilst the $\tilde{\varepsilon}_L$ proportional current only has a significant contribution from the $|\tilde{\varepsilon}_L|^2$ proportional (and thus much smaller) purely exotic term. The exotic parameters change the angular spectrum due to the way they modify the internal spin dynamics and momentum exchange as well as by generating left-handed anti-neutrinos which changes the impact of the helicity-chirality relation.
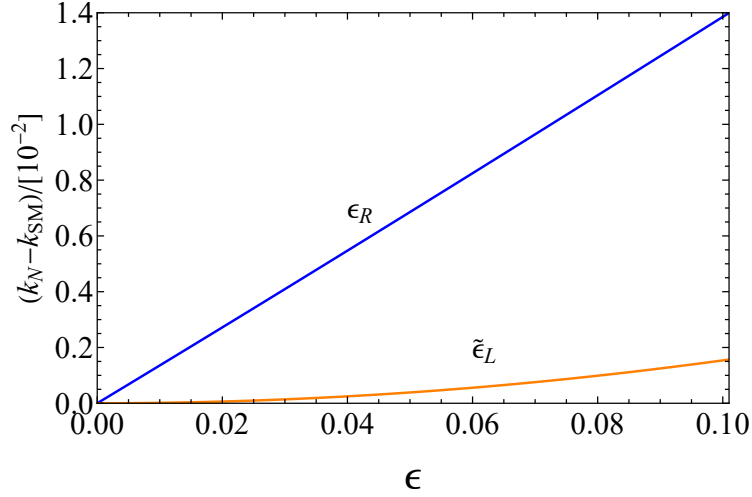
Figure 4.2: Deviation of the angular correlation factor k from the SM value k_{SM} as a function of exotic parameters for the right-handed hadronic current, ε_R and the right-handed leptonic current, $\tilde{\varepsilon}_L$.

4.3 Individual Currents

Ultimately, what is of most interest is to consider the sensitivity that can be reached to the parameters ε_X and $\tilde{\varepsilon}_X$ which give the overall strength of the contribution of these exotic currents. With this in mind, I apply the procedure described in Section 3.7 to quantify the impact of these currents for an idealised experiment looking across the entire energy or angular spectrum. I consider an experiment which has a total of 10^{18} events detected, this matches with the requirements for the next generation of experiments which aim to reach full sensitivity to the neutrino mass in the case of inverted ordering. For the energy measurements the spectrum is split into 20 equal sized bins, this is small to account for the finite energy resolution of the experiment and large enough to capture the scale of changes to the spectrum. For the angular measurements the total number of events in the hemispheres aligned to and against the spin of the tritium nucleus are measured. For the statistical analysis the χ^2 test is used with the equation Eq. (3.59). The exotic contribution, $N_{\text{BSM}}(\varepsilon_X)$, is calculated as a function of the exotic parameter for the modified spectrum and the standard result, N_{SM}, comes from the unmodified expressions of Eqs. (3.22) and (3.25). The nuisance parameter A is used to reflect the uncertainty in tritium beta decay measurements to the total decay rate and is thus minimised over.
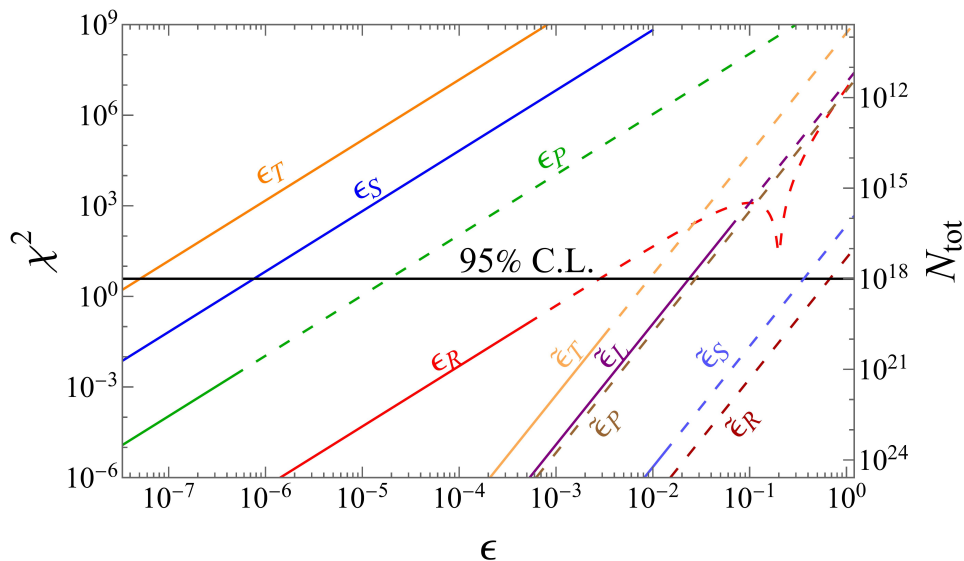
Figure 4.3: The χ^2 deviation for exotic current contributions as a function of the relevant coupling constant, using the tritium energy distribution. The curves are plotted in solid below the coupling constant's upper bound (cf. Table 4.2) and dashed above. The horizontal black line is the 95% CL sensitivity for $N_{tot} = 10^{18}$ events, while the N_{tot} scale on the right-hand axis shows the number of events required to reach a 95% CL sensitivity. The labels denote the relevant parameter for the current.

Figure 4.3 shows the variation in the χ^2 difference due to the contribution of a single exotic current as a function of the relevant exotic parameter. Of interest is the horizontal line which shows the 95% CL critical value of 3.84, for an experiment with 10^{18} events the upper bound that can be placed on the parameter is given by the value at which this line is crossed. For example, this plot shows that there is a greater sensitivity to currents such as the left-handed tensor and scalar currents which are further to the left of the plot than the right-handed scalar and pseudoscalar currents further to the right. The right-side horizontal axis also allows for the consideration of different numbers of total events. The line for each current gives the total number of events required to provide a 95% CL upper bound for the given value of the parameter. This value is inversely proportional to the χ^2 value which scales proportionally with N_{tot}. For each of the currents the line is shown as solid below the pre-existing experimental upper bound (as shown in Table 4.2) and dashed above this. Any line that is still solid at the critical value thus shows the possibility for an improvement in its measurement by a tritium beta decay experiment.

Overall, the dependency shown in this plot shows the clear difference in sensitivity to left and right-handed currents. For the left-handed currents (those without a tilde) the main contribution comes from the interference term meaning that the χ^2 scales with ε^2. Whilst for the right-handed currents the proportionality to the neutrino mass in the interference term (due to the chiral flip) makes this term negligible, the dominant term is the purely exotic term and the χ^2 scales with ε^4. Given the size of ε this means that measurements are more sensitive to the left-handed currents which have a shallower gradient than the right-handed currents. The variation in sensitivity to different currents is due to their exact spectral form. In particular, the lack of sensitivity to the overall scale of the spectrum (reflected in the χ^2 by the normalisation nuisance parameter) means that those terms that are closest in form to the standard result are going to have a reduced sensitivity. This is most clearly exemplified by the terms with right-handed leptonic contributions (parameters ε_R and $\tilde{\varepsilon}_R$) which each have the weakest sensitivity for the left and right-handed hadronic currents. The sharp dip that occurs in the right-handed leptonic current at $\varepsilon_R \approx 10^{-1}$ is due to near perfect cancellation between the interference and purely-exotic terms which become comparable in size but opposite in sign at this value.

An identical test can be performed when looking instead at the angular distribution, in which the exotic currents affect the ratio of electrons emitted in the hemispheres aligned and anti-aligned to the nuclear spin (calculated assuming total polarisation). As can be seen in Fig. 4.4, the results in this case are similar, except for some currents which gain a much increased sensitivity. As before, the left and right-handedness dictates the slope and general sensitivity of the different currents. The left-handed scalar and tensor currents show only a marginal increase in their sensitivity. This is because in both cases the primary variation in the energy and angular spectra due to the exotic current comes from the a term of Eq. (3.12) which contributes to both rather than the b term that contributes only to the angular spectrum. Conversely, for the right-handed leptonic current (denoted by ε_R) the b term is of a much different form than the standard result, unlike the small variation in a, and thus taking an angular measurement gives a significant increase in sensitivity.
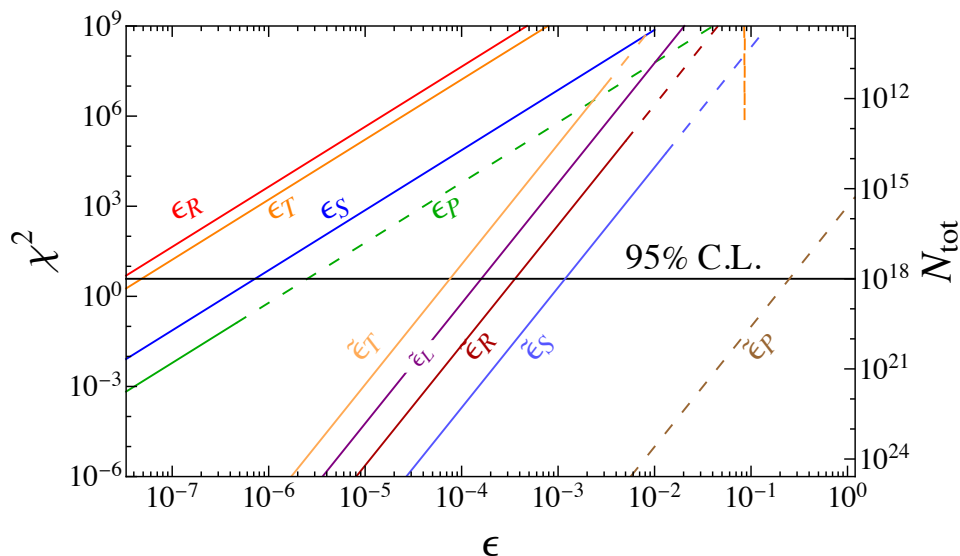
Figure 4.4: As Fig. 4.3, but using the angular distribution.

For similar reasons, for nearly all of the right-handed hadronic terms there is a significant increase in sensitivity. Not only does the angular measurement thus provide a second avenue for measuring these exotic currents, for the majority of them it is more sensitive and would lead to the placing of stronger upper bounds.

It is worth noting that in the above figures I have taken the assumption that ε is real and positive for the sake of ease of visualisation. The assumption of positivity is irrelevant as the sign of the interference term is lost in the χ^2 and would only make a difference if there was significant cancellation or addition between the interference and purely exotic terms (as was noted for a very small range of values of ε_R). As for the assumption of reality, in practice, as can be seen from Eq. (4.5), those terms for which the limit is interference term dominated (the left-handed hadronic) the limit should be taken as being on $|Re(\varepsilon_X)|$ and for those that are purely exotic dominated (the right-handed hadronic) the limit should be taken as being on $|\tilde{\varepsilon}_X|$.

In addition, for the angular plot I have assumed full polarisation of the tritium nuclei. In practice, this is likely to be impossible so a factor of the fractional polarisation, f, (see Eq. (3.17)) should be multiplying the spin. When worked through the calculation, this will lead to a reduction in the sensitivity to the angular measurements with the χ^2 being reduced by a factor of approximately f^2.

4.4 Multiple Currents

In the above I have considered the presence of a single additional exotic current to the standard result. However, in practice multiple of these currents could exist simultaneously and may act to enhance or cancel out the changes to the energy and angular spectra. Because of this, a spectrum that contains two exotic currents could be statistically indistinguishable from the Standard Model spectrum. I consider this using the same method as before, making sure to include interference terms not just between the exotic terms and Standard Model term but also with each other. The test statistic now is expressed as a function of both exotic parameters. As there are now two parameters of interest the critical value is increased to 5.99. The results of this test can be seen in Fig. 4.5, which shows the χ^2 deviation for three different examples of pairs of exotic currents for both the energy and angular distributions. In all cases there is a 'region of similarity' in which the χ^2 value is less than the critical value and the result is indistinguishable from having no exotic currents.

In the upper two plots a scalar current is added alongside a tensor (left) or pseudoscalar (right) current. In both cases the contributions from each of the currents are of a similar form and thus the region of similarity with the Standard Model appears as a straight line band, corresponding to the linear combination of the two currents that will lead to a cancellation. If the figures were viewed on a different scale, it would be possible to see that this linear cancellation eventually breaks down as the quadratic, purely exotic terms begin to also contribute to the spectrum. Thus their regions of similarity are finite in size. In the scalar-tensor case the dominant contribution to the modification of the spectra comes from the a term and thus the energy and angular regions of similarity are nearly identical. However, in the scalar-pseudoscalar case the angular distribution is much more sensitive to the pseudoscalar current than the energy distribution and thus the lines have different gradients. This shows that for certain combinations the performance of an angular measurement provides additional information. If both energy and angular tests are found to be compatible with the Standard Model, then the upper bounds on the currents can be restricted to the overlap region depicted.
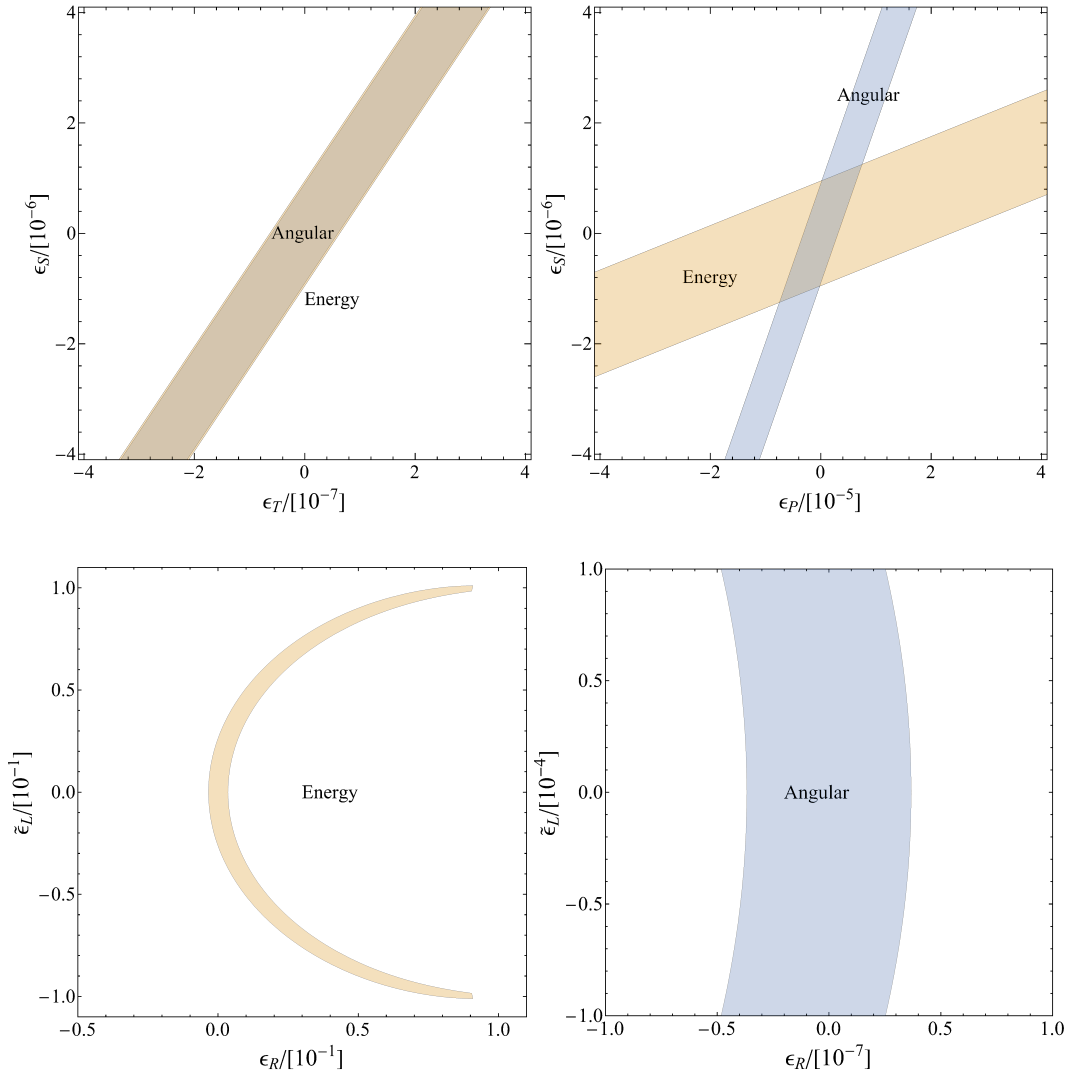
Figure 4.5: 95% CL regions for BSM contributions driven by two exotic currents for $N_{tot} = 10^{18}$ events. The region based on the energy (angular) distribution is in orange (blue). The combinations of currents are: scalar and tensor (top left), scalar and pseudoscalar (top right), right-handed hadronic and right-handed leptonic (bottom, left for energy and right for angular).

In the lower plot of this figure the effects of a right-handed hadronic current are compared to that of a right-handed leptonic current. In this case the regions for the energy and angular distributions have to be plotted separately as the impact upon the angular distribution from these currents is significantly greater than for the energy distribution, the axes of the right figure are many orders of magnitude smaller. In both cases the shape of their regions of similarity is now curved rather than straight. This is because, as explained before, the dominant contribution for a

right-handed leptonic current will be the quadratic, purely exotic term rather than the linear, interference term. This means that the region of similarity will follow an approximately parabolic shape, centred around both exotic parameters being 0. As with the other pairs, this approximate parabolic shape breaks down as the quadratic part of the right-handed hadronic current become significant and thus once again the region of similarity is kept finite. The difference between the energy and angular regions is not just in the much greater angular sensitivity but also that it curves in a different direction. This is due to the difference in sign of the interference term for the right-handed hadronic current between the two terms *a* and *b*. Once again, the measurement of the angular distribution means that much tighter bounds can be placed on the exotic currents but this time almost exclusively due to the much greater angular sensitivity.

4.5   Outcome

Overall, these results demonstrate the potential for improved sensitivity to exotic currents from tritium single beta decay measurements. Whilst the energy measurements represent an improvement for only some of the currents, the angular measurements have an increased sensitivity for all but the pseudoscalar currents. Although there is the potential for cancellation between multiple currents leading to an obscuring of their presence, the use of simultaneous energy and angular measurements would greatly reduce the parameter space in which this could occur in many cases.

Recalling the origin of these exotic currents as coming from some new physics at an energy scale Λ, the probing of these currents down to the level of $\varepsilon_R = 10^{-8}$ means the potential for sensitivity to energy scales of $\Lambda \sim 10^4 \, M_W \sim 10^6$ GeV. Whilst this isn't dramatically large, it is significant when searching for any effect which is only apparent when considering interactions between different types of fermions which might be undetectable in measurements such as propagation experiments.

Chapter 5

Sterile Neutrinos in Tritium Beta Decay

The discovery of additional neutrinos beyond those in the Standard Model would be ground breaking and could potentially help to solve important outstanding questions in physics, such as the composition of Dark Matter in the universe [157]. Unlike the Standard Model neutrinos whose masses are tightly constrained by oscillation and single beta decay experiments, the mass of any sterile states is completely free, potentially ranging from ultra-light to ultra-heavy. Of greatest interest for tritium beta decay experiments is the search for sterile states with masses below the total available energy for the decay, which could thus be produced on-shell as an outgoing state from the decay. In this chapter I will look at how these states would impact upon the neutrino spectrum, how sensitive future experiments would be to them as a function of their mass and how this sensitivity varies depending upon whether they are produced via active-sterile mixing or through exotic currents. The work in this chapter largely follows my previously published results in [82].

5.1   Active-Sterile Mixing

One way in which heavy neutrinos could be produced is through their mixing with the active states. This would involve the flavour eigenstate ν_e being composed of the conventional mass eigenstates along with a new heavy state. Considering a

simplified scenario of one light state and one heavy state with mixing V_{eN} gives

$$v_e = \sqrt{1 - V_{eN}^2}\; v_1 + V_{eN}\; v_2,$$
$$N = -V_{eN}\; v_1 + \sqrt{1 - V_{eN}^2}\; v_2. \tag{5.1}$$

In the case that shall generally be taken here of $V_{eN} \ll 1$, the state N is an entirely sterile state which is mostly composed of the heavy state v_2 whilst the active state v_e is mostly composed of v_1 (in order to match with experimental limits). Of particular interest is when $m_2 \lesssim 18.6$ keV (the total energy given off in the decay) meaning that it can be directly produced in the decay.

Implementing the inclusion of heavy states to the decay calculation is simple. They are merely included as the other light states are to the previously calculated expressions Eqs. (3.22) and (3.25). In this case the equations are extended with $i = 1, \ldots, 3 + n_s$ for n_s heavy states with masses $m_4, \ldots, m_{3+n_s}$ and mixing matrix elements $V_{e4}, \ldots, V_{e(3+n_s)}$. This uses an extension of the PMNS matrix to include additional mixing terms between the three active & n_s sterile flavours with the three light & n_s heavy mass neutrinos. An assumption is made that the full mixing matrix is still unitary, meaning that the larger the active-sterile mixing angle, the greater the reduction in the mixing angle to the active states. This doesn't conflict with experimental results as the uncertainty on the mixing is large enough to be consistent with active-sterile mixing angles of the magnitude considered here [65].

The impact on the spectrum of having an additional heavy state mixed into the electron neutrino can be seen in Fig. 5.1. The most clearly visible impact of the sterile neutrino is the kink in the spectrum which occurs at an energy below the endpoint equal to the mass of the sterile state. For electrons with energy above the kink there is insufficient remaining energy to generate the heavy state whilst below it sterile neutrinos can be produced. Kinks do also occur for the light neutrinos but their masses are so small that so far their kinks cannot be experimentally resolved and would also not be visible on a figure of this scale (Fig. 3.1 uses a scale in which these kinks are visible). Above the kink, the spectrum is the same as the Standard
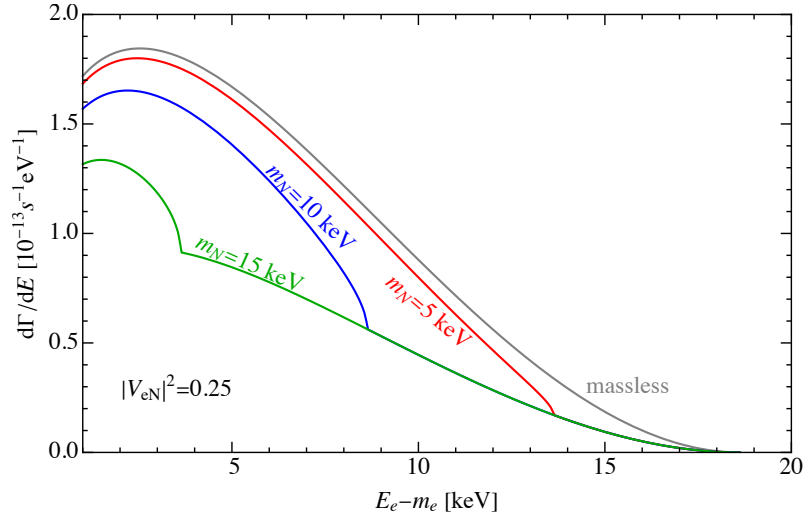
Figure 5.1: Differential decay rate in terms of the electron kinetic energy, for a massless and various heavy, mostly-sterile neutrinos with a mixing of $|V_{eN}|^2 = 0.25$.

Model result but scaled down due to the reduction in the PMNS mixing to the active states, as explained above. Below the kink, there is an increase in the spectrum due to the additional possibility of decay to the heavy state. The heavier the sterile neutrino, the less the increase in the spectrum as the phase space available for such a decay is reduced.

As well as impacting the energy spectrum, the addition of a sterile neutrino would also change the angular distribution. The effect of this can be seen in Fig. 5.2 for the addition of a single heavy neutrino. The change to the angular spectrum is 0 for sterile neutrinos which are either massless or have masses equal to the maximum electron kinetic energy. In the massless case this is because the angular spectrum will

Figure 5.2: Deviation of the angular correlation factor k from the SM value k_{SM} as a function of the sterile neutrino mass for different values of the active-sterile mixing V_{eN}.

merely be identical to that of an active neutrino, in the heaviest mass case it is because the state is too heavy to contribute. In between these two extremes the impact rises and falls, the angular correlation factor is made more positive by the

heavy state (recalling that $k_{SM} < 0$) thus diminishing in magnitude. This is because the anti-neutrino of right-handed chirality has a weaker preference for being right-handed helicity if its mass is greater. The link thus generated between the spin of the nucleus and the momentum directions of the particles (as explained in Section 3.3.2) is diminished and the magnitude of k is reduced. It is worth comparing the change in k here to that of Fig. 4.2; here the change in k is two orders of magnitude smaller (10^{-4} versus 10^{-2}). It can be seen from this that using angular measurements to try and detect sterile neutrinos produced from mixing will be poor with much weaker sensitivity than from looking at the energy spectrum.

Given the lack of sensitivity from angular measurements, I choose to focus on the sensitivity to the mixing from the energy spectrum. In Fig. 5.3 the limit that can be placed upon the active-sterile mixing is plotted against the mass of the heavy sterile state for a future CRES based experiment. Also included in this figure are the pre-existing limits from tritium [158, 159, 160, 161] and nickel [162] single beta decay experiments, and astrophysical limits from X-ray [163], cosmological [164] and supernova [165] studies. There are also the predicted sensitivities for the KATRIN and TRISTAN experiments [121] as well as another experiment HUNTER [166]. These experiments have been chosen as they have sensitivities to sterile neutrinos in the same $0 - 18.6$ keV mass range that a future CRES experiment would be searching for. The physical origins of these limits will be described in the following paragraphs.

The pre-existing limits on the sterile masses from beta decay experiments are due to measurements similar as to those described here. By analysing (at least part of) the electron energy spectrum and comparing it to the expected spectrum an upper bound can be placed on the active-sterile mixing. For tritium experiments the bounds are mostly limited to a few keV as most neutrino mass measurement experiments have concentrated only near the endpoint of the spectrum. For the nickel experiment a dedicated search was made for sterile neutrinos in the mass range of $4 - 30$ keV as this region was largely unmeasured at the time [162].

The astrophysical measurements (labelled as X-ray, Supernova and CMB+BAO+H_0)
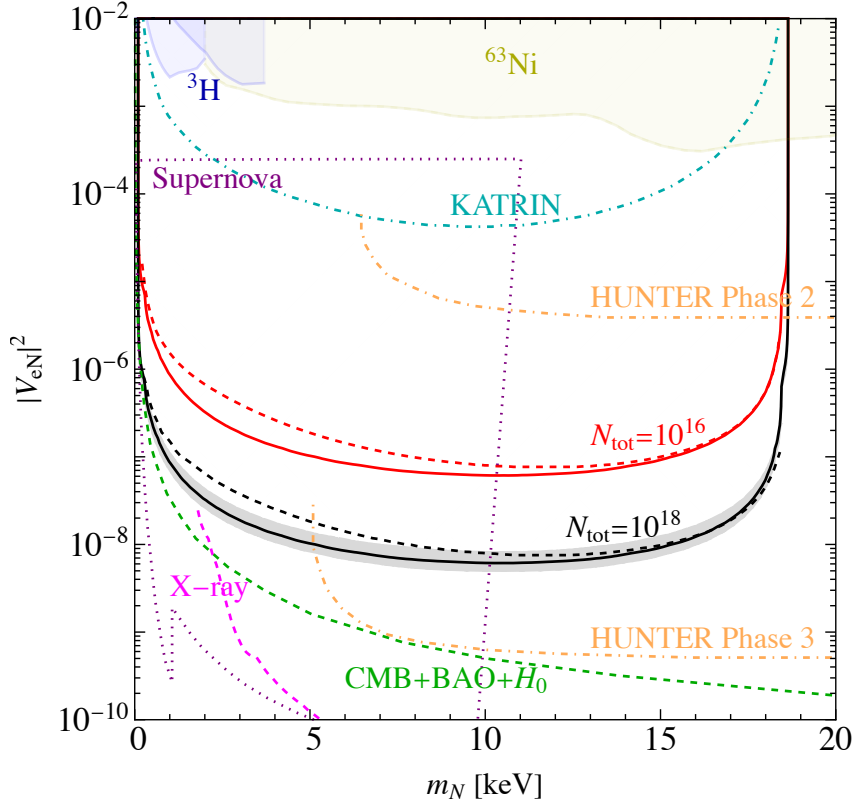
Figure 5.3: Projected sensitivities to the active-sterile mixing $|V_{eN}|^2$ as a function of sterile neutrino mass m_N at 95% CL, for a total number of events $N_{tot} = 10^{16}$ (red solid) and $N_{tot} = 10^{18}$ (black solid), alongside corresponding expected sensitivities of TRISTAN (dashed red and dashed black). The gray shaded band corresponds to the 1σ variation of the 95% CL for a large number of simulations. The shaded regions are excluded by ^{3}H (blue) and ^{63}Ni (yellow) searches together with future experimental constraints expected from KA-TRIN (cyan dot-dashed) and HUNTER (orange dot-dashed). The dotted lines show current astrophysical constraints from: X-ray data (pink), CMB+BAO+H_0 observations (green) and supernova data (purple).

provide a strong means of constraining active-sterile mixing, provided that the underlying astrophysical processes are accurately modelled. The search for neutrino sourced X-rays places a very strong limit for lower mass neutrinos. If sterile neutrinos were present and produced in the early universe then it is expected that their decay to lighter states over time would produce mono-energetic photons in the X-ray region. The NuSTAR experiment found no evidence for unexpected lines in the X-ray spectrum and thus were able to place strong upper bounds for neutrinos with masses less than 12 keV [163]. Cosmological measurements are particularly sensitive to neutrinos because of the way in which they act differently from other matter,

they follow fermionic statistics but are much lighter and more weakly interacting than any of the other fermions. The presence of a decoupled heavy neutrino state would affect the time evolution of the early universe as well as causing variations due to heavy neutrino decay. Studying recombination era observables such as the Cosmic Microwave Background (CMB), Baryon Acoustic Oscillations (BAO) and the Hubble Constant (H_0) can provide limits on the presence of these sterile states in the early universe and thus their mixing into the active states that we know were present. Such measurements include that of the value of the Hubble constant, the scale of the BAO and the CMB shift-parameter which gives the value of the first peak in the power spectrum of the anisotropies in the CMB temperature [167]. Such studies limit the impact that these neutrinos could have with the upper bound on their mixing scaling roughly as $|V_{eN}|^2 \sim 1/m_N^2$ [164]. Finally, the study of Type-II supernovas also acts as a probe intro sterile masses due to the way that sterile neutrino production could disrupt the explosion event. Firstly, sufficient numbers of neutrinos must be trapped in the core in the collapse prior to explosion, neutrinos mixed away into sterile states will escape without redepositing their energy which would cause the explosion to stall out. Secondly, the transition of light neutrinos into heavy state would take away energy from the collapse, cooling it down too rapidly. Finally, the movement of sterile neutrinos into the core would cause the production of electron neutrinos with energies above 50 MeV, a supernova signal that thus far hasn't been detected. The fact that current supernova detection rates match the model predictions can be used with these conditions to place constraints on active-sterile mixing [165].

The future constraints on sterile neutrinos from KATRIN and TRISTAN were previously discussed in Section 3.6.1. Here the result for KATRIN assumes the current detector technology with a total count of 6×10^{11} events - corresponding to a 7 day run with a count rate of 10^6 cps. The results for TRISTAN are those labelled by the total counts of 10^{16} and 10^{18} events, the former refers to the realistic expected limit given the systematic uncertainties whilst the latter is that reached by taking the statistical limit [121]. The other future experiment aiming to search

for sterile neutrinos in this range is that of HUNTER. HUNTER is planning to use magnetically trapped caesium-131 atoms in a vacuum which will undergo beta decay after the capture of a ground state orbital electron. As this is a two-body decay the nuclear recoil should be uniquely determined by the neutrino mass. Precision measurements of the nuclear recoil will thus search for a secondary decay peak in addition to that coming from the decay to the light neutrinos. This technology is limited by the uncertainties in the measurement of the nuclear recoil and thus is insensitive to sterile neutrinos at the low keV level which will affect the recoil too insignificantly. Phase 1 of the experiment, currently under construction, will only be sensitive to neutrinos in the 50-280 keV range. The future phases 2 & 3 shown here are based upon higher resolutions of the detector which will allow for searches down to lower masses, these results are based upon conceptual predictions for future experimental uncertainties [166].

Finally, Fig. 5.3 also shows the expected sensitivity of a future CRES experiment to sterile neutrinos for count rates of 10^{16} and 10^{18} events. These results are very similar to the TRISTAN results given that the underlying process and exposure are the same. The greatest sensitivity to the active-sterile mixing is for masses around half of the total available kinetic energy. For massless sterile neutrinos there is no difference between them and the active states so the result will be indistinguishable. Conversely, sterile neutrinos with masses equal to or larger than the maximum kinetic energy will be kinematically impossible to produce. They will lead to a reduction in the overall spectrum due to the change to the PMNS mixing but experiments are insensitive to the overall rate so this effect is lost (reflected by the normalisation over A in the χ^2 calculation of Eq. (3.59)). The band around the limit for 10^{18} events reflects the 1σ variation, due to statistical fluctuations, in the limit that would be reached for a given run of the experiment.

Overall, the potential for future tritium beta decay experiments to probe for active-sterile mixing is significant if they utilise CRES technology to probe the entire energy spectrum. In practice, however, any real experiment will face additional systematic uncertainties that make these results merely an upper bound for

the future sensitivity. Such systematics include limits on the determination of the cyclotron magnetic field and background from recombined molecular tritium. For lighter masses the x-ray and supernova data leads to stronger limits whilst the cosmological results are stronger across the entire mass range. However, these results are based upon highly complex models for universe and stellar evolution and alternative models may lead to much weaker limits than those given here. Ideally, the presence of sterile neutrinos would be observed via a direct detection experiment such as using single beta decay as considered here.

5.2 Exotic Sterile Currents

The second way in which sterile neutrinos could be generated in single beta decay is through exotic currents which directly lead to the emission of the sterile state. These currents would be similar to those explored in the previous chapter but with the emission of a purely heavy/sterile state (which may or may not mix with the light states). I don't consider the underlying mechanism that generates these heavy states but instead include these additional terms as effective operators (the same as in the previous chapter). Decays directly to the sterile state can be parametrised similarly to before where, taking J as j of Table 4.1 but with $\nu_e \to N$, the Lagrangian is

$$
\begin{aligned}
\mathscr{L}_{\text{exotic}}^N = -\frac{G_F}{\sqrt{2}} V_{ud} \bigg(& \varepsilon_L^N H_{V-A}^\mu J_{\mu,V-A} + \tilde{\varepsilon}_L^N H_{V-A}^\mu J_{\mu,V+A} \\
& + \varepsilon_R^N H_{V+A}^\mu J_{\mu,V-A} + \tilde{\varepsilon}_R^N H_{V+A}^\mu J_{\mu,V+A} \\
& + \varepsilon_S^N H_S J_S^- + \tilde{\varepsilon}_S^N H_S J_S^+ - \varepsilon_P^N H_P J_P^- - \tilde{\varepsilon}_P^N H_P J_P^+ \\
& + \varepsilon_T^N H_{T-}^{\mu\nu} J_{T-,\mu\nu} + \tilde{\varepsilon}_T^N \tilde{H}_{T+}^{\mu\nu} \tilde{J}_{T+,\mu\nu} \bigg).
\end{aligned} \tag{5.2}
$$

Here, the ε_i^N, $\tilde{\varepsilon}_i^N$ equivalently parameterise the strength of the exotic sterile currents. This Lagrangian also has an additional left-handed vector-axial contribution parametrised by ε_L^N (which was neglected in the previous case as it could just be absorbed into a redefinition of G_F).

From this Lagrangian the new decay rate can be calculated. This will follow exactly the same procedure as before with the exotic Lagrangian leading to addi-
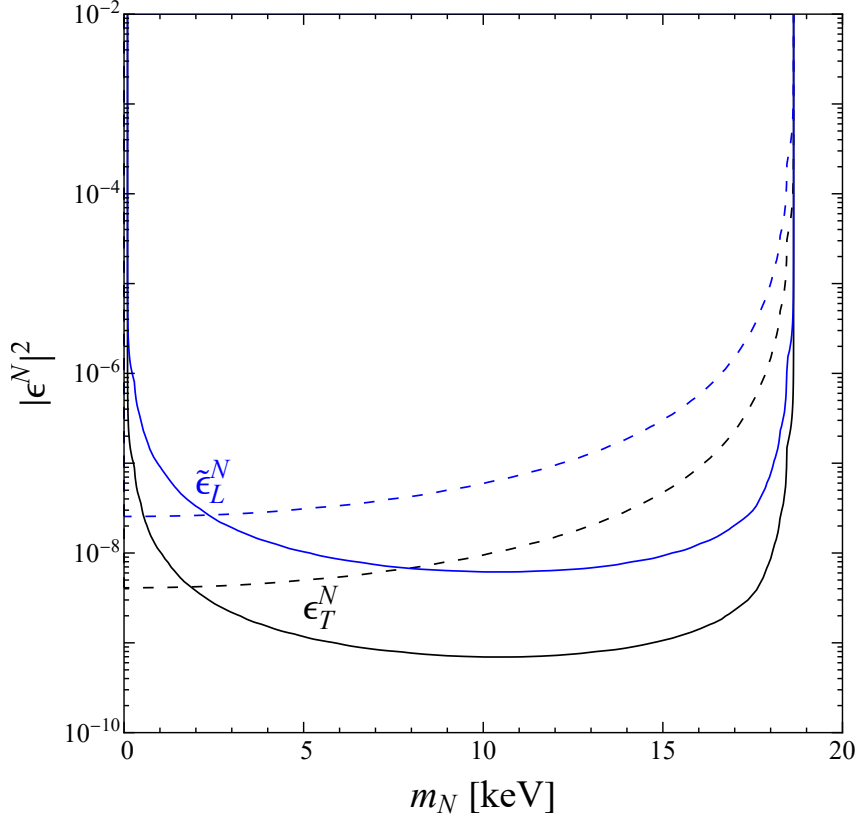
Figure 5.4: Sensitivity at 95% CL to tensor and right-handed leptonic exotic currents as a function of the sterile neutrino mass using the energy (solid) and angular (dashed) distributions for currents parametrised by ε_T^N (black) and $\widetilde{\varepsilon}_L^N$ (blue). The active-sterile mixing is set to zero, $|V_{eN}|^2 = 0$.

tional matrix element terms which finally add on to the decay rate expression. In fact, because the Lagrangian is identical to before, just with $\nu_e \to N$, the individual terms will also be identical (see Appendix A) just with the heavy state neutrino mass being used, m_N. However, unlike in the previous chapter in which the exotic currents interfered with the standard model current, as the sterile neutrino is a different particle from the active neutrino there can be no interference term here. This means that the energy and angular terms will take the form

$$a(E_e) = a_{\text{SM}}(E_e) + |\varepsilon_Y^N|^2 a_Y(E_e), \tag{5.3}$$

$$b(E_e) = b_{\text{SM}}(E_e) + |\varepsilon_Y^N|^2 b_Y(E_e). \tag{5.4}$$

As is to be expected, the sensitivity to these exotic currents will depend upon
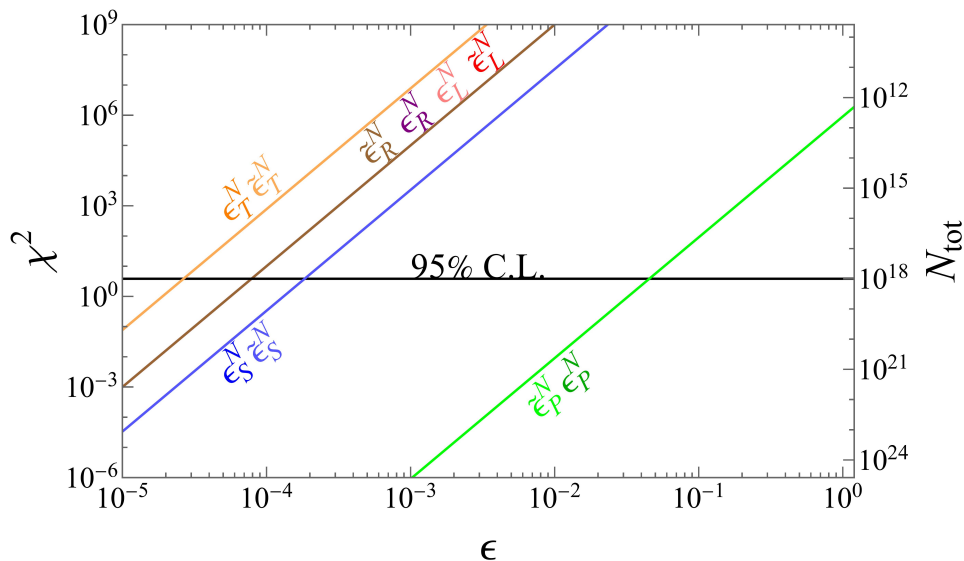
Figure 5.5: The χ^2 deviation from an energy measurement for sterile exotic current contributions as a function of the relevant coupling constant ($m_N = 10\,\text{keV}$). The horizontal black line is the 95% CL sensitivity for $N_{\text{tot}} = 10^{18}$ events, while the N_{tot} scale on the right-hand axis shows the number of events required to reach a 95% CL sensitivity. The labels denote the relevant coupling constant contributing individually.

the mass of the sterile neutrino being generated. The sensitivity to the square of two of these exotic parameters as a function of the sterile mass is shown in Fig. 5.4. For the sensitivity due to energy spectrum measurements the results are largely the same as for active-sterile mixing in the previous section. For near massless sterile neutrinos the contribution due to the additional current is lost due to the normalisation uncertainty. The reason why the change due to ε_T^N is much less than it was for ε_T, the light neutrino exotic current, is due to the lack of an interference term. The interference terms are typically of a much more different spectral shape compared to the standard result than the purely exotic terms are. Thus the change induced by these terms, and thus the sensitivity to the parameter in front of them, is much larger. For the heaviest sterile neutrinos the impact vanishes as before, if the neutrinos cannot be kinematically produced they have no impact upon the spectrum. The sensitivity to the sterile exotic current for an angular measurement is of a comparable magnitude to that from the energy measurement, similarly to the case of active exotic currents but unlike that of active-sterile mixing. For the same reason as the energy measurement, the sensitivity here vanishes for the heaviest
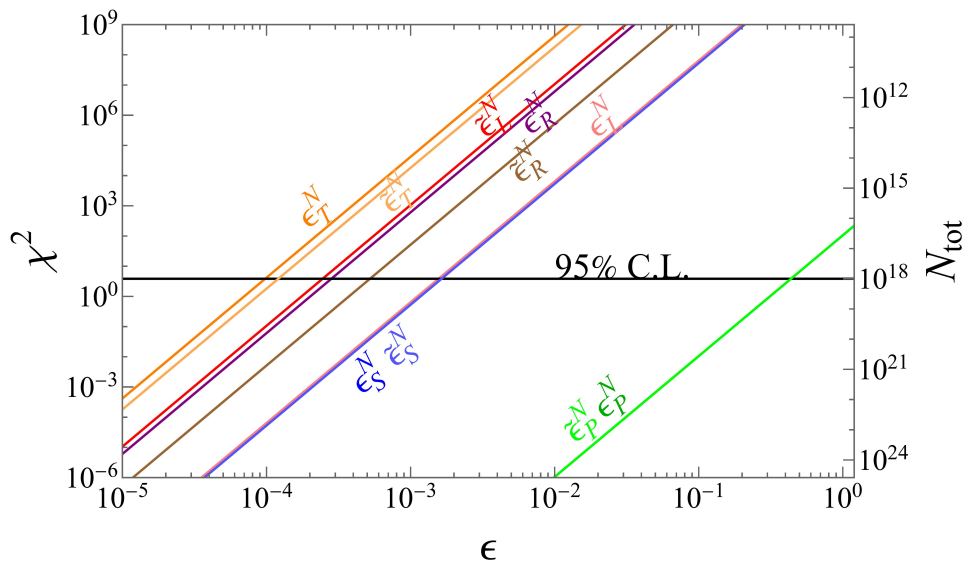
Figure 5.6: As Fig. 5.5 but for an angular measurement.

sterile neutrinos. However, for the lightest sterile neutrinos the sensitivity remains
high. This is because the a_X and b_X exotic terms differ from the standard results
by different amounts that are not simultaneously obscured by the normalisation
uncertainty. Compared to the case of active neutrino exotic currents, the heavy
mass of the sterile neutrino serves to weaken the angular correlation (because of the
aforementioned weakening of the chirality-helicity link) and thus the sensitivity is
worse. Overall, for most of the range of sterile masses an energy measurement is
more sensitive except for those lightest sterile states where an angular measurement
can be stronger instead.

In the same way as before, in order to quantify the sensitivity to these exotic
sterile currents I perform a χ^2 analysis. This is done with the same setup as the
previous chapter including 10^{18} events, 20 energy bins and 2 angular bins. Simi-
larly as to before, I plot in Figs. 5.5 and 5.6 the dependence of the χ^2 deviation as
a function of the exotic parameters looking at both the energy and angular distri-
butions. This is evaluated for a sterile mass of $m_N = 10$ keV, chosen because, as
seen in Fig. 5.4, this is where the spectrum is most sensitive to the exotic currents.
Identically as in Fig. 4.3 all of the dependency follows a straight line, in this case
all of the sterile contributions are quadratic and so all of the lines scale with $|\varepsilon_X^N|^4$.
Here, for the energy sensitivity, there is a significant overlap between many of the

different currents. This is because many of them have identical or approximately identical functional forms for the purely exotic term. Once again the pseudoscalar terms have the weakest sensitivity and the tensor terms the strongest. For the angular distribution the additional angular contributions break the degeneracy between different currents. For the most part, however, the angular distribution provides no stronger limits than that from the energy distribution. This is because, looking back at Fig. 5.4, the impact of the additional angular term is weak compared to the energy contribution so this additional term can only make a marginal difference.

The impact of systematics will be different for the angular measurements than the energy ones. Angular measurements are not subject to the same problems with measuring the magnetic field and are barely affected by whether the tritium is molecular or atomic. However, no experimental method has yet been designed for the measurement of the angular spectrum and whatever method is used will carry its own systematic uncertainties. This can be mitigated against by using the fact that only the hemisphere of emission is of interest and potentially by applying angular cuts to the data.

5.3   Comparing the Impact of Mixing and Exotic Currents

Here I have considered two possible mechanisms by which the heavy neutrinos could be generated, directly through exotic currents or indirectly through active-sterile mixing as a component of the electron neutrino. Given this, it is worth considering whether in the case of a deviation from expectation it is possible to ascertain whether this is due to active-sterile mixing or sterile exotic currents.

Firstly, it is worth considering the limits that can be placed in the case of there being no statistically significant deviation from the Standard Model result. This 'null' type bound is shown in the plots of Fig. 5.7. It can be seen in these plots that bounds on sterile exotic currents and active-sterile mixing are to some extent interchangeable. In the energy case the results are all very similar regardless of the chosen sterile exotic current or sterile mass. The primary signature of a sterile
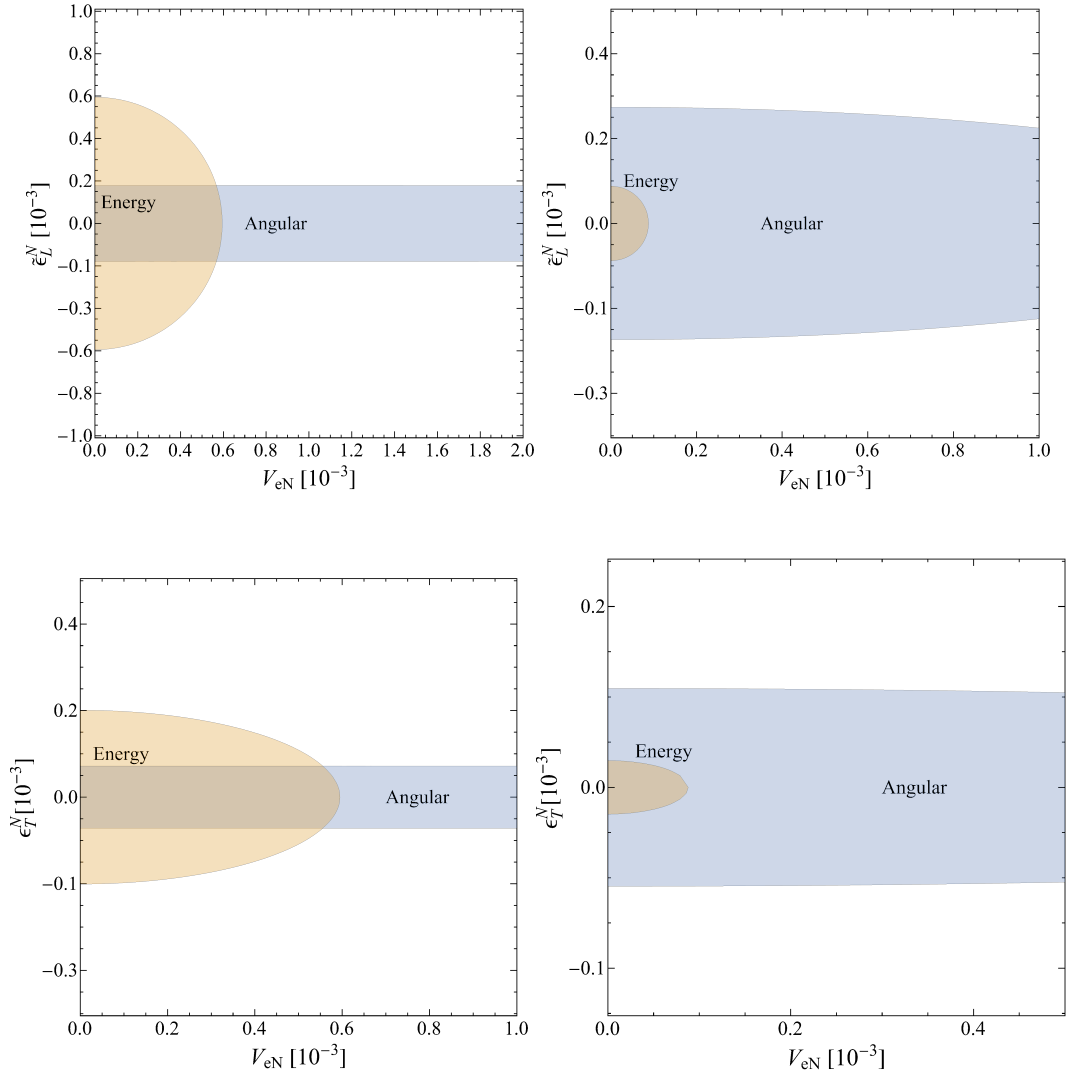
Figure 5.7: 95% CL regions for sterile neutrino contributions coming from sterile exotic currents and active-sterile mixing for $N_{\rm tot} = 10^{18}$ events. The region based on the energy (angular) distribution is in orange (blue). The top plots are for an exotic sterile current with right-handed leptonic current for $m_N = 0.5$ keV (left) or 10 keV (right). The bottom two are for a tensor exotic sterile current also with $m_N = 0.5$ keV or 10 keV. Note the use of different scales between the figures. None of the exotic sterile current parameters have pre-existing limits whilst the limit on $|V_{eN}|$ for either of these masses is too high to be visible here.

state in the energy distribution is the kink in the spectrum which occurs in both sterile exotic currents and active-sterile mixing. Thus the sensitivity to both types is roughly of the same scale with limits being on the order of $10^{-4} - 10^{-3}$ in all of the cases here. For the angular distribution, however, the result is quite different with significant differences between the different mass cases. Recalling Fig. 5.4, the sensitivity of angular measurements is greatest for low sterile masses because
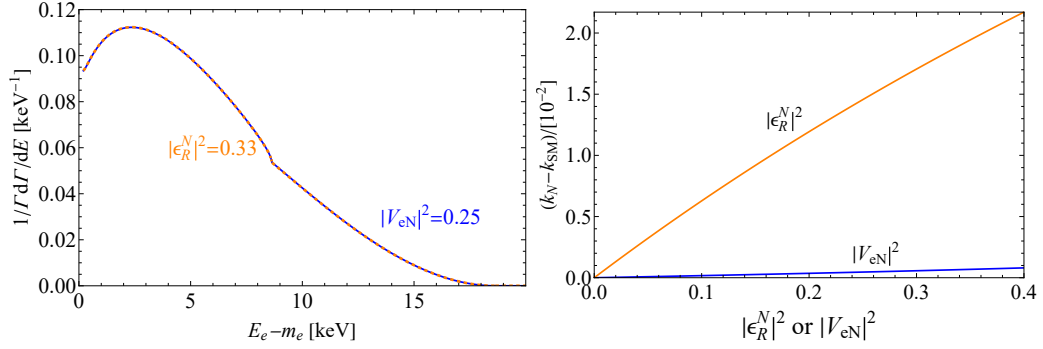
Figure 5.8: Energy and angular distributions showcasing the difference between an active-sterile mixing and an exotic right-handed leptonic current for producing a 10 keV neutrino. Left: Normalised energy distributions with active-sterile mixing, $|V_{eN}|^2 = 0.25$ (blue, dashed), overlapping with an exotic sterile $|\varepsilon_R^N|^2 = 0.33$ (orange) contribution. Right: Deviation of the angular correlation factor k from the SM value as a function of the active-sterile mixing $|V_{eN}|$ or the right-handed leptonic current parameter $|\varepsilon_R^N|$.

the heavy state has a diminished angular effect when it is heavier due to the weakening of the helicity-chirality link. This means that for $m_N = 0.5$ keV the angular measurements are more sensitive to the sterile exotic current than the energy measurements in both cases, but not for $m_N = 10$ keV. In all of the cases the angular measurement is much more sensitive to exotic sterile currents than to active-sterile mixing. For light sterile states the impact of active-sterile mixing is merely to diminish the Standard Model term and add on a term that is nearly identical. When the sterile state is heavier the sterile term differs to a greater extent from the Standard Model term but still not significantly (hence the slight sensitivity to it on the right hand plots). Conversely, the sterile exotic currents introduce terms with an entirely different energy dependence. Whilst the a_Y terms coming from sterile exotic currents are similar to the Standard Model result the exotic b_Y terms differ significantly which is why the angular distribution has a very different shape from the energy distribution.

It is worth also considering the counter-example of a detected kink in the spectrum and asking whether it is possible to tell if this kink is the signature of sterile neutrinos produced by active-sterile mixing or by sterile exotic currents. In Fig. 5.8 the impact is shown on the energy and angular spectra of sterile neutrino production through these two mechanisms. In the left plot, it is shown how a particular pair of

values of the mixing $|V_{eN}|^2$ and exotic current $|\varepsilon_R^N|^2$ for a 10 keV sterile neutrino lead to nearly identical changes in the energy spectrum. Using only the energy spectrum these two cases would be indistinguishable - there will always be a pair of values across the two cases that leads to identical results. However, looking at the right plot it can be seen that the impact on the angular spectrum of this exotic current is much greater than that for active-sterile mixing. The pair of values that would lead to identical angular spectra are significantly different from the pair of values that would lead to the same energy spectrum. Thus a simultaneous measurement of both quantities would allow the two scenarios to be distinguished between.

5.4 Outcome

Overall, whilst cosmological and astrophysical limits upon the sterile neutrino mass are very strong, tritium beta decay experiments represent a significant opportunity for direct detection searches. Although this search is often interpreted in terms of an active-sterile mixing, the possibility of sterile exotic currents is worth examining too with experiments having significant sensitivity to these. If a detection does occur, the simultaneous use of energy and angular measurements would be invaluable for distinguishing between these two scenarios.

Chapter 6

Lorentz Violation in Single Beta Decay

One of the greatest strengths of the quantum field theory formulation of the Standard Model is the way in which it incorporates Special Relativity. This is included by maintaining Lorentz invariance, with all terms in the Standard Model Lagrangian being overall Lorentz scalars which maintain the same functional form in all inertial frames of reference. This provides limitations upon the types of interactions and propagations of the fundamental fields of the Standard Model. Over the years there have been many searches for signatures of Lorentz invariance violation, motivated by theoretical expectations for small amounts of Lorentz violation in quantum theories of gravity [168], particularly within string theory [169]. These searches have used a wide range of techniques including astrophysical measurements of photon propagation [170], collider synchotron radiation [171], precision mass measurements [172] and atomic transition frequencies [173]. So far, no evidence has been found for Lorentz violation.

There are many different ways in which Lorentz violation could occur. Systematic attempts to consider this often look at modifications to the Standard Model through the addition of terms which break Lorentz symmetry. For example, in [174] all possible terms involving fermions, covariant derivatives and boson field tensors are considered up to dimension-6. These terms break the Lorentz symmetry by coupling together the Lorentz vectors and tensors of the Standard Model (such as

the spinor bilinear $\overline{\Psi}\gamma^\mu\Psi$ which transforms as a Lorentz vector) with constant factors which are invariant under the Lorentz transformations. These combined terms within the Lagrangian are no longer Lorentz invariant and will appear different in different inertial frames. In this formulation the Lorentz violating tensors will enter as multiplicative factors, when set to zero Lorentz invariance is restored. It is these factors which can be searched for and for which limits can be derived as bounds upon Lorentz violation.

The two effects that I consider here affect different aspects of single beta decay, the first is a modification to the Fermi interaction mediating the decay whilst the second affects the propagation of all of the fermions involved in the decay.

6.1   Lorentz Violating Interaction

The first type of Lorentz violation I consider here is a modification to the four-fermion beta decay interaction. This could come from a range of different types of high-energy new physics and would manifest itself as an effective field theory term of dimension-6. This could take the form of a modification to the low energy W-boson propagator [175]

$$\langle W^{\mu+}W^{\nu-}\rangle = -i\frac{\eta_{\mu\nu}+\chi_{\mu\nu}}{M_W^2}. \tag{6.1}$$

Here $\eta_{\mu\nu}$ is the Minkowski metric and $\chi_{\mu\nu}$ is a constant Lorentz violating factor where it is assumed $\chi^\mu_\mu = 0$ (the trace part doesn't violate Lorentz symmetry and could be absorbed into the W boson mass). No further assumption is made about $\chi_{\mu\nu}$ other than that it is small compared to 1 (due to a lack of observation in experiments thus far), it is taken to potentially have real and imaginary parts.

Given this the squared matrix element from Eq. (3.20) is modified to become

$$
\begin{aligned}
|M_\chi|^2 = &16G_F^2|V_{ud}|^2(\eta_{\lambda\mu}+\chi_{\lambda\mu})((\eta_{\rho\sigma}+\chi^*_{\rho\sigma}) \\
&Tr[(\slashed{P}_{\mathrm{He}}+m_{\mathrm{He}})(g_V\gamma^\lambda-g_A\gamma^\lambda\gamma^5)(1+\gamma^5\slashed{s})(\slashed{P}_{\mathrm{H}}+m_{\mathrm{H}})(g_V\gamma^\rho-g_A\gamma^\rho\gamma^5)] \\
&Tr[(\slashed{P}_e+m_e)\gamma^\mu(1-\gamma^5)\slashed{P}_\nu\gamma^\sigma(1-\gamma^5)],
\end{aligned} \tag{6.2}
$$

where the $*$ denotes complex conjugation and here I choose to neglect the neutrino mass which would have negligible impact upon the calculations due to its magnitude.

From this the matrix element and decay rate can be calculated. At this point I use the small magnitude of χ to make the assumption that terms quadratic in χ can be neglected, keeping the term which represents the interference between the Standard Model result and this Lorentz violation. There will be no effect that makes the linear terms particularly small (unlike in Chapter 4 where the chirality flip lead to neutrino mass proportionality and the dominance of the quadratic terms) so this is a safe assumption to make. The full matrix element is given in Appendix B.

In order to simplify the consideration of this Lorentz violating parameter, I split it into scalar, vector and tensor parts (so called because $\chi_{\mu\nu}$ is treated as being a constant in spacetime so its spatial components will transform with spatial rotations in the usual manner as for fixed vectors or tensors). This is written as

$$\chi^{\mu\nu} = \begin{pmatrix} \chi^{00} & \chi^{0j} \\ \chi^{j0} & \chi^{jk} \end{pmatrix},$$

where j and k label the spatial indices from 1 to 3.

Whilst there are many terms which contribute to the decay rate, the final expressions for each term often simplify from the long form shown in Appendix B. In many cases this comes from the vanishing of terms when evaluated in the tritium rest frame and that after integration over the neutrino direction the only remaining vectors upon which the decay could depend are $\vec{p}_e$ and $\hat{s}$ meaning that many of the Levi-Civita sums vanish. In order to more plainly see the impact of this Lorentz violation, I calculate a more approximate expression for the decay rate similar to that in [175] using the same approximation as before that $m_{\mathrm{H}} \approx m_{\mathrm{He}} \gg E_e, m_e$. In many cases approximately similar terms cancel out whilst others are much smaller

on the scale of $|\vec{p}_e|/m_H$. This gives as the approximate expression then

$$
\begin{aligned}
\frac{d\Gamma_\chi}{dE_e d\cos\theta_e} \approx \Bigg[&(3g_A^2 + g_V^2) - (2g_A^2 - 2g_A g_V)\frac{|\vec{p}_e|}{E_e}\hat{p}_e^j \hat{s} \\
&- 2(g_A^2 - g_V^2)\chi_r^{00} + (2g_A^2 + 2g_A g_V)\frac{|\vec{p}_e|}{E_e}\hat{p}_e^j \hat{s}\chi_r^{00} \\
&- 2g_V^2 \frac{|\vec{p}_e|}{E_e}\hat{p}_e^j \chi_r^{0j} - 2g_A g_V \hat{s}^j \chi_r^{0j} + 2g_A g_V \frac{|\vec{p}_e|}{E_e}\chi_i^{0j}(\hat{p}_e \times \hat{s})^j \\
&+ 2g_A^2 \frac{|\vec{p}_e|}{E_e}\hat{p}_e^j \chi_r^{j0} + 2g_A g_V \hat{s}^j \chi_r^{j0} + 2g_A^2 \frac{|\vec{p}_e|}{E_e}\chi_i^{j0}(\hat{p}_e \times \hat{s})^j \\
&- 2g_A^2 \frac{|\vec{p}_e|}{E_e}\chi_r^{jk}\hat{p}_e^j \hat{s}^k - 2g_A g_V \frac{|\vec{p}_e|}{E_e}\chi_r^{jk}\hat{s}^j \hat{p}_e^k \\
&- 2g_A^2 \frac{|\vec{p}_e|}{E_e}\chi_i^{jk}\hat{p}_e^l \varepsilon^{jkl} - 2g_A^2 \chi_i^{jk}\hat{s}^l \varepsilon^{jkl} \Bigg] \frac{4\pi a_{SM}(E_e)}{3g_A^2 + g_V^2},
\end{aligned}
\tag{6.3}
$$

where a_{SM} is the result from Eq. (3.22) and χ_r and χ_i are the real and imaginary parts of χ, respectively.

As can be seen from this expression, nearly all of the components of χ each modify both the energy and angular distributions for the beta decay. Of particular note is that the terms involving χ^{j0} and those involving χ^{0j} do not take exactly the same form meaning there will be differences in the sensitivity to them. This is because the first index of $\chi^{\mu\nu}$ couples to the hadronic part of the matrix element whilst the second couples to the leptonic part. In the final decay rate there are only two 3-vectors upon which χ^{0j} can be dotted with, $\hat{p}_e$ and $\hat{s}$, which fixes the types of terms that can arise. However, the proportionality factor for these terms can be, and is, different. The only term which doesn't appear is χ_i^{00} which has no impact upon the spectrum, even in the full non-approximated form. This is because they appear in terms such as $\chi_i^{00}\varepsilon_{0jkl}\,\hat{p}_e^j\,\hat{p}_v^k\,\hat{s}^l$ which vanish once the neutrino momentum integral is performed.

In the following subsections I calculate the sensitivity to the scalar, vector and tensor parts of χ using the prescription described in Section 3.7. This assumes 10^{18} total events measured across 20 energy bins and 2 angular bins. The uncertainty in the total decay rate for tritium beta decay is captured by performing a minimisation over a normalisation parameter for the Standard Model spectrum. Experimental

limits on χ have been found in a range of decay experiments where they are always expressed in the sun-centred frame, meaning that z is in the direction of the earth's axis of rotation and the x and y coordinates are assumed to be fixed relative to the sun. Sensitivity to $\chi_r^{0j} + \chi_r^{j0}$ from kaon decay gives the strongest limits on χ_r^{0x} & χ_r^{0y} [176]. In muon decay the combination of χ_r^{00}, χ_r^{0j} & $\varepsilon^{jkl}\chi_i^{jk}$ gives the best limit on χ_r^{0z} [177]. Limits have also been found for χ_r^{jk} in pion decay [178] and for $\varepsilon^{jkl}\chi_i^{jk}$ in the decay of sodium nuclei [179] but these are not the strongest. Limits from all of these experiments are typically in the range of $10^{-3} - 10^{-5}$ (assuming that each component only contributes individually, i.e. there is no significant cancellation). The strongest limits for all the remaining measured parameters come from the study of first-order forbidden decays of yttrium and caesium [180]- all of these limits were found to be in the range $10^{-6} - 10^{-8}$. Thus the current best limits at 95% CL are,

$$
|\chi_r| < \begin{pmatrix}
3 \times 10^{-6} & 6.3 \times 10^{-5} & 6.3 \times 10^{-5} & 7.4 \times 10^{-3} \\
2 \times 10^{-8} & 1 \times 10^{-6} & 1 \times 10^{-6} & 1 \times 10^{-6} \\
2 \times 10^{-8} & 1 \times 10^{-6} & 1 \times 10^{-6} & 1 \times 10^{-6} \\
1 \times 10^{-8} & 1 \times 10^{-6} & 1 \times 10^{-6} & 1 \times 10^{-6}
\end{pmatrix},
$$

$$
|\chi_i| < \begin{pmatrix}
- & - & - & - \\
- & - & 2 \times 10^{-8} & 4 \times 10^{-8} \\
- & 2 \times 10^{-8} & - & 4 \times 10^{-8} \\
- & 4 \times 10^{-8} & 4 \times 10^{-8} & -
\end{pmatrix},
$$

where a $-$ denotes that no limit has previously been measured.

6.1.1 Scalar

The scalar component, χ^{00}, affects both the energy and angular distributions of the beta decay process. As a scalar, it adds no additional directional information and doesn't violate rotational invariance. However, it affects the energy and momentum exchange within the decay leading to additional contributions to both the
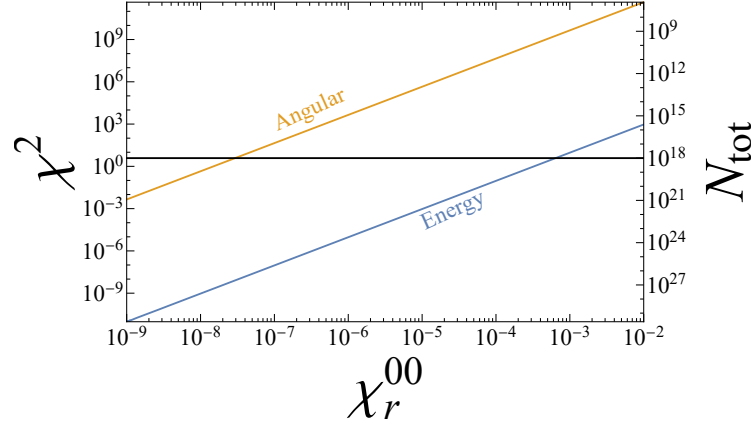
Figure 6.1: The χ^2 deviation due to the real scalar component of the Lorentz violating factor, χ_r^{00}, using the tritium energy distribution. The horizontal black line is the 95% CL sensitivity for $N_{\text{tot}} = 10^{18}$ events, while the N_{tot} scale on the right-hand axis shows the number of events required to reach a 95% CL sensitivity. The labels denote the measurement using energy or angular binning.

spin-independent and spin-dependent parts of the decay rate. In order to observe the impact of this term, measurements of the energy distribution and the angular asymmetry for a polarised nucleus can be performed and compared to the Standard Model result. There is no χ_i^{00} dependence in the decay rate as sensitivity to this term would require measurements also of the neutrino or nuclear momentum after the decay.

In Fig. 6.1 the sensitivity to χ_r^{00} can be seen. For both considerations, the relationship between the χ^2 and the component χ^{00} is quadratic (a straight line on this logarithmic plot) because χ^{00} appears as a linear term within the decay rate. The energy distribution is a much weaker measurement than the angular distribution. Most of the sensitivity in the energy measurement is lost due to the normalisation uncertainty and the fact that the approximate forms given in Eq. (6.3) have the same energy dependence as the Standard Model expression. However, the exact form, as calculated from Appendix B and used in my analysis, does have a slightly different form leading to the weak sensitivity here. For the angular distribution, the factor of $2g_A^2 + 2g_A g_V$ is approximately an order of magnitude larger than the Standard Model value which helps to enhance the sensitivity to this term. The sensitivity reached here from the angular measurement is approximately an order of magnitude improvement on that from experiment.

6.1.2 Vector

There are two vector components, χ^{0j} and χ^{j0}, with there being a small difference in the sensitivity to the two of them due to the different factors of g_A and g_V which multiply the terms in which they appear. As they are vectors, they will act to violate rotational invariance and impact upon the decay rate through their interaction with the other two vector-quantities, the electron momentum and the nuclear spin. The measurements that can be made will give the components of χ^{0j} relative to these vectors. In this case, there are three terms involving these which affect the decay rate, each of which are best approached differently. The first term of the form $\hat{p}_e^j \chi_r^{0j}$ measures the real vector component and leads to asymmetries in the electron momentum angular distribution. The measurement of the components of χ^{0j} thus involves taking an ensemble of unpolarised nuclei and comparing decay rates to opposing hemispheres. Any difference between the opposite hemispheres will imply the presence of a corresponding component of χ^{0j}. Performing this for three perpendicular pairs of hemispheres will give the three components of χ^{0j}. Secondly, there is the term $\hat{s}^j \chi_r^{0j}$ which also measures the real vector component. It would be searched for by polarising the nuclei and measuring for a change in the total rate when the spin direction is flipped. This again would need to be performed for three perpendicular axes. Finally, the term $\chi_i^{0j} \cdot (\hat{p}_e \times \hat{s})^j$ is dependent upon the imaginary vector component and induces an asymmetry in the distribution which is perpendicular to the direction of the spin. Measurements of hemispheres perpendicular to the spin direction allows for the determination of the components of χ_i^{0j} perpendicular to the spin and choice of hemisphere. Two components could be found for each choice of polarisation (from two choices of hemisphere perpendicular to the spin) so the nucleus would need to be polarised in multiple directions to determine all of χ_i^{0j}. Any measurement using the energy spectrum only would be very poor, the $\hat{p}_e$ proportional terms would vanish and the spin only term has an approximately identical energy dependence which would be largely obscured by the normalisation uncertainty. This is thus not considered here.

The sensitivity to these measurements is shown in Fig. 6.2. As can be seen,
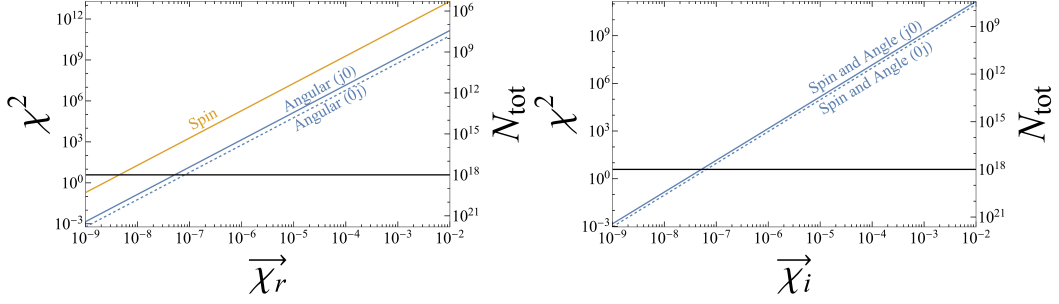
Figure 6.2: As Fig. 6.1 but for the real (left) and imaginary (right) components of the vector terms χ^{0j} and χ^{j0}.

there is a slight difference in the sensitivity to χ^{0j} and χ^{j0} in both the angular measurement of the real parts and in the measurement of the imaginary parts, with the χ^{j0} component being the stronger in both cases. For the real component, the spin measurement is stronger than the angular measurement as it isn't suppressed by the kinematic factor $|\vec{p}_e|/E_e$. The angular measurement would represent an improvement on the limits for χ_r^{0j} but not for χ_r^{j0} for which the limits are much stronger. The spin measurement however has a comparable sensitivity to χ_r^{j0} as the pre-existing limits. For χ_i^{j0} and χ_i^{0j} limits do not yet exist so a measurement of spin-perpendicular asymmetries would provide original bounds on this quantity.

6.1.3 Tensor

For the tensor component there are three different methods of measurement, one for the real part and two for the imaginary. For the real part, the term looks like $(g_A^2 \hat{p}_e^j \hat{s}^k + g_A g_V \hat{s}^j \hat{p}_e^k) \chi_r^{jk}$ meaning that the nucleus would need to be polarised and an asymmetry searched for in hemispheres both parallel and perpendicular to the spin. A measurement performed over a j aligned hemisphere for the spin in the k direction will measure the quantity $R^{jk} = g_A^2 \chi_r^{jk} + g_A g_V \chi_r^{kj}$, a combination of the tensor components. However, comparison of this term with the measurement for a k aligned hemisphere with the spin in the j direction can utilise the fact that $g_A \neq g_V$ to extract the individual components: $\chi_r^{jk} = (g_A R^{jk} - g_V R^{kj})/(g_A^3 - g_A g_V^2)$. For the imaginary component, the tensor part appears only as $\tilde{\chi}_i^l = \varepsilon^{jkl} \chi_i^{jk}$ meaning that the sensitivity is only to this combined quantity. The vector quantity $\tilde{\chi}_i^l$ couples to the spin and momentum in the same way as the vector component χ^{0j} and thus the mea-
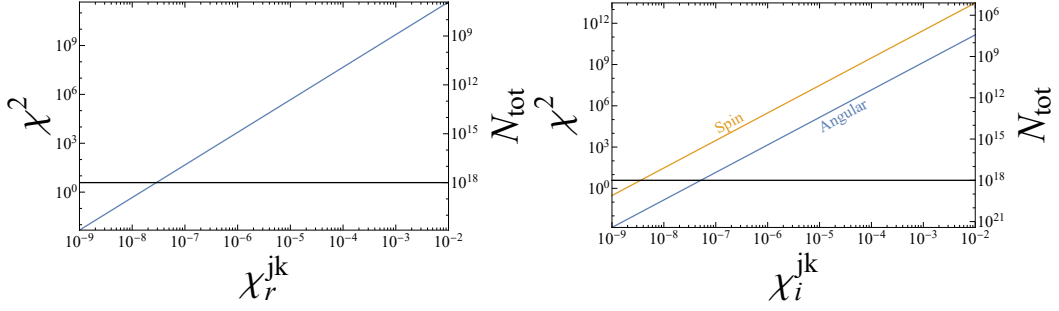
Figure 6.3: As Fig. 6.1 but for the real (left) and imaginary (right) components of the tensor term χ^{jk}.

surement techniques of using separate hemispheres or different spins is the same as before. As before, measurements just using the energy spectrum are ignored as they would have no sensitivity to χ_r^{jk} and very weak sensitivity to $\tilde{\chi}_i^l$.

The sensitivity to the real and imaginary parts is shown in Fig. 6.3. For the real part, the sensitivity shown is actually to R^{jk}, however the relationship between this and χ_r^{jk} is such that the sensitivity is nearly identical. What is shown here is the potential for a nearly two orders of magnitude improvement in the upper bound. For the imaginary part, once again the spin measurement is more sensitive than the angular measurement. Whilst the angular measurement is too weak, the spin measurement shows a slight improvement from the pre-existing bounds.

The tracelessness of $\chi^{\mu\nu}$ ($\chi_\mu^\mu = 0$) means that $\chi^{00} = -\sum_j \chi^{jj}$. This could be used as a consistency check to compare the results for the measurements of the real parts. However, as has been seen the imaginary part has no sensitivity to either χ_i^{00} or the diagonal elements χ_i^{jj} so this cannot provide any further information for determining these.

6.1.4 Summary

Thus to summarise, improvements are possible for nearly all of the components of χ but are reliant upon polarisation of the nucleus and/or taking angular measurements. For χ^{00}, an order of magnitude improvement is possible for the real part using angular measurements whilst the imaginary part has no effect upon the decay. For χ^{0j} and χ^{j0}, although the limits on χ_r^{j0} are much stronger, improvements can be made upon the limits for the real parts of both using polarisation based measurements; the

imaginary part is currently unmeasured and would require both polarisation and angular measurements to detect but there is the potential for first limits being placed. Finally, for χ^{jk} the use of angular measurements on a polarised nucleus could lead to two orders of magnitude improvements in the real part, however the imaginary part remains only sensitive through $\tilde{\chi}_i^l = \varepsilon^{jkl}\chi_i^{jk}$ with spin measurements only representing a minor improvement on the pre-existing limits. Of course, all of the limits described here are idealised experimental setups and represent upper bounds on the capabilities of future experiments. They do, however, show that angular measurements and the ability to polarise the nucleus in variable ways is essential for probing Lorentz violation of this nature.

6.2 Lorentz Violating Propagation

There are many ways in which the propagation of fermionic states could be modified by Lorentz violating effects. These are often parametrised in terms of their effect on the dispersion relation of the propagating field. For example, modifications due to quantum gravity may take the form

$$E^2 = |\vec{p}|^2 + m^2 + \varepsilon|\vec{p}|^2 \left(\frac{|\vec{p}|}{M}\right)^n,$$ (6.4)

for some heavy mass scale, M, power, n, and modification parameter, ε [181]. In this case $n > -2$ so that energy doesn't diverge at low momentum and M comes from some high energy theory scale which modifies the propagation of fields in a similar way as an electromagnetic plasma. Experimental searches of cosmic ray processes have placed limits requiring M to be orders of magnitude larger than the Planck mass when n is positive. Similar studies for $n = 0$, in which the maximum speed of propagation is modified to $v^2 = 1 + \varepsilon$, have placed stringent bounds of $\varepsilon < 10^{-23}$ [182].

Other attempts to modify the dispersion relation have also been considered, such as that of [183] in which the relation becomes

$$E^2 = |\vec{p}|^2 + m^2 + 2\lambda|\vec{p}|,$$ (6.5)

for some parameter λ. Such a result could have interesting implications for neutrino oscillations if λ is flavour dependent or for high-energy cosmic rays when λ is large.

In all of these cases the phenomenological study begins from the dispersion relation. However, here I consider a Lagrangian level Lorentz violating modification that affects the propagation of fermions [184]. Such a violation could come from many different types of Standard Model Extension (SME) which incorporate perturbative violations of Lorentz and CPT symmetry. These could come from UV theories such as non-commutative geometry [185] or compactified spatial dimensions [186].

6.2.1 Field Redefinition and Modified Decay Rate

Taking one of the terms from [174], the Standard Model Lagrangian is modified through the addition of the term

$$\mathscr{L}_a = -a_f^\mu \, \overline{\psi}_f \, \gamma_\mu \, \psi_f, \tag{6.6}$$

where a_f^μ is a constant 4-vector (assumed to be real) which may take different values for different fermions. The effect this has on the Dirac equation is thus to give

$$[i\gamma_\mu(\partial^\mu + ia_f^\mu) - m_f]\psi_f = 0 \tag{6.7}$$

which leads to the dispersion relation

$$(E - a_f^0)^2 = m_f^2 + (\vec{p} - \vec{a}_f)^2 \tag{6.8}$$

for $a^\mu = (a^0, \vec{a})$. This has the effect not only of modifying the relation between the energy and the magnitude of the momentum but also of adding a violation of rotational invariance due to the 'preferred direction' of the 3-vector part of a.

Considering the propagation of states with such a relation is mathematically inconvenient, instead it is more advantageous to perform a field redefinition in order

to recover the original free propagation. This can be done by taking

$$\psi_f = e^{-ia_f^{\mu} x_{\mu}} \psi_f' \quad \Rightarrow \quad (i\gamma_{\mu}\partial^{\mu} - m_f)\psi_f' = 0. \tag{6.9}$$

This recovers the original dispersion relation with the modified state's momentum satisfying $P_f'^2 = m_f^2$. The relation between the momenta of the modified and unmodified states is given by $P_f' = P_f - a_f$. From this it can be seen that, in the absence of any interactions, the Lorentz violating term would have no effect. The newly defined states have effectively absorbed the modification and propagate as before. Lorentz violation of this type is called 'countershaded' because it doesn't affect the group velocity of the neutrinos and cannot be detected through propagation measurements [187]. However, interaction terms defined using the unmodified states will also need to be reparameterised in terms of the new states, a transformation that will modify their form and lead to sensitivity to this Lorentz violation. Note here that if a were to have imaginary parts this would lead to an exponential growth in the modified field which is unphysical, hence it is here taken to be real valued.

For diagonal interactions, involving a bilinear of the same fermion and no derivatives, there is no modification to the interaction. This can be seen for the photon interaction term

$$\mathscr{L}_{\gamma\psi\psi} = -iqA^{\mu}\overline{\psi}\gamma_{\mu}\psi = -iqA^{\mu}\overline{\psi}'\gamma_{\mu}\psi' \tag{6.10}$$

where the term is identical regardless of the choice to express the interaction using the field ψ or ψ'. This will be true also for the strong force interactions which similarly do not mix between different types of fermion. Mathematically, the transformation here is identical in form to the sort of U(1) transformations shown in Section 2.2 in the special case of $\alpha = -a^{\mu} x_{\mu}$.

However, a change does arise when considering the fermion-changing interactions of the weak force. Performing the same field redefinition as before (and assuming that the nuclei can be treated as having a single Lorentz violating factor in a manner equivalent to the fundamental particles) gives a Lagrangian redefined

in terms of the modified fields:

$$\mathcal{L}_{Fermi} = -\frac{G_F}{\sqrt{2}}V_{ud}\left[\overline{{}^3\text{He}}\gamma_\mu\left(g_V - g_A\gamma^5\right){}^3\text{H}\right]\left[\bar{e}\gamma^\mu(1-\gamma^5)v_e\right]$$

$$= -\frac{G_F}{\sqrt{2}}V_{ud}\left[\overline{{}^3\text{He}}'\gamma_\mu\left(g_V - g_A\gamma^5\right){}^3\text{H}'\right]\left[\bar{e}'\gamma^\mu(1-\gamma^5)v'_e\right]e^{-i\Sigma_f a_f^\mu x_{f,\mu}}$$

$$(6.11)$$

where the sum in the exponential is being performed over all four fermions involved, with x_f the spatial position of each fermion.

Given that the only impact of these Lorentz violating terms is an additional exponential in the Fermi interaction, the derivation of the decay rate largely follows that given previously in Sections 3.1 and 3.3. The only change to the derivation comes in the modification of momentum conservation [184]. When calculating the matrix element, each fermion spinor will contribute a factor of the form $e^{iP_\mu x^\mu}$ for their momentum P and spatial position x. These terms will add within the exponent to the Lorentz violating terms. A series of spatial integrals is then performed with the final integral giving rise to an expression very similar to Eq. (3.1)

$$d\Gamma = \frac{1}{2m_\text{H}}\frac{d^3\vec{p}'_e}{(2\pi)^3 2E'_e}\frac{d^3\vec{p}'_v}{(2\pi)^3 2E'_v}\frac{d^3\vec{p}'_\text{He}}{(2\pi)^3 2E'_\text{He}}|M|^2(2\pi)^4\delta^4(P'_\text{H}+a-P'_\text{He}-P'_e-P'_v).$$

$$(6.12)$$

Thus the resultant effect of the Lorentz violation is to enforce a modified form of momentum conservation within the interaction

$$P'_\text{H}+a=P'_\text{He}+P'_e+P'_v, \quad a=a_\text{H}-a_\text{He}-a_e+a_v, \qquad (6.13)$$

with subscripts denoting the relevant field. Taking the Standard Model electromagnetic charge ratios for the Lorentz violating parameters ($a_\text{H} : a_\text{He} : a_e : a_v = 1 : 2 : -1 : 0$) would give $a = 0$ and the Lorentz violation would vanish. This is because this would make the transformation between fields identical in form to the $U(1)_Q$ symmetry of the Standard Model which is respected by the Fermi interaction.

Overall, what has been achieved by the field redefinition is to shift the impact

of the Lorentz violating terms. For the original fields the Lorentz violation causes a change in propagation from the typical dispersion relation whilst for the modified fields the dispersion relation is as normal but any fermion changing interaction will no longer follow conventional rules of momentum conservation. In either case the calculation is different from before, but it is much easier and more useful to limit the impact of Lorentz violation to the point of interaction. In addition, given the many experiments that have failed to find Lorentz violation in particle propagation, as explained above, it is more appropriate to identify the actual physical states that are measured with the modified states. This is in some sense analogous to the difference between the flavour and mass eigenstate formulations of neutrinos, it is more convenient to perform calculations with the 'physical' states being the mass eigenstates (propagating with conventional dispersion relations) which interact with modified interactions (due to their mixing within flavour states) than the other way around. There is, however, no Lorentz violation equivalent here of flavour mixing as the transformation between states leads merely to a boost to their momentum.

From here the calculation of the decay rate can be performed. In my original calculation in Section 3.3 I derived the results in Eqs. (3.22) and (3.25) by directly expressing the matrix element in terms of E_v and $\cos\theta_v$ to be integrated over directly. However, an alternative approach, as laid out in [184], is easier here. I begin by re-expressing Eq. (3.21) in a slightly different format to explicit pull out the elements to be integrated

$$
\begin{aligned}
|M|^2 = {} & 16G_F^2 |V_{ud}|^2 \\
& \times \Big\{ \big((g_A + g_V)^2 (P_{e,\mu} P_{\mathrm{H},\sigma}) + (g_A - g_V)^2 (P_e \cdot P_\mathrm{H}) \eta_{\mu\sigma} \big) P_{\mathrm{He}}^\mu P_v^\sigma \\
& + \big((g_A^2 - g_V^2) m_\mathrm{H} m_\mathrm{He} P_{e,\mu} \big) P_v^\mu \\
& + \big((g_A^2 - g_V^2) m_\mathrm{He} \big[(P_e \cdot S) P_{\mathrm{H},\mu} - (P_\mathrm{H} \cdot P_e) S_\mu \big] \big) P_v^\mu \\
& + \big((g_A - g_V)^2 m_\mathrm{H} P_e \cdot S \eta_{\mu\sigma} - (g_A + g_V)^2 m_\mathrm{H} P_{e,\mu} S_\sigma \big) P_{\mathrm{He}}^\mu P_v^\sigma \Big\}, \qquad (6.14)
\end{aligned}
$$

where from now on I stop including the primes on all of the effective momenta for ease of notation, results henceforth will treat the modified states as the states that

are being directly measured.

The integrals that need to be calculated to evaluate the decay rate are that of P_ν^μ and $P_\nu^\mu P_{\text{He}}^\sigma$. The final results of these integrals must have the same Lorentz structure as before. Also, of the four independent particle momenta, the two being integrated over in addition to one constraint of momentum conservation means that there is only one free momentum left over. These integrals can only be a function of this momentum. I choose to express this momentum parameter to be $w = P_{\text{H}} - P_e + a$ which gives a convenient form for these expressions. Using this, the integrals must give $P_\nu^\mu P_{\text{He}}^\sigma \to f(w^2)w^\mu w^\sigma + g(w^2)\eta^{\mu\sigma}$ and $P_\nu^\mu \to h(w^2)w^\mu$ where f, g and h are functions to be found through contraction over the indices and with w^μ. They are given by [184]

$$f(w^2) = \frac{\pi}{3}\frac{1}{w^6}\left[w^4 + (m_{\text{He}}^2 + m_\nu^2)w^2 - 2(m_{\text{He}}^2 - m_\nu^2)^2\right]$$
$$\sqrt{(w^2 - (m_{\text{He}} + m_\nu)^2)(w^2 - (m_{\text{He}} - m_\nu)^2)}, \qquad (6.15)$$

$$g(w^2) = \frac{\pi}{6}\frac{1}{w^4}\left[w^4 - 2(m_{\text{He}}^2 + m_\nu^2)w^2 + (m_{\text{He}}^2 - m_\nu^2)^2\right]$$
$$\sqrt{(w^2 - (m_{\text{He}} + m_\nu)^2)(w^2 - (m_{\text{He}} - m_\nu)^2)}, \qquad (6.16)$$

$$h(w^2) = \pi\frac{1}{w^4}(w^2 - (m_{\text{He}}^2 - m_\nu^2))$$
$$\sqrt{(w^2 - (m_{\text{He}} + m_\nu)^2)(w^2 - (m_{\text{He}} - m_\nu)^2)} \qquad (6.17)$$

Inserting this into the expression for the decay rate thus gives

$$\frac{d\Gamma_a}{dE_e d\cos\theta_e} = \frac{G_F^2|V_{ud}|^2}{8\pi^4 m_{\text{H}}}C(E_e)|\vec{p}_e|\sum_{i=1}^{3}|U_{ei}|^2$$
$$\left[(g_A + g_V)^2(P_{\text{H}}\cdot w\, P_e\cdot w f_i(w^2) + P_{\text{H}}\cdot P_e g_i(w^2))\right.$$
$$+ (g_A - g_V)^2\, P_e\cdot P_{\text{H}}(w^2 f_i(w^2) + 4g_i(w^2))$$
$$+ (g_A^2 - g_V^2)m_{\text{H}}m_{\text{He}}\, P_e\cdot w\, h_i(w^2)$$
$$+ (g_A^2 - g_V^2)m_{\text{He}}(P_{\text{H}}\cdot w\, P_e\cdot S - P_{\text{H}}\cdot P_e\, S\cdot w)\, h_i(w^2)$$
$$+ (g_A - g_V)^2 m_{\text{H}}\, P_e\cdot S(w^2 f_i(w^2) + 4g_i(w^2))$$
$$\left. - (g_A + g_V)^2 m_{\text{H}}(P_e\cdot w\, S\cdot w\, f_i(w^2) + P_e\cdot S\, g_i(w^2))\right], \qquad (6.18)$$

where here the subscript *i* has been added to the functions to signify that they are a function of the neutrino mass and thus are being summed over all three mass eigenstates (although the impact of the neutrino mass is negligible). The dot products here are again evaluated in the rest frame of the tritium (as defined by the effective 3-momentum vanishing [184]) with the terms involving the Lorentz violating *a* being given by

$$P_{\mathrm{H}} \cdot w = m_{\mathrm{H}}(m_{\mathrm{H}} - E_e + a^0) \tag{6.19}$$

$$P_e \cdot w = E_e(m_{\mathrm{H}} - E_e + a^0) + E_e^2 - m_e^2 - |\vec{p}_e||\vec{a}|\cos\theta_{ea} \tag{6.20}$$

$$S \cdot w = |\vec{p}_e|\cos\theta_e - |\vec{a}|\cos\theta_a \tag{6.21}$$

$$w^2 = (m_{\mathrm{H}} - E_e + a^0)^2 - E_e^2 + m_e^2 + 2|\vec{p}_e||\vec{a}|\cos\theta_{ea} - |\vec{a}|^2 \tag{6.22}$$

where θ_{ea} and θ_a are the angles of the 3-vector component of *a* to the electron momentum and the nuclear spin, respectively. θ_e is as before the angle between the electron momentum and nuclear spin. The three angles cannot be treated as independent of each other and must instead be related by

$$\cos\theta_{ea} = \cos\theta_e\cos\theta_a + \cos\varphi\sin\theta_a\sin\theta_e \tag{6.23}$$

where the angle φ is the difference in azimuthal angle about the spin for the electron momentum and the Lorentz violating factor. Effectively, the mutual angle is constrained by $\cos(\theta_e - \theta_a) \geq \cos(\theta_{ea}) \geq \cos(\theta_e + \theta_a)$. Evaluation of Eq. (6.18) in the case of $a = 0$ would recover the results of Eqs. (3.22) and (3.25).

Whilst this calculation gives the decay rate, it is worth also considering how the electrons are to be detected and whether the results need to be re-expressed in the original electron properties rather than the modified ones. In both current beta decay detectors, using high pass filters, and future ones, using cyclotron radiation, the electron is measured using electromagnetic properties. As shown by Eq. (6.10) the form of photonic interactions with electrons is unchanged by the field redefinition. Thus the conventional understanding of how the detector measures the electron properties is unaffected and there is no need for a re-expression in terms of
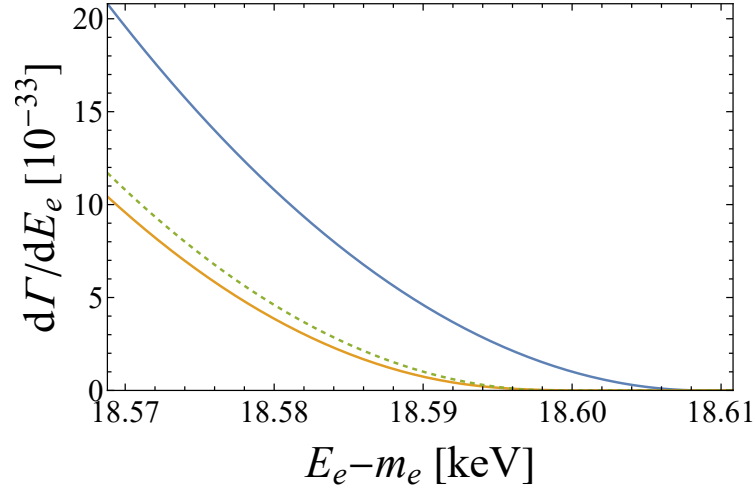
Figure 6.4: Decay rate near the endpoint for tritium single beta decay without Lorentz violation (green, dashed) and with $|\vec{a}| = 100\,\text{keV}$ (orange) and $a^0 = 10\,\text{eV}$ (blue).

the unmodified properties.

The impact of the Lorentz violating factor is greatest near the endpoint of the spectrum, as shown in Fig. 6.4. The most significant consequence of the Lorentz violation is the way in which it modifies the location of the endpoint, due to the change to momentum conservation. The endpoint is reached when the terms under the square root in Eqs. (6.15) to (6.17) become 0; this is clearly changed by the impact of a upon w^2. The presence of the time-like component, a^0, shifts the endpoint by a value approximately equal to a^0. This impacts upon the entire spectrum because of the sharp rise in the spectrum below the endpoint, as can be seen for a kinetic energy of 18.57 keV the rate is nearly twice that in the modified case compared to the original. Unlike the neutrino mass, which shifts the endpoint and changes the spectral shape, the shape of the spectrum is largely unchanged by a^μ; a plot of the Standard Model spectrum with an energy shifted by an amount equal to a^0 would be indistinguishable in the figure from the spectrum modified by a^0. The impact of $\vec{a}$ is also to shift the endpoint, but by a much smaller value with an equivalently smaller overall shift to the spectrum. This can be seen coming from the form of w^2 where a^0 modifies the electron energy linearly whereas $|\vec{a}|$ appears quadratically and will cause a shift approximately equal to $|\vec{a}|^2/m_{\text{H}}$.
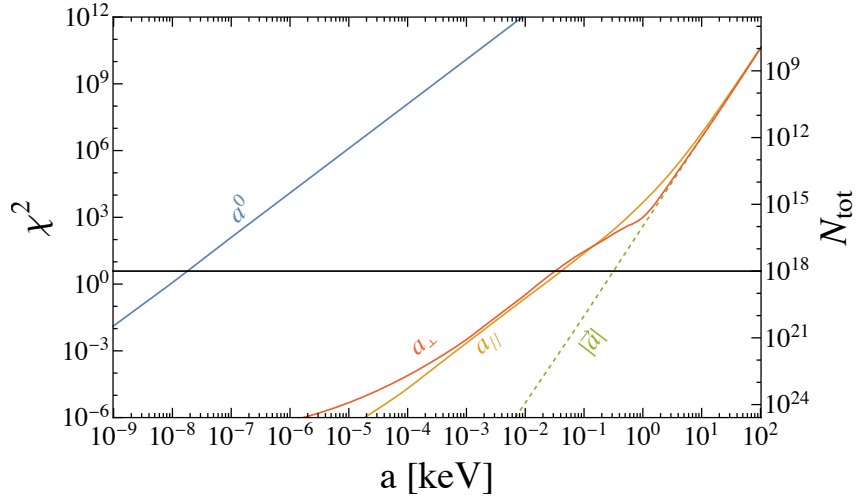
Figure 6.5: The χ^2 deviation due to the Lorentz violating factor a as a function of the relevant component, using the tritium energy distribution. The horizontal black line is the 95% CL sensitivity for $N_{\text{tot}} = 10^{18}$ events, while the N_{tot} scale on the right-hand axis shows the number of events required to reach a 95% CL sensitivity. The labels denote the relevant parameter as explained in the text.

6.2.2 Statistical Analysis

Given that the Lorentz violation can be seen to have an impact upon the beta decay it is worth quantifying this by performing another χ^2 analysis in the manner described in Section 3.7. In this case I will be considering the sensitivity within four measurements: to the zeroth component, a^0; to the magnitude of the 3-vector component when the nucleus is unpolarised, $|\vec{a}|$, and to the parallel, $a_{\|}$, and perpendicular, $a_{\perp}$, components to the nuclear spin, $\hat{s}$, of $\vec{a}$ when the nucleus is polarised. This will again be performed considering measurements binned across the energy spectrum and in hemispheres of the angular distribution.

I begin by first looking at how sensitive χ^2 measurements are to shifts in the energy spectrum. This can be seen in Fig. 6.5. Firstly, the parameter to which measurements are most sensitive is a^0. This is to be expected, in Fig. 6.4 an a^0 of 10 eV is shown to have a larger impact than a $|\vec{a}|$ of 100 keV. The sensitivity is linear as the impact upon the endpoint is linear. The sensitivity to measurements of $\vec{a}$ is much more interesting and shows behaviour not seen in any of the other examples of new physics examined herein. The first thing to notice is the significant difference between the sensitivity with and without polarising the nucleus. In all of the
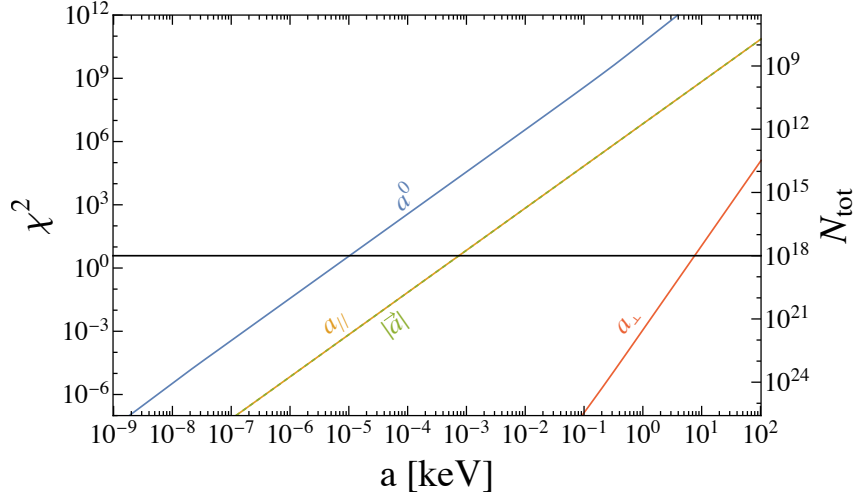
Figure 6.6: As Fig. 6.5 but for angular binning.

previous single beta decay cases examined here, polarisation of the nucleus made no difference to energy measurements as polarisation merely increased the rate to one hemisphere by an equal amount to the decrease in the other hemisphere; with integration over the entire sphere the energy spectrum was unchanged. This, however, is not the case here in which the many complex angular dependencies, upon θ_e, θ_a & θ_{ea}, significantly changes the behaviour. These arise from the Lorentz violation introducing a 'special direction' which has a coupling to both the electron momentum and the spin. Whether or not polarising the nucleus has a significant impact depends upon which Lorentz violating terms are dominant in the decay rate. For large values of $|\vec{a}|$ the term in which it is quadratic dominates. This term has no angular dependence and the polarised and unpolarised measurements are identical. When $|\vec{a}|$ is smaller it is the terms proportional to $|\vec{a}| \cos \theta_{ea}$ which have the greatest impact, in particular in the way they non-linearise the angular dependence of the spin dependent terms. There is no distinction in this term between $a_\perp$ and $a_\parallel$ and thus when integrating over the entire sphere the sensitivity to these terms is approximately identical with the only difference coming from the additional small contribution of the $|\vec{a}| \cos \theta_a = a_\parallel$ dependent term.

The results for the same analysis performed with angular measurements are significantly different for $\vec{a}$ than from those for the energy measurement, as can be seen in Fig. 6.6. There is still a significant sensitivity to a^0 despite it having no

directional information. This is because changes to the energy spectrum affect the kinematics and thus the strength of angular polarisation so this method still has a reasonable sensitivity to this component, albeit less than the energy measurements. When it comes to $\vec{a}$, of the three measurements now it is the perpendicular component in the polarised case which has a much weaker sensitivity. Angular measurements performed with hemispheres aligned to $\vec{a}$ have strong sensitivity due to the dependence upon $\cos\theta_{ea}$, particularly where it appears linearly in $P_e \cdot w$. This is true regardless of whether the nucleus is unpolarised or polarised [1]. Much poorer is the attempt to measure $\vec{a}$ through hemispheres perpendicular to it. When the nucleus is polarised and the hemispheres chosen to be in the spin direction there is a weak sensitivity due to the impact of $\vec{a}$ upon the energy spectrum, in the same manner as for a^0. If the nucleus is unpolarised then symmetry dictates that there can be no sensitivity whatsoever arising from measurements perpendicular to $\vec{a}$.

6.2.3 Experimental Limits and Future Sensitivity

Given these results the best ways of searching for this Lorentz violation is as follows. For the component a^0 the strongest method is through energy measurements with the sensitivity being, in the best case scenario, strong enough to measure down to $a^0 \sim 10^{-5}$ eV. However, this assumes that the endpoint energy is known exactly. In practice, the uncertainty on the theoretical prediction for the beta decay endpoint from precision nuclear mass measurements is 0.07 eV [188]. This combined with any systematic uncertainties in determining the endpoint energy (including the endpoint modification described in Section 3.4 due to atomic effects and the determination of the neutrino mass) will be a limitation on the potential of future experiments to measure this effect. As for $\vec{a}$, the impact on the energy spectrum alone will allow for detection of $|\vec{a}|$ down to the level of keV. This can be improved by polarising the nucleus, the subsequent rate reduction giving sensitivity down to the level of 10s of eV. Finally, this can be further improved through the use of angular measurements with the associated asymmetry increasing the level down to sub-eV. This

---

[1]Not shown here, for ease of visualisation, is the case in which the polarisation is perpendicular to $\vec{a}$ but integration still performed in hemispheres aligned with $\vec{a}$. Such a measurement would give near identical results to the other $\vec{a}$-aligned measurements.

method also has the added benefit of giving the direction of $\vec{a}$ as determined by the directions of the hemispheres of asymmetry.

It is worth comparing the results found here to pre-existing limits from tritium decay experiments. This requires a slight reparameterisation of a. The vector $\vec{a}$ is generally taken to be a fundamental Lorentz violation existing in the universe, it is fixed within the cosmological frame. On Earth, the rotation of the Earth will cause the relative direction of $\vec{a}$ to any experiments to shift over time. To accommodate for this, a reparametrisation is chosen in which $\vec{a}$ is broken down into spherical harmonics about this axis rotation. This leads to the alternative prescription [189]

$$a_{00} = \sqrt{4\pi}\, a^0 \tag{6.24}$$

$$a_{10} = -\sqrt{\frac{4\pi}{3}}\, a^z \tag{6.25}$$

$$a_{11} = \sqrt{\frac{2\pi}{3}}\, (a^x + ia^y) \tag{6.26}$$

$$a_{1-1} = a_{11}^* \tag{6.27}$$

where z is pointed in the axis of the earth's rotation.

The current best limits on these parameters come from the KATRIN experiment in which a search was performed for an oscillation in the endpoint energy with frequency equal to the Earth's rotation [190]. They found upper bounds of $|a_{00}| < 0.03$ keV, $|a_{10}| < 640$ keV and $|a_{11}| < 3.7$ keV at 90% CL. Clearly there is the potential for significant improvement upon these results, energy measurements alone can give a three orders of magnitude improvements on $|a_{10}|$ and angular measurements can probe both this and $|a_{11}|$ down to the sub-eV level. Further improvements upon $|a_{00}|$ will be systematics limited but the use of atomic (rather than molecular) tritium in future CRES experiments should lead to significant improvements in this. Overall, future experiments have significant potential for measuring this form of Lorentz violation to a much stronger degree.

Chapter 7

Correction Factors for Double Beta Decay

In Section 3.4 I described all of the corrections factors that are applied in the case of single beta decay for atomic tritium. Many of these correction factors are also relevant for double beta decay and have an impact upon the decay spectrum. In this chapter I look at the most important of these, the radiative corrections, which is often neglected in calculations. I also use a range of approximations to calculate a modification to the Fermi function due to the mutual repulsion between the two electrons being emitted from the decay.

The main elements that I will be considering in my analysis are Calcium-48, Germanium-76, Molybdenum-100 and Xenon-136. These have been chosen for their range of nuclear charges and half-lives out of the commonly measured elements. A summary of their properties is given in Table 7.1 with endpoint energies and $2\nu\beta\beta$ half-lives from [131] along with the current lower bounds on their $0\nu\beta\beta$ half lives from [133, 135, 137, 140].

7.1 Radiative Corrections in Double Beta Decay

As described previously, radiative corrections are present in beta decays due to the emission of soft photons in the final state which carry away negligible amounts of energy. These photons can come from the tritium, helium or electron. In the calculation of this effect, making sure to include the exchange of soft virtual photons

	Ca-48	Ge-76	Mo-100	Xe-136
Z	22	34	42	54
$KE^{\text{max}}_{2\nu\beta\beta}$ [MeV]	4.27	2.04	3.03	2.46
$T^{2\nu\beta\beta}_{1/2}$ [yr]	6.4×10^{19}	1.9×10^{21}	7.1×10^{18}	2.2×10^{21}
$T^{0\nu\beta\beta}_{1/2}$ [yr] $>$	5.6×10^{22}	1.4×10^{26}	2.8×10^{24}	2.3×10^{26}

Table 7.1: Properties of double beta decay elements including their $2\nu\beta\beta$ half lives and the lower bounds on their $0\nu\beta\beta$ half lives, $KE^{\text{max}}_{2\nu\beta\beta} = E^{\text{max}}_{2\nu\beta\beta} - 2m_e$.

between the charged states and summing up to infinite emission of photons resolves any divergences and leads to the correction factor [100]

$$
G(E_e, E_e^{\text{max}}) = \left(\frac{E_e^{\text{max}} - E_e}{m_e} \right)^{(2\alpha/\pi)t(\beta)} \left\{ 1 + \frac{2\alpha}{\pi} \left[t(\beta) \left(\ln 2 - \frac{3}{2} + \frac{E_e^{\text{max}} - E_e}{E_e} \right) \right. \right.
$$
$$
+ \frac{1}{4}(t(\beta)+1) \left(2(1+\beta^2) - 2\ln\left(\frac{2}{1-\beta} \right) + \frac{(E_e^{\text{max}} - E_e)^2}{6E_e^2} \right)
$$
$$
\left. \left. + \frac{1}{2\beta} \left(L(\beta) - L(-\beta) + L\left(\frac{2\beta}{1+\beta} \right) + \frac{1}{2}L\left(\frac{1-\beta}{2} \right) - \frac{1}{2}L\left(\frac{1+\beta}{2} \right) \right) \right] \right\},
$$
$$
(7.1)
$$

where E_e is the energy of the electron, E_e^{max} the endpoint or maximum energy that it can take, $\beta = |\vec{p}_e|/E_e$, $t(\beta) = \text{arctanh}(\beta)/\beta - 1$ and $L(x) = \int_0^x \frac{\ln(1-y)}{y} dy$ is Spence's function. Significantly the spectrum depends upon two things, both the energy of the electron E_e and the energy remaining left to the other particles $E_e^{\text{max}} - E_e$. This result has been calculated for nuclei of any charge Z with the assumption that their nuclear recoil can be neglected. This means that the function has no Z dependence as effectively the interactions of photons with the nuclei are being ignored. This is a safe assumption to make as such terms would be of order q/m_{H} and the terms involving the photon interacting with the electron will have the dominant impact upon the electron spectrum. Radiative corrections will also impact upon the hadronic process through the modification of the form factors g_V and g_A. However, as their values are measured from experiment this effect will already have been included in their determination.

The shape of this function for a range of different endpoint energies is shown
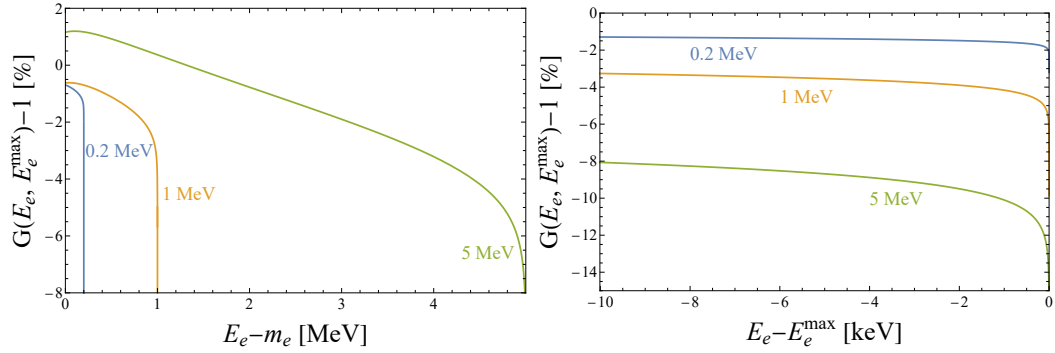
Figure 7.1: Radiative correction factor, $G(E_e, E_e^{\max})$, as a function of the electron energy for endpoints $E_e^{\max} = 0.2$ MeV (blue), 1 MeV (orange) and 5 MeV (green). Shown for the entire energy range (left) and for the final 10 keV of their ranges (right).

in Fig. 7.1. As can be seen, the smaller the endpoint energy the greater the effect of the correction factor for a given energy. However, looking across the entire spectrum, the overall impact of this correction will be greatest for those elements with the highest endpoint energies as the correction increases in magnitude for higher energies. This can be seen in the right figure in which the impact upon the final 10 keV of the range is shown to be greatest for largest endpoint energies. This effect is over four times as large for an endpoint of 5 MeV compared to that for 0.2 MeV.

Across most of the spectrum the correction decreases the decay rate apart from at the lowest energies for a decay with an endpoint larger than around $E_e^{\max} \approx 3$ MeV. This is because of the way in which the addition of soft photons affects the phase space calculation; they act as additional degrees of freedom that can increase the phase space but they also reduce the phase space available by taking away energy from the other particles. The value of the endpoint affects the energy that can be taken by the photons or other particles and changes in it change the balance between these two competing effects. Overall, the increase in phase space can only occur when the electron has a low energy and the endpoint is large enough for there to be sufficient energy available to the non-electron particles.

For double beta decay two factors of G will appear, one for each emitted elec-

tron. Using the expressions of Eqs. (3.55) and (3.56) the corrected spectrum is

$$d\Gamma'_{2,G} \propto G(E_1, E^{\text{max}}_{2\nu\beta\beta}) \, G(E_T - E_1, E^{\text{max}}_{2\nu\beta\beta}) \, F(Z, E_1) \, F(Z, E_T - E_1)$$

$$p_1 \, E_1 \, \sqrt{(E_T - E_1)^2 - m_e^2} \, (E_T - E_1)$$

$$(E^{\text{max}}_{2\nu\beta\beta} - E_T)^5 \, dE_1 \, dE_T, \tag{7.2}$$

$$d\Gamma'_{0,G} \propto G(E_1, E^{\text{max}}_{0\nu\beta\beta}) \, G(E_T - E_1, E^{\text{max}}_{0\nu\beta\beta}) \, F(Z, E_1) \, F(Z, E_T - E_1)$$

$$p_1 \, E_1 \, \sqrt{(E_T - E_1)^2 - m_e^2} \, (E_T - E_1)$$

$$\delta(E^{\text{max}}_{0\nu\beta\beta} - E_T) \, dE_1 \, dE_T, \tag{7.3}$$

where here the decay rate is reparametrised in terms of $E_T = E_1 + E_2$, the sum of the individual electron's energies. In applying these two factors of G, it is assumed that each beta decay can be treated separately. There is no problem with this for the inclusion of soft photon emission or interactions between the electrons and the nucleus as each can happen concurrently without affecting the other, particularly given that G has no Z dependence so the 'order' of the decays is irrelevant. However this does neglect the electron-electron photon exchange which will be instead discussed in the next section.

To measure the change to the spectrum due to additional corrections I define the quantity

$$\Delta_i(E_l) \equiv \left(\frac{d\Gamma'_{i,G}}{dE_l} \bigg/ \frac{d\Gamma_i}{dE_l} \right) - 1, \tag{7.4}$$

where $i = 0$, 2 refers to $0\nu\beta\beta$ or $2\nu\beta\beta$ decays and $l = 1$, T labels the individual energy, E_1, or the total energy, $E_T = E_1 + E_2$.

The impact of the radiative corrections on the decay spectrum for $2\nu\beta\beta$ can be seen in Fig. 7.2 which shows the proportional changes to the spectrum as a function of both the individual electron energy and the total energy. In both cases, the primary reason for the difference between the elements is the difference in maximum endpoint energy $E^{\text{max}}_{2\nu\beta\beta}$ available to the pair of electrons (see Appendix C for a longer mathematical discussion of the variation of the correction with the endpoint).
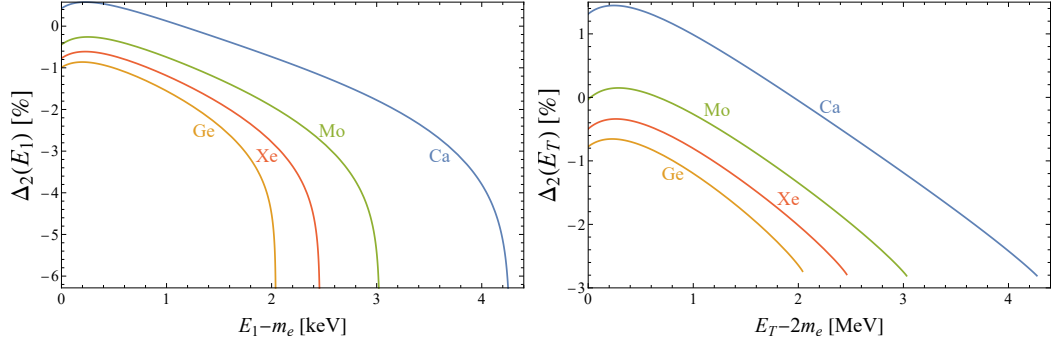
Figure 7.2: Proportional change to the $2\nu\beta\beta$ spectrum as a function of individual electron energy E_1 (left) and total electron energy E_T (right) due to radiative corrections.

For the individual electron spectrum, the impact of the correction is a reduction in the spectrum for all energies, apart from the lowest energy part of the calcium spectrum. This is the same for the spectrum as a function of the total energy, except with molybdenum also seeing a slight increase at low energies. When considering the difference between the total and individual energy spectra it is worth remembering that the decay rate is calculated by integrating over the second electron, either from 0 to $E_e^{max} - E_1$ in the case of the individual energy spectrum or from 0 to E_T for the total energy spectrum. This means that when E_1 is large the individual spectrum will take a smaller contribution from high energies (where the correction is more negative) whereas when E_T is large the total spectrum takes a greater contribution from high energies. This leads to the total energy spectrum having a significant enhancement at low energies (with both electrons necessarily having low energies) whereas the enhancement to the individual energy spectrum is much less (in which significant contribution comes from the other electron being of a high energy).

In practice, most neutrino-less double beta decay experiments are sensitive only to the total energy of both electrons and, as they are searching for a peak

	Ca-48	Ge-76	Mo-100	Xe-136
Experiment	CANDLES	LEGEND-200	CROSS	KLZ-800
ROI [keV]	310	4.4	8.4	147
$2\nu\beta\beta$	-2.43%	-2.73%	-2.79%	-2.54%

Table 7.2: Percentage change in the count rate due to radiative corrections. Calculated for the region of interest (ROI) of the total energy for current experiments.
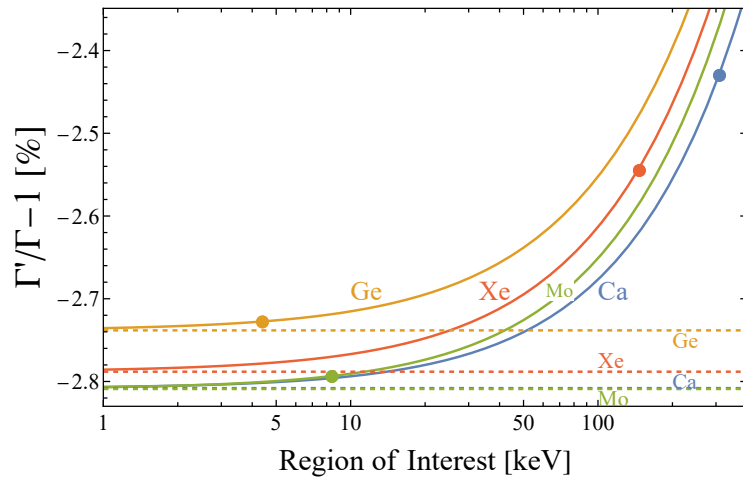
Figure 7.3: Proportional change in the count rate to the region of interest as a function of its size. The dots on each line show the ROI for each experiment from Table 7.2.

beyond the endpoint from $0\nu\beta\beta$ decay, they will focus only on a window at the highest energy of the spectrum. The optimum size of this window will be different depending upon the element and the experimental setup. The size of this window and the change in the expected rate of $2\nu\beta\beta$ for an experiment looking in this region is given in Table 7.2 calculated for windows from [135, 131]. The impact of the radiative corrections will vary with the choice of size of this region of interest (ROI), the larger the region the smaller the reduction in count rate, as can be seen in Fig. 7.3. This is because of the increase in the magnitude of the correction with the energy of the electron, a larger region of interest includes lower energy electrons that are less affected by this correction so the overall change is reduced. This is not the case for $0\nu\beta\beta$ for which the spectrum is merely a δ peak in terms of E_T. Given the finite energy resolution of the experiment the spectrum will be measured as a Gaussian about this peak. So long as the ROI already captures all of this peak, further increases in it will have no impact as there are no lower energy electrons to detect. Given that the ROI will always be chosen to be much larger than the energy resolution (otherwise the results of the experiment would be meaningless) effectively changes to the ROI will have no impact upon the reduction to the $0\nu\beta\beta$ spectrum.

The equivalent impact upon the $0\nu\beta\beta$ spectrum for the individual electron energy is shown in Fig. 7.4. In this case the behaviour is much different, the δ-
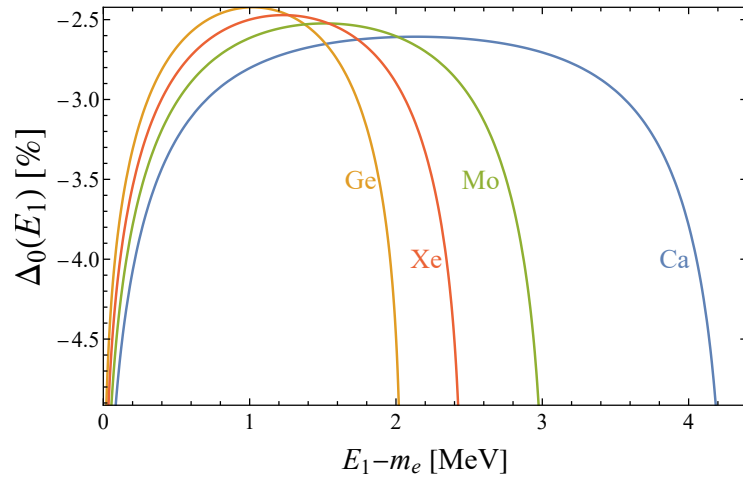
Figure 7.4: Proportional change to the $0\nu\beta\beta$ spectrum as a function of the individual electron energy, E_1, due to radiative corrections.

function in the $0\nu\beta\beta$ decay spectrum Eq. (7.3) means that the integral over E_T is trivial. The ratio of the two functions mathematically ends up being only the product of the two G correction factors, with all of the other terms cancelling. In practice, this means that there is a significant reduction in the highest and lowest energy parts of the spectrum (corresponding in both cases to one of the electrons having nearly the maximum energy) with a few % level reduction throughout the rest of the spectrum. Once again, the calcium spectrum is reduced the most due to it having the highest endpoint. Similarly, Table 7.3 shows the impact of the correction on the $0\nu\beta\beta$ peak in the total energy spectrum. As this is a δ peak it cannot be plotted, but the reduction in the multiplicative factor of this term can be calculated. In practice, any experiment will have a finite energy resolution and this peak will be smeared into a Gaussian of finite area directly proportional to the factor in front of the δ function. As the table shows, the reduction of the peak is nearly identical across all four elements, ranging from $2.7 - 2.8\%$ with the larger values being for the elements with higher endpoints. As this reduction is on the δ peak the size of

Nucleus	Ca-48	Ge-76	Mo-100	Xe-136
$\Delta_0(E_T)[\%]$	-2.81	-2.74	-2.81	-2.79

Table 7.3: Percentage change to the height of the δ-peak in the endpoint of the $0\nu\beta\beta$ as a function of the total electron energy, E_T, due to radiative corrections.

the region of interest is irrelevant; so long as it is larger than the energy resolution (which it will have been chosen to be in order to be experimentally useful) then the whole peak will be captured and the result is as given here.

Overall, the impact of this radiative correction upon neutrino-less double beta decay experiments is roughly the same across all of the elements and for both $2\nu\beta\beta$ and $0\nu\beta\beta$. Within the region of interest near the endpoint of the total energy spectrum, to which the experiments are sensitive, there will be a roughly $2.4 - 2.8\%$ reduction in the count rate. This effect will be slightly larger for the very highest total energies in the case of $2\nu\beta\beta$ and will be a flat reduction to any observation of the peak of $0\nu\beta\beta$. This has a limited impact upon the sensitivity to $0\nu\beta\beta$ through the reduction to the rate, thus making it harder to distinguish from the $2\nu\beta\beta$ background. However, if $0\nu\beta\beta$ were to be detected, this effect would need to be accounted for in the calculation of $m_{\beta\beta}$ from the decay rate.

7.2   Mutual Repulsion Between Emitted Electrons in Double Beta Decay

Whilst many correction factors exist to take account of the electromagnetic interaction between the emitted electrons and the other particles in double beta decay there is currently no correction due to the interaction existing between the two emitted electrons; the Fermi function, F, accounts only for their interaction with the nucleus and the screening factor, S, only for them with the orbital electrons. The effect of the positive nuclear charge is to increase the phase space available to the emitted electrons, this is reflected by the fact that the Fermi function $F \geq 1$ in all cases. Similarly to this, there will be a mutual repulsion between the two emitted electrons which should lead to a reduction in the decay rate. This reduction will be variable, a function not only of both electrons' energies but also of the angle between their emission momenta. Here I present a range of different approximations to calculate the effect of this correction upon the spectrum.

The starting point for calculating this effect is to look at the full Hamiltonian. Both electrons emitted in double beta decay will carry a charge, and will interact

with both the daughter nucleus and each other. If this is written in the momentum dependent form (i.e. taking $\psi \sim exp(iP \cdot x)$ for 4-momentum P and position x) then this takes the form [191]:

$$E_1 \psi_1 = H_{12} \psi_1 =$$
$$\left(i\gamma^0 \vec{\gamma} \cdot (\vec{p}_1 - \vec{A}_1) - \frac{Z\alpha}{r_1} + \frac{\alpha}{r_{12} - \vec{r}_{12} \cdot \vec{v}_2} + \gamma^0 m_e \right) \psi_1$$
$$E_2 \psi_2 = H_{21} \psi_2 \tag{7.5}$$

where $\vec{r}_1$ and $\vec{r}_2$ are the positions of the two electrons with $\vec{v}_1$, $\vec{v}_2$ their velocities and H_{21} is H_{12} with all labels reversed $1 \leftrightarrow 2$. The mutual electron repulsion is given by the Liénard-Wiechart potential with retarded displacement $\vec{r}_{ij} = \vec{r}_i - \vec{r}'_j$ for $\vec{r}'_j$ the retarded position of the secondary electron and vector potential $\vec{A}_i$ [192]. In this the nuclear charge is treated as point-like and the screening effect of the orbital electrons is neglected. Given that the two emitted electrons are identical the combined wavefunction which solves these will need to be anti-symmetrised with respect to their exchange. Given the spatial symmetry of this expression, this will have to be achieved by using an anti-symmetric spin combination. As we are not considering a polarised nucleus here this will have no effect on the emission kinematics and will henceforward be assumed to be included implicitly.

Fully analytically solving Eq. (7.5) is impossible (many attempts have been made with the similar system of Helium with two bound electrons [193]), however an approximation of the energy dependence can be made, here taking inspiration from the existing calculation of the Fermi function. In the standard calculation for the beta decay matrix element, formally the wave-function for the electron in a Coulomb field should be used. However, as this is too analytically challenging, instead a plane wave is used which is then weighted by the Fermi function (which gives the ratio of probabilities of an electron to be found at the nuclear radius with a given momentum when it has a coulomb waveform compared to a plane wave-form [194]). Following this method, treating the electrons as plane waves but with a modified Fermi function is one way of approaching this problem. I will eventually

do this by effectively absorbing the electron repulsion into a perturbed, velocity-dependent Z_{eff} which treats each electron as partially screening the nucleus from the other electron. In the following I consider how this can be done, as well as how the problem can be approached using a perturbative method.

7.2.1   Neglecting the electron-electron repulsion

The usual method for evaluating this Hamiltonian is simply to ignore the interaction between the electrons altogether. Neglecting the term $\alpha/(r_{12} - \vec{r}_{12} \cdot \vec{v}_2)$ in Eq. (7.5) leads to independent wavefunctions that each satisfy the same expression. In this case the Hamiltonian becomes entirely separable in terms of $\vec{r}_1$ and $\vec{r}_2$ and the solution to each of these is found individually in the manner presented previously in Section 3.4.1. I present here again the result,

$$F(Z,E) = 4e^{\pi\eta} \left| (2pR_n)^{(\gamma-1)} \frac{\Gamma(\gamma+i\eta)}{\Gamma(2\gamma+1)} \right|^2, \tag{7.6}$$

where $\eta = \alpha Z E_e / |\vec{p}_e|$ and $\gamma = \sqrt{1 - (\alpha Z)^2}$. In the construction of this, the choice $|\kappa| = 1$ (corresponding to an $S_{1/2}$ state) has been taken. This means that γ will be imaginary if $|Z| > 1/\alpha \approx 137$, a case which will arise later in some extreme cases. This possibility has been considered within the derivation and leads here to the modulus being taken over more terms than is conventionally written.

For this simplest of approximations, the spectrum is modified simply by multiplying the two additional Fermi factors, one for each electron, onto the result derived from the integrated matrix element. The result is then, from Eqs. (3.55)

and (3.56),

$$d\Gamma_2 \propto F(Z,E_1)F(Z,E_T-E_1)$$
$$p_1\,E_1\,\sqrt{(E_T-E_1)^2-m_e^2}\,(E_T-E_1)$$
$$(E_{2\nu\beta\beta}^{\max}-E_T)^5\,dE_1\,dE_T, \tag{7.7}$$
$$d\Gamma_0 \propto F(Z,E_1)\,F(Z,E_T-E_1)$$
$$p_1\,E_1\,\sqrt{(E_T-E_1)^2-m_e^2}\,(E_T-E_1)$$
$$\delta(E_{0\nu\beta\beta}^{\max}-E_T)\,dE_1\,dE_T. \tag{7.8}$$

This result is the standard one used in calculating the double beta decay spectrum and is the one against which I shall compare future improved approximations. This calculation has been improved upon in [114], where the effects of the finite size of the nuclear charge and the screening of the orbital electrons have been approximated. These effects will be safely neglected when considering the corrections herein as they are sufficiently small that when comparing differences proportionally they would make negligible difference to the sensitivity.

7.2.2 Static Approximation

The simplest approximation for accounting for the mutual repulsion between the electrons is to treat each electron as seeing the other as a static charge at the centre of the nucleus. In practice, this means taking $Z \to Z_{\text{eff}} = Z - 1$ in Eq. (7.6).

In Fig. 7.5 (bottom) the impact of this simplest approximate correction can be seen (with Δ_i taking the same meaning as Eq. (7.4) but with $\Gamma'_{i,G} \to \Gamma'_{i,F}$ where in this case $\Gamma'_{i,F} = \Gamma_i(Z \to Z-1)$). At the lowest energies the reduction is greatest, in this case the electron has the greatest probability density near the nucleus and thus feels the repulsion of the other electron the most. At higher energies the effect is reduced, with the reduction changing more slowly as the energy becomes larger. This is because further increases to the electron energy have diminishing impact upon the wavefunction with the integral over E_T always including some low energy electron contributions which are the dominant cause of the reduction here. The

difference between the elements comes from their different nuclear charges, the larger the nuclear charge the greater the effect of reducing it by 1 (apart from at particularly low energies). This is because the impact of the nuclear charge is two-fold: it increases the strength of the potential that is felt by the electron and it increases the probability density for the electron to be nearer the nucleus. Overall, the electron is within a stronger potential and has a greater weighting within the phase space integral to where the potential is stronger. These two factors combine to create a greater than exponential increase in the Fermi function as a function of Z. Thus the impact of reducing the value of Z is more significant for larger Z values than for smaller ones. This can be seen in the top plot of Fig. 7.5 in which
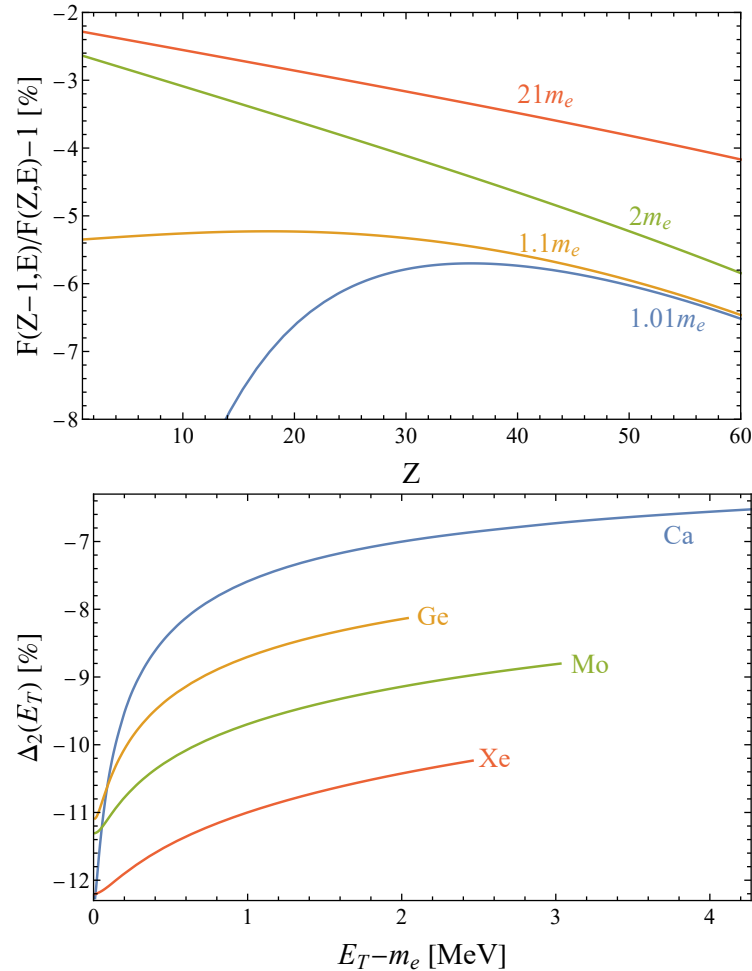
Figure 7.5: Ratio of $F(Z-1,E)/F(Z,E)$ as a function of Z for a range of energies (top). Proportional change to the $2\nu\beta\beta$ spectrum as a function of total electron energy for the simplest mutual repulsion correction of $Z \rightarrow Z-1$ (bottom).

the proportional difference between the reduced-charge Fermi function compared to the original Fermi function is shown to be greater in magnitude for larger values of Z. The only exception is for sub-relativistic energies where the different dispersion relation affects the phase space available and leads to a decreasing change in *F* for low Z values.

7.2.3 Perturbative Calculation

In quantum mechanics, the standard approach to deal with introducing a new effect that cannot be analytically solved is to consider a perturbative approach. In this case, the perturbation is the addition of the extra electron charge relative to the charge of the nucleus. This change can be seen as small if the expansion parameter is taken to be the ratio of the nuclear to electron charge, $1/Z$ (recalling that $Z \geq 22$ for the elements considered here). The dependence of the potential upon $1/r_{12}$, the electrons' separation, means that this perturbation can become potentially infinite in magnitude. However, when performing the full phase space integral to calculate the overlap between the electrons' wavefunctions the region in which this term diverges is sufficiently small that the contribution remains finite and an attempt at continuum perturbation theory can still be made. In order to calculate this I follow the method for perturbations in the continuum as given by [195]. This calculation contains multiple stages of integrals over the wavefunction $\Psi(E_1, \vec{r}_1, E_2, \vec{r}_2)$ (the full list of variables upon which Ψ depends at times being suppressed for ease of notation). The goal is to find a new modified wavefunction which can be evaluated at the nuclear radius in the same manner as before to find a modified Fermi function.

As the interaction is happening internally to the two electron system and is in the continuum, the total energy between the two electrons cannot change. The choice then of perturbed state Ψ_i is defined in terms of the unperturbed state Ψ_0 so that is has the same perturbed energy under the perturbed Hamiltonian as the unperturbed state does under the unperturbed Hamiltonian (to first order in $1/Z$),

$$H_0\Psi_0 = E_0\Psi_0, \quad (H_0 + V)\Psi_i = E_0(1 + O(1/Z))\Psi_i, \tag{7.9}$$

where H_0 is the unperturbed Hamiltonian with unperturbed energy E_0 and V the perturbation.

Despite the fact that the total energy cannot change, the perturbed state potentially receives contributions from unperturbed states of all possible energies. The perturbed wave-function which satisfies this energy condition is, as the continuum analogue of the usual bound state perturbation expression,

$$\Psi_i(E_1, E_2) = \Psi_0(E_1, E_2) + \sum_{\mu, \kappa} \int \int \frac{U_{i,0}(E_1, E_2, E_1', E_2')}{E_1 + E_2 - E_1' - E_2'} \Psi_0(E_1', E_2') \mathrm{d}E_1' \mathrm{d}E_2',$$

$$(7.10)$$

where $U_{i,0}$ is the transition element between the two states, given below. The sum is performed over all possible values of the angular momentum quantum numbers μ, κ for both of the initial and final state electron wavefunctions with all possible unperturbed states contributing to the final state. The unperturbed state is that found assuming no electron-electron interaction, $\Psi_0 = \psi(E_1, \vec{r}_1) \psi(E_2, \vec{r}_2)$, with ψ being given by Eqs. (3.32) and (3.37). The perturbation matrix element is given by

$$U_{i,0}(E_1, E_2, E_1', E_2') = \int \int \psi(E_1, \vec{r}_1)^\dagger \psi(E_2, \vec{r}_2)^\dagger$$
$$\frac{\alpha}{|\vec{r}_1 - \vec{r}_2|} \psi(E_1', \vec{r}_1) \psi(E_2', \vec{r}_2) \mathrm{d}^3 r_1 \mathrm{d}^3 r_2, \qquad (7.11)$$

where each of the states here may have different angular momentum quantum numbers μ, κ.

Recalling the derivation in Section 3.4.1, the Fermi function is calculated by evaluating the wavefunction of the electron at the nuclear radius R_n. Here, I calculate the perturbed wavefunction Ψ_i as a perturbation of the wavefunctions that lead to the conventional Fermi function. This perturbed wavefunction is then used instead in the derivation to generate a modified Fermi function. In practice, calculating these perturbed wavefunctions is highly computationally expensive as they require double energy integrals over the matrix element which itself is a double spatial integral with non-trivial energy dependence due to the complexity of the wavefunctions involved. Instead as a computational simplification, I consider the

perturbation of only one of the electrons with the other state treated as a charge fixed at a distance R_n from the nucleus. I choose this distance because, as in the derivation of the usual Fermi function before, ultimately the wave-functions will be evaluated at this point to derive the perturbed Fermi function. Mathematically this means taking both functions of $\vec{r}_2$ to be given by $\psi(\vec{r}_2) \propto \delta(\vec{r}_2 - \vec{R}_n)$ where $|\vec{R}_n| = R_n$. Using this the calculation is reduced to only a single spatial integral with the transition matrix element thus being given by $U_{i,0} = U_{i,0}(E_1, E_1')$. Inserting this into the expression for the perturbed wavefunction gives a perturbed function $\psi_i(E_1, \vec{r}_1)$ which can be expressed in terms of modified functions f_i and g_i in the manner of Eq. (3.32). Using Eq. (3.38), in the same manner as the Fermi function was derived from the unmodified wavefunction, the modified wavefunction is then evaluated at $|\vec{r}_1| = R_n$ and used to derive a modified Fermi function using

$$F'(Z,W) = (f_i^2 + g_i^2)\frac{\pi}{2pW}. \tag{7.12}$$

The use of the simplification of fixing the location of one of the electrons greatly reduces the computational requirements but does make the approximation substantively less valid. I also only include in my calculation contributions from $\kappa = -1$ states, those of the lowest angular momentum which are the ones that are included in the conventional Fermi function. Contributions from higher angular momentum states are small and diminish with increasing quantum number.

Due to the simplified consideration of only one electron being dynamically altered, I end up with a modified Fermi function only of the individual electron's energy, $F'(E_1)$ (the angle between the electrons momentum and the other electron has no impact as it is 'smeared out' by the spatial integral to give a purely energy dependent transition element). I insert this modified Fermi function into Eq. (7.7) to give a modified decay rate and compare this to the unmodified spectrum in Fig. 7.6. As can be seen, the impact is to give a similar percentage reduction and identical ordering with Z as the static approximation but with a greater variation with energy and a smaller variation between elements. This is because this much simplified result misses much of the structure of the more advanced method. For example, the
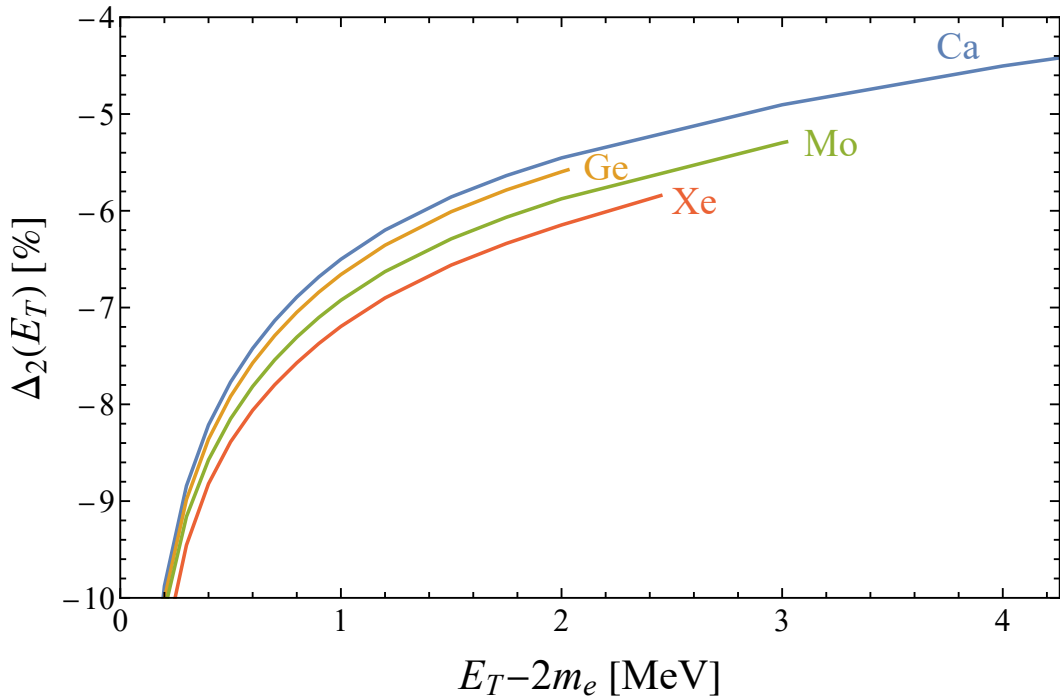
Figure 7.6: Proportional change to the $2\nu\beta\beta$ spectrum due to mutual electron repulsion as a function of total electron energy. This is calculated using a perturbative approach.

loss of the angular information due to the consideration of only lowest angular momentum state contributions causes the loss of the sharp angular dependence when the two electrons are emitted close to each other which would reduce the change in the spectrum. This method also enhances the reduction at low energies because the non-dynamical second electron is fixed close to the nucleus (and thus closer to the other electron) rather than moving away. Overall, this perturbation method could be more successful given greater computational power and fewer approximations but has some limited validity as is. It does serve to confirm the previous conclusions that larger Z values lead to a greater correction and that the effect will be largest for low energies and diminish for higher energies. It also confirms that the effect should be around the value of several % in magnitude.

7.2.4 Effective Nuclear Charge Approximation

I now return to an analytic approximation for calculating this effect. The way to improve upon the static approximation used before is to allow for the 'secondary' electron to be dynamic. Whilst solving the problem fully is impossible, I aim to

approximately account for the motion of the secondary electron by defining a modified Z_{eff} which incorporates the mutual dynamics of the electrons to define a reduced effective nuclear charge to be used within the Fermi function.

Given the form of the potential in Eq. (7.5), the aim of my approximation is to derive an expression for some Z_{eff} which can incorporate some of the kinematics of the decay, $Z_{\text{eff}} = Z_{\text{eff}}(v_1, v_2, \cos\theta)$ where v_1, v_2 are the speeds of the electrons, $v_i = |\vec{p}_i|/E_i$, and $\cos\theta$ is the cosine of the angle between the direction of their momenta. There will be two Z_{eff}, one for each of the electrons, because if they have different speeds then the effect each has on the other will be different. The two expressions will, however, be related merely by changing the labels $1 \leftrightarrow 2$ in the expressions given the symmetry of the setup. In calculating this I consider the primary electron as the one for which the Z_{eff} is being calculated with the change $Z \to Z_{\text{eff}}$ being caused by the presence of the secondary electron. The way in which I calculate this starts from the potential felt by the electron

$$V(\vec{r}_1, \vec{r}_2, \vec{v}_2) = \frac{Z}{r_1} - \frac{1}{r_{12} - \vec{r}_{12} \cdot \vec{v}_2} \tag{7.13}$$

In order to use a modified form of the Fermi function involving simply the change $Z \to Z_{\text{eff}}$ I wish to effectively absorb the second part of this potential into the definition of Z_{eff}. I do this by considering the relationship between r_1, r_2, $\vec{v}_1$ and $\vec{v}_2$ for the relativistic exchange of a photon, taking account of the finite speed of photon propagation that gives a retarded potential. In this, I neglect the vector potential (which is small compared to the momentum[1]) and model both electrons as having approximately constant velocities with the photon travelling between

Figure 7.7: Diagrammatic depiction of the exchange of a single photon between two electrons with the photon emitted at time t_i and absorbed at time t_f. Given are the relations between length and speed assuming constant speeds.

---
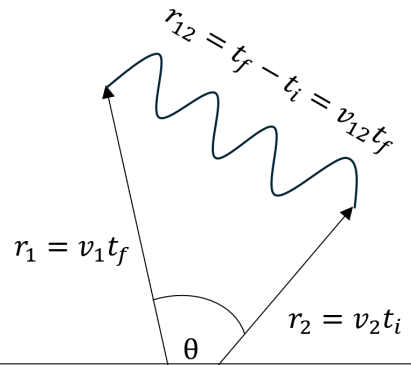
[1]Both the scalar and vector potentials can become very large for small separations, however this happens at the point of production near the nucleus where the nuclear charge, a factor of Z larger, will dominate the behaviour and 'blow up' faster.

them at the speed of light, as is depicted in Fig. 7.7. Doing this will allow for approximate expressions to be found for r_{12} and $\vec{r}_{12} \cdot \vec{v}_2$ in terms of r_1 by solving geometrically.

To begin, I derive a relation between the times of photon emission t_i and absorption t_f as a function of v_1, v_2 & $\cos\theta$. This is found to have a direct proportionality $t_i \propto t_f$. I express this relationship through the definition of a 'retarded speed', such that $v_2' = v_2\, t_i/t_f$, which is given by

$$v_2' = v_2 \left(\frac{E_2}{m_e}\right)^2 \left((1 - v_1 v_2 \cos\theta) - \sqrt{(1 - v_1 v_2 \cos\theta)^2 - \frac{m_e^4}{E_1^2 E_2^2}} \right). \qquad (7.14)$$

Using this result and the dependence of r_{12} upon v_1 and v_2 enables the determination of r_{12} also in direct proportionality to t_f. Again this is expressed in terms of a 'relative speed' v_{12} satisfying $r_{12} = (r_1/v_1)\, v_{12}$ to give

$$v_{12} = \sqrt{v_1^2 + {v_2'}^2 - 2 v_1 v_2' \cos\theta}. \qquad (7.15)$$

Finally, using this to find the angle between the second electron's speed and the direction of the photon gives

$$\vec{r}_{12} \cdot \vec{v}_2 = r_{12} v_2 \left(\frac{v_1 \cos\theta - v_2'}{v_{12}} \right). \qquad (7.16)$$

The equivalent expressions for the emission of a photon from the primary electron to the secondary electron defines r_{21} identically but with $1 \leftrightarrow 2$. The new speeds that have been defined here, v_2' and v_{12}, are not physical speeds but merely parameters related to the retarded distance between the electrons.

Using all of these expressions in the potential of Eq. (7.5) gives

$$Z_{\text{eff}} = Z - \frac{v_1}{v_{12} + v_2(v_2' - v_1 \cos\theta)}, \qquad (7.17)$$

and vice versa with $1 \leftrightarrow 2$. In theory this gives the possibility of $Z_{\text{eff}} \to -\infty$ for

$v_1 = v_2$ and $\cos\theta = 1$ ($\Rightarrow v_{12} \to 0$) corresponding to the complete overlap of the two electrons. This might seem problematic but the blowing up of this is no different from the blowing up of the conventional Fermi function term Z/v_1 for $v_1 = 0$ i.e. the electron is entirely fixed at the nucleus. This is acceptable in the latter case because it merely represents that the electron has a finite probability of being located at the nucleus because of its charge, when the usual direct proportionality to $|\vec{p}_1|$ in the decay rate forbids this. This occurs for the same reason in the former but the other way around, the repulsion between the electrons completely forbids the electrons from having identical velocities, as is to be expected. In either case, the actual phase space for this occurring is small enough to give only a finite contribution to a full integral over the entire phase space.

This modified Z can finally be inserted into the usual derivation of the Fermi function. When this is carried through, this in turn modifies the values of γ and η in Eq. (7.6), which both carry a Z dependence. This gives a new 'corrected' Fermi function

$$F'(Z, E_1, E_2, \cos\theta) = F(\gamma \to \gamma_{\text{eff}}, \eta \to \eta_{\text{eff}}). \tag{7.18}$$

Whilst this derivation relies upon some strong approximations, it is useful because it crucially captures the edge cases of how Z would appear to the primary electron to vary as a function of the energy of the secondary electron. For example, in the case $v_2 = 0 \Rightarrow v_{12} = v_1$, we find $Z_{\text{eff}} = Z - 1$. This corresponds exactly to what is physically expected and which was used in the previously discussed simplest approximation of one static electron near the nucleus reducing the nuclear charge by 1 as it appears for the other. Equivalently, $v_1 = 0$ gives $Z_{\text{eff}} = Z$. The static primary electron has a potential dominated by the nuclear charge which blows up with the $1/v_1$ dependence and thus the moving electron is negligible by comparison. In addition to these cases there is also that of when the primary electron has a very high energy $v_1 \to 1 \Rightarrow v_{12} \to 1$ (excluding the highly tuned case of both electrons being co-linear and of similar energies). This gives $Z_{\text{eff}} = Z - 1$, effectively the primary electron sees the secondary electron and the nucleus as a combined charge.

This reflects the finite propagation of the photon with the secondary electron's retarded potential appearing to be sourced at the nucleus. Finally, there is the highly tuned case mentioned before in which both electrons have the same velocity and $Z_{\text{eff}} \to -\infty$. This causes the Fermi function to go to 0 and this outcome is forbidden as would be expected. Thus overall, in creating this effective charge a great range of the kinematics that is to be expected has been included within it. Whilst it is not an exact expression, it is useful as an indication of how each electron's velocity will affect the other and is an improvement upon the simpler approximation before of just using $Z - 1$ regardless of the electron velocities.

Within the decay spectrum there will be two Fermi functions, one for each of the emitted electrons. Each of these must be corrected to take account of the interaction with the other, giving corrected spectra:

$$
\begin{aligned}
d\Gamma'_{2,F} \propto & F'(Z, E_1, E_2, \cos\theta) F'(Z, E_2, E_1, \cos\theta) \\
& p_1 E_1 p_2 E_2 (E^{\max}_{2\nu\beta\beta} - E_1 - E_2)^5 \left(1 \mp \frac{p_1}{E_1} \frac{p_2}{E_2} \cos\theta \right) \\
& dE_1 dE_2 d\cos\theta,
\end{aligned} \tag{7.19}
$$

$$
\begin{aligned}
d\Gamma'_{0,F} \propto & F'(Z, E_1, E_2, \cos\theta) F'(Z, E_2, E_1, \cos\theta) \\
& p_1 E_1 p_2 E_2 \left(1 \mp \frac{p_1}{E_1} \frac{p_2}{E_2} \cos\theta \right) \delta(E^{\max}_{0\nu\beta\beta} - E_1 - E_2) \\
& dE_1 dE_2 d\cos\theta
\end{aligned} \tag{7.20}
$$

where the minus (plus) sign is for left (right) handed currents [196]. For $2\nu\beta\beta$ it has been experimentally shown that the decay is predominantly left-handed, however it is possible that there are right-handed contributions from effective operators in the same manner as was considered here before for single beta decay. The $0\nu\beta\beta$ process has never been observed so could potentially be mediated by left or right-handed interactions.

The impact of replacing the Fermi function with its modified form compared to the original spectrum is shown in Fig. 7.8 for both left and right-handed interactions. As expected, both left and right-handed interactions tend towards the same
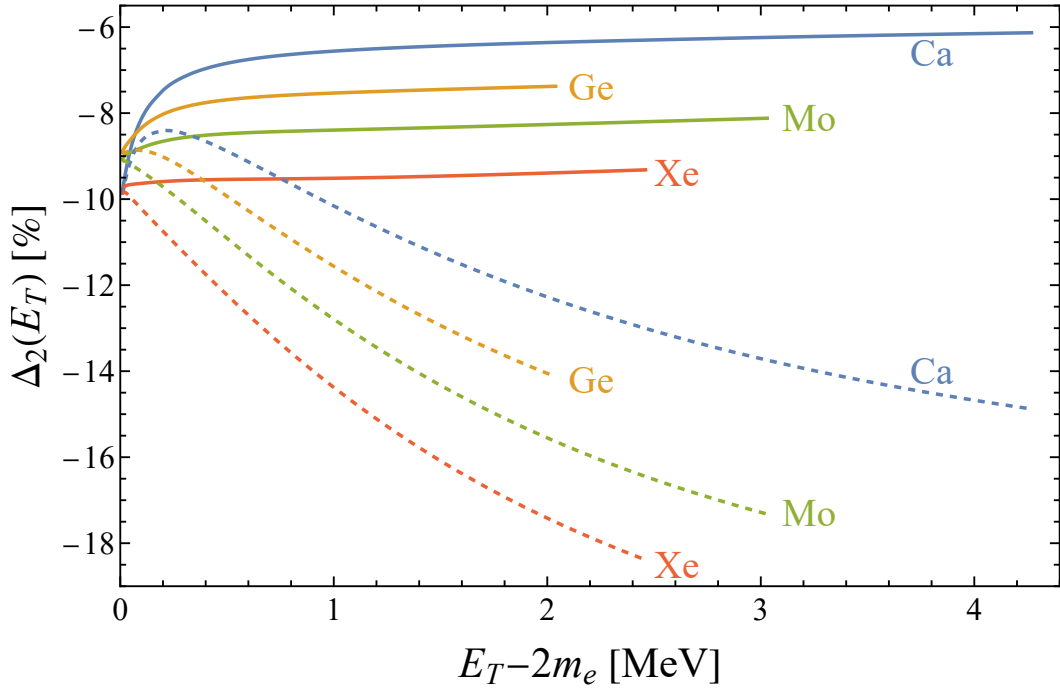
Figure 7.8: Proportional correction to the $2\nu\beta\beta$ spectrum as a function of the total electron energy due to the mutual electron repulsion. This is with both left-handed (solid) and right-handed (dashed) mediated interactions for a range of double beta decay elements.

magnitude of reduction for negligible total energy. This is because the strength of the angular correlation is proportional to the product of their momenta, meaning that there is no difference between the two cases when the momenta tend to zero. As their energy and momenta increase, the angular correlation becomes stronger and there is an increasing divergence between the left and right-handed interactions. For the left-handed currents the correction tends towards an asymptotic value. This is because in these cases the electrons are ultra-relativistic, over the vast majority of the range of the integral over their energies, and the retarded potential from the other electron appears as if it is sourced from the position of the nucleus. Further increases in energy thus have little impact as the electron is already moving close to the speed of light. Compared to the static approximation, the reduction in the spectrum is smaller. The angular correlation means that the electrons will typically be emitted in opposing directions, meaning that the separation between the two electrons will typically be larger than that between them and the nucleus. The higher the energy, the stronger the angular effect and thus the further apart the electrons

	Ca-48	Ge-76	Mo-100	Xe-136
LH	−6.1%	−7.4%	−8.1%	−9.3%
RH	−14.9%	−14.1%	−17.3%	−18.4%

Table 7.4: Percentage change to the $0\nu\beta\beta$ rate for left handed (LH) and right handed (RH) currents.

will on average be. This means that with this approximation the reduction in Z will average out to being less than the reduction by 1 used in the static approximation. Conversely, for the right-handed current the electrons are more likely to be emitted with a small angle between them making the impact of their repulsion larger and leading to a larger correction to the spectrum. The right-handed correction would eventually level off for the same reason as the left-handed, but this would require much higher electron energies than is available from their decays given their smaller angular separation. Once again, the correction in both cases is larger for higher Z values for the reasons explained before.

The impact upon the $0\nu\beta\beta$ rate is given by Table 7.4. In this case, the signature of $0\nu\beta\beta$ is a δ-peak in the total energy at the endpoint, thus the percentages given here are reductions in the expected count rate at this peak. This follows the same pattern as $2\nu\beta\beta$ with a much greater reduction for right-handed currents than for left-handed and a stronger effect for higher Z values. As $0\nu\beta\beta$ has never been observed and there is no prediction for its rate there is no experimental result to compare this to. However, the ultimate aim of these experiments is to extract the value of $m_{\beta\beta}$, the effective double beta decay neutrino mass, from the rate of this decay so this correction will be relevant if precision measurements of $0\nu\beta\beta$ are made.

Ultimately, whilst this effect appears to cause a substantial reduction in the decay spectrum for $2\nu\beta\beta$ (nearly 10% in some cases), in practice most of this effect will already be accounted for in experimental measurements. As described in Section 3.5 the decay rate is proportional to both the Nuclear Matrix Element (NME) and the axial-vector coupling g_A^{eff}, both of which take different values for different elements. The double beta decay rate has for many elements a direct proportionality

	Ca-48	Ge-76	Mo-100	Xe-136
Experiment	CANDLES	LEGEND-200	CROSS	KLZ-800
N_{tot}	1.1×10^5	5.7×10^6	2.1×10^7	7.3×10^6
χ^2	0.30	21	23	3.1
N_{req}	1.4×10^6	1.0×10^6	3.6×10^6	9.0×10^6

Table 7.5: χ^2 difference between the corrected and uncorrected spectra for various elements calculated using total counts, N_{tot}, in current experiments. Also, the average total count required, N_{req}, to reach observation at a 95% confidence level.

to the fourth power of the axial coupling, g_A^{eff} [197]; attempts to generate a theoretical prediction for its value vary significantly depending upon the model used with different calculations finding $g_A^{\text{eff}} = 0.57$ or $g_A^{\text{eff}} = 0.72$ in the case of Xenon [198]. Many attempts have also been made to calculate the NME theoretically. However, the different methods employed lead to significantly different results with variations to the decay rate of factors of up to 9 [106]. Rather than using theoretical calculations, most often the value of both of these quantities is extracted from experimental measurements for each element. Separation of the product of the NME with g_A^{eff} can be done by considering the different intermediate states with which the double beta decay can occur, each having different energy dependencies [199]. Ultimately, the determination of these terms from experiment without the mutual electron repulsion correction being considered means that most of the effect of this correction will already have been accounted for in the determination of g_A^{eff}. As the theoretical uncertainty is so large, there has been no result to compare the experimental measurements to which would show the reduction in the apparent value of g_A^{eff} due to this correction. All that remains as a signature of this correction is the shape of the energy dependency. This is largest for small Z elements at around 3% for Ca-48 (see Fig. 7.8).

Given the magnitude of the effect upon the $2\nu\beta\beta$ spectrum it is interesting to ask whether current or future experiments will be sensitive to the impact of this correction. Here I use the χ^2 methodology explained in Section 3.7 to analyse whether the impact of this correction upon the spectrum is statistically significant, in this case measuring the energy spectrum using 20 bins and with a total number of events

taken from each element's relevant experiment. I again apply the minimisation over a nuisance parameter multiplying the overall decay rate to reflect the theoretical uncertainty in the total decay rate. The results are shown in Table 7.5, calculated using idealised experimental double beta data taken from [131, 135, 200, 201, 202, 203]. Recalling that for a test of this type the 95% CL critical value is 3.84, it is clear that LEGEND-200 and CROSS should be weakly sensitive to this correction with KamLAND-Zen being nearly sensitive. For each of the experiments there is also given the required total count rate to reach the critical value, for those experiments already sensitive this is lower than their current count rate, for CANDLES an order of magnitude improvement in count total is required before the correction will have a consistently measurable impact. This calculation would imply that this correction factor is significant enough that it needs to be included in double beta decay measurement analyses. However, these results have been calculated for highly idealised setups in which the only limitation on the data is statistical and issues of energy resolution can be neglected.

7.3 Case Study: Impact upon KamLAND-Zen

Whilst it is of interest to perform the idealised calculation of the sensitivity above, looking at real experimental uncertainties can be more informative. To do this, I use the experimental uncertainties from the KamLAND-Zen experiment found in [204] which cover the energy range $E_T = 0.80 - 2.15$ MeV using 27 bins. The uncertainty varies significantly across the different bins but is generally lowest at low energies and becomes substantially larger for higher energies due to the low statistics (see Appendix D for the values). In the standard form of the χ^2 used previously a Poissonian distribution in each bin has been assumed, with a standard deviation given by $\sqrt{N_{\text{SM}}}$ as in Eq. (3.59). Here instead I use the percentage error from the experiment, which gives standard deviations as great as over 40% larger

(the greatest increases being at lower energies). This gives

$$t = \min_A \left[\sum_{i=1}^{N_{\text{bins}}} \left(\frac{N_{\text{corr}}^{(i)} - (1+A)N_{\text{uncorr}}^{(i)}}{(1+A)\sigma^{(i)}N_{\text{uncorr}}^{(i)}} \right)^2 + \left(\frac{A}{\sigma_A} \right)^2 \right], \qquad (7.21)$$

where $\sigma^{(i)}$ is the percentage uncertainty of bin i. I do this for the impact both of the radiative corrections and the mutual electron repulsion.

If the minimisation over A were not performed, the result of this test would be $t = 11.5$ for the radiative corrections and $t = 931$ for the mutual electron repulsion. If the total $2\nu\beta\beta$ rate were known exactly then the roughly 1% deviation in the spectrum due to the radiative corrections and 10% deviation due to the mutual electron repulsion would be greatly significant and accurate theoretical predictions would be highly dependent upon this correction. However, with the minimisation the values are instead $t_{\text{min}} = 0.94$ for the radiative corrections and $t_{\text{min}} = 0.011$ for the mutual electron repulsion. In both cases nearly the entire impact of the corrections are absorbed into the uncertainty in the total rate and the remaining energy dependence of the correction is too small to detect given the levels of uncertainty. The variation with energy of the radiative correction is much more substantial across this range than the variation for the electron repulsion which is why the former value is much larger than the latter after minimisation. Given the scaling with the uncertainty, in order to reach significant levels the percentage uncertainty would need to be reduced by approximately a factor of 2 for the radiative corrections and 20 for the electron repulsion. Whilst the former is achievable the latter is something that will be very experimentally challenging.

Clearly the experimental uncertainty as it currently stands is too large for either of these corrections to be observable. Given this, I wish to see how varying the strength of the correction (which could come from using a higher endpoint element in the radiative correction case or a lower Z element for the mutual electron repulsion) affects the sensitivity to it. In order to calculate this, I define a new scaled
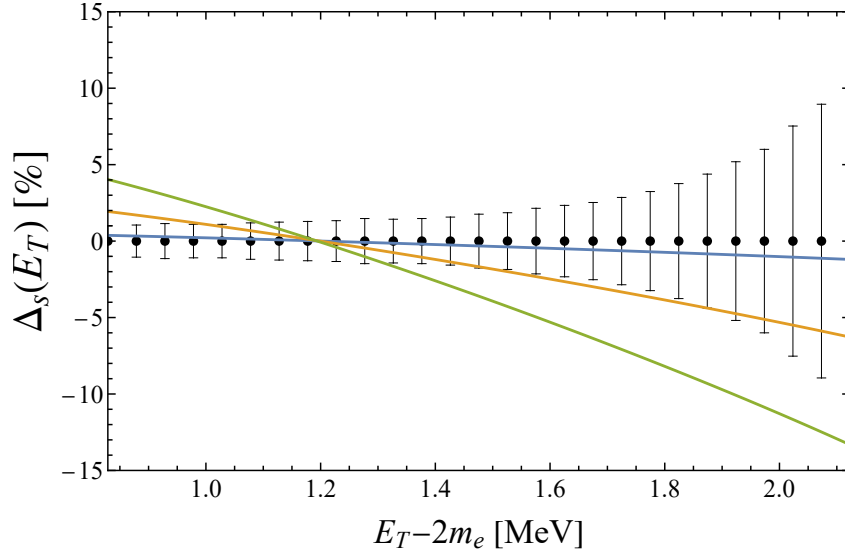
Figure 7.9: Proportional difference between the corrected and uncorrected $2\nu\beta\beta$ spectra due to the radiative correction, weighted to minimise the χ^2 deviation, as a function of the total electron energy alongside the uncertainties from KamLAND-Zen (black). The scaling of the correction is $s = 1$ (blue), $s = 5$ (orange) and $s = 10$ (green).

variant of the correction as

$$d\Gamma'_{s,F} = \left[1 + s\left(\frac{F'(Z,E_1,E_2,\cos\theta)}{F(Z,E_1)}\frac{F'(Z,E_2,E_1,\cos\theta)}{F(Z,E_2)} - 1\right)\right] d\Gamma_2, \qquad (7.22)$$

$$d\Gamma'_{s,G} = \left[1 + s(G(E_1,E^{\max}_{2\nu\beta\beta})G(E_2,E^{\max}_{2\nu\beta\beta} - 1)\right] d\Gamma_2, \qquad (7.23)$$

where $d\Gamma_2$ is as in Eq. (7.8). Thus here, $s = 0$ gives the uncorrected spectrum, $s = 1$ gives the corrected spectrum and $s > 1$ gives an exaggerated size of correction.

In order to compare these scaled spectra to the uncertainty in a way that reflects the lack of sensitivity to the total rate, it is useful to define a new weighted proportional difference

$$\Delta_s(E_T) \equiv \left[\frac{d\Gamma'_{s,c}}{dE_T} \middle/ \left((1+A)\frac{d\Gamma_2}{dE_T}\right)\right] - 1, \qquad (7.24)$$

where $c = F$, G denotes the correction used and A takes its value from Eq. (7.21) such that the χ^2 difference is minimised.

The result of calculating this difference for the values $s = 1$, $s = 5$ and $s = 10$ is shown in Figs. 7.9 and 7.10 where they are compared to the uncertainty values. As
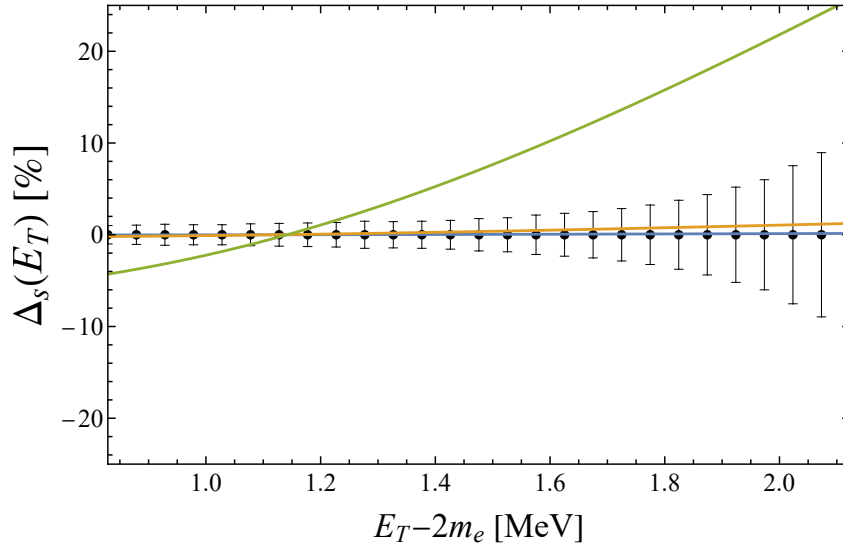
Figure 7.10: As Fig. 7.9 but for the mutual electron repulsion.

can be seen, in both cases the deviation for $s = 1$ fits clearly within the uncertainties reflecting the fact that this experiment is not sensitive to these corrections. For the radiative corrections the difference for $s = 5$ is significant enough that both at the lowest energies and for total kinetic energies in the range $1.5 - 1.8$ keV the deviation is slightly larger than the uncertainties, with the χ^2 value in this case being $t_{\min} = 26$. This reflects how this experiment is close to being sensitive to the radiative corrections, with a moderate increase in scaling leading to a highly significant deviation. A similar experiment with an element with higher endpoint value, for which there will be a greater variation in G, could thus be sensitive to the correction's impact. The increase to $s = 10$ approximately doubles the deviation leading to a highly significant change to the spectrum. For the mutual electron repulsion the behaviour is quite different. The increase in the correction for $s = 5$ is barely visible in the figure, whereas for $s = 10$ it is substantial. This is due to the non-linearity of the correction as a function of the total energy. The significant increase in the magnitude of the correction at low energies (only just captured in this energy range) is not obscured by the normalisation uncertainty. However, for Xenon this variation is too small to be substantial unless artificially scaled up as in this case. This does, however, imply that for elements with a greater variation with energy this correction may play a more crucial role. As seen in Fig. 7.8, the lower

Z elements have a larger variation with energy even whilst their overall correction is smaller. This is reflected in Table 7.5 in which the required number of events to measure the correction is lower for the lower *Z* elements. Whilst this will lead to a higher sensitivity, it is most likely not enough to be detectable and would also require a reduction in the experimental uncertainties.

To conclude, the current experiment of KamLAND-Zen is not sensitive to either of these corrections with the sensitivity to the mutual electron repulsion being particularly weak. The impact of the radiative corrections will be more substantial for those elements with higher endpoint energies, $E_{2\nu\beta\beta}^{\max}$, and, given the current sensitivity levels, the impact of this correction on the spectrum may soon be apparent and need to be included in theoretical calculations. For the mutual electron repulsion, conversely, the sensitivity is very weak. Whilst for low *Z* nuclei the effect may be larger, experiments will need to significantly improve their uncertainties before this correction has a significant impact.

Chapter 8

Conclusions

Given the immense power of the Standard Model and the vast array of accurate predictions it has made, pushing beyond to reach a greater understanding of the forces which underlie everything has been one of the greatest challenges of the last few decades. Fortunately, the discovery of neutrino oscillations has acted as a key window into new physics beyond the Standard Model. The future generation of experiments seeking to probe more deeply into the neutrino sector offers an important opportunity to search for new effects and the breaking of the understood rules.

In Chapters 2 and 3, I gave an overview of our understanding to date of how neutrinos fit into the Standard Model and of how they are measured in single and double beta decay experiments. Crucially, the discovery of neutrino oscillations led to the conclusion that neutrinos must have a mass, something not predicted in the Standard Model. There are many ways in which this mass could be added such as the effective Weinberg operator or with the addition of right-handed neutrino states for which there is no theoretical prohibition upon them having a Majorana mass. The attempt to measure the absolute value of the neutrino masses in single beta decay requires precise measurements of the energy spectrum for the emitted electron, particularly the endpoint of the spectrum. The nature of this process means that these measurements are sensitive to new physics, whether it affects the nucleus or leptons involved. I here focus my study to those decays involving tritium, the current favoured element for the future of single beta decay experiments. Searches for a Majorana neutrino mass in double beta decay are immensely important, a

positive signal would be the first evidence of lepton number violation as well as helping to explain the process by which neutrinos gain their mass. It is important that the decay spectrum is well understood so that any precision measurements in the future are accurate.

The way in which new physics acting at high energy scales would manifest in current experiments can be described through the language of effective operators. In Chapter 4, I considered how the effective operators relevant to single beta decay would affect both the energy and angular spectra of the electron. I do this by considering all possible spinor bilinears with sensitivity being given to the parameters $\varepsilon_X \sim (M_W/\Lambda_{NP})^2$ which quantify the strength of this relative to the Standard Model weak decay. The results vary significantly depending upon the current with energy based measurements giving at best $\varepsilon_T \lesssim 3 \times 10^{-8}$ and at worst $\tilde{\varepsilon}_R \lesssim 8 \times 10^{-1}$ for a total count rate of $N_{\text{tot}} = 10^{18}$ events (see Fig. 4.3). Unlike for the energy based measurements for which single beta decay offers improved sensitivity to only a few of these parameters, the angular sensitivity is much stronger with improvements for nearly all of the different currents. For example, the sensitivity improves significantly to $\tilde{\varepsilon}_R \lesssim 2 \times 10^{-4}$ for the angular measurements, an order of magnitude improvement on the current limits (Fig. 4.4). This assumes that the nuclei can be perfectly polarised with the limits scaling inversely with the fraction of polarisation. Considering these results in the context of new physics, this translates to a sensitivity to energy scales of up to $\Lambda \sim 10^4 \, M_W \sim 10^6$ GeV.

Many models which seek to explain neutrino masses also include additional heavy states which are neutral under all the Standard Model charges and are thus called sterile neutrinos. Provided that these states are light enough to be produced, their presence could have a significant impact upon single beta decay. I considered in Chapter 5 the two mechanisms through which this could occur, through the mixing of the active and sterile neutrino states and through sterile exotic currents. Whilst much interest and work has been performed in analysing the case of active-sterile mixing, spurred on by oscillation experiment results and the search for dark matter, no work has yet been done in directly placing limits on the ster-

ile exotic currents. Energy measurements have a relatively consistent sensitivity across the spectrum to active-sterile mixing, capable of providing limits in the range $|V_{eN}|^2 \sim 10^{-7} - 10^{-8}$ for a keV-mass sterile neutrino (apart from sterile neutrinos with masses equal to within a few 100s of eV of zero or the endpoint energy, see Fig. 5.3). For the sterile exotic currents the case is rather similar to the active exotic currents considered before with a significant variation in sensitivity between the different types of currents. The strongest is to tensor currents with $\varepsilon_T^N \lesssim 2 \times 10^{-5}$ and the weakest to pseudoscalar with $\varepsilon_P^N \lesssim 5 \times 10^{-2}$, again for an experiment with 10^{18} total events (Fig. 5.6). However in this case, the mass of the heavy state reduces its impact on the angular spectrum making energy measurements better than angular measurements for all currents. In both cases, the greatest impact upon the energy spectrum is through the kink that occurs at the endpoint of the heavy neutrino spectrum. This is significant as it means that there is a high level of degeneracy between these two cases for energy based measurements. Whilst angular measurements don't provide any greater sensitivity to either active-sterile mixing or sterile exotic currents, they do provide a means of distinguishing between the two cases. The sterile exotic currents have a much greater impact upon the angular spectrum than any active-sterile mixing meaning that, as can be seen in Fig. 5.8, simultaneous measurements of both energy and angular spectra enables discrimination between the two possibilities.

The inclusion of special relativity within the quantum field theory description of the Standard Model is essential given the relativistic energies involved in many physics processes. However, Lorentz symmetry violation is predicted by many theories that go beyond the Standard Model such as quantum theories of gravity and string theory. In Chapter 6, I have analysed two ways in which this could affect single beta decay, with a modification to the 4-point Fermi interaction and with a change to the propagation of the particles involved. In the first case, the modification to the Fermi interaction could come from a change to the W boson propagator with the change to the factor $\eta^{\mu\nu} \to \eta^{\mu\nu} + \chi^{\mu\nu}$ introducing a small degree of symmetry breaking. The 32 variables that make up the Lorentz violating tensor $\chi^{\mu\nu}$

could be split into real and imaginary parts of scalar, vector and tensor terms (classified with respect to spatial rotations). Each of these terms impact the spectrum differently, whether through their interactions with the nuclear spin or electron momentum or their modification of the energy spectrum. The current best limits on the parameters come from beta decay experiments such as for caesium and yttrium. For future tritium experiments, the most significant improvements on these limits come in the measurement of χ_r^{0j}, which could have a three orders of magnitude improvement through rate measurements for different nuclear polarisations, and the first measurement of the imaginary vector terms χ_i^{0j} and χ_i^{j0}, provided that angular measurements could be made perpendicular to the spin of a polarised nucleus. The other type of Lorentz violation I consider involves adding the propagation modifying terms a_f^μ. These terms are countershaded, meaning that their impact upon propagation can be removed mathematically by a field redefinition. Instead, the impact of these is manifested at the weak decay vertex with a violation of conservation of 4-momentum. The component a^0 has the strongest impact upon the decay, leading to a shift in the endpoint by a comparable amount $\Delta E_e^{\max} \sim a^0$. Precision measurement of the expected endpoint from mass measuring experiments imply this quantity should currently by limitable down to $a^0 \lesssim 0.07$ eV. The impact of the vector component $\vec{a}$ is much smaller but still measurable. By introducing a preferred direction in space, this introduces the effect that polarising the nucleus will change the total decay rate, something not predicted for the Standard Model result. However, the strongest sensitivity to this component comes once again from angular measurements which can probe this term potentially down to the sub-eV level.

Finally, in Chapter 7 I have looked at two corrections to the double beta decay spectrum, radiative corrections (due to soft photon emission) and the mutual repulsion between the two emitted electrons. I have considered the impact of these corrections for a range of elements commonly used in double beta decay experiments. For the radiative corrections the impact is strongest near the endpoint of the spectrum, the region of interest for searches for neutrinoless double beta decay. If neutrinoless double beta decay is observed, precision measurements will

be performed in order to infer the effective double beta decay mass to which the rate of the process is proportional. I have found that radiative corrections are expected to lead to an approximately $2.7 - 2.8\%$ decrease in the decay rate for $0\nu\beta\beta$. Calculating the impact of the mutual repulsion between the emitted electrons is analytically impossible, so instead I have shown a range of approximations for this effect. The most advanced of these is one which considers an effective nuclear charge $Z_{\text{eff}}(v_1, v_2, \cos\theta_{12})$ which is a function of the speeds of the electrons and their angular separation. The impact of this correction is large, an up to 10% decrease in the spectrum for the elements considered here. Crucially, the energy dependence of this correction is almost entirely at the lowest energies with the effect being relatively constant for total electron energies above $\sim 0.1 - 0.5$ MeV. This means that most of the impact of the correction is degenerate with the large theoretical uncertainties upon the nuclear matrix elements that give the total rates of this process. In an attempt to quantify the sensitivity to these corrections for a real experiment, I calculate whether the KamLAND-Zen experiment should be sensitive to them given its uncertainties. Whilst the radiative corrections do have a statistically larger impact, neither correction is significant enough to be observed yet.

The future generations of single and double beta decay experiments have many exciting prospects in their attempts to measure the neutrino mass and search for neutrinoless double beta decay. The high levels of statistics required offer a precise measurement of the spectrum which can be utilised in the search for new physics. Detailed understanding of both the single and double beta decay spectra will prove essential for seeking out unexpected signatures. As well as the conventional attempts to measure the energy spectrum, I hope I have shown here the great potential there can be from attempting to polarise the nuclei involved and perform angular measurements of the emitted electrons. Not only can these improve the sensitivity to processes and resolve degeneracies between them, it also adds new windows to the observation of certain effects. Overall, what can be said for certain is that in the years to come neutrino based experiments will continue to play a significant role in the continued search for new physics beyond the Standard Model.

Appendix A

Analytic Expressions for Exotic Currents in Single Beta Decay

The β-decay rate can be generally written in the form

$$\frac{d\Gamma}{dE_e d\Omega_e} = a(E_e) + b(E_e)\cos\theta_e \qquad (A.1)$$

If two effective operators $\mathcal{O}_X$, $\mathcal{O}_Y$ contribute to the decay for a given neutrino mass eigenstate, the transition matrix element may be composed as

$$M = \varepsilon_X M_X + \varepsilon_Y M_Y, \qquad (A.2)$$

where M_X and M_Y are the individual matrix elements and ε_X, ε_Y are the associated effective coupling constants. The terms in the differential decay rate Eq. (A.1) can then be written as

$$a(E_e) = |\varepsilon_X|^2 a_X(E_e) + \text{Re}(\varepsilon_X \varepsilon_Y^*) a_{X,Y}(E_e) + |\varepsilon_Y|^2 a_Y(E_e), \qquad (A.3)$$

$$b(E_e) = |\varepsilon_X|^2 b_X(E_e) + \text{Re}(\varepsilon_X \varepsilon_Y^*) b_{X,Y}(E_e) + |\varepsilon_Y|^2 b_Y(E_e). \qquad (A.4)$$

Most importantly, as the SM contribution with both left-handed lepton and quark vector currents is always present, we consider its interference with an exotic operator. Thus, $X = LL$, $\varepsilon_X = 1$ (for a single active neutrino) and Y is one of the exotic operators.

Below are presented the exact expressions for some of these terms. I concentrate on the individual contribution of each operator and the interference of exotic operators with that in the SM. The expressions are written in terms of a single generic neutrino mass eigenstate ν with mass m_ν, which can be either one of the active neutrinos, $\nu_{1,2,3}$, or a sterile neutrino ν_N. In the latter case, there is no interference with any contributions from active neutrinos. For simplification, we define

$$\widetilde{C}(E_e) = \frac{1}{4\pi} \frac{G_F^2 |V_{ud}|^2}{2\pi^3} C(E_e) \Theta(E_e^{\text{max}} - E_e - m_\nu),$$

$$m_{12}^2 = (p_{\text{H}} - p_e)^2 = m_{\text{H}}^2 - 2m_{\text{H}} E_e + m_e^2,$$

$$|\vec{p}_e| = \sqrt{E_e^2 - m_e^2},$$

$$\mu = (m_\nu + m_{\text{He}})/m_{\text{H}},$$

$$y = E_e^{\text{max}} - E_e,$$

$$\widetilde{y} = \sqrt{y \left(y + m_\nu \frac{2m_{\text{He}}}{m_{\text{H}}} \right)}$$

$$\alpha = m_{\text{H}} E_e^{\text{max}} + m_\nu^2 + m_{\text{He}} m_\nu. \tag{A.5}$$

A.1 Individual SM and Exotic Contributions

Here I give the electron energy dependent expressions for the purely exotic terms. Some of these terms can be related to each other through either $\gamma^5 \to -\gamma^5$ (which has no impact upon the final expression as only even multiples contribute) and/or $g_A \to -g_A$. For the angular expressions any relation of $\gamma^5 \to -\gamma^5$ must also come with $S \to -S$ to ensure the spin-up state is still the one being projected out.

Vector Currents *LL*, *RR*, *RL*, *LR*

The SM contribution (*LL*) is related to that of $\widetilde{\varepsilon}_R$ (*RR*) by using $\gamma_5 \to -\gamma_5$ (and

$S \rightarrow -S$). This has the same energy distribution and reverse angular correlation,

$$a_{LL}(E_e) = a_{RR}(E_e)$$

$$= \widetilde{C}(E_e) \frac{m_H^2 |\vec{p}_e|}{m_{12}^2} \widetilde{y}$$

$$\times \left\{ (g_V + g_A)^2 \left[\frac{m_H(m_H - E_e)}{m_{12}^2} \frac{m_H E_e - m_e^2}{m_{12}^2} (y + \mu m_\nu)(y + \mu m_{He}) - \frac{m_H^2 |\vec{p}_e|^2}{3m_{12}^4} \widetilde{y}^2 \right] \right.$$

$$\left. + (g_V - g_A)^2 E_e \left(y + m_\nu \frac{m_{He}}{m_H} \right) + (g_A^2 - g_V^2) m_{He} \frac{m_H E_e - m_e^2}{m_{12}^2} (y + \mu m_\nu) \right\},$$

$$\tag{A.6}$$

$$b_{LL}(E_e) = -b_{RR}(E_e)$$

$$= -\widetilde{C}(E_e) \frac{m_H}{m_{12}^2} |\vec{p}_e|^2 \widetilde{y}$$

$$\times \left\{ \left[(g_A - g_V)^2 m_H + (g_A^2 - g_V^2) m_{He} \frac{m_H(m_H - E_e)}{m_{12}^2} \right. \right.$$

$$+ (g_A^2 - g_V^2) \frac{m_H m_{He}}{m_{12}^2} E_e + (g_A + g_V)^2 \frac{m_H}{m_{12}^2} (\alpha - m_e^2)$$

$$\left. - (g_A + g_V)^2 \frac{m_H^2}{m_{12}^2} (y + \mu m_\nu) \frac{m_H(m_H - E_e)}{m_{12}^2} \right] (y + \mu m_\nu)$$

$$\left. - (g_A - g_V)^2 m_\nu^2 - \frac{1}{3} (g_A + g_V)^2 \frac{m_H^3(m_H - E_e)}{m_{12}^4} \widetilde{y}^2 \right\}.$$

$$\tag{A.7}$$

The contributions related to $\tilde{\varepsilon}_L$ (LR) and ε_R (RL) can be obtained from the SM (LL) terms by applying $g_A \rightarrow -g_A$ with an additional $S \rightarrow -S$ for the right-handed lepton term,

$$a_{LR}(E_e) = a_{RL}(E_e) = a_{LL}(E_e)(g_A \rightarrow -g_A), \tag{A.8}$$

$$b_{LR}(E_e) = -b_{RL}(E_e) = -b_{LL}(E_e)(g_A \rightarrow -g_A). \tag{A.9}$$

This makes a negligible difference in form.

Scalar Currents

$$a_S(E_e) = a_{\tilde{S}}(E_e) = \frac{1}{2}g_S^2 \widetilde{C}(E_e) \frac{m_{\rm H}^2 |\vec{p}_e|}{m_{12}^2} \widetilde{y}$$

$$\times \left\{ (m_{\rm He} + m_{\rm H} - E_e) \frac{m_{\rm H} E_e - m_e^2}{m_{12}^2} (y + \mu m_\nu) - \frac{1}{3} \frac{m_{\rm H}^2 |\vec{p}_e|^2}{m_{12}^4} \widetilde{y}^2 \right.$$

$$\left. - \frac{m_{\rm H}(m_{\rm H} - E_e)}{m_{12}^2} \frac{m_{\rm H} E_e - m_e^2}{m_{12}^2} (y + \mu m_\nu)^2 \right\}, \tag{A.10}$$

$$b_S(E_e) = b_{\tilde{S}}(E_e) = 0. \tag{A.11}$$

Pseudoscalar Currents

$$a_P(E_e) = a_{\tilde{P}}(E_e) = \frac{1}{2}g_P^2 \widetilde{C}(E_e) \frac{m_{\rm H}^2 |\vec{p}_e|}{m_{12}^2} \widetilde{y}$$

$$\times \left\{ -(m_{\rm He} - m_{\rm H} + E_e) \frac{m_{\rm H} E_e - m_e^2}{m_{12}^2} (y + \mu m_\nu) - \frac{1}{3} \frac{m_{\rm H}^2 |\vec{p}_e|^2}{m_{12}^4} \widetilde{y}^2 \right.$$

$$\left. - \frac{m_{\rm H}(m_{\rm H} - E_e)}{m_{12}^2} \frac{m_{\rm H} E_e - m_e^2}{m_{12}^2} (y + \mu m_\nu)^2 \right\}, \tag{A.12}$$

$$b_P(E_e) = b_{\tilde{P}}(E_e) = 0. \tag{A.13}$$

Tensor Currents

$$a_T(E_e) = a_{\tilde{T}}(E_e) =$$

$$= 16\widetilde{C}(E_e)g_T^2 \frac{m_{\rm H}^2 |\vec{p}_e|}{m_{12}^2} \widetilde{y} \left[\frac{m_{\rm H}(m_{\rm H} - E_e)}{m_{12}^2} \frac{m_{\rm H} E_e - m_e^2}{m_{12}^2} (y + \mu m_\nu)(3y + 2\mu m_{\rm He} + \mu m_\nu) \right.$$

$$\left. - \frac{1}{3} \frac{m_{\rm H}^2 |\vec{p}_e|^2}{m_{12}^4} \widetilde{y}^2 + 2E_e \left(y + m_\nu \frac{m_{\rm He}}{m_{\rm H}} \right) - 2(m_{\rm H} - E_e)(y + \mu m_\nu) \frac{m_{\rm H} E_e - m_e^2}{m_{12}^2} \right], \tag{A.14}$$

$$b_T(E_e) = -b_{\tilde{T}}(E_e)$$

$$= 16\widetilde{C}(E_e)g_T^2 \frac{m_{\rm H}^2}{m_{12}^2} |\vec{p}_e|^2 \widetilde{y} \left[\frac{1}{3} \frac{m_{\rm H}(m_{\rm H} - E_e)}{m_{12}^2} \frac{m_{\rm H} |\vec{p}_e|}{m_{12}^2} \widetilde{y} \right.$$

$$\left. + \left(2 + \frac{m_{\rm H} E_e - m_e^2}{m_{12}^4} m_{\rm H}(y + \mu m_\nu) - \frac{m_{\rm H} E_e}{m_{12}^2} - \frac{2m_\nu^2}{m_{\rm H} |\vec{p}_e|} \right) (y + \mu m_\nu) \right]. \tag{A.15}$$

A.2 Interference Terms

Here I give the interference terms between the Standard Model current (here labelled as *LL* because it has a left-handed vector-axial hadronic current and left-handed vector-axial leptonic current). These terms cannot be related to each other as before because the Standard Model term is fixed as *LL*.

Vector Currents: (LL) **with** (LR)

$$a_{LL,LR}(E_e) = \widetilde{C}(E_e) m_e m_\nu \frac{m_H |\vec{p}_e|}{m_{12}^2} \widetilde{y} \left[2(g_A^2 - g_V^2) m_{He} + (g_A^2 + g_V^2)(m_H - E_e) \right.$$

$$\left. - (g_A^2 + g_V^2) \frac{m_H(m_H - E_e)}{m_{12}^2}(y + \mu m_\nu) \right], \tag{A.16}$$

$$b_{LL,LR}(E_e) = -\widetilde{C}(E_e) g_A g_V m_e m_\nu |\vec{p}_e|^2 \frac{m_H}{m_{12}^2} \widetilde{y} \left[1 - \frac{m_H}{m_{12}^2}(y + \mu m_\nu) \right]. \tag{A.17}$$

Vector Currents: (LL) **with** (RL)

$$a_{LL,RL}(E_e) = -\widetilde{C}(E_e) \frac{m_H |\vec{p}_e|}{m_{12}^2} \widetilde{y}$$

$$\times \left\{ (g_A^2 - g_V^2) \left[\frac{m_H(m_H - E_e)}{m_{12}^2} \frac{m_H E_e - m_e^2}{m_{12}^2}(y + \mu m_\nu)(y + \mu m_{He}) - \frac{m_H^2 |\vec{p}_e|^2}{3 m_{12}^4} \widetilde{y}^2 \right] \right.$$

$$\left. + (g_A^2 - g_V^2) E_e \left(y m_\nu \frac{m_{He}}{m_H} \right) + (g_A^2 + g_V^2) m_{He} \left(\frac{m_H E_e - m_e^2}{m_{12}^2}(y + \mu m_\nu) \right) \right\}, \tag{A.18}$$

$$b_{LL,RL}(E_e) = -\widetilde{C}(E_e) \frac{m_H}{m_{12}^2} |\vec{p}_e|^2 \widetilde{y}$$

$$\times \left\{ \left[(g_A^2 - g_V^2) m_H + (g_A^2 + g_V^2) m_{He} \frac{m_H(m_H - E_e)}{m_{12}^2} + (g_A^2 + g_V^2) \frac{m_H m_{He}}{m_{12}^2} E_e \right. \right.$$

$$\left. + (g_A^2 - g_V^2) \frac{m_H}{m_{12}^2}(\alpha - m_e^2) - (g_A^2 - g_V^2) \frac{m_H^2}{m_{12}^2}(y + \mu m_\nu) \frac{m_H(m_H - E_e)}{m_{12}^2} \right] (y + \mu m_\nu)$$

$$\left. - (g_A^2 - g_V^2) m_\nu^2 - \frac{1}{3}(g_A^2 - g_V^2) \frac{m_H^3(m_H - E_e)}{m_{12}^4} \widetilde{y}^2 \right\}. \tag{A.19}$$

Vector Currents: (LL) **with** (RR)

$$a_{LL,RR}(E_e) = -\widetilde{C}(E_e) m_e m_\nu \frac{m_H^2 |\vec{p}_e|}{m_{12}^2} \widetilde{y} \left[(2(g_A^2 + g_V^2) m_{He} + (g_A^2 - g_V^2)(m_H - E_e) \right.$$
$$\left. - (g_A^2 - g_V^2) \frac{m_H(m_H - E_e)}{m_{12}^2} (y + \mu m_\nu) \right],$$

(A.20)

$$b_{LL,RR}(E_e) = 0.$$

(A.21)

LL with Left-handed Scalar Current

$$a_{LL,S}(E_e) = \widetilde{C}(E_e) g_S g_V m_e \frac{m_H |\vec{p}_e|}{m_{12}^2} \widetilde{y}$$
$$\times \left[m_H \left(1 + \frac{m_{He}(m_H - E_e)}{m_{12}^2} \right) (y + \mu m_\nu) - m_\nu^2 \right],$$

(A.22)

$$b_{LL,S}(E_e) = -\widetilde{C}(E_e) g_S g_A m_e m_{He} \frac{m_H^2}{m_{12}^2} \frac{|\vec{p}_e|^2}{m_{12}^2} \widetilde{y}(y + \mu m_\nu).$$

(A.23)

LL with Right-handed Scalar Current

$$a_{LL,\tilde{s}}(E_e) = -\widetilde{C}(E_e) g_S g_V m_\nu \frac{m_H |\vec{p}_e|}{m_{12}^2} \widetilde{y}$$
$$\times \left[(m_H + m_{He}) E_e - m_e^2 - m_H \frac{m_H E_e - m_e^2}{m_{12}^2} (y + \mu m_\nu) \right],$$

(A.24)

$$b_{LL,\tilde{s}}(E_e) = -\widetilde{C}(E_e) g_S g_A m_\nu M \frac{|\vec{p}_e|^2}{m_{12}^2} \widetilde{y} \left[\frac{m_H^2}{m_{12}^2} (y + \mu m_\nu) - (m_H + m_{He}) \right].$$

(A.25)

LL with Left-handed Pseudoscalar Current

$$a_{LL,P}(E_e) = \widetilde{C}(E_e) g_P g_A m_e \frac{m_H |\vec{p}_e|}{m_{12}^2} \widetilde{y}$$
$$\times \left[m_H \left(\frac{m_{He}(m_H - E_e)}{m_{12}^2} - 1 \right) (y + \mu m_\nu) + m_\nu^2 \right],$$

(A.26)

$$b_{LL,P}(E_e) = -\widetilde{C}(E_e) g_P g_V m_e m_{He} \frac{m_H^2}{m_{12}^2} \frac{|\vec{p}_e|^2}{m_{12}^2} \widetilde{y}(y + \mu m_\nu).$$

(A.27)

LL with Right-handed Pseudoscalar Current

$$a_{LL,\tilde{P}}(E_e) = \widetilde{C}(E_e) g_P g_A m_\nu \frac{m_H |\vec{p}_e|}{m_{12}^2} \widetilde{y}$$

$$\times \left[(m_H - m_{He}) E_e - m_e^2 - m_H \frac{m_{He} E_e - m_e^2}{m_{12}^2} (y + \mu m_\nu) \right], \qquad \text{(A.28)}$$

$$b_{LL,\tilde{P}}(E_e) = \widetilde{C}(E_e) g_P g_V m_\nu m_H \frac{|\vec{p}_e|^2}{m_{12}^2} \widetilde{y} \left[\frac{m_H^2}{m_{12}^2} (y + \mu m_\nu) - (m_H - m_{He}) \right]. \quad \text{(A.29)}$$

LL with Left-handed Tensor Current

$$a_{LL,T}(E_e) = -12 \widetilde{C}(E_e) g_T m_e \frac{m_H |\vec{p}_e|}{m_{12}^2} \widetilde{y}$$

$$\times \left[m_H \left((g_A + g_V) \frac{m_{He}(m_H - E_e)}{m_{12}^2} + (g_A - g_V) \right) (y + \mu m_\nu) - (g_A - g_V) m_\nu^2 \right],$$

$$\text{(A.30)}$$

$$b_{LL,T}(E_e) = 12 \widetilde{C}(E_e) g_T (g_A + g_V) m_e m_{He} \frac{m_H^2}{m_{12}^2} \frac{|\vec{p}_e|^2}{m_{12}^2} \widetilde{y}(y + \mu m_\nu). \qquad \text{(A.31)}$$

LL with Right-handed Tensor Current

$$a_{LL,\tilde{T}}(E_e) = 12 \widetilde{C}(E_e) g_T m_\nu \frac{m_H |\vec{p}_e|}{m_{12}^2} \widetilde{y}$$

$$\times \left[(g_A + g_V) \left(m_H E_e - m_e^2 - m_H \frac{m_H E_e - m_e^2}{m_{12}^2} (y + \mu m_\nu) \right) + (g_A - g_V) m_{He} E_e \right],$$

$$\text{(A.32)}$$

$$b_{LL,\tilde{T}}(E_e) = 4 \widetilde{C}(E_e) g_T m_\nu m_H \frac{|\vec{p}_e|^2}{m_{12}^2} \widetilde{y}$$

$$\times \left[3(g_A - g_V) m_{He} + (g_A + g_V) m_H - (g_A + g_V) \frac{m_H^2}{m_{12}^2} (y + \mu m_\nu) \right]. \quad \text{(A.33)}$$

Appendix B

Lorentz Violating Interaction Matrix

Here are the terms linear in the parameter $\chi^{\mu\nu}$ (defined in Section 6.1) which contribute to the Lorentz violating interaction. This is split into spin independent and dependent terms $|M|^2 = |M_0|^2 + |M_s|^2$

$$
\begin{aligned}
|M_0|^2 = \Lambda\big(& g_A^2 (P_{\mathrm{H}} \cdot P_\nu \, P_e \cdot P_{\mathrm{He}} + P_{\mathrm{H}} \cdot P_e \, P_{\mathrm{He}} \cdot P_\nu + m_{\mathrm{H}} m_{\mathrm{He}} P_e \cdot P_\nu \\
& + P_{\mathrm{He}} \cdot P_\nu \, P_{\mathrm{H}}^\mu \, P_e^\sigma \, \chi_{\mu\sigma}^r - P_e \cdot P_\nu \, P_{\mathrm{H}}^\mu \, P_{\mathrm{He}}^\sigma \, \chi_{\mu\sigma}^r \\
& + P_{\mathrm{He}} \cdot P_e \, P_{\mathrm{H}}^\mu \, P_\nu^\sigma \, \chi_{\mu\sigma}^r - P_{\mathrm{He}} \cdot P_{\mathrm{H}} \, P_e^\mu \, P_\nu^\sigma \, \chi_{\mu\sigma}^r \\
& + P_{\mathrm{He}} \cdot P_{\mathrm{H}} \, P_\nu^\mu \, P_e^\sigma \, \chi_{\mu\sigma}^r - P_e \cdot P_\nu \, P_{\mathrm{He}}^\mu \, P_{\mathrm{H}}^\sigma \, \chi_{\mu\sigma}^r \\
& + P_{\mathrm{H}} \cdot P_\nu \, P_{\mathrm{He}}^\mu \, P_e^\sigma \, \chi_{\mu\sigma}^r + P_{\mathrm{H}} \cdot P_e \, P_{\mathrm{He}}^\mu \, P_\nu^\sigma \, \chi_{\mu\sigma}^r \\
& - m_{\mathrm{H}} m_{\mathrm{He}} \, P_\nu^\mu \, P_e^\sigma \, \chi_{\mu\sigma}^r - m_{\mathrm{H}} m_{\mathrm{He}} \, P_e^\mu \, P_\nu^\sigma \, \chi_{\mu\sigma}^r \\
& + m_{\mathrm{H}} m_{\mathrm{He}} \, \chi^{i\mu\sigma} \, P_e^\lambda \, P_\nu^\rho \, \varepsilon_{\mu\sigma\lambda\rho} + P_{\mathrm{H}} \cdot P_{\mathrm{He}} \, \chi^{i\mu\sigma} \, P_e^\lambda \, P_\nu^\rho \, \varepsilon_{\mu\sigma\lambda\rho} \\
& + P_{\mathrm{He}\mu} \, \chi^{i\mu\sigma} \, P_{\mathrm{H}}^\lambda \, P_e^\alpha \, P_\nu^\rho \, \varepsilon_{\sigma\lambda\alpha\rho} - P_{\mathrm{H}\mu} \, \chi^{i\mu\sigma} \, P_{\mathrm{He}}^\lambda \, P_e^\alpha \, P_\nu^\rho \, \varepsilon_{\sigma\lambda\alpha\rho}) \\
& + g_V^2 (\text{as above with } m_{\mathrm{He}} \to -m_{\mathrm{He}}) \\
& + 2g_A g_V (P_{\mathrm{H}} \cdot P_\nu \, P_e \cdot P_{\mathrm{He}} - P_{\mathrm{H}} \cdot P_e \, P_{\mathrm{He}} \cdot P_\nu \\
& + P_{\mathrm{He}} \cdot P_\nu \, P_e^\mu \, P_{\mathrm{H}}^\sigma \, \chi_{\mu\sigma}^r - P_{\mathrm{H}} \cdot P_\nu \, P_e^\mu \, P_{\mathrm{He}}^\sigma \, \chi_{\mu\sigma}^r \\
& - P_{\mathrm{He}} \cdot P_e \, P_\nu^\mu \, P_{\mathrm{H}}^\sigma \, \chi_{\mu\sigma}^r + P_{\mathrm{H}} \cdot P_e \, P_\nu^\mu \, P_{\mathrm{He}}^\sigma \, \chi_{\mu\sigma}^r \\
& + P_e \cdot P_\nu \, \chi^{i\mu\sigma} \, P_{\mathrm{H}}^\lambda \, P_{\mathrm{He}}^\rho \, \varepsilon_{\mu\sigma\lambda\rho} \\
& + P_{\nu\sigma} \, \chi^{i\mu\sigma} \, P_{\mathrm{H}}^\lambda \, P_e^\alpha \, P_{\mathrm{He}}^\rho \, \varepsilon_{\mu\lambda\alpha\sigma} + P_{e\sigma} \, \chi^{i\mu\sigma} \, P_{\mathrm{H}}^\lambda \, P_\nu^\alpha \, P_{\mathrm{He}}^\rho \, \varepsilon_{\mu\lambda\alpha\sigma}) \big),
\end{aligned}
$$

$$(\text{B.1})$$

$$
\begin{aligned}
|M_s|^2 = \Lambda\big(g_A^2 \big(&m_{\text{He}}P_{\text{H}} \cdot P_\nu \, P_e \cdot S + m_{\text{H}}P_{\text{He}} \cdot P_\nu \, P_e \cdot S \\
&- m_{\text{He}}P_{\text{H}} \cdot P_e \, P_\nu \cdot S + m_{\text{H}}P_{\text{He}} \cdot P_e \, P_\nu \cdot S \\
&+ m_{\text{He}}P_\nu \cdot S \, P_e^\mu \, P_{\text{H}}^\sigma \, \chi_{\mu\sigma}^r + m_{\text{H}}P_\nu \cdot S \, P_e^\mu \, P_{\text{He}}^\sigma \, \chi_{\mu\sigma}^r \\
&- m_{\text{He}}P_{\text{H}} \cdot P_\nu \, P_e^\mu S^\sigma \chi_{\mu\sigma}^r - m_{\text{H}}P_{\text{He}} \cdot P_\nu \, P_e^\mu S^\sigma \chi_{\mu\sigma}^r \\
&- m_{\text{He}}P_e \cdot S \, P_\nu^\mu \, P_{\text{H}}^\sigma \, \chi_{\mu\sigma}^r - m_{\text{H}}P_e \cdot S \, P_\nu^\mu \, P_{\text{He}}^\sigma \, \chi_{\mu\sigma}^r \\
&+ m_{\text{He}}P_{\text{H}} \cdot P_e \, P_\nu^\mu \, S^\sigma \, \chi_{\mu\sigma}^r + m_{\text{H}}P_{\text{He}} \cdot P_e \, P_\nu^\mu \, S^\sigma \, \chi_{\mu\sigma}^r \\
&+ m_{\text{He}}P_e \cdot P_\nu \, \chi^{i\mu\sigma} \, P_{\text{H}}^\lambda \, S^\rho \, \varepsilon_{\mu\sigma\lambda\rho} + m_{\text{H}}P_e \cdot P_\nu \, \chi^{i\mu\sigma} \, P_{\text{He}}^\lambda \, S^\rho \, \varepsilon_{\mu\sigma\lambda\rho} \\
&+ m_{\text{He}}P_{\nu\sigma} \, \chi^{i\mu\sigma} \, P_{\text{H}}^\lambda \, P_e^\alpha \, S^\rho \, \varepsilon_{\mu\lambda\alpha\rho} + m_{\text{He}}P_{e\sigma} \, \chi^{i\mu\sigma} \, P_{\text{H}}^\lambda \, P_\nu^\alpha \, S^\rho \, \varepsilon_{\mu\lambda\alpha\rho} \\
&- m_{\text{H}}P_{\nu\sigma} \, \chi^{i\mu\sigma} \, P_e^\lambda \, P_{\text{He}}^\alpha \, S^\rho \, \varepsilon_{\mu\lambda\alpha\rho} - m_{\text{H}}P_{e\sigma} \, \chi^{i\mu\sigma} \, P_\nu^\lambda \, P_{\text{He}}^\alpha \, S^\rho \, \varepsilon_{\mu\lambda\alpha\rho}\big) \\
+ g_V^2 &(\text{as above with } m_{\text{He}} \to -m_{\text{He}}) \\
+ 2g_A g_V \big(&- m_{\text{H}}P_{\text{He}} \cdot P_\nu \, P_e \cdot S - m_{\text{H}}P_{\text{He}} \cdot P_e \, P_\nu \cdot S \\
&+ m_{\text{H}}P_{\text{He}} \cdot S P_e^\mu \, P_\nu^\sigma \chi_{\mu\sigma}^r + m_{\text{H}}P_{\text{He}} \cdot S P_\nu^\mu \, P_e^\sigma \chi_{\mu\sigma}^r \\
&- m_{\text{H}}P_\nu \cdot S \, P_{\text{He}}^\mu \, P_e^\sigma \chi_{\mu\sigma}^r - m_{\text{H}}P_e \cdot S \, P_{\text{He}}^\mu \, P_\nu^\sigma \chi_{\mu\sigma}^r \\
&+ m_{\text{H}}P_e \cdot P_\nu \, P_{\text{He}}^\mu \, S^\sigma \, \chi_{\mu\sigma}^r + m_{\text{H}}P_e \cdot P_\nu \, S^\mu \, P_{\text{He}}^\sigma \, \chi_{\mu\sigma}^r \\
&- m_{\text{H}}P_{\text{He}} \cdot P_\nu \, S^\mu \, P_e^\sigma \, \chi_{\mu\sigma}^r - m_{\text{H}}P_{\text{He}} \cdot P_e \, S^\mu \, P_\nu^\sigma \, \chi_{\mu\sigma}^r \\
&+ m_{\text{H}}P_{\text{He}} \cdot S \chi^{i\mu\sigma} \, P_e^\lambda \, P_\nu^\rho \, \varepsilon_{\mu\sigma\lambda\rho} \\
&- m_{\text{H}}S_\mu \chi^{i\mu\sigma} \, P_e^\lambda \, P_\nu^\alpha \, P_{\text{He}}^\rho \, \varepsilon_{\sigma\lambda\alpha\rho} - m_{\text{H}}P_{\text{He}\mu} \chi^{i\mu\sigma} \, P_e^\lambda \, P_\nu^\alpha \, S^\rho \, \varepsilon_{\sigma\lambda\alpha\rho}\big)\big),
\end{aligned}
$$

$$(\text{B.2})$$

where $\Lambda = 16 G_F^2 |V_{ud}|^2$ and ε is the standard Levi-Civita tensor. The terms χ^r and χ^i are the real and imaginary parts of χ, respectively.

Appendix C

Radiative Corrections in Double Beta Decay: Endpoint Dependence

In Section 7.1 it was shown that the primary variation in the impact of the radiative corrections between different nuclei is due to their different endpoints, the maximum kinetic energy available to the emitted electrons. In this Appendix I explore in greater detail the mathematical cause for and interesting dependence upon the endpoint energy. In Fig. C.1 the proportional deviation in the rate can be seen for a range
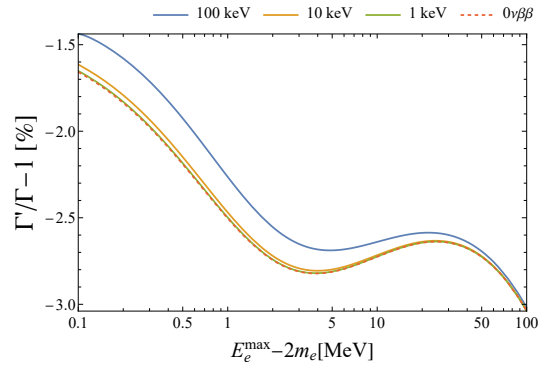
Figure C.1: Proportional variation in the rate for various ROI below the endpoint as a function of endpoint value E_0 (calculated for $Z = 50$).

of regions in the $2\nu\beta\beta$ spectrum and for the delta peak of $0\nu\beta\beta$ as a function of the endpoint energy. This has an interesting behaviour with the deviation largely growing in magnitude with the value of the endpoint apart from a bump for an endpoint of the order of 10 MeV. To understand this bump it is necessary to consider the decay spectra being modified and the behaviour of G with variations in the endpoint.

The decay spectra as a function of individual electron energy for $2\nu\beta\beta$ and $0\nu\beta\beta$ are given in Fig. C.2. As can be seen, in both the $0\nu\beta\beta$ and the windowed $2\nu\beta\beta$ cases the spectrum peaks at half the endpoint energy. This is to be expected

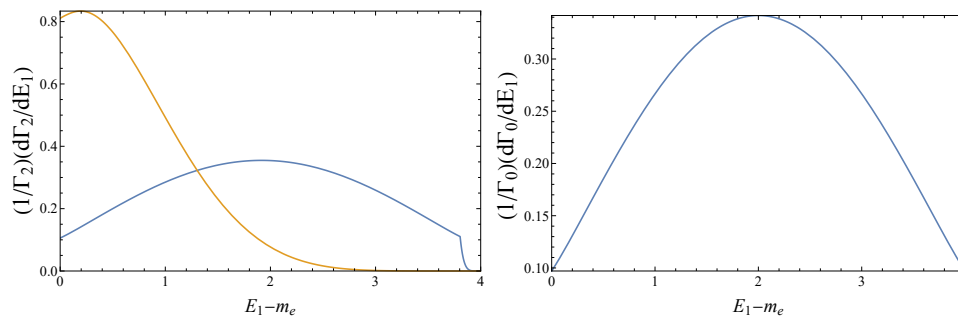**Figure C.2:** Fractional partial decay spectra for $2\nu\beta\beta$ (left) and $0\nu\beta\beta$ (right). For $2\nu\beta\beta$ the spectrum has been evaluated by integrating over the entire range of total energies (orange) and for a total energy within a 100 keV window of the endpoint (blue) (calculated for $Z = 50$).

given the symmetry between the two electrons and that in both these cases the total energy is required to be equal (or nearly equal) to the maximal value. Thus the individual electrons are most likely to have half the maximum kinetic energy. This means that these spectra are more sensitive to corrections near the midpoint of the spectrum than at the extremes. Conversely, the $2\nu\beta\beta$ spectrum for total energy across the entire range peaks nearly at 0, meaning this spectrum will be most sensitive to reductions at low energies.

Figure C.3 shows the variations in a single G factor (left) and a product of G factors, as appears in Eqs. (7.2) and (7.3) for double beta decay, (right) . For this second plot, the sum of the energies for each factor is equal to the endpoint value as happens exactly for $0\nu\beta\beta$ and approximately when looking at the endpoint window for $2\nu\beta\beta$. These figures are plotted as functions of the fraction of the total available kinetic energy taken by the electron so that different endpoint values can be compared equivalently. For the individual G factor, increasing the endpoint leads to a decrease at higher energies and an increase for lower energies. For the product of G factors, as the endpoint value is increased the middle part of the spectrum is diminished whilst the higher and lower energy parts are increased. This is because for the individual G the increase in the lower energy part is greater than the decrease in the higher energy part, overall making the extremes of the product of two G factors increase. However, the point at which the individual G begins decreasing is at less
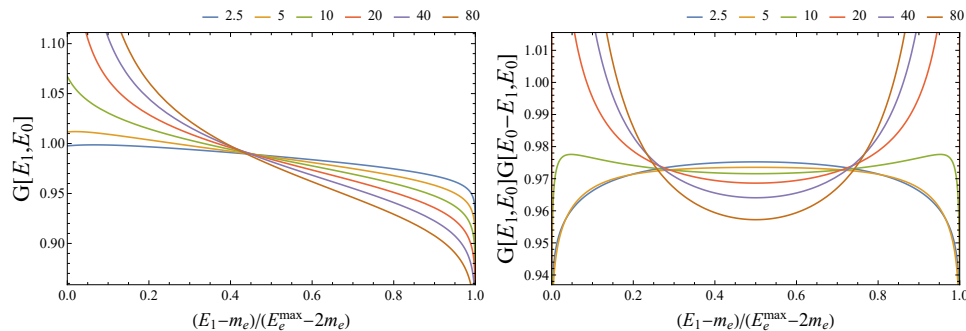
Figure C.3: Plots showing the behaviour of the correction factor G (left) and the product of two G factors (right) as a function of the ratio of the individual kinetic energy to the maximum kinetic energy available for a range of maximum energies (calculated for $Z = 50$). For the product of Gs the sum of the energies between them equals the total energy.

than half the endpoint; the region around the midpoint for the product of G factors has greater contributions from the decreasing part of the individual spectrum than from the increasing part. Overall, this behaviour informs the variations in the proportional difference as a function of the endpoint. As explained before, corrections to the central part of the spectrum are more significant than those at the endpoint when the total energy is near the maximum, leading in general to a greater decrease for larger endpoints. However, when going from endpoints of around 2.5 MeV to 20 MeV the increase in the lower and higher parts of the spectrum are of significantly larger magnitude as to outweigh the decrease in the central region leading to an overall decrease in the magnitude of the correction to the double beta spectrum. This is what leads to the bump around 10 MeV in Fig. C.1 It is this complex behaviour that leads to the dependence upon the choice of region of interest.

Appendix D

KamLAND-ZEN Uncertainty Data

In Section 7.2.4 I used data taken from [203] to calculate the sensitivity to the mutual electron repulsion. This is calculated using the proportional uncertainties in the spectrum for each of 27 bins across the spectrum. The data is as follows:

Energy [MeV]	Uncertainty [%]	Energy [MeV]	Uncertainty [%]
0.80-0.85	2.0	1.5-1.55	3.7
0.85-0.90	2.1	1.55-1.60	4.3
0.90-0.95	2.3	1.60-1.65	4.7
0.95-1.00	2.2	1.65-1.70	5.1
1.00-1.05	2.2	1.70-1.75	5.7
1.05-1.10	2.3	1.75-1.80	6.5
1.10-1.15	2.4	1.80-1.85	7.5
1.15-1.20	2.5	1.85-1.90	8.8
1.20-1.25	2.6	1.90-1.95	10.4
1.25-1.30	3.0	1.95-2.00	12.0
1.30-1.35	2.9	2.00-2.05	15.1
1.35-1.40	3.0	2.05-2.10	17.9
1.40-1.45	3.1	2.10-2.15	22.1
1.45-1.50	3.5		

Table D.1: Experimental uncertainty in 27 bins over the energy range $E_T = 0.8 - 2.15$ MeV from KamLAND-Zen data.

Bibliography

[1] J. J. Thomson. Xl. cathode rays. *The London, Edinburgh, and Dublin Philosophical Magazine and Journal of Science*, 44(269):293–316, 1897.

[2] G. Aad et al. Observation of a new particle in the search for the standard model higgs boson with the atlas detector at the lhc. *Physics Letters B*, 716(1):1–29, 2012.

[3] S. Chatrchyan et al. Observation of a new boson at a mass of 125 gev with the cms experiment at the lhc. *Physics Letters B*, 716(1):30–61, 2012.

[4] W. Pauli. Dear radioactive ladies and gentlemen. *Phys. Today*, 31N9:27, 1978.

[5] E. Fermi. An attempt of a theory of beta radiation. 1. *Z. Phys.*, 88:161–177, 1934.

[6] F. Reines and C. L. Cowan. Detection of the free neutrino. *Phys. Rev.*, 92:830–831, Nov 1953.

[7] S. H. Neddermeyer and C. D. Anderson. Note on the nature of cosmic-ray particles. *Phys. Rev.*, 51:884–886, May 1937.

[8] M. L. Perl et al. Evidence for anomalous lepton production in $e^+ - e^-$ annihilation. *Phys. Rev. Lett.*, 35:1489–1492, Dec 1975.

[9] G. Danby et al. Observation of high-energy neutrino reactions and the existence of two kinds of neutrinos. *Phys. Rev. Lett.*, 9:36–44, Jul 1962.

[10] K. Kodama et al. Observation of tau neutrino interactions. *Physics Letters B*, 504(3):218–224, 2001.

[11] J. Beringer et al. Review of particle physics. *Phys. Rev. D*, 86:010001, Jul 2012.

[12] M. M. Ivanov et al. Cosmological parameters and neutrino masses from the final *planck* and full-shape boss data. *Phys. Rev. D*, 101:083504, Apr 2020.

[13] T. D. Lee and C. N. Yang. Parity nonconservation and a two-component theory of the neutrino. *Phys. Rev.*, 105:1671–1675, 3 1957.

[14] C. S. Wu et al. Experimental test of parity conservation in beta decay. *Phys. Rev.*, 105:1413–1415, 2 1957.

[15] R. P. Feynman and M. Gell-Mann. Theory of the fermi interaction. *Phys. Rev.*, 109:193–198, 1 1958.

[16] C. N. Yang and R. L. Mills. Conservation of isotopic spin and isotopic gauge invariance. *Phys. Rev.*, 96:191–195, Oct 1954.

[17] J. Schwinger. A theory of the fundamental interactions. *Annals of Physics*, 2(5):407–434, 1957.

[18] S. L. Glashow. Partial-symmetries of weak interactions. *Nuclear Physics*, 22(4):579–588, 1961.

[19] A. Salam and J. Ward. Electromagnetic and weak interactions. *Physics Letters*, 13(2):168–171, 1964.

[20] F. Englert and R. Brout. Broken symmetry and the mass of gauge vector mesons. *Phys. Rev. Lett.*, 13:321–323, Aug 1964.

[21] P. W. Higgs. Broken symmetries and the masses of gauge bosons. *Phys. Rev. Lett.*, 13:508–509, Oct 1964.

[22] G. S. Guralnik et al. Global conservation laws and massless particles. *Phys. Rev. Lett.*, 13:585–587, Nov 1964.

[23] S. Weinberg. A model of leptons. *Phys. Rev. Lett.*, 19:1264–1266, Nov 1967.

[24] A. Salam. Weak and Electromagnetic Interactions. *Conf. Proc. C*, 680519:367–377, 1968.

[25] C. M. G. LATTES et al. Observations on the tracks of slow mesons in photographic emulsions. *Nature*, 160(4066):453–456, 1947.

[26] G. D. ROCHESTERDr. and C. C. BUTLERDr. Evidence for the existence of new unstable elementary particles. *Nature*, 160(4077):855–857, 1947.

[27] M. Gell-Mann. The Eightfold Way: A Theory of strong interaction symmetry. *CTSL-20, TID-12608*, 3 1961.

[28] M. Gell-Mann. A Schematic Model of Baryons and Mesons. *Phys. Lett.*, 8:214–215, 1964.

[29] G. Zweig et al. *An SU(3) model for strong interaction symmetry and its breaking. Version 2*, pp. 22–101. Hadronic Press, 2 1964.

[30] F. Gross et al. 50 years of quantum chromodynamics. *The European Physical Journal C*, 83(12):1125, 2023.

[31] D. J. Gross and F. Wilczek. Ultraviolet behavior of non-abelian gauge theories. *Phys. Rev. Lett.*, 30:1343–1346, Jun 1973.

[32] H. D. Politzer. Reliable perturbative results for strong interactions? *Phys. Rev. Lett.*, 30:1346–1349, Jun 1973.

[33] G. Gabrielse et al. Towards an improved test of the standard model's most precise prediction. *Atoms*, 7(2), 2019.

[34] G. Arnison et al. Experimental Observation of Isolated Large Transverse Energy Electrons with Associated Missing Energy at $\sqrt{s} = 540$ GeV. *Phys. Lett. B*, 122:103–116, 1983.

[35] G. Arnison et al. Experimental Observation of Lepton Pairs of Invariant Mass Around 95-GeV/c^2 at the CERN SPS Collider. *Phys. Lett. B*, 126:398–410, 1983.

[36] R. T. D'Agnolo and D. Teresi. Sliding naturalness: New solution to the strong-cp and electroweak-hierarchy problems. *Phys. Rev. Lett.*, 128:021803, Jan 2022.

[37] R. N. Mohapatra. No axion solution to strong cp using parity and supersymmetry. *The European Physical Journal Special Topics*, 229(21):3229–3241, 2020.

[38] R. N. Cahn. The eighteen arbitrary parameters of the standard model in your everyday life. *Rev. Mod. Phys.*, 68:951–959, Jul 1996.

[39] D. P. Aguillard et al. Measurement of the positive muon anomalous magnetic moment to 0.20 ppm. *Phys. Rev. Lett.*, 131:161802, Oct 2023.

[40] R. Abbasi et al. Search for gev-scale dark matter annihilation in the sun with icecube deepcore. *Phys. Rev. D*, 105:062004, Mar 2022.

[41] D. O. Jones et al. Cosmological results from the raisin survey: Using type ia supernovae in the near infrared as a novel path to measure the dark energy equation of state. *The Astrophysical Journal*, 933(2):172, jul 2022.

[42] B. Pontecorvo. Neutrino experiments and the problem of conservation of leptonic charge. *Sov. Phys. JETP*, 26(984-988):165, 1968.

[43] Z. Maki et al. Remarks on the Unified Model of Elementary Particles. *Progress of Theoretical Physics*, 28(5):870–880, 11 1962.

[44] R. Davis et al. Search for neutrinos from the sun. *Phys. Rev. Lett.*, 20:1205–1209, May 1968.

[45] Y. Fukuda et al. Measurement of the flux and zenith-angle distribution of upward throughgoing muons by super-kamiokande. *Phys. Rev. Lett.*, 82:2644–2648, Mar 1999.

[46] Q. R. Ahmad et al. Direct evidence for neutrino flavor transformation from neutral-current interactions in the sudbury neutrino observatory. *Phys. Rev. Lett.*, 89:011301, Jun 2002.

[47] K. Eguchi et al. First results from kamland: Evidence for reactor antineutrino disappearance. *Phys. Rev. Lett.*, 90:021802, Jan 2003.

[48] P. F. de Salas et al. Neutrino mass ordering from oscillations and beyond: 2018 status and future prospects. *Frontiers in Astronomy and Space Sciences*, 5, 2018.

[49] V. A. Kostelecký and M. Mewes. Neutrinos with lorentz-violating operators of arbitrary dimension. *Phys. Rev. D*, 85:096005, May 2012.

[50] J. Lesgourgues and S. Pastor. Massive neutrinos and cosmology. *Physics Reports*, 429(6):307–379, 2006.

[51] Planck Collaboration et al. Planck 2018 results - vi. cosmological parameters. *A&A*, 641:A6, 2020.

[52] E. W. Otten and C. Weinheimer. Neutrino mass limit from tritium beta decay. *Rept. Prog. Phys.*, 71:086201, 2008.

[53] A. Faessler et al. Arbitrary mass majorana neutrinos in neutrinoless double beta decay. *Phys. Rev. D*, 90:096010, Nov 2014.

[54] M. Aker et al. Direct neutrino-mass measurement with sub-electronvolt sensitivity. *Nature Physics*, 18(2):160–166, 2022.

[55] W. C. Pettus. Overview of Project 8 and Progress Towards Tritium Operation. *J. Phys. Conf. Ser.*, 1342(1):012040, 2020.

[56] R. Saakyan. Determination of absolute neutrino mass using quantum technologies. *Talk at the UK HEP Forum 2020: Quantum leaps to the dark side, `https: // conference. ippp. dur. ac. uk/ event/ 934/ contributions/ 4944/`*, 2020.

[57] LEGEND Collaboration et al. LEGEND-1000 Preconceptual Design Report. *arXiv e-prints*, pp. arXiv:2107.11462, July 2021.

[58] R. Nakamura et al. Research and development toward KamLAND2-Zen. *J. Phys. Conf. Ser.*, 1468(1):012256, 2020.

[59] W. Pauli. Über den zusammenhang des abschlusses der elektronengruppen im atom mit der komplexstruktur der spektren. *Zeitschrift für Physik*, 31(1):765–783, 1925.

[60] N. Cabibbo. Unitary symmetry and leptonic decays. *Phys. Rev. Lett.*, 10:531–533, Jun 1963.

[61] M. Kobayashi and T. Maskawa. CP Violation in the Renormalizable Theory of Weak Interaction. *Prog. Theor. Phys.*, 49:652–657, 1973.

[62] R. L. Workman and Others. Review of Particle Physics. *PTEP*, 2022:083C01, 2022.

[63] A. Dar and G. Shaviv. Standard solar neutrinos. *Astrophys. J.*, 468:933–946, 1996.

[64] C. Giganti et al. Neutrino oscillations: The rise of the PMNS paradigm. *Prog. Part. Nucl. Phys.*, 98:1–54, 2018.

[65] R. L. W. et al. Neutrino masses, mixing, and oscillations. *Prog. Theor. Exp. Phys.*, 08 2022.

[66] K. Abe et al. Constraint on the matter-antimatter symmetry-violating phase in neutrino oscillations. *Nature*, 580(7803):339–344, 2020.

[67] A. Aguilar et al. Evidence for neutrino oscillations from the observation of $\overline{\nu}_e$ appearance in a $\overline{\nu}_\mu$ beam. *Phys. Rev. D*, 64:112007, Nov 2001.

[68] A. A. Aguilar-Arevalo et al. Improved search for $\overline{\nu}_\mu \rightarrow \overline{\nu}_e$ oscillations in the miniboone experiment. *Phys. Rev. Lett.*, 110:161801, Apr 2013.

[69] P. Abratenko et al. First constraints on light sterile neutrino oscillations from combined appearance and disappearance searches with the microboone detector. *Phys. Rev. Lett.*, 130:011801, Jan 2023.

[70] J. M. Hardin et al. New clues about light sterile neutrinos: preference for models with damping effects in global fits. *Journal of High Energy Physics*, 2023(9):58, 2023.

[71] G. Lanfranchi et al. The search for feebly interacting particles. *Annual Review of Nuclear and Particle Science*, 71(Volume 71, 2021):279–313, 2021.

[72] E. Bagnaschi et al. Smeft analysis of mw. *Journal of High Energy Physics*, 2022(8):308, 2022.

[73] W. Dekens and P. Stoffer. Low-energy effective field theory below the electroweak scale: matching at one loop. *Journal of High Energy Physics*, 2019(10):197, 2019.

[74] H. Liu et al. An eft hunter's guide to two-to-two scattering: Heft and smeft on-shell amplitudes. *Journal of High Energy Physics*, 2023(5):241, 2023.

[75] R. Lehnert. Beta-decay spectrum and lorentz violation. *Physics Letters B*, 828:137017, 2022.

[76] E. Majorana. Teoria simmetrica dell'elettrone e del positrone. *Il Nuovo Cimento (1924-1942)*, 14(4):171–184, 1937.

[77] M. Lindner et al. Seesaw mechanisms for dirac and majorana neutrino masses. *Phys. Rev. D*, 65:053014, Feb 2002.

[78] A. Boyarsky et al. Sterile neutrino dark matter. *Progress in Particle and Nuclear Physics*, 104:1–45, 2019.

[79] M. Dentler et al. Decaying sterile neutrinos and the short baseline oscillation anomalies. *Phys. Rev. D*, 101:115013, Jun 2020.

[80] G. Aad et al. Search for heavy neutral leptons in decays of w bosons produced in 13 tev pp collisions using prompt and displaced signatures with the atlas detector. *Journal of High Energy Physics*, 2019(10):265, 2019.

[81] E. Cortina Gil et al. Search for heavy neutral lepton production in k+ decays to positrons. *Physics Letters B*, 807:135599, 2020.

[82] J. A. L. Canning et al. Sensitivity of future tritium decay experiments to New Physics. *JHEP*, 03:144, 2023.

[83] P. O. Ludl and W. Rodejohann. Direct neutrino mass experiments and exotic charged current interactions. *Journal of High Energy Physics*, 2016(6):40, 2016.

[84] S. S. Masood et al. Exact relativistic β decay endpoint spectrum. *Phys. Rev. C*, 76:045501, Oct 2007.

[85] G. Audi et al. The ame2003 atomic mass evaluation: (ii). tables, graphs and references. *Nuclear Physics A*, 729(1):337–676, 2003. The 2003 NUBASE and Atomic Mass Evaluations.

[86] P. B. Pal. *An Introductory Course of Particle Physics*. CRC Press, 2014.

[87] Y. A. Akulov and B. A. Mamyrin. Determination of the ratio of the axial-vector to the vector coupling constant for weak interaction in triton beta decay. *Phys. Atom. Nucl.*, 65:1795–1797, 2002.

[88] T. Sumikama et al. Test of the Conserved Vector Current Hypothesis by beta-ray Angular Distribution Measurement in the Mass-8 System. *Phys. Rev. C*, 83:065501, 2011.

[89] F. Šimkovic et al. Exact relativistic tritium β-decay endpoint spectrum in a hadron model. *Phys. Rev. C*, 77:055502, May 2008.

[90] G.-y. Huang et al. Effective neutrino masses in katrin and future tritium beta-decay experiments. *Phys. Rev. D*, 101:016003, Jan 2020.

[91] R. Shrock. New tests for and bounds on neutrino masses and lepton mixing. *Physics Letters B*, 96(1):159–164, 1980.

[92] S. Mertens et al. Sensitivity of next-generation tritium beta-decay experiments for kev-scale sterile neutrinos. *Journal of Cosmology and Astroparticle Physics*, 2015(02):020, feb 2015.

[93] M. Kleesiek et al. β-decay spectrum, response function and statistical model for neutrino mass measurements with the katrin experiment. *The European Physical Journal C*, 79(3):204, 2019.

[94] M. Rose. *Relativistic Electron Theory*. Wiley, 1961.

[95] J. J. Simpson. Measurement of the β-energy spectrum of ^{3}H to determine the antineutrino mass. *Phys. Rev. D*, 23:649–662, Feb 1981.

[96] L. Hayen et al. High precision analytical description of the allowed β spectrum shape. *Rev. Mod. Phys.*, 90:015008, Mar 2018.

[97] H. Behrens and W. Bühring. *Electron radical wave functions and nuclear beta-decay / Heinrich Behrens, Wolfgang Bühring*. International series of monographs on physics. Clarendon, Oxford, 1982.

[98] D. Wilkinson. Analysis of neutron β-decay. *Nuclear Physics A*, 377(2):474–504, 1982.

[99] C. K. Hargrove et al. Measurement of the screening potential in ^{3}H β decay. *Phys. Rev. C*, 60:034608, Aug 1999.

[100] W. W. Repko and C.-E. Wu. Radiative corrections to the endpoint of the tritium beta decay spectrum. *Phys. Rev. C*, 28:2433–2436, 1983.

[101] R. D. Williams and S. E. Koonin. Atomic final-state interactions in tritium decay. *Phys. Rev. C*, 27:1815–1817, Apr 1983.

[102] M. Tanabashi et al. Review of particle physics. *Phys. Rev. D*, 98:030001, Aug 2018.

[103] W. C. Haxton. Atomic effects and heavy-neutrino emission in beta decay. *Phys. Rev. Lett.*, 55:807–809, Aug 1985.

[104] B. J. P. Jones. The Physics of Neutrinoless Double Beta Decay: A Beginners Guide. *PoS*, TASI2020:007, 2021.

[105] C. Augier et al. Measurement of the $2\nu\beta\beta$ Decay Rate and Spectral Shape of Mo100 from the CUPID-Mo Experiment. *Phys. Rev. Lett.*, 131(16):162501, 2023.

[106] M. Agostini et al. Probing the mechanism of neutrinoless double-beta decay in multiple isotopes. *Journal of High Energy Physics*, 2023(2):172, 2023.

[107] J. Engel and J. Menéndez. Status and future of nuclear matrix elements for neutrinoless double-beta decay: a review. *Reports on Progress in Physics*, 80(4):046301, mar 2017.

[108] F. Šimkovic et al. Relation between the $0\nu\beta\beta$ and $2\nu\beta\beta$ nuclear matrix elements reexamined. *Phys. Rev. C*, 83:015502, Jan 2011.

[109] R. A. Sen'kov and M. Horoi. Neutrinoless double-*beta* decay of ^{48}Ca in the shell model: Closure versus nonclosure approximation. *Phys. Rev. C*, 88(6):064312, 2013.

[110] M. Fukugita and T. T. Yanagida. *Physics of neutrinos : and applications to astrophysics / Masataka Fukugita, Tsutomu Yanagida.* Texts and monographs in physics. Springer, Berlin ;, 2003.

[111] Z.-z. Xing and Z.-h. Zhao. The effective neutrino mass of neutrinoless double-beta decays: how possible to fall into a well. *The European Physical Journal C*, 77(3):192, 2017.

[112] P. B. Denton and J. Gehrlein. Survey of neutrino flavor predictions and the neutrinoless double beta decay funnel. *Phys. Rev. D*, 109:055028, Mar 2024.

[113] M. Agostini et al. Testing the inverted neutrino mass ordering with neutrinoless double-β decay. *Phys. Rev. C*, 104:L042501, Oct 2021.

[114] J. Kotila and F. Iachello. Phase-space factors for double-β decay. *Phys. Rev. C*, 85:034316, Mar 2012.

[115] V. N. Aseev et al. An upper limit on electron antineutrino mass from Troitsk experiment. *Phys. Rev. D*, 84:112003, 2011.

[116] C. Kraus et al. Final results from phase ii of the mainz neutrino mass searchin tritium β decay. *The European Physical Journal C - Particles and Fields*, 40(4):447–468, 2005.

[117] J. Angrik et al. KATRIN design report 2004. Technical report, KATRIN, 2 2005.

[118] M. Aker et al. Search for kev-scale sterile neutrinos with the first katrin data. *The European Physical Journal C*, 83(8):763, 2023.

[119] M. Aker et al. KATRIN: status and prospects for the neutrino mass and beyond. *J. Phys. G*, 49(10):100501, 2022.

[120] T. Houdy et al. Hunting kev sterile neutrinos with katrin: building the first tristan module. *Journal of Physics: Conference Series*, 1468:012177, 02 2020.

[121] S. Mertens et al. A novel detector system for katrin to search for kev-scale sterile neutrinos. *Journal of Physics G: Nuclear and Particle Physics*, 46:065203, 06 2019.

[122] M. Drewes et al. A White Paper on keV Sterile Neutrino Dark Matter. *JCAP*, 01:025, 2017.

[123] B. Monreal and P. . Collaboration. Project 8: Update on a radiofrequency tritium spectrometer. In *AIP Conference Proceedings*, volume 1441, pp. 441–443. American Institute of Physics, 2012.

[124] P. J. Doe et al. Project 8: Determining neutrino mass from tritium beta decay using a frequency-based method. In *Snowmass 2013: Snowmass on the Mississippi*, 9 2013.

[125] G. Hupin et al. Ab initio predictions for polarized deuterium-tritium thermonuclear fusion. *Nature Communications*, 10(1):351, 2019.

[126] M. Mikirtychyants et al. The Polarized H and D Atomic Beam Source for ANKE at COSY-Jülich. *Nucl. Instrum. Meth. A*, 721:83–98, 2013.

[127] G. Ciullo et al. The polarised internal target for the pax experiment. *Journal of Physics: Conference Series*, 295:012150, 05 2011.

[128] A. A. Esfahani et al. The Project 8 Neutrino Mass Experiment. In *Snowmass 2021*, 3 2022.

[129] A. Ashtari Esfahani et al. Determining the neutrino mass with cyclotron radiation emission spectroscopy—Project 8. *J. Phys. G*, 44(5):054004, 2017.

[130] B. Clark. Magnetic Trapping of Atomic Tritium for Neutrino Mass Measurement. *California Institute of Technology*, 2014.

[131] M. Agostini et al. Toward the discovery of matter creation with neutrinoless $\beta\beta$ decay. *Rev. Mod. Phys.*, 95:025002, May 2023.

[132] S. Goswami et al. Neutrinoless double beta decay: 2015 review. *Advances in High Energy Physics*, 2016:2162659, 2016.

[133] S. Abe et al. Search for the majorana nature of neutrinos in the inverted mass ordering region with kamland-zen. *Phys. Rev. Lett.*, 130:051801, Jan 2023.

[134] M. Chen. Neutrinoless double beta decay experiments. *Journal of Physics: Conference Series*, 598:012008, 04 2015.

[135] S. Ajimura et al. Low background measurement in candles-iii for studying the neutrinoless double beta decay of ^{48}Ca. *Phys. Rev. D*, 103:092008, May 2021.

[136] K.-H. Ackermann et al. The gerda experiment for the search of $0\nu\beta\beta$ decay in 76ge. *The European Physical Journal C*, 73(3):2330, 2013.

[137] M. Agostini et al. Final results of gerda on the search for neutrinoless double-β decay. *Phys. Rev. Lett.*, 125:252502, Dec 2020.

[138] G. Marshall. Legend-200 first operational results. In *2023 IoP Joint APP and HEPP Annual Conference*, 2023.

[139] W. Armstrong et al. CUPID pre-CDR. working paper, September 2019.

[140] K. Alfonso et al. Cupid: The next-generation neutrinoless double beta decay experiment. *Journal of Low Temperature Physics*, 211(5):375–383, 2023.

[141] J. Shirai. KamLAND-Zen experiment. *PoS*, HQL2018:050, 2018.

[142] A. Li et al. Kamnet: An integrated spatiotemporal deep neural network for rare event searches in kamland-zen. *Phys. Rev. C*, 107:014323, Jan 2023.

[143] K. Ichimura. Recent results from KamLAND-Zen. *PoS*, NOW2022:067, 2023.

[144] G. Cowan et al. Asymptotic formulae for likelihood-based tests of new physics. *The European Physical Journal C*, 71(2), Feb 2011.

[145] M. González-Alonso and J. Martin Camalich. Isospin breaking in the nucleon mass and the sensitivity of β decays to new physics. *Phys. Rev. Lett.*, 112:042501, Jan 2014.

[146] T. Bhattacharya et al. Neutron electric dipole moment and tensor charges from lattice qcd. *Phys. Rev. Lett.*, 115:212002, Nov 2015.

[147] A. Falkowski et al. Eft at faserν. *Journal of High Energy Physics*, 2021(10):86, 2021.

[148] J. C. Hardy and I. S. Towner. Superallowed $0^+ \rightarrow 0^+$ nuclear β decays: A new survey with precision tests of the conserved vector current hypothesis and the standard model. *Phys. Rev. C*, 79:055502, May 2009.

[149] T. Bhattacharya et al. Probing novel scalar and tensor interactions from (ultra)cold neutrons to the lhc. *Phys. Rev. D*, 85:054512, Mar 2012.

[150] V. Cirigliano et al. Non-standard charged current interactions: beta decays versus the lhc. *Journal of High Energy Physics*, 2013(2):46, 2013.

[151] M. Bychkov et al. New precise measurement of the pion weak form factors in $\pi^+ \rightarrow e^+ \nu \gamma$ decay. *Phys. Rev. Lett.*, 103:051802, Jul 2009.

[152] M. Allet et al. Search for time-reversal violation in the beta decay of li^8. *Phys. Rev. Lett.*, 68:572–575, Feb 1992.

[153] V. Cirigliano et al. Beta decays and non-standard interactions in the lhc era. *Progress in Particle and Nuclear Physics*, 71:93–118, 2013. Fundamental Symmetries in the Era of the LHC.

[154] N. Severijns et al. Tests of the standard electroweak model in nuclear beta decay. *Rev. Mod. Phys.*, 78:991–1040, Sep 2006.

[155] V. Cirigliano et al. Semileptonic decays of light quarks beyond the standard model. *Nuclear Physics B*, 830(1):95–115, 2010.

[156] T. E. Chupp et al. Search for a *t*-odd, *p*-even triple correlation in neutron decay. *Phys. Rev. C*, 86:035505, Sep 2012.

[157] A. Boyarsky et al. Sterile neutrino Dark Matter. *Prog. Part. Nucl. Phys.*, 104:1–45, 2019.

[158] K. H. Hiddemann et al. Limits on neutrino masses from the tritium beta spectrum. *Journal of Physics G: Nuclear and Particle Physics*, 21(5):639, may 1995.

[159] C. Kraus et al. Limit on sterile neutrino contribution from the mainz neutrino mass experiment. *The European Physical Journal C*, 73(2):2323, 2013.

[160] A. I. Belesev et al. The search for an additional neutrino mass eigenstate in the 2–100 ev region from 'troitsk nu-mass' data: a detailed analysis. *Journal of Physics G: Nuclear and Particle Physics*, 41(1):015001, dec 2013.

[161] J. N. Abdurashitov et al. First measurements in search for kev sterile neutrino in tritium beta-decay in the troitsk nu-mass experiment. *JETP Letters*, 105(12):753–757, 2017.

[162] E. Holzschuh et al. Search for heavy neutrinos in the β-spectrum of 63ni. *Physics Letters B*, 451(1):247–255, 1999.

[163] K. C. Ng et al. New constraints on sterile neutrino dark matter from nustar m31 observations. *Physical Review D*, 99(8):083005, 2019.

[164] A. C. Vincent et al. Revisiting cosmological bounds on sterile neutrinos. *Journal of Cosmology and Astroparticle Physics*, 2015(04):006, 2015.

[165] X. Shi and G. Sigl. A Type II supernovae constraint on electron-neutrino - sterile-neutrino mixing. *Phys. Lett. B*, 323:360–366, 1994. [Erratum: Phys.Lett.B 324, 516–516 (1994)].

[166] C. Martoff et al. Hunter: precision massive-neutrino search based on a laser cooled atomic source. *Quantum Science and Technology*, 6(2):024008, 2021.

[167] I. Mocioiu et al. Low-energy limits on the antisymmetric tensor field background on the brane and on the non-commutative scale. *Physics Letters B*, 489(3):390–396, 2000.

[168] J. Alfaro. Quantum gravity and lorentz invariance violation in the standard model. *Phys. Rev. Lett.*, 94:221302, Jun 2005.

[169] V. A. Kostelecký and S. Samuel. Spontaneous breaking of lorentz symmetry in string theory. *Phys. Rev. D*, 39:683–685, Jan 1989.

[170] H. Martínez-Huerta et al. Lorentz invariance violation tests in astroparticle physics. *Symmetry*, 12(8), 2020.

[171] B. Altschul. Laboratory bounds on electron lorentz violation. *Phys. Rev. D*, 82:016002, Jul 2010.

[172] Y. Ding and M. F. Rawnak. Lorentz and *cpt* tests with charge-to-mass ratio comparisons in penning traps. *Phys. Rev. D*, 102:056009, Sep 2020.

[173] P. Wolf et al. Cold atom clock test of lorentz invariance in the matter sector. *Phys. Rev. Lett.*, 96:060801, Feb 2006.

[174] V. A. Kostelecký and Z. Li. Gauge field theories with lorentz-violating operators of arbitrary dimension. *Phys. Rev. D*, 99:056016, Mar 2019.

[175] J. P. Noordmans et al. Lorentz violation in neutron decay and allowed nuclear β decay. *Phys. Rev. C*, 87:055502, May 2013.

[176] K. K. Vos et al. Exploration of Lorentz violation in neutral-kaon decay. *Phys. Lett. B*, 729:112–116, 2014.

[177] J. P. Noordmans et al. Question of lorentz violation in muon decay. *Phys. Rev. D*, 93:116001, Jun 2016.

[178] B. Altschul. Contributions to Pion Decay from Lorentz Violation in the Weak Sector. *Phys. Rev. D*, 88:076015, 2013.

[179] S. E. Müller et al. First test of lorentz invariance in the weak decay of polarized nuclei. *Phys. Rev. D*, 88:071901, Oct 2013.

[180] J. P. Noordmans et al. Limits on Lorentz violation from forbidden β decays. *Phys. Rev. Lett.*, 111(17):171601, 2013.

[181] G. Amelino-Camelia et al. Tests of quantum gravity from observations of γ-ray bursts. *Nature*, 393(6687):763–765, 1998.

[182] S. Coleman and S. L. Glashow. High-energy tests of lorentz invariance. *Phys. Rev. D*, 59:116008, Apr 1999.

[183] J. M. Carmona and J. L. Cortes. Testing Lorentz invariance violations in the tritium beta decay anomaly. *Phys. Lett. B*, 494:75–80, 2000.

[184] R. Lehnert. Beta-decay spectrum and lorentz violation. *Physics Letters B*, 828:137017, 2022.

[185] I. Mocioiu et al. Low-energy limits on the antisymmetric tensor field background on the brane and on the non-commutative scale. *Physics Letters B*, 489(3):390–396, 2000.

[186] F. Klinkhamer. A cpt anomaly. *Nuclear Physics B*, 578(1):277–289, 2000.

[187] J. S. Díaz et al. Relativity violations and beta decay. *Phys. Rev. D*, 88:071902, Oct 2013.

[188] E. G. Myers et al. Atomic masses of tritium and helium-3. *Phys. Rev. Lett.*, 114:013003, Jan 2015.

[189] V. A. Kostelecký and M. Mewes. Neutrinos with lorentz-violating operators of arbitrary dimension. *Phys. Rev. D*, 85:096005, May 2012.

[190] M. Aker et al. Search for Lorentz-invariance violation with the first KATRIN data. *Phys. Rev. D*, 107(8):082005, 2023.

[191] H. W. Crater and P. Van Alstine. Two-body dirac equations for particles interacting through world scalar and vector potentials. *Phys. Rev. D*, 36:3007–3036, Nov 1987.

[192] J. Aguirregabiria et al. The liénard–wiechert potential and the retarded shape of a moving sphere. *American journal of physics*, 60(7):597–599, 1992.

[193] F. Bischoff et al. Computing many-body wave functions with guaranteed precision: The first-order moller-plesset wave function for the ground state of helium atom. *The Journal of chemical physics*, 137:104103, 09 2012.

[194] J. P. Noordmans et al. Lorentz violation in neutron decay and allowed nuclear β decay. *Phys. Rev. C*, 87:055502, May 2013.

[195] L. D. Landau and L. M. Lifshitz. *Quantum Mechanics Non-Relativistic The-ory, Third Edition: Volume 3*. Butterworth-Heinemann, 3 edition, January 1981.

[196] M. Doi et al. Double Beta Decay and Majorana Neutrino. *Progress of Theo-retical Physics Supplement*, 83:1–175, 03 1985.

[197] J. Suhonen and J. Kostensalo. Double β decay and the axial strength. *Fron-tiers in Physics*, 7:29, 03 2019.

[198] J. T. Suhonen. Value of the Axial-Vector Coupling Strength in β and $\beta\beta$ Decays: A Review. *Front. in Phys.*, 5:55, 2017.

[199] F. Šimkovic et al. Improved description of the $2\nu\beta\beta$-decay and a possibil-ity to determine the effective axial-vector coupling constant. *Phys. Rev. C*, 97:034315, Mar 2018.

[200] B. Pritychenko. Systematic analysis of double-beta decay half lives. *Nuclear Physics A*, 1033:122628, 2023.

[201] M. Schwarz et al. Liquid Argon Instrumentation and Monitoring in LEGEND-200. *EPJ Web Conf.*, 253:11014, 2021.

[202] I. C. Bandac et al. The $0\nu2\beta$-decay CROSS experiment: preliminary results and prospects. *JHEP*, 01:018, 2020.

[203] M. Koga. Kamland-zen 800 status and future prospects. Paper presented at ICNFP (available online), 2017.

[204] A. Gando et al. Precision analysis of the ^{136}Xe two-neutrino $\beta\beta$ spectrum in kamland-zen and its impact on the quenching of nuclear matrix elements. *Phys. Rev. Lett.*, 122:192501, May 2019.